THÈSE POUR OBTENIR LE GRADE DE DOCTEUR
DE L'UNIVERSITÉ DE MONTPELLIER

Spécialité :	Mathématiques et Modélisation
École doctorale :	Information, Structures, Systèmes
Unité de recherche :	Institut Montpelliérain Alexander Grothendieck
Partenariat international :	Politecnico di Milano, Italie

Méthodes Hybrides d'Ordre Élevé pour les problèmes d'interface

Présentée par Florent CHAVE

Le 12 novembre 2018

Sous la direction de Daniele A. Di Pietro & Luca Formaggia

Devant le jury composé de

Stefano BERRONE	Professeur des universités	Politecnico di Torino	Rapporteur
Daniele A. DI PIETRO	Professeur des universités	Université de Montpellier	Directeur
Luca FORMAGGIA	Professeur des universités	Politecnico di Milano	Co-directeur
Florence HUBERT	Professeur des universités	Aix-Marseille Université	Présidente du jury
Roland MASSON	Professeur des universités	Université de Nice Sophia Antipolis	Rapporteur

UNIVERSITÉ DE MONTPELLIER

POLITECNICO MILANO 1863

UNIVERSITÉ FRANCO ITALIENNE | UNIVERSITÀ ITALO FRANCESE

Acknowledgements

"Festina lente"

Je tiens avant tout à remercier **Daniele A. Di Pietro** pour l'encadrement exceptionnel dont j'ai bénéficié depuis mon stage de Master et qui a débuté avec cet adage latin, véritable maître-mot des années qui suivirent. Tes encouragements et ton soutien sans faille durant toutes ces années ont été plus qu'appréciés, et tes qualités humaines ont rendu le déroulement de cette thèse on ne peut plus agréable.

I would like to express my huge gratitude to my second supervisor, **Luca Formaggia**, for welcoming me in Politecnico di Milano within best conditions. Thank you for your kindness, your listening and for all the time we have spent together discussing the problems I encountered working on reduced models.

I would also like to express my sincere gratitude to **Stefano Beronne** and **Roland Masson**, who have accepted the heavy task to be referees, for the interest they shown in my work and their pertinent suggestions. Je remercie également vivement **Florence Hubert** d'avoir accepté de présider ce jury.

À l'IMAG, je souhaite remercier **Fabien Marche** avec qui j'ai eu l'opportunité de travailler durant mon stage de Master, l'ensemble des membres permaments avec qui j'ai eu l'occasion d'échanger, notamment **Vanessa Lleras**, et ceux dont j'ai eu la chance d'être l'élève durant mes années d'études. Un grand merci au personnel administratif, ces héros de l'ombre, et notamment à **Bernadette Lacan** pour son efficacité redoutable et son extrême patience. Je remercie enfin les (anciens) (post) doctorants pour leur bonne humeur quotidienne, et plus particulièrement ceux avec qui j'ai partagé mon bureau : les anciens **Walid Al Akhras**, **Fatima Palacios-Rodriguez**, **Alice Raeli**, **Roberta Tittarelli**, les nouveaux **Tom Ferragut** et **Samia Louchene** (bon courage à vous), et bien entendu à **Michele Botti** avec qui j'ai partagé des moments mémorables lors de conférences aux quatres coins du globe. Une pensée à la nouvelle génération HHO **André Harnist** : du courage h^{k+2} !

Au Politecnico, un *grazie* à **Francesco Bonaldi** et à l'équipe de l'ancien **Tender** pour cette année sportive et ces *aperitivo* improvisés de fin de journée.

Je suis très reconnaissant envers **Françoise Darrieumerlou**, qui a eu la gentillesse et le courage de passer au crible les coquilles d'une partie de ce manuscrit.

Une pensée également aux personnes rencontrées le temps d'une conférence qui ont donné à ces voyages une dimension humaine.

En dehors de cette belle aventure scientifique, je souhaiterais remercier mes amis proches qui ont fait en sorte que ces années aient été supportables au jour le jour et qui ont contribué, à leur manière, à la réalisation de cette thèse: **Alexandre** Baldare, **Paul** Bartholmey, **Aurélien** Binet, **Michele** Botti, **Maxime** Bruguet, **Swan** Brun, **Coralie** François, **Anaïs-Taos** Himeur, **Arthur** Jean-Angèle, **Severin** Maran, **Félix** Marcotte-Ruffin, **Timothée** Mauranyapin **François** Meynard, **Chloé** Michelluti, **Thomas** Morel, **Perrine** Morizot, **Adrien** Peñas, **Alexandre** Puyguiraud, **Rita** Riedlbeck, **Celia** Salgues et ses trois hommes, **Dorian** Vérone, **Quentin** Vazel, **Kyllian** Wecke, et mes excuses à ceux et celles que j'aurais oublié de mentionner. Pour avoir fait des kilomètres quand j'étais à Paris ou Milan, pour avoir tendu l'oreille quand il le fallait, pour m'avoir extirpé de ce quotidien parfois usant de la thèse pour lever le coude ou pour m'avoir fait l'honneur de votre présence en ce jour si particulier : tout simplement merci.

L'aventure milanaise n'aurait certainement pas été la même sans **Arnaud** Castanet, **Bastien** Hamlat, **Joffrey** Dumont, **Tom** Irigoyen, et bien évidemment **Pauline** Boichon qui nous a supportés, mon frère et moi, tout le long de cette année italienne et avec qui nous formions un formidable trio.

Une pensée aux sportifs de haut niveau, **Pierre-Etienne** Alary et **Baptiste** Oger, que j'ai honteusement lâchés durant cette dernière ligne droite.

C'est à présent à ma famille que je souhaite exprimer mon éternelle reconnaissance tant ils ont fait pour moi. Merci à mes grands-parents d'être si présent à mes côtés depuis mon plus jeune âge. Merci à mes frangins pour ces moments de complicité qui ont su faire passer la thèse au second plan à maintes reprises. Une mention spéciale à Dorian, toujours à l'écoute, sans qui l'aventure milanaise aurait été beaucoup moins marrante et festive. Enfin, merci à mes parents pour tout l'amour dont ils m'ont entouré, pour l'éducation dont j'ai bénéficié, les valeurs qu'ils m'ont inculqué et pour le support inconditionnel dont ils font preuve depuis si longtemps déjà. Merci d'avoir déplacé des montagnes pour que je puisse écrire ces lignes aujourd'hui. Les mots me manque pour vous dire à quel point je vous suis éperdument reconnaissant et tant je suis si fier de vous avoir à mes côtés.

Je ne peux terminer sans remercier Cynthia pour sa présence et son immuable soutien, tous deux précieux en cette période de rédaction : merci d'être là.

Contents

Introduction

Contents

In this Ph.D. thesis we develop Hybrid High-Order methods for the numerical approximation of interface problems. Specifically, two kinds of interfaces are considered here: diffuse interfaces and interfaces that act as internal boundaries. In this introductive chapter, we discuss the motivations and the context of the Ph.D. thesis, illustrate the problems we focus on, and summarize the main results.

1 Motivations, context, and manuscript structure

The main goal of this Ph.D. thesis is to apply the recently introduced Hybrid High-Order (HHO) technology to interface problems. In this section we provide a brief state-of-the-art for HHO methods, then we discuss their advantageous features in the context of the interface problems considered here. We close this section by describing the structure of the manuscript.

Hybrid High-Order methods: A state-of-the-art

Hybrid High-Order methods are a family of new generation numerical methods for Partial Differential Equations (PDEs) originally introduced in [77, 83]. The term *Hybrid* refers to the fact that two kinds of discrete unknowns are used, namely broken polynomial on the mesh and its skeleton. The term *High-Order* emphasizes the possibility to arbitrarily increase the approximation order to accelerate convergence in the presence of (locally) regular solution or when resorting to adaptive techniques.

The cornerstones of HHO methods are: (i) *local reconstructions* of the relevant (differential) operators obtained by mimicking integration by parts formulas where the hybrid discrete unknowns play the role of the function inside each element and on its faces; (ii) *stabilization terms* obtained by penalizing high-order residuals which vanish when applied to the interpolate of polynomial functions up to a suitable degree. This subtle construction confers a number of attractive features to the method: (i) it supports fairly general polytopal meshes, possibly containing polygonal elements and nonmatching faces; (ii) it allows arbitrary approximation orders; (iii) it delivers inf-sup stable discretizations of mixed problems; (iv) it is locally conservative; (v) it can be efficiently implemented by statically condensing element-based discrete unknowns; (vi) its construction is independent of the space dimension.

Since their introduction, HHO methods have experienced a vigorous development, and have been used to discretize several linear and nonlinear PDE problems arising in various fields of computational physics. Besides the original works on variable diffusion [78, 82, 83] and quasi incompressible linear elasticity [77, 80], we can cite applications to locally degenerate diffusion-advection-reaction [75], poroelasticity [29], creeping flows [5] possibly driven by volumetric forces with large irrotational part [84], electrostatics [85, 88], incompressible flows governed by the Oseen [6] or Navier–Stokes equations [37, 86], nonlinear elasticity and poroelasticity [38, 39], finite deformations of hyperelastic materials [2], incremental associative plasticity with small deformations [1], adaptive yield surface detection for Bingham pipe flows [54], spectral approximation of elliptic operators [53], or elliptic interface [50], elliptic obstacle problems [64], Kirchhoff–Love plate bending [32], nonlinear Leray–Lions elliptic operators [73, 74], the Brinkman problem [36] and highly oscillatory elliptic problems [65]. In [63], authors present a generic implementation of the HHO method on arbitrary-dimensional polytopal meshes. Recent extensions of the original method include, e.g., the adaptive [88] and *hp*-versions [7] as well as the support of meshes with curved faces [35],

We conclude this introductory section by noticing that polytopal methods are a very active research subject, and links exist between HHO and other recent

technologies, including Hybridizable Discontinuous Galerkin methods [55, 69], mixed [21] and nonconforming [18] Virtual Element methods, and Gradient Discretizations [91]. The lowest-order version can additionally be bridged to Mixed [90] and Hybrid [96] Finite Volumes and Mimetic Finite Differences methods [47, 48, 117]. For the details, we refer the reader to [31, 68, 76].

Applications to interface problems

Besides the general features discussed in the previous section, HHO methods display specific advantages in the context of the interface problems considered in this manuscript, which we briefly discuss here.

Diffuse interface models

Diffuse interface models describe the evolution of systems where two (or, possibly, more) non-miscible phases are present. These models are based on a thermodynamic description of fluids endowed with *internal capillarity*, i.e., such that their energy depends not only on its density and temperature but also on its density gradient; see [114]. Several industrial processes involve multiphase flows driven by capillary effects. The original motivation for the application considered in Chapter 1 was a collaboration with Saint–Gobain Recherche, where diffuse interface models are used to simulate phenomena such as (i) the fouling of tubes of thermoplastic elastomers used in beverage distribution and (ii) the early stages of glass production, which involve wetting liquid on grains more resistant to melting. The optimization of these processes requires a better understanding of local phenomena, which, considering the involved scales, are strongly influenced by capillary forces.

The defining feature of diffuse interface models is that the interface is not explicitly tracked, but rather described by means of a smooth function c, called *order-parameter*, which takes a constant value (typically ± 1) inside each phase and varies continuously between these two values over a characteristic length γ; see Figure 1a. As explained in [42, 113], the diffuse interface approach can be regarded as a regularization of sharp-interface models, where each phase is governed by a system of PDEs and links among the phases are established by enforcing transmission conditions at the interface. In sharp interface models the interface between the two phases is often numerically described as the zero level set of a smooth function, and the calculations of the exact sharp-interface equations generally require adaptive, interface fitting grids. In practice, the sharp-interface approach presents serious challenges for flows which, like the ones considered here, involve a large number of interfaces as well as splitting and coalescence phenomena; see, e.g., Figure 1b, where we display the simulation of the early stage

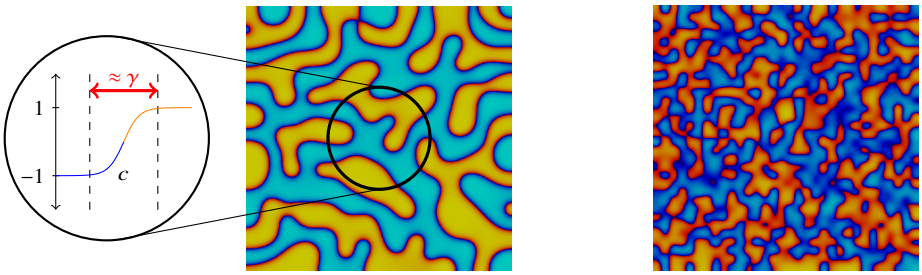

(a) Variation of the order parameter between two phases

(b) Numerical simulation of the early stage of a spinodal decomposition

Figure 1: Description of phases using diffuse interface models (left) and simulation of a spinodal decomposition involving a large number of interfaces (right).

of a spinodal decomposition. These difficulties are even more pronounced in three space dimensions. In diffuse interface models, on the other hand, concentrated terms and discontinuities at the interface are smoothed out by distributing them over thin but numerically resolvable layers, and calculations can be carried out on fixed grids. This entails significant simplifications from a practical point of view.

In the context of diffusive interface modelling, the selected discretization method has to match some requirements in order to obtain simulations that capture the phase separation with sufficient accuracy. As a matter of fact, high gradient areas are located near the interface and, when considering spinodal decomposition (see Section 2 below), these areas are spread all over the computational domain, making local adaptation ineffective; see, e.g., Figure 1b. Since HHO methods are based on fully discontinuous polynomial spaces, they can accomodate by construction these abrupt varations between the phases. Additionally, the possibility to increase the approximation order makes it possible to capture fine details also on relatively coarse meshes. Finally, when considering problems with localized interfaces, for which local mesh adaptation is an effective option, HHO methods provide an unprecedented flexibility thanks to the seamless support of nonconforming mesh refinement or derefinement by element agglomeration; see [35, 88].

The main contribution of this Ph.D. thesis to the numerical approximation of diffuse interface models is the design and analysis of a novel HHO method for the Cahn–Hilliard equations, a diffuse interface model used to describe the process of phase separation. Using a variant of the original HHO method of [83] with enriched element spaces, we are able to prove the well posedness of the discrete formulation and optimal convergence rates for the energy-norm of the discretization error. The analysis hinges on new discrete functional analysis results on hybrid polynomial spaces valid in two and three space dimensions, namely discrete Agmon and

Gagliardo–Nirenberg–Poincaré inequalities. A comprehensive panel of numerical experiments is proposed to confirm the theoretical results and showcase the ability of the method to track interfaces, even in the presence of strong advective fields. These works have given rise to one full-length paper appeared in SIAM Journal on Numerical Analysis [59], as well as to a conference proceeding [58].

Internal boundaries

The second kind of interfaces considered here are internal boundaries. Specifically, we focus on the numerical approximation of flow and passive transport in fractured porous media. This is an extremely active research field in computational geosciences due to the very large number of possible applications including, e.g.: oil recovery, hydraulic fracturing, geological CO_2 storage or toxic/radioactive waste underground burying.

Fractures in the subsurface are ubiquitous, and can be caused by tectonic forces, changes of temperature, drying processes, by leaching in the plane of stratification, or by schistosity; see, e.g., [123]. Generally grouped in the category of fractures are: *cracks*, i.e., partial or incomplete fractures; *fissures*, which exhibit a distinct separation of the surfaces; *joints*, i.e., surfaces of fracture without displacement; *gashes*, that are small-scale tension fissures from several centimeters to a few decimeters in length and from several millimeters to a few centimeters in width.

The relevant feature of fractures is that the characteristic dimension in one direction is much smaller than the other two. Despite this difference of scales, their presence in a porous medium can have a sizeable impact on the flow patterns. As a matter of fact, fractures can have dramatically different permeability values with respect to the surrounding porous medium, and can therefore act as natural barriers for the flow, or, on the contrary, act as natural conduits and accelerate the migration process of hazardous contaminants. In the context of oil recovery it has been observed, e.g., that fractures near boreholes tend to increase the productivity of wells; see, e.g., [127] and references therein. In the context of the geological isolation of radioactive waste, on the other hand, the presence of fractures in the disposal areas (e.g., due to tunnel excavation) can drastically accelerate the migration process of radionuclides.

Developing robust and accurate numerical schemes to capture such phenomena is crucial to carry out reliable numerical simulations, a paramount tool to ensure environmental and human protection. In this context, the robustness of HHO methods with respect to the anisotropy and heterogeneity of the physical coefficients consistutes a real asset. Moreover, as pointed out in the previous section, the broken polynomial spaces underlying HHO methods can accommodate abrupt variations of the unknowns across the fracture. Also, the support of general polyhedral meshes enables a seamless treatment of complex geometric features

such as hanging nodes and nonmatching fracture interfaces. Finally, the local conservation properties of HHO play a key role not only in reproducing key physical principles at the discrete level, but also in the flow-transport coupling.

The main contributions of this Ph.D. thesis are (i) the design and analysis of a HHO method for reduced models of Darcy flows in fracture porous media, that is, models where fractures are treated as interfaces; (ii) the introduction, stability analysis, and numerical validation of a new reduced model, based on an energy argument, describing passive transport in fractured porous media. To obtain the flow, we use a mixed [78] combined with a primal [82] HHO method for variable diffusion, and prove the well posedness of the discrete formulation and optimal convergence rates for the energy-norm of the discretization error. The analysis hinges in the close link between error estimate of mixed and primal HHO formulations. On the other hand, using the HHO method of [75], we solve the new reduced passive transport model driven by a velocity field solution of the decoupled flow problem. Both works contain extensive numerical validation, displaying the ability of the method to capture the flow behavior and the resulting passive transport phenomena accounting for the presence, location, and permeability of fractures. These works have given rise to one full-length paper appeared in SIAM Journal on Scientific Computing [56] and one full-length paper submitted to the International Journal on Geomathematics [57].

Structure of the manuscript

The manuscript is organized as follows. In **Chapter** 1, taken from [59], we develop a fully implicit HHO algorithm for the Cahn–Hilliard problem, a diffuse interface model used to describe the process of phase separation. This work was originally motivated by an industrial collaboration with Saint–Gobain Research. We define the discrete local tools, set the global discrete problem and perform a detailed stability and convergence study, proving optimal convergence rates in energy-like norms. Numerical validation is also provided using some of the most common tests in the literature.

In **Chapter** 2, taken from [56], we develop a HHO method for the simulation of Darcy flows in fractured porous media. We define the discrete local tools in the porous medium and in the fracture, and set the global discrete problem. We then prove the well-posedness of the discrete problem and optimal convergence of the discretization error measured in an energy-like norm. In the error estimate, we explicitly track the dependence of the constants on the problem data, showing that the multiplicative constant have only a mild dependence on the variations of the latter. The numerical validation on a comprehensive set of test cases confirms the theoretical results.

In **Chapter** 3, taken from [57], we propose a new reduced model for the passive

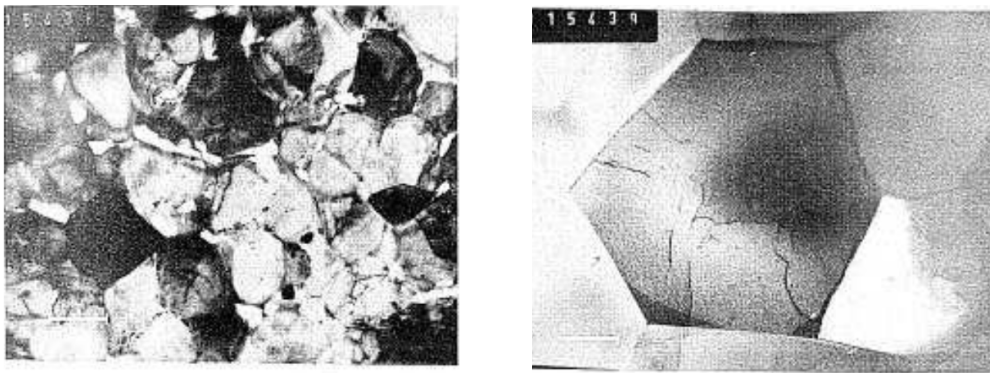

(a) Directly after *hypertrempe* (b) *Hypertrempe* after 30min at 235°c

Figure 2: Spinodal decomposition: Zinc-Aluminium alloy

transport of a solute in a fractured porous medium. The transmission conditions are derived using an energy argument and, unlike other works in the literature, enable jumps of the solute concentration across the fracture. We define the discrete local tools of the HHO method, then set the global discrete problem and study its stability. We study numerically the convergence rate delivered by the method, and display numerical experiments in which we treat fractures as barriers or conduits.

In **Appendix** A, taken from [58], we treat the convective Cahn–Hilliard problem. We recall the HHO discrete settings from **Chapter 1** and define, locally, a convective derivative reconstruction operator by mimicking an integration by parts formula using the hybrid discrete unknowns. We set the global discrete problem and an extensive numerical validation is presented, which shows the robustness of the method with respect to some user parameters.

2 The Cahn–Hilliard problem

In this section we introduce the Cahn–Hilliard equations and resume our main contributions to their numerical approximation.

The Cahn–Hilliard equations model *phase separation*, that is, the process by which a binary fluid separates into regions pure in each component. Such a process can be observed, e.g., when the binary fluid is heated to a high temperature for a certain time and then abruptly cooled: the fluid becomes inhomogeneous with phases separated in well-defined high concentration areas, and we observe a partial or total nucleation, called *spinodal decomposition*.

In what follows, we provide a few examples of physical processes where phase separation occurs. In Figure 2, we display snapshots of a Zinc-Aluminium (ZA) 9.35%a.t. alloy observed by electron microscopy; see [124]. The alloy has been

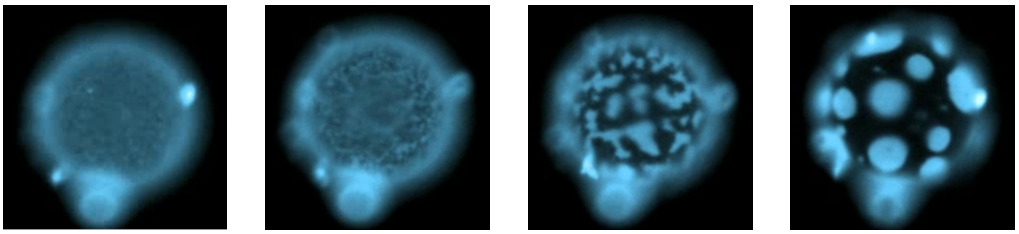

(a) $t = 0$ (b) $t = 5$ (c) $t = 10$ (d) $t = 20$

Figure 3: Spinodal decomposition: unsaturated lipids (in black) and saturated lipids with cholesterol (in blue)

prepared according to the following protocol, called *hypertrempe*: in a vacuum chamber, a small quantity of alloy is brought to the liquid state, then projected and crushed between two copper plates. It is then cut to have samples whose thickness varies between 60 and 140 microns. In Figure 2a we depict the ZA alloy directly after hypertrempe while, in Figure 2b we show the same alloy after 30 minutes in the liquid state (235°C), displaying a clear separation of the alloy components.

Another example is the spinodal decomposition of a lipid sample[1]; see Figure 3 (the size of the sphere is approximatively 20-30μm). We depict the evolution of the interactions between the lipids with respect to the time t (in seconds), that lead to the formation of groups of, respectively, saturated lipids and cholesterol (in blue), and unsaturated lipids (in black). At $t = 0$, the mixture is homogeneous, at $t = 10$ we start seeing the two different phases that emerge and, finally, at $t = 20$ we can clearly see the distinction between phases.

Other examples of phenomena which can be modelled by the Cahn–Hilliard equations include tumor growth [9, 104, 105, 130], image inpainting, to fill parts of missing or damaged images using information from surrounding areas of grayvalued [34, 61] or colored images [60], and even the structure of Saturn's rings in astronomy [126].

Formulation of the model

From the mathematical point of view, denoting by Ω the computational domain and by $(0, t_F)$ the time interval, the isothermal Cahn–Hilliard model for diphasic fluids is driven by the minimisation of an energy, called *free-energy*, that can be written in its simplest form as

$$\mathcal{F}(c) = \int_\Omega \Phi(c) + \frac{\gamma^2}{2}|\nabla c|^2, \quad \text{with} \quad \Phi(c) = 1/4(1 - c^2)^2. \tag{1}$$

[1]Credits: https://www.youtube.com/watch?v=kDsFP67_ZSE

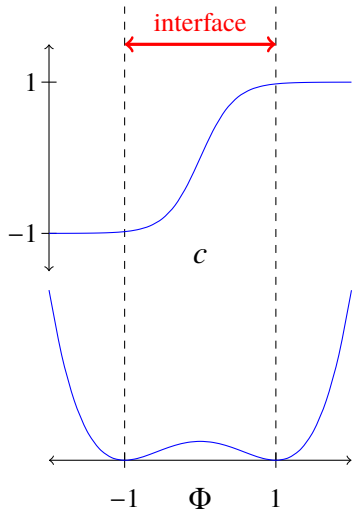

Figure 4: Variations of the order-parameter c between the two phases (top) and double-well structure of the potential Φ (bottom)

The free-energy (1) is composed of two terms: (i) the *potential term* $\Phi(c)$ models the immiscilibity of the fluid components. It has a double-well structure with minima at $c = \pm 1$ corresponding to the pure phases; see Figure 4. Its minimisation tends to reduce the interfacial zone; (ii) the *capillary term* $\frac{\gamma^2}{2}|\nabla c|^2$ which, on the contrary, penalizes the strong variations of c. Its minimization therefore tends to increase the interfacial zone.

To obtain the Cahn–Hilliard equations, we define the chemical potential w as the rate of change of the free energy $\mathcal{F}$ with respect to c, that is, the functional derivative of the free-energy by the order parameter c:

$$\int_\Omega w = \frac{\partial \mathcal{F}}{\partial c} = \int_\Omega \Phi'(c) - \gamma^2 \Delta c.$$

Using classical Fick laws and assuming unit mobility, the Cahn–Hilliard equations read

$$\begin{aligned}
\mathrm{d}_t c &= \Delta w && \text{in } \Omega \times (0, t_F), && \text{(2a)}\\
w &= \Phi'(c) - \gamma^2 \Delta c && \text{in } \Omega \times (0, t_F), && \text{(2b)}\\
c(\cdot, 0) &= c_0(\cdot) && \text{in } \Omega, && \text{(2c)}\\
-\nabla c \cdot \boldsymbol{n} &= -\nabla w \cdot \boldsymbol{n} = 0 && \text{on } \partial\Omega \times (0, t_F). && \text{(2d)}
\end{aligned}$$

From the formulation (2) stem two important properties. The first one is the *conservation of mass*, that is to say the preservation of the amount of each phase

in Ω

$$\frac{\partial}{\partial t}\int_\Omega c = \int_\Omega \mathrm{d}_t c = \int_\Omega \Delta w = \int_{\partial\Omega} \nabla w \cdot \boldsymbol{n} = 0.$$

The second one is the *dissipation of energy*: the total free-energy of the system is always nonincreasing in time :

$$\begin{aligned}\frac{\partial}{\partial t}\mathcal{F}(c) &= \int_\Omega \left(\Phi'(c)\mathrm{d}_t c + \gamma^2 \nabla c \cdot \nabla \mathrm{d}_t c\right) = \int_\Omega \left(\Phi'(c) - \gamma^2 \Delta c\right) \mathrm{d}_t c \\ &= \int_\Omega w(\Delta w) = -\int_\Omega |\nabla w|^2 \leq 0.\end{aligned}$$

The two properties are in accordance with the requirement that the evolution of a non-equilibrium composition is to a composition of lower energy whilst conserving the mass.

By further coupling (2) with the Navier–Stokes equations, we obtain a model that can be used to describe, e.g., the spinodal decomposition of phase separating systems in an external field, the spatiotemporal evolution of the morphology of steps on crystal surfaces, or the growth of thermodynamically unstable crystal surfaces with strongly anisotropic surface tension; see [107] and references therein. A first step towards coupling is to add a convective term in the conservation equation (2a), a development considered in **Appendix** A.

The numerical approximation of the Cahn–Hilliard equation (2) has been considered in several works. Different aspects of standard finite element schemes have been studied, e.g., in [70, 93, 94]; cf. also the references therein. Mixed finite elements are considered in [99]. In [129], the authors study a nonconforming method based on C^0 shape functions for the fourth-order primal problem obtained by plugging (2b) into (2a). Discontinuous Galerkin (dG) methods have also received extensive attention. We can cite here: [131], where a local dG method is proposed for a Cahn–Hilliard system modelling multi-component alloys, and a stability analysis is carried out; [98], where optimal error estimates are proved for a dG discretization of the Cahn–Hilliard problem in primal form; [115], which contains optimal error estimates for a dG method based on the mixed formulation of the problem including a convection term; [110], where a multi-grid approach is proposed for the solution of the systems of algebraic equations arising from a dG discretization of the Cahn–Hilliard equation. In all of the above references, standard meshes are considered. General polygonal meshes in dimension $d = 2$, on the other hand, are supported by the recently proposed C^1-conforming Virtual Element (VE) method of [14] for the problem in primal formulation. Therein, the convergence analysis is carried out under the assumption that the discrete order-parameter satisfies a $C^0(L^\infty)$-like a priori bound.

Main contributions and perspectives

In **Chapter** 1, we propose a novel HHO scheme for the Cahn–Hilliard equations (2). For a fixed polynomial degree $k \geq 0$, our method is based on discrete unknowns that are polynomials of degree $(k+1)$ inside mesh elements, and polynomials of degree k on mesh faces. With this choice, and using a backward Euler scheme to march in time, we are able to prove stability of the discretization and optimal convergence as $(h^{k+1} + \delta t)$ in $C^0(H^1)$-like norm for the order-parameter and in $L^2(H^1)$-like norm for the chemical potential (with h and δt denoting, respectively, the spatial and temporal mesh sizes).

The stability of the discretization is obtained in terms of subtle uniform a priori bounds on several norms of discrete solutions. Concerning the error analysis, we estimate the difference between discrete solutions and projections of the exact ones. A higher polynomial degree inside each mesh element is requiered to obtain optimal approximation order on the energy-part of the discretization error while dealing with the nonlinear term.

From this rigorous analysis, two new discrete functional analysis results of general interest emerge: (i) the discrete Agmon's inequality of Lemma 1.7, and (ii) the discrete Gagliardo–Niremberg–Poincaré's inequalities of Lemma 1.14. Both are valid on general quasi-uniform meshes in two and three space dimensions. To prove these results, a first key point consists in defining the discrete conterpart of the Laplace and Green's operators by using an L^2-like inner product on the space of discrete unknowns. A second key point consists in replacing the standard nodal interpolator used in the proofs of [115, Lemmas 2.2 and 2.3] with the L^2-orthogonal projector which, unlike the former, is naturally defined for meshes containing polyhedral elements; see [73, 74] for a comprehensive study. We mention, in passing, that it is the first discrete analysis of the HHO method on a system of nonlinear PDEs.

We implement the method in C++ using the `hho` software platform[2], and numerically study the convergence of the method by imposing analytical solutions on the order-parameter and the chemical potential. As expected, theoretical results are confirmed by the numerical simulations. The performance of the method is demonstrated using a set of classical test cases from the literature: the evolutions of an elliptic and of a cross-shaped interface and an example of spinodal decomposition. The numerical results for the latter test case are depicted in Figure 5.

In **Appendix** A, we consider the convective Cahn–Hilliard equations and treat the convective term in the spirit of [75], where a HHO method fully robust with respect to the Péclet number was presented for a locally degenerate diffusion-

[2]Agence pour la Protection des Programmes, deposit number IDDN.FR.001.220005.000.S.P.2016.000.1080

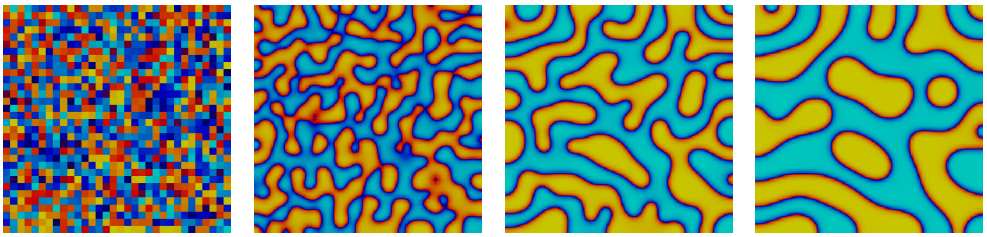

Figure 5: Numerical simulation of a spinodal decomposition

advection-reaction problem. A thorough numerical validation shows the robustness of the HHO scheme with respect to the size of the interface and the value of the Péclet number, as well as its ability to capture the interface dynamics subject to strong velocity fields. The stability and a priori error analysis of the discretization could be the subject of further work.

The results obtained in both **Chapter** 1 and **Appendix** A demonstrate the potential of the HHO method in tracking the interface dynamics. In view of its design and the features it offers, the method is a well suited tool in the context of diffuse interface simulation, and the extension towards coupling with the Navier–Stokes equations seems promising.

3 Fractured porous media

We now move to the second kind of interface model considered in this manuscript, namely interface as internal boundary. More specifically, we consider interface that represent fractures in porous media. In this section, we justify the need of reduced models in the context of fractured porous media flows and passive transport, present the reduced models we focus on, and review the main contributions of this thesis.

Continuous model for flows

We start by describing the continuous model focusing, for the sake of simplicity, on a domain crossed by a single fracture; see Figure 6. By *continuous*, we mean that the fracture is not a hyperplane, but a subdomain with a real thickness within the domain of interest Ω. We call this model *continuous* since in this case the natural conditions at the interfaces between bulk and fracture are the continuity of pressure and velocity (mass) fluxes. We can decompose $\Omega := \Omega_1 \cup \Omega_{\text{fract}} \cup \Omega_2$ in three disjoint subdomains, such that $\overline{\Omega_1} \cap \overline{\Omega_2} = \emptyset$ and $|\Omega_1|_d \approx |\Omega_2|_d \gg |\Omega_{\text{fract}}|_d > 0$, with $|\cdot|_d$ denoting the d-dimensional Hausdorff measure. The latter assumption is often verified in practice: in the context of petroleum bassin simulation, e.g., the typical thickness of a fracture is of the order of meters, while the typical length

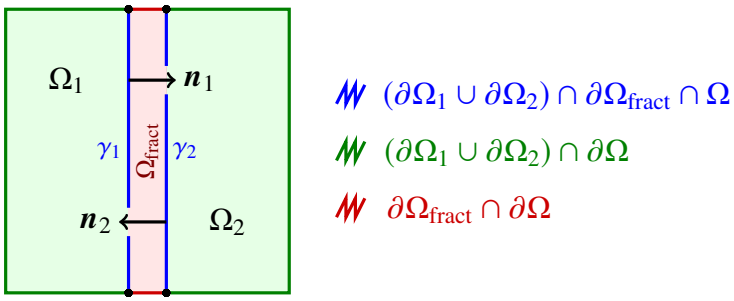

Figure 6: Illustration of the notations for the continuous model.

scale for a bassin is of the order of kilometers. For $j \in \{1,2\}$, we denote by $\gamma_j := \partial\Omega_j \cap \partial\Omega_{\text{fract}} \cap \Omega$ the boundary intersection of the subdomains Ω_j and Ω_{fract}, and by $\boldsymbol{n}_j$ the unit normal vector to γ_j pointing outward Ω_j; see Figure 6 for a representation of the notations.

Then, the continuous model for flows in fractured porous media reads (see, e.g., [101]): For all $i \in \{1, 2, \text{fract}\}$, find the Darcy velocity $\boldsymbol{u}_i : \Omega_i \to \mathbb{R}^d$ and the pressure $p_i : \Omega_i \to \mathbb{R}$ such that

$$\boldsymbol{u}_i + \boldsymbol{K}_i \nabla p_i = 0 \quad \text{in } \Omega_i, \tag{3a}$$
$$\nabla \cdot \boldsymbol{u}_i = f_i \quad \text{in } \Omega_i, \tag{3b}$$

along with adequate boundary conditions. Here, $f_i : \Omega_i \to \mathbb{R}$ is a source term that can be interpreted as modelling injection and production wells in the context of oil recovery, and $\boldsymbol{K}_i : \Omega_i \to \mathbb{R}^{d\times d}$ is the permeability tensor. Transmission conditions on γ_j for $j \in \{1,2\}$ close the problem and read as follows

$$p_j = p_{\text{fract}} \quad \text{on } \gamma_j, \tag{4a}$$
$$\boldsymbol{u}_j \cdot \boldsymbol{n}_j = \boldsymbol{u}_{\text{fract}} \cdot \boldsymbol{n}_j \quad \text{on } \gamma_j. \tag{4b}$$

These conditions express the continuity of the pressure and conservation of mass on γ_j, $j \in \{1,2\}$.

The discretization of problem (3)–(4) requires a fine mesh around the fracture to capture its length scale. On one hand, this may unduly increase the number of elements, making the simulation too expensive. On the other hand, it may result in poor mesh quality, affecting the accuracy of the numerical results. These difficulties can be overcome by resorting to a *reduced (or hybrid-dimensional) models* for the fracture, where the latter is treated as a surface of co-dimension one. Reduced models make the object of the following section.

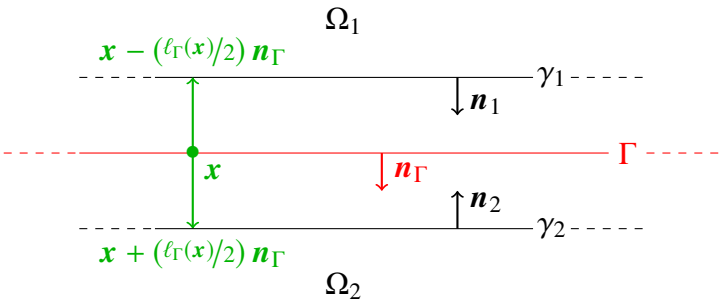

Figure 7: Representation of the averaging process along the thickness of the fracture.

Reduced model for flows

We next outline the derivation of the reduced model introduced in [120]; see also [101]. The derivation is done in two steps: first, we contract the domain Ω_{fract} into a hyperplane, then, we derive transmission conditions between the two regions.

Averaged Darcy law and conservation equation. We start by making a few assumptions on the geometry of the problem and on the data. We assume that there exists a hyperplane Γ, a fracture thickness function $\ell_\Gamma : \Gamma \to (0; +\infty)$ and a unit vector with a fixed orientation $\boldsymbol{n}_\Gamma \approx \boldsymbol{n}_1 \approx -\boldsymbol{n}_2$, normal to Γ, such that the fracture subdomain can be written as follows

$$\Omega_{\text{fract}} = \left\{ \tilde{\boldsymbol{x}} \in \Omega \ : \ \exists \boldsymbol{x} \in \Gamma \text{ and } r \in \left[-\frac{\ell_\Gamma(\boldsymbol{x})}{2}, \frac{\ell_\Gamma(\boldsymbol{x})}{2} \right] \text{ s.t. } \tilde{\boldsymbol{x}} = \boldsymbol{x} + r\boldsymbol{n}_\Gamma \right\},$$

see Figure 7 for a representation of the notations. We moreover assume that the fracture permeability tensor $\boldsymbol{K}_{\text{fract}}$ has a block-diagonal structure, that is to say

$$\boldsymbol{K}_{\text{fract}} = \begin{bmatrix} \kappa_\Gamma^n & 0 \\ 0 & \kappa_\Gamma^\tau \end{bmatrix},$$

with $\kappa_\Gamma^n : \Omega_{\text{fract}} \to \mathbb{R}$ and $\kappa_\Gamma^\tau : \Omega_{\text{fract}} \to \mathbb{R}^{(d-1)\times(d-1)}$, both constant on each transverse section of Ω_{fract}, denoting the normal and tangential fracture permeability, respectively. The first step of the derivation is to contract the domain Ω_{fract} on the hyperplane Γ. To do so, we decompose the fracture Darcy law (3a) into tangential and normal directions, and the divergence operator in the fracture conservation equation (3b) as the sum of its tangential and normal contributions. Then, we integrate the fracture tangential Darcy law and conservation equation along each transverse section

$$\mathcal{I}(\boldsymbol{x}) \coloneqq \left[\boldsymbol{x} - \frac{\ell_\Gamma(\boldsymbol{x})}{2}\boldsymbol{n}_\Gamma, \boldsymbol{x} + \frac{\ell_\Gamma(\boldsymbol{x})}{2}\boldsymbol{n}_\Gamma \right] \text{ for all } \boldsymbol{x} \in \Gamma,$$

and, using the Green formula on the normal divergence and recalling the continuity of the normal component of the flux (4b) on γ_j for $j \in \{1,2\}$, we obtain the following fracture-averaged tangential Darcy law and conservation equation:

$$\boldsymbol{u}_\Gamma + \kappa_\Gamma^\tau \ell_\Gamma \nabla_\tau p_\Gamma = 0 \qquad \text{in } \Gamma, \tag{5a}$$

$$\nabla_\tau \cdot \boldsymbol{u}_\Gamma = \ell_\Gamma f_\Gamma + [\![\boldsymbol{u}]\!]_\Gamma \cdot \boldsymbol{n}_\Gamma \qquad \text{in } \Gamma, \tag{5b}$$

with $[\![\boldsymbol{u}]\!]_\Gamma := \boldsymbol{u}_{|\Omega_1} - \boldsymbol{u}_{|\Omega_2}$ denoting the jump across the surrounding flux across the fracture. Plugging the averaged tangential Darcy law (5a) into the averaged tangential conservation equation (5b), we obtain the primal form of the Darcy equation in the fracture:

$$-\nabla_\tau \cdot (\kappa_\Gamma^\tau \ell_\Gamma \nabla_\tau p_\Gamma) = \ell_\Gamma f_\Gamma + [\![\boldsymbol{u}]\!]_\Gamma \cdot \boldsymbol{n}_\Gamma \qquad \text{in } \Gamma. \tag{6}$$

The jump of the flux across the fracture in the right-hand side of (6) originates from the normal divergence of the fracture flux, and hence acts as a source term. On the left-hand side of (6), ∇_τ and $\nabla_\tau\cdot$ stand for the tangential gradient and tangential divergence operators, respectively. The averaged fracture pressure p_Γ, flux $\boldsymbol{u}_\Gamma$, and source term f_Γ are defined such that, for all $\boldsymbol{x} \in \Gamma$,

$$p_\Gamma(\boldsymbol{x}) = \frac{1}{\ell_\Gamma} \int_{\mathcal{I}(\boldsymbol{x})} p_{\text{fract}}, \quad \boldsymbol{u}_\Gamma(\boldsymbol{x}) = \int_{\mathcal{I}(\boldsymbol{x})} \boldsymbol{u}_{\text{fract}}^\tau \quad \text{and} \quad f_\Gamma(\boldsymbol{x}) = \frac{1}{\ell_\Gamma} \int_{\mathcal{I}(\boldsymbol{x})} f_{\text{fract}},$$

with p_{fract}, $\boldsymbol{u}_{\text{fract}}^\tau$ and f_{fract} denoting the continuous fracture pressure, flux tangential component, and source term of the continuous model (12) with $i = \text{fract}$, respectively.

Transmission conditions. To close the problem, the second step is to derive transmission conditions that relate the unknowns of the porous medium with the ones in the reduced fracture Γ.

The first transmission equation is then given by the fracture normal Darcy law. Averaging the latter in the normal direction along each transverse section $\mathcal{I}(\boldsymbol{x})$ for all $\boldsymbol{x} \in \Gamma$, using the trapezoidal rule and the continuity of the normal component of the flux (4b) on γ_j for $j \in \{1,2\}$ to treat the flux term, together with a Green formula and the continuity of the pressure (4a) on γ_j for $j \in \{1,2\}$, we obtain a relation between the average of the normal component of the surrounding flux with the jump of the surrounding pressure, weighted by a coefficent depending on the thickness of the fracture and on the normal fracture permeability:

$$\frac{\ell_\Gamma}{\kappa_\Gamma^n} \{\{\boldsymbol{u}\}\}_\Gamma \cdot \boldsymbol{n}_\Gamma = [\![p]\!]_\Gamma \qquad \text{on } \Gamma. \tag{7}$$

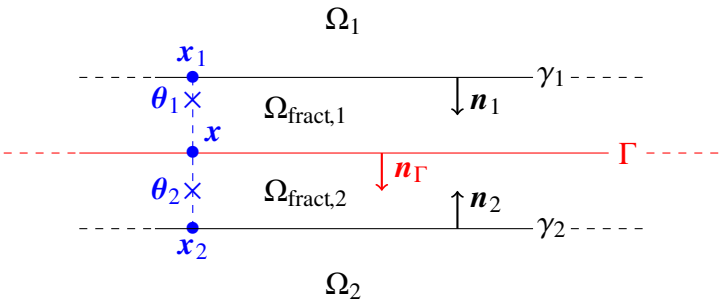

Figure 8: Representation of the Taylor expansion.

The second transmission equation arises from more technical arguments. For all $\boldsymbol{x} \in \Gamma$, we use the following truncated Taylor expansion of the continuous fracture pressure on $\Omega_{\text{fract},1}$ and $\Omega_{\text{fract},2}$

$$\begin{cases} p_{\text{fract}}(\boldsymbol{x}) = p_{\text{fract}}(\boldsymbol{x}_1) + \dfrac{\ell_\Gamma(\boldsymbol{x})}{2} \nabla p_{\text{fract}}(\boldsymbol{\theta_1}) \cdot \boldsymbol{n}_\Gamma, \\ p_{\text{fract}}(\boldsymbol{x}) = p_{\text{fract}}(\boldsymbol{x}_2) - \dfrac{\ell_\Gamma(\boldsymbol{x})}{2} \nabla p_{\text{fract}}(\boldsymbol{\theta_2}) \cdot \boldsymbol{n}_\Gamma, \end{cases} \tag{8}$$

where $\boldsymbol{x}_1 = \boldsymbol{x} - \frac{\ell_\Gamma}{2}\boldsymbol{n}_\Gamma$, $\boldsymbol{x}_2 = \boldsymbol{x} + \frac{\ell_\Gamma}{2}\boldsymbol{n}_\Gamma$, $\boldsymbol{\theta}_1 = \boldsymbol{x} - \xi_1 \frac{\ell_\Gamma}{2}\boldsymbol{n}_\Gamma$ and $\boldsymbol{\theta}_2 = \boldsymbol{x} + \xi_2 \frac{\ell_\Gamma}{2}\boldsymbol{n}_\Gamma$ with $(\xi_1, \xi_2) \in [0,1]^2$; see Figure 8 for a representation of the notations. We further assume that the normal components of the fracture fluxes vary linearly on Ω_{fract}, i.e.,

$$\begin{cases} \boldsymbol{u}_{\text{fract}}(\boldsymbol{\theta}_1) \cdot \boldsymbol{n}_\Gamma = \xi_1 \boldsymbol{u}_1(\boldsymbol{x}_1) \cdot \boldsymbol{n}_\Gamma + (1-\xi_1)\boldsymbol{u}_2(\boldsymbol{x}_2) \cdot \boldsymbol{n}_\Gamma, \\ \boldsymbol{u}_{\text{fract}}(\boldsymbol{\theta}_2) \cdot \boldsymbol{n}_\Gamma = \xi_1 \boldsymbol{u}_2(\boldsymbol{x}_2) \cdot \boldsymbol{n}_\Gamma + (1-\xi_2)\boldsymbol{u}_1(\boldsymbol{x}_1) \cdot \boldsymbol{n}_\Gamma. \end{cases} \tag{9}$$

Combining (8) with (9), recalling the continuity of the pressure (4a) and of the normal component of the flux (4b) on γ_j for $j \in \{1,2\}$ in addition to the first transmission condition (7), we get

$$\begin{cases} p_{\text{fract}}(\boldsymbol{x}) = \{\{p\}\}_\Gamma - \dfrac{\ell_\Gamma(\boldsymbol{x})}{\kappa_\Gamma^n} \left(\dfrac{\xi_1}{2} - \dfrac{1}{4}\right) [\![\boldsymbol{u}]\!]_\Gamma \cdot \boldsymbol{n}_\Gamma, \\ p_{\text{fract}}(\boldsymbol{x}) = \{\{p\}\}_\Gamma - \dfrac{\ell_\Gamma(\boldsymbol{x})}{\kappa_\Gamma^n} \left(\dfrac{\xi_2}{2} - \dfrac{1}{4}\right) [\![\boldsymbol{u}]\!]_\Gamma \cdot \boldsymbol{n}_\Gamma. \end{cases} \tag{10}$$

From (10), further enforcing the single-valuedness of the fracture pressure, it immediately follows that $\xi_1 = \xi_2 = \xi$. Then, by averaging along the transverse section $\mathcal{I}(\boldsymbol{x})$, we obtain the last transmission condition that relates the jump and average of the surrounding flux and pressure, respectively, with the averaged fracture pressure:

$$\frac{\ell_\Gamma}{\kappa_\Gamma^n} \left(\frac{\xi}{2} - \frac{1}{4}\right) [\![\boldsymbol{u}]\!]_\Gamma \cdot \boldsymbol{n}_\Gamma = \{\{p\}\}_\Gamma - p_\Gamma \qquad \text{on } \Gamma. \tag{11}$$

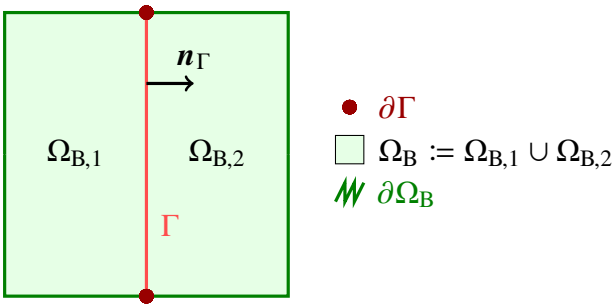

Figure 9: Illustration of notations for the reduced problem.

Reduced formulation. Now that the fracture has been reduced to a hyperplane, we denote the porous medium domain by $\Omega_B := \Omega \setminus \overline{\Gamma}$, also called *bulk* (hence, the subscript "B" in Ω_B); see Figure 9 for a representation of notations. In the bulk, we keep the formulation of the continuous model and consider the Darcy law (3a) and the conservation equation (3b). In the fracture, the averaged tangential primal formulation (6) is preferred to the mixed one (5), since only the averaged fracture pressure is involved in the transmission conditions 7 and 11. In summary, the reduced problem reads as follows: Find the Darcy velocity $\boldsymbol{u} : \Omega_B \to \mathbb{R}^d$, the bulk pressure $p : \Omega_B \to \mathbb{R}$ and the averaged fracture pressure $p_\Gamma : \Gamma \to \mathbb{R}$ such that

$$\boldsymbol{u} + \boldsymbol{K}\nabla p = 0 \qquad \text{in } \Omega_B, \tag{12a}$$

$$\nabla \cdot \boldsymbol{u} = f \qquad \text{in } \Omega_B, \tag{12b}$$

$$-\nabla_\tau \cdot (\kappa_\Gamma^\tau \ell_\Gamma \nabla_\tau p_\Gamma) = \ell_\Gamma f_\Gamma + [\![\boldsymbol{u}]\!]_\Gamma \cdot \boldsymbol{n}_\Gamma \qquad \text{in } \Gamma, \tag{12c}$$

$$\frac{\ell_\Gamma}{\kappa_\Gamma^n} \{\{\boldsymbol{u}\}\}_\Gamma \cdot \boldsymbol{n}_\Gamma = [\![p]\!]_\Gamma \qquad \text{on } \Gamma, \tag{12d}$$

$$\frac{\ell_\Gamma}{\kappa_\Gamma^n} \left(\frac{\xi}{2} - \frac{1}{4}\right) [\![\boldsymbol{u}]\!]_\Gamma \cdot \boldsymbol{n}_\Gamma = \{\{p\}\}_\Gamma - p_\Gamma \qquad \text{on } \Gamma. \tag{12e}$$

along with adequate boundary conditions.

State-of-the-art Several discretization methods for the reduced model (12) have been proposed in the literature. A brief (and by far non exhaustive) overview of works related with the present manuscript is provided hereafter. In [46], the authors consider lowest-order vertex- and face-based Gradient Schemes, and prove convergence in h for the energy-norm of the discretization error; see also [43] and the very recent work [92] concerning two-phase flows. Extended Finite Element methods (XFEM) are considered in [17, 28] in the context of fracture networks, and their convergence properties are numerically studied. In [24], the authors compare XFEM with the recently introduced Virtual Element Method (VEM), and

numerically observe convergence in both cases in $N_{\mathrm{DOF}}^{1/2}$ for the energy-norm of the discretization error, where N_{DOF} stands for the number of degrees of freedom; see also [23, 25]. Discontinuous Galerkin methods are also considered in [16] for a single-phase flow; see also [15]. Therein, an hp-error analysis in the energy norm is carried out on general polygonal/polyhedral meshes possibly including elements with unbounded number of faces, and numerical experiments are presented. A discretization method based on a mixed formulation in the mortar space has also been very recently proposed in [33], where an energy-error estimate in h is proved.

Reduced model for passive transport

We next discuss a reduced model that describes the passive transport of a solute in a fractured porous medium.

Let us start by discussing the modeling of the passive transport process in the different domains. The fluxes $\boldsymbol{u}$ and $\boldsymbol{u}_\Gamma = -\kappa_\Gamma^\tau \ell_\Gamma \nabla_\tau p_\Gamma$ are obtained by solving (12), along with no-flux boundary conditions and zero mean value compatibility conditions on source terms and the fracture pressure. This means that the flow through the porous medium is entirely driven by source terms f and f_Γ, which typically model injection or production wells. In what follows, we decompose source terms into their positive and negative parts: $f = f^+ - f^-$ and $f_\Gamma = f_\Gamma^+ - f_\Gamma^-$. Then, denoting by $c : \Omega_{\mathrm{B}} \to \mathbb{R}$ the bulk solute concentration and by $c_\Gamma : \Gamma \to \mathbb{R}$ its fracture counterpart, the transport inside the bulk and in the fracture are driven by the following PDEs, to be completed by homogeneous Neumann boundary conditions:

$$\begin{aligned} \phi \mathrm{d}_t c + \nabla \cdot \boldsymbol{F}_{\mathrm{B}} + f^- c &= f^+ \widehat{c} && \text{in } \Omega_{\mathrm{B}}, \\ \ell_\Gamma \phi_\Gamma \mathrm{d}_t c_\Gamma + \nabla_\tau \cdot \boldsymbol{F}_\Gamma + \ell_\Gamma f_\Gamma^- c_\Gamma &= \ell_\Gamma f_\Gamma^+ \widehat{c_\Gamma} + [\![\boldsymbol{F}_{\mathrm{B}}]\!]_\Gamma \cdot \boldsymbol{n}_\Gamma && \text{in } \Gamma, \end{aligned} \tag{13}$$

where $\phi : \Omega_{\mathrm{B}} \to \mathbb{R}$ and $\phi_\Gamma : \Gamma \to \mathbb{R}$ stand for the porosity of the bulk and of the fracture, respectively, and the total fluxes $\boldsymbol{F}_{\mathrm{B}} : \Omega_{\mathrm{B}} \to \mathbb{R}^d$ and $\boldsymbol{F}_\Gamma : \Gamma \to \mathbb{R}^d$ are defined as

$$\boldsymbol{F}_{\mathrm{B}} = \boldsymbol{u} c - \boldsymbol{D}(\boldsymbol{u}) \nabla c \qquad \text{in } \Omega_{\mathrm{B}}, \tag{14a}$$

$$\boldsymbol{F}_\Gamma = \boldsymbol{u}_\Gamma c_\Gamma - D_\Gamma(\boldsymbol{u}_\Gamma) \nabla_\tau c_\Gamma \qquad \text{in } \Gamma. \tag{14b}$$

The bulk molecular diffusivity tensor $\boldsymbol{D}(\boldsymbol{u})$, depending on the flux $\boldsymbol{u}$, is such that

$$\boldsymbol{D}(\boldsymbol{u}) = \phi d_{\mathrm{m}} \boldsymbol{I}_2 + \phi |\boldsymbol{u}| (d_{\mathrm{l}} \boldsymbol{E}(\boldsymbol{u}) + d_{\mathrm{t}} (\boldsymbol{I}_2 - \boldsymbol{E}(\boldsymbol{u}))),$$

where $|\boldsymbol{u}|$ is the Euclidean norm of $\boldsymbol{u}$, $\boldsymbol{E}(\boldsymbol{u}) = |\boldsymbol{u}|^{-2} (\boldsymbol{u} \otimes \boldsymbol{u})$, while d_{m}, d_{l} and d_{t} denote, respectively, the molecular diffusion, longitudinal, and transverse dispersion coefficients. The fracture molecular diffusivity $D_\Gamma(\boldsymbol{u}_\Gamma)$ is defined is the same way using the fracture flux $\boldsymbol{u}_\Gamma$.

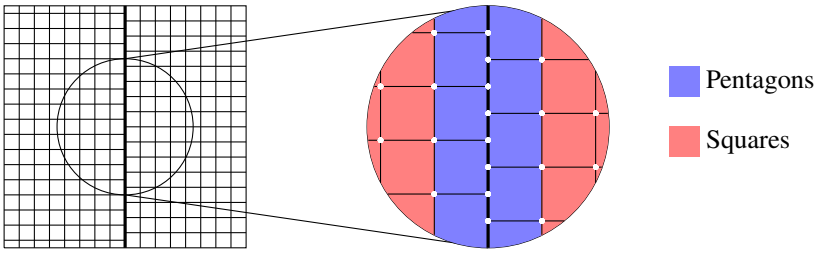

Figure 10: Treatment of nonconforming fracture discretizations.

What is left to define in order to close the problem (13)–(14) are transmission conditions across the reduced fracture Γ. In the literature, we can find models that assume continuity of the bulk concentration of the transported solute across the fracture but, as for the flows, this assumption is not appropriate in the context of impermeable fractures, where the bulk solute concentration may be discontinous across the fracture.A possible alternative would be to consider transmission conditions similar to (12d) and (12e), but using the total flux (14a) on the left-hand side instead. This choice, however, does not seem to give rise to a well-posed problem.

Following this observation, we derive in **Chapter** 3 new transmission conditions based on an energy argument, expressing the fact that the advective part of the total bulk flux does not contribute to the energy-balance of the system. These novel transmission conditions give raise to a well-posed problem, and allow the bulk solute concentration to jump across the fracture.

Main contributions and perspectives

In **Chapter** 2, we develop a novel HHO discretisation of the reduced model for flows in fractured porous media (12) focusing, for the sake of simplicity, on the two-dimensional case (the extension to the three-dimensional is is also briefly addressed; see Remark 2.10). The fracture is discretized using mesh skeleton elements, which means that the mesh is compliant with the fracture.

This choice, however, is not restrictive in the context of methods that can handle meshes containing polytopal/polyhedral elements, even when the fracture discretization is nonconforming in the classical sense. Consider, e.g., the situation illustrated in Figure 10, where the fracture lies at the intersection of two nonmatching Cartesian submeshes. In this case, no special treatment is required provided the mesh elements in contact with the fracture are treated as pentagons with two coplanar faces instead of rectangles.

For a polynomial degree $k \geq 0$, the discrete formulation of the HHO method is based on discrete unknowns that are, for the bulk flux, polynomials of degree k on each mesh face, single-valued except on fracture faces, and permeability-

weighted gradient of polynomials of degree k inside each mesh element. For the bulk pressure, the discrete unknowns are polynomials of degree k on each mesh element. On the other hand, the discrete unknowns for the fracture pressure are polynomials of degree k on each fracture face and point values on each fracture vertex. The discrete counterparts of jump and average terms of the bulk flux are jump and average of the face-based unknowns of the discrete bulk flux, respectively.

We prove stability of the discretization in the form of an inf-sup condition, as well as optimal error estimates in h^{k+1} for an energy-like norm of the error (with h denoting the spatial meshsize). Specifically, the key ingredient for the stability result of Theorem 2.11 is the commuting property of the discrete divergence reconstruction. In the the error estimate of Theorem 2.12, the dependence of the constant on the problem parameters is carefully tracked, showing full robustness with respect to the heterogeneity of the permeability coefficients in both the bulk and the fracture, and only a mild dependence on the square root of the local anisotropy ratio in the bulk. To prove the error estimate, we proceed in three steps. First, we estimate the error in terms of conformity error, using the coercivity of the global bilinear form and the inf-sup condition on the discrete divergence bilinear form. Then, we bound the conformity error by writing the discrete bulk bilinear forms so as to reveal a bulk pressure gradient, with the help of a local well-defined elliptic projector as in the error estimate procedure while considering primal formulations. This second step is the mainstay of this error analysis, since it links error estimate of mixed HHO formulations to error estimate of primal HHO formulations. We end the proof by combining the previous results.

We implement the method in `C++` using the `hho` software platform, and we numerically study its convergence properties, as well as its behaviour with respect to the local bulk anisotropy ratio. Both the theorical convergence rates and the expected robustness are observed in practice. Moreover, optimal error estimate in h^{k+2} for the L^2-norm of the error is observed for both the bulk and fracture pressure. A set of *physical* test cases is also proposed to assess the properties of the method in more realistic configurations. Specifically, we consider the quarter five-spot problem, a classical pattern in petroleum engineering used for oil recovery, and study the impact of the permeability of the fracture on the surrounding flow. We also measure the flow across the fracture for both the permeable and impermeable fracture configuration, and observe, for each configuration, convergence to a value using a h-refinement. Faster convergence is observed while increasing the polynomial degree. In a second numerical test, we study of the impact of the bulk permeability on the flow. The bulk permeability is fixed so as to obtain a nonmatching superposition of layers of different permeability. As expected, high permeability zones are prone to let the fluid flow towards the fracture, in contrast to the low permeability zones in which the pressure variations are larger.

In **Chapter** 3, we introduce a new reduced model for the passive transport of a

solute in a fractured medium, driven by a velocity field solution of the decoupled reduced flow problem. New transmission conditions between the bulk and fracture are presented using an energy-based argument, which postulates that the convective terms do not contribute to the energy balance of the global system. Unlike others proposed in the literature, these transmission conditions allow the bulk solute concentration to jump across the fracture.

Concerning the discretization, we develop a HHO method in the two-dimensional case and assume mesh compliance with the fracture, as for the reduced flows model. For a polynomial degree $k \geq 0$, the resolution is carried out in two steps.

In the first step, we compute the bulk and fracture flow by solving the discrete reduced flows problem of **Chapter** 2 using polynomials of degree $2k$. The use of polynomials of degree $2k$ is required to obtain a well-posed discrete reduced passive transport scheme, as first observed in [11] where authors model miscible displacements in a non-fractured porous media using the HHO method. Then, we prove that the method is locally conservative and identify the conservative numerical fluxes in both the bulk and fracture regions. These numerical fluxes are used to formulate the convective terms for the discrete reduced passive transport model, and their identifications is the mainstay of the stability of the reduced passive transport discretization.

The second step is the resolution of the discrete HHO formulation of the reduced passive transport problem. Also at the discrete level, the transmission conditions are designed so as to reproduce the energy argument from which they originate.

We implement the method in `C++` using the `hho` software platform, and numerically study the convergence of the method by imposing analytical solutions on the bulk and fracture solute concentration. We observe convergence in h^{k+1} for an energy-like norm of the error on the bulk and fracture solute concentration. Also in this reduced model, optimal error estimate in h^{k+2} for the L^2-norm of the error is numerically observed for both the bulk and fracture solute concentration. We remark an atypical behavior of the error measured in the L^2-norm for the fracture solute concentration while using the lowest approximation order $k = 0$. This behavior will be investigated in a further work, where a complete discrete analysis of this reduced model will be carried out. We then run the method on some test cases, where the fracture is considered as a barrier or as a conduit. In both cases, the method captures the passive transport process according to the permeability of the fracture and the location of injecting or producing wells. As expected, abrupt variations of the bulk solute concentration at the vicinity of the fracture are well captured by the method.

From what we present in **Chapters** 2 and 3, it seems that the HHO method is very competitive and well suited also in the context of fractured porous media flows and passive transport. Regarding the new reduced passive transport model,

the transmission conditions are prone to let the solute concentration move towards the fracture, or on the contrary, to force the solute concentration to move from the injection well to the production one avoiding the fracture, depending on the permeability of the fracture. This result, although expected, was not guaranteed at first. With the help of numerical simulations provided in this manuscript, it is reasonable to say that these equations govern the desired phenomenon.

Chapter 1

The Cahn–Hilliard problem

This chapter has been published in the following peer-reviewed journal (see [59]):

SIAM Journal on Numerical Analysis, 2016.
Volume 54, Issue 3, Pages 1873–1898.

Contents

1.1 Introduction

Let $\Omega \subset \mathbb{R}^d$, $d \in \{2, 3\}$, denote a bounded connected convex polyhedral domain with boundary $\partial\Omega$ and outward normal $\boldsymbol{n}$, and let $t_F > 0$. The Cahn–Hilliard problem, originally introduced in [51, 52] to model phase separation in a binary alloy, consists in finding the order-parameter $c : \Omega \times (0, t_F) \to \mathbb{R}$ and chemical potential $w : \Omega \times (0, t_F) \to \mathbb{R}$ such that

$$\mathrm{d}_t c - \Delta w = 0 \qquad \text{in } \Omega \times (0, t_F), \tag{1.1a}$$

$$w = \Phi'(c) - \gamma^2 \Delta c \qquad \text{in } \Omega \times (0, t_F), \tag{1.1b}$$

$$c(\cdot, 0) = c_0(\cdot) \qquad \text{in } \Omega, \tag{1.1c}$$

$$-\nabla c \cdot \boldsymbol{n} = -\nabla w \cdot \boldsymbol{n} = 0 \qquad \text{on } \partial\Omega \times (0, t_F), \tag{1.1d}$$

where $c_0 \in H^2(\Omega) \cap L^2_0(\Omega)$ such that $-\nabla c_0 \cdot \boldsymbol{n} = 0$ on $\partial\Omega$ denotes the initial datum, $\gamma > 0$ the interface parameter (usually taking small values), and Φ the free-energy such that

$$\Phi(c) \coloneqq \frac{1}{4}(1 - c^2)^2. \tag{1.2}$$

Relevant extensions of problem (1.1) (not considered here) include the introduction of a flow which requires, in particular, to add a convective term in (1.1a); cf., e.g., [19, 40, 41, 113, 115, 116].

The discretization of the Cahn–Hilliard equation (1.1) has been considered in several works. Different aspects of standard finite element schemes have been studied, e.g., in [70, 93, 94]; cf. also the references therein. Mixed finite elements are considered in [99]. In [129], the authors study a nonconforming method based on C^0 shape functions for the fourth-order primal problem obtained by plugging (1.1b) into (1.1a). Discontinuous Galerkin (dG) methods have also received extensive attention. We can cite here [131], where a local dG method is proposed for a Cahn–Hilliard system modelling multi-component alloys, and a stability analysis is carried out; [98], where optimal error estimates are proved for a dG discretization of the Cahn–Hilliard problem in primal form; [115], which contains optimal error estimates for a dG method based on the mixed formulation of the problem including a convection term; [110], where a multi-grid approach is proposed for the solution of the systems of algebraic equations arising from a dG discretization of the Cahn–Hilliard equation. In all of the above references, standard meshes are considered. General polygonal meshes in dimension $d = 2$, on the other hand, are supported by the recently proposed C^1-conforming Virtual Element (VE) method of [14] for the problem in primal formulation; cf. also [22] for VE methods with arbitrary regularity. Therein, the convergence analysis is carried out under the assumption that the discrete order-parameter satisfies a $C^0(L^\infty)$-like a priori bound.

In this work, we develop and analyze a fully implicit Hybrid High-Order (HHO) algorithm for problem (1.1) where the space discretization is based on the HHO($k+1$) variation proposed in [67] of the method of [83]. The method hinges on hybrid degrees of freedom (DOFs) located at mesh elements and faces that are polynomials of degree $(k+1)$ and k, respectively. The nonlinear term in (1.1b) is discretized by means of element unknowns only. For the second-order diffusive operators in (1.1a) and (1.1b), on the other hand, we rely on two key ingredients devised locally inside each element: (i) A potential reconstruction obtained from the solution of (small) Neumann problems and (ii) a stabilization term penalizing the lowest-order part of the difference between element- and face-based unknowns. See also [69, 119, 128] for related methods for second-order linear diffusion operators, each displaying a set of distinctive features. The global discrete problem is then obtained by a standard element-by-element assembly procedure. When using a first-order (Newton-like) algorithm to solve the resulting system of nonlinear algebraic equations, element-based unknowns can be statically condensed. As a result, the only globally coupled unknowns in the linear subproblems are discontinuous polynomials of degree k on the mesh skeleton for both the order-parameter and the chemical potential. With a backward Euler scheme to march in time, the $C^0(H^1)$-like error on the order-parameter and the $L^2(H^1)$-like error on the chemical potential are proved to optimally converge as $(h^{k+1}+\delta t)$ (with h and δt denoting, respectively, the spatial and temporal mesh sizes) provided the solution has sufficient regularity.

The proposed method has several advantageous features: (i) It supports general meshes possibly including polyhedral elements and nonmatching interfaces (resulting, e.g., from nonconforming mesh refinement); (ii) it allows one to increase the spatial approximation order to accelerate convergence in the presence of (locally) regular solutions; (iii) it is (relatively) inexpensive. When $d=2$, e.g., the number of globally coupled spatial unknowns for our method scales as $2\,\mathrm{card}(\mathcal{F}_h)(k+1)$ (with $\mathrm{card}(\mathcal{F}_h)$ denoting the number of mesh faces) as opposed to $\mathrm{card}(\mathcal{T}_h)(k+3)(k+2)$ (with $\mathrm{card}(\mathcal{T}_h)$ denoting the number of mesh elements) for a mixed dG method delivering the same order of convergence (i.e., based on broken polynomials of degree $k+1$). Additionally, thanks to the underlying fully discontinuous polynomial spaces, the proposed method can accomodate abrupt variations of the unknowns in the vicinity of the interface between phases.

Our analysis adapts the techniques originally developed in [115] in the context of dG methods. Therein, the treatment of the nonlinear term in (1.1b) hinges on C^0-in-time a priori estimates for various norms and seminorms of the discrete order-parameter. Instrumental in proving these estimates are discrete functional analysis results, including discrete versions of Agmon's and Gagliardo–Nirenberg–Poincaré's inequalities for broken polynomial functions on quasi-uniform matching simplicial meshes. Adapting these tools to hybrid polynomial spaces on general

meshes entails several new ideas. A first key point consists in defining appropriate discrete counterparts of the Laplace and Green's operators. To this end, we rely on a suitably tailored L^2-like hybrid inner product which guarantees stability estimates for the former and optimal approximation properties for the latter. Another key point consists in replacing the standard nodal interpolator used in the proofs of [115, Lemmas 2.2 and 2.3] by the L^2-orthogonal projector which, unlike the former, is naturally defined for meshes containing polyhedral elements. We show that this replacement is possible thanks to the $W^{s,p}$-stability and approximation properties of the L^2-orthogonal projector on broken polynomial spaces recently presented in a unified setting in [74]; cf. also the references therein for previous results on this subject.

The material is organized as follows: In Section 1.2 we introduce the notation for space and time meshes and recall some key results on broken polynomial spaces; in Section 3.4 we introduce hybrid polynomial spaces and local reconstructions, and state the discrete problem; in Section 1.4 we carry out the stability analysis of the method, while the convergence analysis is detailed in Section 1.5; Section 2.5 contains an extensive numerical validation of the proposed algorithm; finally, in Section 1.7 we give proofs of the discrete functional analysis results used to derive stability bounds and error estimates.

1.2 Discrete setting

In this section we introduce the discrete setting and recall some basic results on broken polynomial spaces.

1.2.1 Space and time meshes

We recall here the notion of admissible spatial mesh sequence from [81, Chapter 1]. For the sake of simplicity, we will systematically use the term polyhedral also when $d = 2$. Denote by $\mathcal{H} \subset \mathbb{R}_*^+$ a countable set of spatial meshsizes having 0 as its unique accumulation point. We consider h-refined mesh sequences $(\mathcal{T}_h)_{h\in\mathcal{H}}$ where, for all $h \in \mathcal{H}$, $\mathcal{T}_h$ is a finite collection of nonempty disjoint open polyhedral elements T of boundary ∂T such that $\overline{\Omega} = \bigcup_{T\in\mathcal{T}_h} \overline{T}$ and $h = \max_{T\in\mathcal{T}_h} h_T$ with h_T standing for the diameter of the element T.

A face F is defined as a planar closed connected subset of $\overline{\Omega}$ with positive $(d-1)$-dimensional Hausdorff measure and such that(i) either there exist $T_1, T_2 \in \mathcal{T}_h$ such that $F \subset \partial T_1 \cap \partial T_2$ and F is called an interface or (ii) there exists $T \in \mathcal{T}_h$ such that $F \subset \partial T \cap \partial\Omega$ and F is called a boundary face. Mesh faces are collected in the set $\mathcal{F}_h$, and the diameter of a face $F \in \mathcal{F}_h$ is denoted by h_F. For all $T \in \mathcal{T}_h$, $\mathcal{F}_T \coloneqq \{F \in \mathcal{F}_h \ : \ F \subset \partial T\}$ denotes the set of faces lying on ∂T and, for all

$F \in \mathcal{F}_T$, $\boldsymbol{n}_{TF}$ is the unit normal to F pointing out of T. Symmetrically, for all $F \in \mathcal{F}_h$, we denote by $\mathcal{T}_F$ the set of one (if $F \in \mathcal{F}_h^{\mathrm{b}}$) or two (if $F \in \mathcal{F}_h^{\mathrm{i}}$) elements sharing F.

Assumption 1.1 (Admissible spatial mesh sequence)**.** We assume that, for all $h \in \mathcal{H}$, $\mathcal{T}_h$ admits a matching simplicial submesh $\mathfrak{T}_h$ and there exists a real number $\varrho > 0$ independent of h such that, for all $h \in \mathcal{H}$, the following properties hold:(i) *Shape regularity:* For all simplex $S \in \mathfrak{T}_h$ of diameter h_S and inradius r_S, $\varrho h_S \le r_S$; (ii) *contact-regularity:* For all $T \in \mathcal{T}_h$, and all $S \in \mathfrak{T}_h$ such that $S \subset T$, $\varrho h_T \le h_S$.

To discretize in time, we consider a uniform partition $(t^n)_{0\le n\le N}$ of the time interval $[0, t_F$ with $t^0 = 0$, $t^N = t_F$ and $t^n - t^{n-1} = \delta t$ for all $1 \le n \le N$ (the analysis can be adapted to nonuniform partitions). For any sufficiently regular function of time φ taking values in a vector space V, we denote by $\varphi^n \in V$ its value at discrete time t^n, and we introduce the backward differencing operator δ_{t} such that, for all $1 \le n \le N$,

$$\delta_{\mathrm{t}}\varphi^n \coloneqq \frac{\varphi^n - \varphi^{n-1}}{\delta t} \in V. \tag{1.3}$$

In what follows, we often abbreviate by $a \lesssim b$ the inequality $a \le Cb$ with a and b positive real numbers and $C > 0$ generic constant independent of both the meshsize h and the time step δt (named constants are used in the statements for the sake of easy consultation). Also, for a subset $X \subset \overline{\Omega}$, we denote by $(\cdot,\cdot)_X$ and $\|\cdot\|_X$ the usual $L^2(X)$-inner product and norm, with the convention that we omit the index if $X = \Omega$. The same notation is used for the vector-valued space $L^2(X)^d$.

1.2.2 Basic results on broken polynomial spaces

The proposed method is based on local polynomial spaces on mesh elements and faces. Let an integer $l \ge 0$ be fixed. Let U be a subset of $\mathbb{R}^d$, H_U the affine space spanned by U, d_U its dimension, and assume that U has a non-empty interior in H_U. We denote by $\mathbb{P}^l(U)$ the space spanned by d_U-variate polynomials on H_U of total degree l, and by π_U^l the L^2-orthogonal projector onto this space. In the following sections, the set U will represent a mesh element or face. The space of broken polynomial functions on $\mathcal{T}_h$ of degree l is denoted by $\mathbb{P}^l(\mathcal{T}_h)$, and π_h^l is the corresponding L^2-orthogonal projector.

We next recall some functional analysis results on polynomial spaces. The following discrete trace and inverse inequalities are proved in [81, Chapter 1] (cf. in particular Lemmas 1.44 and 1.46): There is $C > 0$ independent of h such that, for all $T \in \mathcal{T}_h$, and all $\forall v \in \mathbb{P}^l(T)$,

$$\|v\|_F \le C h_F^{-\frac{1}{2}} \|v\|_T \qquad \forall F \in \mathcal{F}_T, \tag{1.4}$$

and

$$\|\nabla v\|_T \le C h_T^{-1} \|v\|_T. \tag{1.5}$$

We will also need the following local direct and reverse Lebesgue embeddings (cf. [74, Lemma 5.1]): There is $C > 0$ independent of h such that, for all $T \in \mathcal{T}_h$, all $q, p \in [1, +\infty]$,

$$\forall v \in \mathbb{P}^l(T), \qquad C^{-1} \|v\|_{L^q(T)} \le h_T^{\frac{d}{q}-\frac{d}{p}} \|v\|_{L^p(T)} \le C \|v\|_{L^q(T)}. \tag{1.6}$$

The proof of the following results for the local L^2-orthogonal projector can be found in [74, Appendix A.2]. For an open set U of $\mathbb{R}^d$, $s \in \mathbb{N}$ and $p \in [1, +\infty]$, we define the seminorm $|\cdot|_{W^{s,p}(U)}$ as follows: For all $v \in W^{s,p}(U)$,

$$|v|_{W^{s,p}(U)} \coloneqq \sum_{\boldsymbol{\alpha} \in \mathbb{N}^d,\, |\boldsymbol{\alpha}|_{\ell^1} = s} \|\partial^{\boldsymbol{\alpha}} v\|_{L^p(U)},$$

where $|\boldsymbol{\alpha}|_{\ell^1} \coloneqq \alpha_1 + \cdots + \alpha_d$ and $\partial^{\boldsymbol{\alpha}} = \partial_1^{\alpha_1} \cdots \partial_d^{\alpha_d}$. For $s = 0$, we recover the usual Lebesgue spaces $L^p(U)$. The L^2-orthogonal projector is $W^{s,p}$-stable and has optimal $W^{s,p}$-approximation properties: There is $C > 0$ independent of h such that, for all $T \in \mathcal{T}_h$, all $s \in \{0, \ldots, l+1\}$, all $p \in [1, +\infty]$, and all $v \in W^{s,p}(T)$, it holds,

$$|\pi_T^l v|_{W^{s,p}(T)} \le C |v|_{W^{s,p}(T)}, \tag{1.7}$$

and, for all $m \in \{0, \ldots, s\}$,

$$|v - \pi_T^l v|_{W^{m,p}(T)} + h_T^{\frac{1}{p}} |v - \pi_T^l v|_{W^{m,p}(\mathcal{F}_T)} \le C h_T^{s-m} |v|_{W^{s,p}(T)}, \tag{1.8}$$

where $W^{m,p}(\mathcal{F}_T)$ denotes the set of functions that belong to $W^{m,p}(F)$ for all $F \in \mathcal{F}_T$. Finally, there is $C > 0$ independent of h such that it holds, for all $F \in \mathcal{F}_h$,

$$\forall v \in H^1(F), \qquad \|v - \pi_F^l v\|_F \le C h |v|_{H^1(F)}. \tag{1.9}$$

In the proofs of Lemmas 1.7 and 1.14 below, we will make use of the following global inverse inequalities, which require mesh quasi-uniformity.

Proposition 1.2 (Global inverse inequalities of broken polynomials)**.** *In addition to Assumption 1.1, we assume that the mesh is quasi-uniform, i.e.,*

$$\forall T \in \mathcal{T}_h, \qquad \varrho h \le h_T. \tag{1.10}$$

Then, for all polynomial degree $l \ge 0$ and all $1 \le p \le q \le +\infty$, it holds

$$\forall w_h \in \mathbb{P}^l(\mathcal{T}_h), \qquad \|w_h\|_{L^q(\Omega)} \le C h^{\frac{d}{q}-\frac{d}{p}} \|w_h\|_{L^p(\Omega)}, \tag{1.11}$$

with real number $C > 0$ independent of h.

Proof. Let $w_h \in \mathbb{P}^l(\mathcal{T}_h)$. We start by proving that, for all $p \in [1, +\infty]$,

$$\forall w_h \in \mathbb{P}^l(\mathcal{T}_h), \qquad \|w_h\|_{L^\infty(\Omega)} \lesssim h^{-\frac{d}{p}} \|w_h\|_{L^p(\Omega)}, \tag{1.12}$$

which corresponds to (1.11) with $q = +\infty$. By the local reverse Lebesgue embeddings (1.6), there is $C > 0$ independent of h such that

$$\forall T \in \mathcal{T}_h, \qquad \|w_h\|_{L^\infty(T)} \le C h_T^{-\frac{d}{p}} \|w_h\|_{L^p(T)} \le C \rho^{-\frac{d}{p}} h^{-\frac{d}{p}} \|w_h\|_{L^p(\Omega)},$$

where we have used the mesh quasi-uniformity assumption (1.10) to conclude. Inequality (1.12) follows observing that $\|w_h\|_{L^\infty(\Omega)} = \max_{T\in\mathcal{T}_h} \|w_h\|_{L^\infty(T)}$. Let us now turn to the case $1 \le q < +\infty$. We have

$$\|w_h\|_{L^q(\Omega)}^q \le \|w_h\|_{L^\infty(\Omega)}^{q-p} \|w_h\|_{L^p(\Omega)}^p \lesssim \left(h^{\frac{d}{q}-\frac{d}{p}} \|w_h\|_{L^p(\Omega)}\right)^q,$$

where the conclusion follows using (1.12). □

1.3 The Hybrid High-Order method

In this section we define hybrid spaces and state the discrete problem.

1.3.1 Hybrid spaces

The discretization of the diffusion operator hinges on the HHO method of [67] using polynomials of degree $(k + 1)$ inside elements and k on mesh faces (cf. Remark 1.16 for further insight on this choice). The global discrete space is defined as

$$\underline{P}_h^{k+1,k} := \left(\bigtimes_{T\in\mathcal{T}_h} \mathbb{P}^{k+1}(T)\right) \times \left(\bigtimes_{F\in\mathcal{F}_h} \mathbb{P}^k(F)\right). \tag{1.13}$$

The restriction of $\underline{P}_h^{k+1,k}$ to an element $T \in \mathcal{T}_h$ is denoted by $\underline{P}_T^{k+1,k}$. For a generic collection of DOFs in $\underline{P}_h^{k+1,k}$, we use the underlined notation $\underline{v}_h = ((v_T)_{T\in\mathcal{T}_h}, (v_F)_{F\in\mathcal{F}_h})$ and, for all $T \in \mathcal{T}_h$, we denote by $\underline{v}_T = (v_T, (v_F)_{F\in\mathcal{F}_T})$ its restriction to $\underline{P}_T^{k+1,k}$. Also, to keep the notation compact, we denote by v_h (no underline) the function in $\mathbb{P}^{k+1}(\mathcal{T}_h)$ such that

$$v_{h|T} = v_T \qquad \forall T \in \mathcal{T}_h.$$

In what follows, we will also need the zero-average subspace

$$\underline{P}_{h,0}^{k+1,k} := \left\{\underline{v}_h \in \underline{P}_h^{k+1,k} \ : \ \int_\Omega v_h = 0\right\}.$$

The interpolator $\underline{I}_h^k : H^1(\Omega) \to \underline{P}_h^{k+1,k}$ is such that, for all $v \in H^1(\Omega)$,

$$\underline{I}_h^k v \coloneqq ((\pi_T^{k+1} v)_{T\in\mathcal{T}_h}, (\pi_F^k v)_{F\in\mathcal{F}_h}). \tag{1.14}$$

We define on $\underline{P}_h^{k+1,k}$ the seminorm $\|\cdot\|_{1,h}$ such that

$$\|\underline{v}_h\|_{1,h}^2 \coloneqq \|\nabla_h v_h\|^2 + |\underline{v}_h|_{1,h}^2, \qquad |\underline{v}_h|_{1,h}^2 \coloneqq s_{1,h}(\underline{v}_h, \underline{v}_h), \tag{1.15}$$

where ∇_h denotes the usual broken gradient on $H^1(\mathcal{T}_h)$ and the stabilization bilinear form $s_{1,h}$ on $\underline{P}_h^{k+1,k} \times \underline{P}_h^{k+1,k}$ is such that

$$s_{1,h}(\underline{v}_h, \underline{z}_h) \coloneqq \sum_{T\in\mathcal{T}_h} \sum_{F\in\mathcal{F}_T} \int_F h_F^{-1} \pi_F^k(v_F - v_T)\pi_F^k(z_F - z_T). \tag{1.16}$$

Using the stability and approximation properties of the L^2-orthogonal projector expressed by (1.7)–(1.8), one can prove that $\underline{I}_h^k$ is H^1-stable:

$$\forall v \in H^1(\Omega), \qquad \|\underline{I}_h^k v\|_{1,h} \lesssim \|v\|_{H^1(\Omega)}. \tag{1.17}$$

The following Friedrichs' inequalities can be proved using the arguments of [74, Lemma 7.2], where element DOFs of degree k are considered (cf. also [49, 79] for related results using dG norms): For all $r \in [1, +\infty)$ if $d = 2$, all $r \in [1, 6]$ if $d = 3$,

$$\forall \underline{v}_h \in \underline{P}_{h,0}^{k+1,k}, \qquad \|v_h\|_{L^r(\Omega)} \lesssim \|\underline{v}_h\|_{1,h}. \tag{1.18}$$

The case $r = 2$ corresponds to Poincaré's inequality. Finally, to close this section, we prove that $\|\cdot\|_{1,h}$ defines a norm on $\underline{P}_{h,0}^{k+1,k}$.

Proposition 1.3 (Norm $\|\cdot\|_{1,h}$)**.** *The map $\|\cdot\|_{1,h}$ defines a norm on $\underline{P}_{h,0}^{k+1,k}$.*

Proof. We only have to show that $\|\underline{v}_h\|_{1,h} = 0 \implies \underline{v}_h = \underline{0}$. By (1.18), $\|\underline{v}_h\|_{1,h} = 0 \implies v_h \equiv 0$, i.e., $v_T \equiv 0$ for all $T \in \mathcal{T}_h$. Plugging this result into the definition (1.15) of $\|\cdot\|_{1,h}$, we get $\sum_{T\in\mathcal{T}_h} \sum_{F\in\mathcal{F}_T} h_F^{-1} \|v_F\|_F^2 = 0$, which implies in turn $v_F \equiv 0$ for all $F \in \mathcal{F}_h$. □

1.3.2 Diffusive bilinear form and discrete problem

For all $T \in \mathcal{T}_h$, we define the potential reconstruction operator $r_T^{k+1} : \underline{P}_T^{k+1,k} \to \mathbb{P}^{k+1}(T)$ such that, for all $\underline{v}_T \in \underline{P}_T^{k+1,k}$, $r_T^{k+1}\underline{v}_T$ is the unique solution of the following Neumann problem:

$$\int_T \nabla r_T^{k+1}\underline{v}_T \cdot \nabla z = -\int_T v_T \Delta z + \sum_{F\in\mathcal{F}_T} \int_F v_F \nabla z \cdot \boldsymbol{n}_{TF} \qquad \forall z \in \mathbb{P}^{k+1}(T), \tag{1.19}$$

with closure condition $\int_T r_T^{k+1}\underline{v}_T = \int_T v_T$. It can be proved that, for all $v \in H^1(T)$, denoting by $\underline{I}_T^k$ the restriction of the reduction map $\underline{I}_h^k$ defined by (1.14) to $H^1(T) \to \underline{P}_T^{k+1,k}$,

$$\int_T \nabla(r_T^{k+1}\underline{I}_T^k v - v)\cdot\nabla z = 0 \qquad \forall z \in \mathbb{P}^{k+1}(T), \tag{1.20}$$

which expresses the fact that $(r_T^{k+1}\circ\underline{I}_T^k)$ is the elliptic projector onto $\mathbb{P}^{k+1}(T)$ (and, as such, has optimal approximation properties in $\mathbb{P}^{k+1}(T)$). The diffusive bilinear form a_h on $\underline{P}_h^{k+1,k}\times\underline{P}_h^{k+1,k}$ is obtained by element-wise assembly setting

$$a_h(\underline{v}_h,\underline{z}_h) \coloneqq \sum_{T\in\mathcal{T}_h}\left(\int_T \nabla r_T^{k+1}\underline{v}_T\cdot\nabla r_T^{k+1}\underline{z}_T + s_{1,h}(\underline{v}_h,\underline{z}_h)\right), \tag{1.21}$$

with stabilization bilinear form $s_{1,h}$ defined by (1.16). Denoting by $\|\cdot\|_{a,h}$ the seminorm defined by a_h on $\underline{P}_h^{k+1,k}$, a straightforward adaptation of the arguments used in [83, Lemma 4] shows that

$$\forall\underline{v}_h \in \underline{P}_h^{k+1,k}, \qquad \|\underline{v}_h\|_{1,h} \lesssim \|\underline{v}_h\|_{a,h} \lesssim \|\underline{v}_h\|_{1,h}, \tag{1.22}$$

which expresses the coercivity and boundedness of a_h. Additionally, following the arguments in [83, Theorem 8], one can easily prove that the bilinear form a_h enjoys the following consistency property: For all $v \in H^{\max(2,l)}(\Omega)\cap L_0^2(\Omega)$, $l \ge 1$, such that $-\nabla v\cdot\boldsymbol{n} = 0$ on $\partial\Omega$,

$$\sup_{\underline{z}_h\in\underline{P}_{h,0}^{k+1,k},\|\underline{z}_h\|_{1,h}=1}\left|a_h(\underline{I}_h^k v,\underline{z}_h) + \int_\Omega \Delta v z_h\right| \lesssim h^{\min(k+1,l-1)}\|v\|_{H^l(\Omega)}. \tag{1.23}$$

Remark 1.4 (Consistency of a_h). For sufficiently regular solutions (i.e., when $l = k+2$), equation (1.23) shows that the consistency error scales as h^{k+1}. This is a consequence of the fact that both the potential reconstruction r_T^{k+1} (cf. (1.19)) and the stabilization bilinear form $s_{1,h}$ (cf. (1.16)) are consistent for exact solutions that are polynomials of degree $(k+1)$ inside each element. In particular, a key point in $s_{1,h}$ is to penalize $\pi_F^k(v_F - v_T)$ instead of $(v_F - v_T)$. A similar stabilization bilinear form had been independently suggested in the context of Hybridizable Discontinuous Galerkin methods in [118, Remark 1.2.4].

The discrete problem reads: For all $1 \le n \le N$, find $(\underline{c}_h^n,\underline{w}_h^n) \in \underline{P}_{h,0}^{k+1,k}\times\underline{P}_h^{k+1,k}$ such that

$$\int_\Omega \delta_{\mathrm{t}}c_h^n\varphi_h + a_h(\underline{w}_h^n,\underline{\varphi}_h) = 0 \qquad \forall\underline{\varphi}_h \in \underline{P}_h^{k+1,k}, \tag{1.24a}$$

$$\int_\Omega w_h^n\psi_h = \int_\Omega \Phi'(c_h^n)\psi_h + \gamma^2 a_h(\underline{c}_h^n,\underline{\psi}_h) \qquad \forall\underline{\psi}_h \in \underline{P}_h^{k+1,k}, \tag{1.24b}$$

and $\underline{c}_h^0 \in \underline{P}_{h,0}^{k+1,k}$ solves

$$a_h(\underline{c}_h^0, \underline{\varphi}_h) = -\int_\Omega \Delta c_0 \varphi_h \qquad \forall \underline{\varphi}_h \in \underline{P}_h^{k+1,k}. \tag{1.25}$$

We note, in passing, that the face DOFs in $\underline{c}_h^0$ are not needed to initialize the algorithm.

Remark 1.5 (Static condensation). Problem (1.24) is a system of nonlinear algebraic equations, which can be solved using an iterative algorithm. When first order (Newton-like) algorithms are used, element-based DOFs can be locally eliminated at each iteration by a standard static condensation procedure.

1.4 Stability analysis

In this section we establish some uniform a priori bounds on the discrete solution. To this end, we need a discrete counterpart of Agmon's inequality; cf. [8, Lemma 13.2] and also [3, Theorem 3]. We define on $\underline{P}_h^{k+1,k}$ the following L^2-like inner product:

$$\begin{aligned}(\underline{v}_h, \underline{z}_h)_{0,h} &\coloneqq \int_\Omega v_h z_h + s_{0,h}(\underline{v}_h, \underline{z}_h),\\ s_{0,h}(\underline{v}_h, \underline{z}_h) &\coloneqq \sum_{T\in\mathcal{T}_h}\sum_{F\in\mathcal{F}_T}\int_F h_F \pi_F^k(v_F - v_T)\pi_F^k(z_F - z_T),\end{aligned} \tag{1.26}$$

and denote by $\|\cdot\|_{0,h}$ and $|\cdot|_{0,h}$ the norm and seminorm corresponding to the bilinear forms $(\cdot,\cdot)_{0,h}$ and $s_{0,h}$, respectively. For further insight on the role of $s_{0,h}$, cf. Remark 1.19. We introduce the discrete Laplace operator $\underline{L}_h^k : \underline{P}_h^{k+1,k} \to \underline{P}_h^{k+1,k}$ such that, for all $\underline{v}_h \in \underline{P}_h^{k+1,k}$,

$$-(\underline{L}_h^k \underline{v}_h, \underline{z}_h)_{0,h} = a_h(\underline{v}_h, \underline{z}_h) \qquad \forall \underline{z}_h \in \underline{P}_h^{k+1,k}, \tag{1.27}$$

and we denote by $L_h^k \underline{v}_h$ (no underline) the broken polynomial function in $\mathbb{P}^{k+1}(\mathcal{T}_h)$ obtained from element DOFs in $\underline{L}_h^k \underline{v}_h$.

Remark 1.6 (Restriction of $\underline{L}_h^k$ to $\underline{P}_{h,0}^{k+1,k} \to \underline{P}_{h,0}^{k+1,k}$). Whenever $\underline{v}_h \in \underline{P}_{h,0}^{k+1,k}$, $\underline{L}_h^k \underline{v}_h \in \underline{P}_{h,0}^{k+1,k}$. To prove it, it suffices to take $\underline{z}_h = \underline{I}_h^k \chi_\Omega$ in (1.27) (with χ_Ω characteristic function of Ω), and observe that the left-hand side satisfies $(\underline{L}_h^k \underline{v}_h, \underline{z}_h)_{0,h} = \int_\Omega L_h^k \underline{v}_h$ while, by definition (1.21) of the bilinear form a_h, the right-hand side vanishes. In what follows, we keep the same notation for the (bijective) restriction of $\underline{L}_h^k$ to $\underline{P}_{h,0}^{k+1,k} \to \underline{P}_{h,0}^{k+1,k}$.

The following result, valid for $d \in \{2,3\}$, will be proved in Section 1.7.

Lemma 1.7 (Discrete Agmon's inequality)**.** *Assume mesh quasi-uniformity* (1.10)*. Then, it holds with real number $C > 0$ independent of h,*

$$\forall \underline{v}_h \in \underline{P}_{h,0}^{k+1,k}, \qquad \|v_h\|_{L^\infty(\Omega)} \le C \|\underline{v}_h\|_{1,h}^{1/2} \|\underline{L}_h^k \underline{v}_h\|_{0,h}^{1/2}. \tag{1.28}$$

We also recall the following discrete Gronwall's inequality (cf. [112, Lemma 5.1]).

Lemma 1.8 (Discrete Gronwall's inequality)**.** *Let two reals $\mu, G > 0$ be given, and, for integers $n \ge 1$, let a^n, b^n, and χ^n denote nonnegative real numbers such that*

$$a^N + \mu \sum_{n=1}^N b^n \le \mu \sum_{n=1}^N \chi^n a^n + G \qquad \forall N \in \mathbb{N}^*.$$

Then, if $\chi^n \mu < 1$ for all n, letting $\varsigma^n := (1 - \chi^n \mu)^{-1}$, it holds

$$a^N + \mu \sum_{n=1}^N b^n \le \exp\left(\mu \sum_{n=1}^N \varsigma^n \chi^n\right) \times G \qquad \forall N \in \mathbb{N}^*. \tag{1.29}$$

We are now ready to prove the a priori bounds.

Lemma 1.9 (Uniform a priori bounds)**.** *Under the assumptions of Lemma 1.7, and further assuming that $\delta t \le L$ for a given real number $L > 0$ independent of h and of δt (but depending on γ^2) and sufficiently small, there is a real number $C > 0$ independent of h and τ such that*

$$\max_{1\le n\le N} \left(\|\underline{c}_h^n\|_{a,h}^2 + \int_\Omega \Phi(c_h^n) + \|w_h^n\|^2 + \|c_h^n\|_{L^\infty(\Omega)} + \|\underline{L}_h^k \underline{c}_h^n\|_{0,h}^2 \right) + \sum_{n=1}^N \delta t \|\underline{w}_h^n\|_{a,h}^2 \le C.$$

Proof. The proof is split into several steps.

(i) We start by proving that

$$\max_{1\le n\le N} \left(\|\underline{c}_h^n\|_{a,h}^2 + \int_\Omega \Phi(c_h^n) \right) + \sum_{n=1}^N \delta t \|\underline{w}_h^n\|_{a,h}^2 \lesssim 1. \tag{1.30}$$

Subtracting (1.24b) with $\underline{\psi}_h = \underline{c}_h^n - \underline{c}_h^{n-1}$ from (1.24a) with $\underline{\varphi}_h = \delta t \underline{w}_h^n$, and using the fact that, for all $r, s \in \mathbb{R}$, $\Phi'(r)(r-s) \ge \Phi(r) - \Phi(s) - \frac{1}{2}(r-s)^2$, it is inferred, for all $1 \le n \le N$, that

$$\gamma^2 a_h(\underline{c}_h^n, \underline{c}_h^n - \underline{c}_h^{n-1}) + \delta t \|\underline{w}_h^n\|_{a,h}^2 + \int_\Omega \Phi(c_h^n) \le \frac{1}{2} \|c_h^n - c_h^{n-1}\|^2 + \int_\Omega \Phi(c_h^{n-1}). \tag{1.31}$$

Notice that $\int_\Omega \Phi(c_h^n) \geq 0$ for all $0 \leq n \leq N$ by definition (1.2) of Φ. Making $\underline{\varphi}_h = \delta t(\underline{c}_h^n - \underline{c}_h^{n-1})$ in (1.24a) and using the Cauchy–Schwarz and Young's inequalities, we infer that

$$\|c_h^n - c_h^{n-1}\|^2 \leq \frac{\delta t}{2}\|\underline{w}_h^n\|_{a,h}^2 + \frac{\delta t}{2}\|\underline{c}_h^n - \underline{c}_h^{n-1}\|_{a,h}^2. \tag{1.32}$$

Additionally, recalling the following formula for the backward Euler scheme:

$$2x(x-y) = x^2 + (x-y)^2 - y^2, \tag{1.33}$$

it holds

$$a_h(\underline{c}_h^n, \underline{c}_h^n - \underline{c}_h^{n-1}) = \frac{1}{2}\left(\|\underline{c}_h^n\|_{a,h}^2 + \|\underline{c}_h^n - \underline{c}_h^{n-1}\|_{a,h}^2 - \|\underline{c}_h^{n-1}\|_{a,h}^2\right). \tag{1.34}$$

Plugging (1.32) and (1.34) into (1.31), we obtain

$$\gamma^2\|\underline{c}_h^n\|_{a,h}^2 + \left(\gamma^2 - \frac{\delta t}{2}\right)\|\underline{c}_h^n - \underline{c}_h^{n-1}\|_{a,h}^2 + \frac{3\delta t}{2}\|\underline{w}_h^n\|_{a,h}^2 + 2\int_\Omega \Phi(c_h^n) \leq \gamma^2\|\underline{c}_h^{n-1}\|_{a,h}^2 + 2\int_\Omega \Phi(c_h^{n-1}).$$

Provided $\delta t < 2\gamma^2$, the bound (1.30) follows summing the above inequality over $1 \leq n \leq N$, and using the fact that $\gamma^2\|c_h^0\|_{a,h} + 2\int_\Omega \Phi(c_h^0) \lesssim 1$. To prove this bound, observe that

$$\begin{aligned}\gamma^2\|c_h^0\|_{a,h} + 2\int_\Omega \Phi(c_h^0) &\lesssim \gamma^2\|\underline{c}_h^0\|_{1,h}^2 + 1 + \|c_h^0\|_{L^4(\Omega)}^4 + \|c_h^0\|^2 \\ &\lesssim \gamma^2\|\underline{c}_h^0\|_{1,h}^2 + 1 + \|\underline{c}_h^0\|_{1,h}^4 + \|\underline{c}_h^0\|_{1,h}^2 \lesssim 1,\end{aligned}$$

where we have used the definition (1.2) of the free-energy Φ in the first line followed by the discrete Friedrichs' inequality with $r = 4, 2$ in the second line and the first bound on the initial datum in (1.46) below to conclude.

(ii) We next prove that

$$\sum_{n=1}^N \delta t\|c_h^n\|_{L^\infty(\Omega)}^4 \lesssim 1. \tag{1.35}$$

The discrete Agmon's inequality (1.28) followed by the first inequality in (1.22) yields

$$\sum_{n=1}^N \delta t\|c_h^n\|_{L^\infty(\Omega)}^4 \lesssim \sum_{n=1}^N \delta t\|\underline{c}_h^n\|_{a,h}^2\|\underline{L}_h^k\underline{c}_h^n\|_{0,h}^2 \lesssim \left(\max_{1\leq n\leq N}\|\underline{c}_h^n\|_{a,h}^2\right) \times \sum_{n=1}^N \delta t\|\underline{L}_h^k\underline{c}_h^n\|_{0,h}^2.$$

The first factor is $\lesssim 1$ owing to (1.30). Thus, to prove (1.35), it suffices to show that also the second factor is $\lesssim 1$. Using the definition (1.27) of $\underline{L}_h^k$ followed by (1.24b) with $\underline{\psi}_h = \underline{L}_h^k \underline{c}_h^n$, we infer that

$$\gamma^2 \|\underline{L}_h^k \underline{c}_h^n\|_{0,h}^2 = -\gamma^2 a_h(\underline{c}_h^n, \underline{L}_h^k \underline{c}_h^n) = \int_\Omega (\Phi'(c_h^n) - w_h^n) L_h^k \underline{c}_h^n. \tag{1.36}$$

Using again (1.27) for the second term in the right-hand side of (1.36) followed by the Cauchy–Schwarz and Young's inequalities, we obtain

$$\begin{aligned}\gamma^2 \|\underline{L}_h^k \underline{c}_h^n\|_{0,h}^2 &= \int_\Omega \Phi'(c_h^n) L_h^k \underline{c}_h^n + a_h(\underline{c}_h^n, \underline{w}_h^n) + s_{0,h}(\underline{L}_h^k \underline{c}_h^n, \underline{w}_h^n) \\ &\le \frac{1}{2\gamma^2} \|\Phi'(c_h^n)\|^2 + \frac{\gamma^2}{2} \|\underline{L}_h^k \underline{c}_h^n\|_{0,h}^2 + \frac{\gamma^2}{2} \|\underline{c}_h^n\|_{a,h}^2 + \frac{1}{2\gamma^2} \|\underline{w}_h^n\|_{a,h}^2 + \frac{1}{2\gamma^2} |\underline{w}_h^n|_{0,h}^2.\end{aligned}$$

Hence, since $|\underline{w}_h^n|_{0,h} \le h |\underline{w}_h^n|_{1,h} \lesssim \|\underline{w}_h^n\|_{a,h}$,

$$\gamma^2 \|\underline{L}_h^k \underline{c}_h^n\|_{0,h}^2 \lesssim \gamma^{-2} \|\Phi'(c_h^n)\|^2 + \gamma^2 \|\underline{c}_h^n\|_{a,h}^2 + \gamma^{-2} \|\underline{w}_h^n\|_{a,h}^2.$$

The fact that $\sum_{n=1}^N \delta t \|\underline{L}_h^k \underline{c}_h^n\|_{0,h}^2 \lesssim 1$ then follows multiplying the above inequality by δt, summing over $1 \le n \le N$, using (1.30) to bound the second and third term in the right-hand side, and observing that

$$\begin{aligned}\|\Phi'(c_h^n)\|^2 &\le \|c_h^n\|_{L^6(\Omega)}^6 + 2\|c_h^n\|_{L^4(\Omega)}^4 + \|c_h^n\|^2 \\ &\lesssim \|\underline{c}_h^n\|_{1,h}^6 + \|\underline{c}_h^n\|_{1,h}^4 + \|\underline{c}_h^n\|_{1,h}^2 \\ &\lesssim 1,\end{aligned} \tag{1.37}$$

where we have used the definition (1.2) to obtain the first bound, Friedrichs' inequality (1.18) with $r = 6, 4, 2$ to obtain the second bound, and (1.30) together with the first inequality in (1.22) to conclude.

(iii) We proceed by proving that

$$\max_{1 \le n \le N} \|w_h^n\|^2 + \gamma^2 \sum_{n=1}^N \delta t \|\delta_t c_h^n\|^2 \lesssim 1. \tag{1.38}$$

Let $w_h^0 := \pi_h^{k+1}(\Phi'(c_h^0) - \gamma^2 \Delta c_0)$. Recalling (1.25), w_h^0 satisfies

$$\int_\Omega w_h^0 \psi_h = \int_\Omega \Phi'(c_h^0) \psi_h + \gamma^2 a_h(\underline{c}_h^0, \underline{\psi}_h) \qquad \forall \underline{\psi}_h \in \underline{P}_h^{k+1,k}. \tag{1.39}$$

For any $1 \le n \le N$, subtracting from (1.24b) at time step n (1.24b) at time step $(n-1)$ if $n > 1$ or (1.39) if $n = 1$, and selecting $\underline{\psi}_h = \underline{w}_h^n$ as a test function in the resulting equation, it is inferred that

$$\int_\Omega (w_h^n - w_h^{n-1}) w_h^n = \delta t \gamma^2 a_h(\delta_{mt} \underline{c}_h^n, \underline{w}_h^n) + \int_\Omega (\Phi'(c_h^n) - \Phi'(c_h^{n-1})) w_h^n.$$

Using (1.24a) with $\underline{\varphi}_h = \delta t\gamma^2 \delta_{\mathrm{t}} \underline{c}_h^n$ to infer $\delta t\gamma^2 a_h(\delta_{\mathrm{t}} \underline{c}_h^n, \underline{w}_h^n) = -\delta t\gamma^2 \|\delta_{\mathrm{t}} c_h^n\|^2$, we get

$$\int_\Omega (w_h^n - w_h^{n-1}) w_h^n + \delta t\gamma^2 \|\delta_{\mathrm{t}} c_h^n\|^2 = \int_\Omega (\Phi'(c_h^n) - \Phi'(c_h^{n-1})) w_h^n. \tag{1.40}$$

From the fact that

$$\Phi'(r) - \Phi'(s) = (r^2 + rs + s^2 - 1)(r - s), \tag{1.41}$$

followed by the Cauchy–Schwarz and Young's inequalities, we infer

$$\left| \int_\Omega (\Phi'(c_h^n) - \Phi'(c_h^{n-1})) w_h^n \right| \le \frac{\delta t\gamma^2}{2} \|\delta_{\mathrm{t}} c_h^n\|^2 + \frac{\delta t C^n}{2} \|w_h^n\|^2, \tag{1.42}$$

with $C^n := C(1 + \|c_h^n\|_{L^\infty(\Omega)}^4 + \|c_h^{n-1}\|_{L^\infty(\Omega)}^4)$ for a real number $C > 0$ independent of h and δt. Using (1.33) for the first term in the left-hand side of (1.40) together with (1.42) for the right-hand side, we get

$$\|w_h^n\|^2 + \|w_h^n - w_h^{n-1}\|^2 + \delta t\gamma^2 \|\delta_{\mathrm{t}} c_h^n\|^2 \le \delta t C^n \|w_h^n\|^2 + \|w_h^{n-1}\|^2. \tag{1.43}$$

Summing (1.43) over $1 \le n \le N$, observing that, thanks to (1.35) and the second bound in (1.46) below, we can have $\delta t C^n < 1$ for all $1 \le n \le N$ provided that we choose δt small enough, and using the discrete Gronwall's inequality (1.29) (with $\mu = \delta t$, $a^n = \|w_h^n\|^2$, $b^n = \gamma^2 \|\delta_{\mathrm{t}} c_h^n\|^2$, $\chi^n = C^n$ and $G = \|w_h^0\|^2$), the estimate (1.38) follows if we can bound $\|w_h^0\|^2$. To this end, recalling the definition of w_h^0 and using the Cauchy–Schwarz inequality, one has

$$\|w_h^0\|^2 = \int_\Omega \Phi'(c_h^0) w_h^0 - \gamma^2 \int_\Omega \Delta c_0 w_h^0 \le \left(\|\Phi'(c_h^0)\| + \gamma^2 \|c_0\|_{H^2(\Omega)} \right) \|w_h^0\|,$$

and the conclusion follows from the regularity of c_0 noting the first bound in (1.46) below and estimating the first term in parentheses as in (1.37).

(iv) We conclude by proving the bound

$$\max_{1 \le n \le N} \left(\|c_h^n\|_{L^\infty(\Omega)} + \|\underline{L}_h^k \underline{c}_h^n\|_{0,h}^2 \right) \lesssim 1. \tag{1.44}$$

Using the Cauchy–Schwarz and Young's inequalities to bound the right-hand side of (1.36) followed by (1.18) with $r = 6, 4, 2$ and the first inequality in (1.22), we obtain, for all $1 \le n \le N$,

$$\begin{aligned} \gamma^2 \|\underline{L}_h^k \underline{c}_h^n\|_{0,h}^2 &\lesssim \gamma^{-2} \left(\|\Phi'(c_h^n)\|^2 + \|w_h^n\|^2 \right) \\ &\lesssim \left(\|c_h^n\|_{L^6(\Omega)}^6 + \|c_h^n\|_{L^4(\Omega)}^4 + \|c_h^n\|^2 \right) + \|w_h^n\|^2 \\ &\lesssim \left(\|c_h^n\|_{a,h}^6 + \|c_h^n\|_{a,h}^4 + \|c_h^n\|_{a,h}^2 \right) + \|w_h^n\|^2 \lesssim 1, \end{aligned} \tag{1.45}$$

where we have concluded using (1.30) multiple times for the terms in parentheses and (1.38) for $\|w_h^n\|^2$. Using the discrete Agmon's inequality (1.28) followed by Young's inequality and the first inequality in (1.22), we infer

$$\max_{1\le n\le N}\|c_h^n\|_{L^\infty(\Omega)} \lesssim \max_{1\le n\le N}\left(\|\underline{c}_h^n\|_{a,h} + \|\underline{L}_h^k\underline{c}_h^n\|_{0,h}\right) \lesssim 1,$$

where the conclusion follows using (1.30) for the first addend in the argument of the maximum and (1.45) for the second.

□

Proposition 1.10 (Bounds for $\underline{c}_h^0$)**.** *Let $\underline{c}_h^0 \in \underline{P}_{h,0}^{k+1,k}$ be defined by (1.25) from an initial datum $c_0 \in H^2(\Omega)\cap L_0^2(\Omega)$ such that $-\nabla c_0\cdot\boldsymbol{n} = 0$ on $\partial\Omega$. It holds, with real number $C>0$ independent of h,*

$$\|\underline{c}_h^0\|_{1,h} + \|c_h^0\|_{L^\infty(\Omega)} \le C\|c_0\|_{H^2(\Omega)}. \tag{1.46}$$

Proof. To prove the first bound in (1.46), let $\underline{\varphi}_h = \underline{c}_h^0$ in (1.25) and use the first inequality in (1.22), the Cauchy–Schwarz inequality and the discrete Poincaré's inequality (1.18) with $r=2$ to infer

$$\|\underline{c}_h^0\|_{1,h}^2 \lesssim a_h(\underline{c}_h^0,\underline{c}_h^0) = -\int_\Omega \Delta c_0 c_h^0 \le \|\Delta c_0\|\|c_h^0\| \lesssim \|c_0\|_{H^2(\Omega)}\|\underline{c}_h^0\|_{1,h}.$$

To prove the second bound in (1.46), we start by noticing that, using the definition (1.27) of $\underline{L}_h^k$ with $\underline{z}_h = -\underline{L}_h^k\underline{c}_h^0$,

$$\|\underline{L}_h^k\underline{c}_h^0\|_{0,h}^2 = -a_h(\underline{c}_h^0,\underline{L}_h^k\underline{c}_h^0) = \int_\Omega \Delta c_0 L_h^k\underline{c}_h^0 \le \|c_0\|_{H^2(\Omega)}\|L_h^k\underline{c}_h^0\|,$$

hence $\|\underline{L}_h^k\underline{c}_h^0\|_{0,h}\le\|c_0\|_{H^2(\Omega)}$. Combining the discrete Agmon's inequality (1.28) with the latter inequality and the first bound in (1.46), one gets

$$\|c_h^0\|_{L^\infty(\Omega)} \le \|\underline{c}_h^0\|_{1,h}^{1/2}\|\underline{L}_h^k\underline{c}_h^0\|_{0,h}^{1/2} \lesssim \|c_0\|_{H^2(\Omega)},$$

and the desired result follows. □

1.5 Error analysis

In this section we carry out the error analysis of the method (1.24).

1.5.1 Error equations

Our goal is to estimate the difference between the discrete solution obtained solving (1.24) and the projections of the exact solution such that, for all $1 \le n \le N$, $\underline{\widehat{w}}_h^n = \underline{I}_h^k w^n$, while, for all $0 \le n \le N$, $\underline{\widehat{c}}_h^n \in \underline{P}_{h,0}^{k+1,k}$ solves

$$a_h(\underline{\widehat{c}}_h^n, \underline{\varphi}_h) = -\int_\Omega \Delta c^n \varphi_h \qquad \forall \underline{\varphi}_h \in \underline{P}_h^{k+1,k},$$

and $\int_\Omega \widehat{c}_h^n = 0$. We define, for all $1 \le n \le N$, the errors

$$\underline{e}_{c,h}^n \coloneqq \underline{c}_h^n - \underline{\widehat{c}}_h^n, \qquad \underline{e}_{w,h}^n \coloneqq \underline{w}_h^n - \underline{\widehat{w}}_h^n. \tag{1.47}$$

By definition (1.25), $\underline{\widehat{c}}_h^0 = \underline{c}_h^0$, which prompts us to set $\underline{e}_{c,h}^0 \coloneqq \underline{0}$. Using Poincaré's inequality (1.18) with $r = 2$ and the consistency (1.23) of a_h, the following estimate is readily inferred: For all $0 \le n \le N$, assuming the additional regularity $c^n \in H^{k+2}(\Omega)$,

$$\|\widehat{c}_h^n - \pi_h^{k+1} c^n\| \lesssim \|\underline{\widehat{c}}_h^n - \underline{I}_h^k c^n\|_{1,h} \lesssim h^{k+1} \|c^n\|_{H^{k+2}(\Omega)}. \tag{1.48}$$

Remark 1.11 (Improved L^2-estimate). We notice, in passing, that, using elliptic regularity (which holds since Ω is convex, cf., e.g., [108]), one can improve this result and show that $\|\widehat{c}_h^n - \pi_h^{k+1} c^n\| \lesssim h^{k+2} \|c^n\|_{H^{k+2}(\Omega)}$.

Recalling (1.24), for all $1 \le n \le N$, the error $(\underline{e}_{c,h}^n, \underline{e}_{w,h}^n) \in \underline{P}_{h,0}^{k+1,k} \times \underline{P}_h^{k+1,k}$ solves

$$\int_\Omega \delta_t e_{c,h}^n \varphi_h + a_h(\underline{e}_{w,h}^n, \underline{\varphi}_h) = \mathcal{E}(\underline{\varphi}_h) \qquad \forall \underline{\varphi}_h \in \underline{P}_h^{k+1,k}, \tag{1.49a}$$

$$\int_\Omega e_{w,h}^n \psi_h = \int_\Omega (\Phi'(c_h^n) - \Phi'(c^n))\psi_h + \gamma^2 a_h(\underline{e}_{c,h}^n, \underline{\psi}_h) \qquad \forall \underline{\psi}_h \in \underline{P}_h^{k+1,k}, \tag{1.49b}$$

where, in (1.49a), we have defined the consistency error

$$\mathcal{E}(\underline{\varphi}_h) \coloneqq -\int_\Omega \delta_t \widehat{c}_h^n \varphi_h - a_h(\underline{\widehat{w}}_h^n, \underline{\varphi}_h), \tag{1.50}$$

while in (1.49b) we have combined the definitions of $\underline{\widehat{w}}_h^n$ and $\underline{\widehat{c}}_h^n$ with (1.1b) to infer

$$\int_\Omega \widehat{w}_h^n \psi_h - \gamma^2 a_h(\underline{\widehat{c}}_h^n, \underline{\psi}_h) = \int_\Omega (w^n + \Delta c^n)\psi_h = \int_\Omega \Phi'(c^n)\psi_h.$$

1.5.2 Error estimate

Theorem 1.12 (Error estimate)**.** *Suppose that the assumptions of Lemma 1.9 hold true. Let* (c, w) *denote the solution to* (1.1)*, for which we assume the following additional regularity:*

$$c \in C^2([0,t_F];L^2(\Omega))\cap C^1([0,t_F];H^{k+2}(\Omega)), \quad w \in C^0([0,t_F];H^{k+2}(\Omega)). \tag{1.51}$$

Then, the following estimate holds for the errors defined by (1.47)*:*

$$\left(\max_{1\le n\le N}\|\underline{e}_{c,h}^n\|_{a,h}^2+\sum_{n=1}^N\delta t\|\underline{e}_{w,h}^n\|_{a,h}^2\right)^{1/2}\le C(h^{k+1}+\delta t), \tag{1.52}$$

with real number $C>0$ *independent of* h *and* δt*.*

Proof. Let $1\le n\le N$. Subtracting (1.49b) with $\underline{\psi}_h=\delta_{\mathrm{t}}\underline{e}_{c,h}^n$ from (1.49a) with $\underline{\varphi}_h=\underline{e}_{w,h}^n$, we obtain

$$\begin{aligned}\|\underline{e}_{w,h}^n\|_{a,h}^2+\gamma^2 a_h(\underline{e}_{c,h}^n,\delta_{\mathrm{t}}\underline{e}_{c,h}^n)&=\mathcal{E}(\underline{e}_{w,h}^n)+\int_\Omega(\Phi'(c^n)-\Phi'(c_h^n))\delta_{\mathrm{t}}e_{c,h}^n\\&:=\mathfrak{T}_1+\mathfrak{T}_2.\end{aligned} \tag{1.53}$$

We proceed to bound the terms in the right-hand side.

(i) *Bound for* $\mathfrak{T}_1$. Let $\underline{\varphi}_h\in\underline{P}_h^{k+1,k}$. Adding to (1.50) the quantity

$$\int_\Omega(\mathrm{d}_t c^n-\Delta w^n)\varphi_h+\int_\Omega(\delta_{\mathrm{t}}\pi_h^{k+1}c^n-\delta_{\mathrm{t}}c^n)\varphi_h=0,$$

(use (1.1a) to prove that the first addend is 0 and the definition of the L^2-orthogonal projector π_h^{k+1} to prove that the second is also 0), we can decompose $\mathcal{E}(\underline{\varphi}_h)$ as follows:

$$\begin{aligned}\mathcal{E}(\underline{\varphi}_h)&=\int_\Omega(\mathrm{d}_t c^n-\delta_{\mathrm{t}}c^n)\varphi_h+\int_\Omega\delta_{\mathrm{t}}(\pi_h^{k+1}c^n-\widehat{c}_h^n)\varphi_h-\left(a_h(\underline{\widehat{w}}_h^n,\underline{\varphi}_h)+\int_\Omega\Delta w^n\varphi_h\right)\\&:=\mathfrak{T}_{1,1}+\mathfrak{T}_{1,2}+\mathfrak{T}_{1,3}.\end{aligned}$$

For the first term, we have

$$|\mathfrak{T}_{1,1}|\le\|\mathrm{d}_t c^n-\delta_{\mathrm{t}}c^n\|\|\varphi_h\|\lesssim\delta t\|c\|_{C^2([0,t_F];L^2(\Omega))}\|\underline{\varphi}_h\|_{1,h}\lesssim\delta t\|\underline{\varphi}_h\|_{1,h}, \tag{1.54}$$

where we have used the Cauchy–Schwarz inequality, a classical estimate based on Taylor's remainder, Poincaré's inequality (1.18) with $r=2$, and we have concluded using the regularity (1.51) for c. For the second term, on the other

hand, using the Cauchy–Schwarz inequality followed by (1.48) together with the C^1-stability of the backward differencing operator (1.3), Poincaré's inequality, and the regularity (1.51) for c, we readily obtain

$$\begin{aligned}|\mathfrak{T}_{1,2}| &\le \|\delta_{\mathrm{t}}(\pi_h^{k+1}c^n - \widehat{c}_h^n)\|\|\varphi_h\| \lesssim h^{k+1}\|c^n\|_{C^1([0,t_F];H^{k+2}(\Omega))}\|\varphi_h\| \\ &\lesssim h^{k+1}\|\underline{\varphi}_h\|_{1,h}.\end{aligned} \tag{1.55}$$

Finally, recalling the consistency properties (1.23) of a_h, we get for the last term

$$\begin{aligned}|\mathfrak{T}_{1,3}| &\lesssim h^{k+1}\|w^n\|_{H^{k+2}(\Omega)}\|\underline{\varphi}_h\|_{1,h} \le h^{k+1}\|w\|_{C^0([0,t_F];H^{k+2}(\Omega))}\|\underline{\varphi}_h\|_{1,h} \\ &\lesssim h^{k+1}\|\underline{\varphi}_h\|_{1,h}.\end{aligned} \tag{1.56}$$

Collecting the bounds (1.54)–(1.56), it is inferred that

$$\$:= \sup_{\underline{\varphi}_h\in\underline{P}_h^{k+1,k},\|\underline{\varphi}_h\|_{1,h}=1} \mathcal{E}(\underline{\varphi}_h) \lesssim h^{k+1} + \delta t, \tag{1.57}$$

so that, for any real $\epsilon > 0$, denoting by $C_\epsilon > 0$ a real depending on ϵ but not on h or δt, and using the second inequality in (1.22) to bound $\|\underline{e}_{w,h}^n\|_{1,h} \lesssim \|\underline{e}_{w,h}^n\|_{a,h}$,

$$|\mathfrak{T}_1| \le \$\|\underline{e}_{w,h}^n\|_{1,h} \lesssim (h^{k+1}+\delta t)\|\underline{e}_{w,h}^n\|_{1,h} \le C_\epsilon(h^{k+1}+\delta t)^2 + \epsilon\|\underline{e}_{w,h}^n\|_{a,h}^2. \tag{1.58}$$

(ii) *Bound for* $\mathfrak{T}_2$. Set, for the sake of brevity, $Q^n := \Phi'(c_h^n) - \Phi'(c^n)$, and define the DOF vector $\underline{z}_h \in \underline{P}_h^{k+1,k}$ such that

$$z_T = \pi_T^{k+1}Q^n \quad \forall T\in\mathcal{T}_h, \qquad z_F = \begin{cases}\pi_F^k\{\{Q^n\}\}_F & \forall F\in\mathcal{F}_h^{\mathrm{i}},\\ \pi_F^k z_{T_F} & \forall F\in\mathcal{F}_h^{\mathrm{b}},\end{cases} \tag{1.59}$$

where $\{\{\cdot\}\}_F$ denotes the usual average operator such that, for any function φ admitting a possibly two-valued trace on $F\in\mathcal{F}_{T_1}\cap\mathcal{F}_{T_2}$, $\{\{\varphi\}\}_F := \frac{1}{2}(\varphi_{|T_1}+\varphi_{|T_2})$, while, for a boundary face $F\in\mathcal{F}_h^{\mathrm{b}}$, T_F denotes the unique element in $\mathcal{T}_h$ such that $F\in\mathcal{F}_{T_F}$. We have, using the definition of π_T^{k+1} followed by (1.49a) with $\underline{\varphi}_h = \underline{z}_h$, (1.57), and the second inequality in (1.22),

$$\mathfrak{T}_2 = (z_h,\delta_{\mathrm{t}}e_{c,h}^n) = \mathcal{E}(\underline{z}_h) - a_h(\underline{e}_{w,h}^n,\underline{z}_h) \lesssim \left(\$ + \|\underline{e}_{w,h}^n\|_{a,h}\right)\|\underline{z}_h\|_{1,h}. \tag{1.60}$$

By Proposition 1.15 below,

$$\|\underline{z}_h\|_{1,h} \lesssim \|\underline{e}_{c,h}^n\|_{a,h} + h^{k+1}, \tag{1.61}$$

hence, for any real $\epsilon > 0$, denoting by $C_\epsilon > 0$ a real number depending on ϵ but not on h or δt, and recalling the bound (1.57) for \$,

$$|\mathfrak{T}_2| \le C_\epsilon\left(\|\underline{e}_{c,h}^n\|_{a,h}^2 + (h^{k+1}+\delta t)^2\right) + \epsilon\|\underline{e}_{w,h}^n\|_{a,h}^2. \tag{1.62}$$

(iii) *Conclusion.* Using (1.58) and (1.62) with $\epsilon = \frac{1}{4}$ to bound the right-hand side of (1.53), it is inferred

$$\|\underline{e}^n_{w,h}\|^2_{a,h} + \gamma^2 a_h(\underline{e}^n_{c,h}, \delta_t \underline{e}^n_{c,h}) \lesssim (h^{k+1} + \delta t)^2 + \|\underline{e}^n_{c,h}\|^2_{a,h}.$$

Multiplying by δt, summing over $1 \le n \le N$, using (1.33) for the second term in the left-hand side, and recalling that, by definition, $\underline{e}^0_{c,h} = \underline{0}$, we get

$$\gamma^2 \|\underline{e}^N_{c,h}\|^2_{a,h} + \sum_{n=1}^{N} \delta t \|\underline{e}^n_{w,h}\|^2_{a,h} \le \sum_{n=1}^{N} C\delta t \|\underline{e}^n_{c,h}\|^2_{a,h} + C(h^{k+1} + \delta t)^2,$$

with $C > 0$ independent of h and δt. The error estimate (1.52) then follows from an application of the discrete Gronwall's inequality (1.29) with $\mu = \delta t$, $a^n = \gamma^2 \|\underline{e}^n_{c,h}\|^2_{a,h}$, $b^n = \|\underline{e}^n_{w,h}\|^2_{a,h}$, $\chi^n = C$, and $G = C(h^{k+1} + \delta t)^2$ assuming δt small enough.

□

Remark 1.13 (BDF2 time discretization). In Section 2.5, we have also used a BDF2 scheme to march in time, which corresponds to the backward differencing operator

$$\delta_t^{(2)} \varphi := \frac{3\varphi^{n+2} - 4\varphi^{n+1} + \varphi^n}{2\delta t},$$

used in place of (1.3). The analysis is essentially analogous to the backward Euler scheme, the main difference being that formula (1.33) is replaced by

$$2x(3x - 4y + z) = x^2 - y^2 + (2x - y)^2 - (2y - z)^2 + (x - 2y + z)^2.$$

As a result, the right-hand side of (1.52) scales as $(h^{k+1} + \delta t^2)$ instead of $(h^{k+1} + \delta t)$.

To prove the bound (1.61), we need discrete counterparts of the following Gagliardo–Nirenberg–Poincaré's inequalities valid for $p \in [2, +\infty)$ if $d = 2$, $p \in [2, 6]$ if $d = 3$, and all $v \in H^2(\Omega) \cap L^2_0(\Omega)$:

$$|v|_{W^{1,p}(\Omega)} \lesssim \|v\|^{1-\alpha} |v|^{\alpha}_{H^2(\Omega)} \lesssim |v|^{1-\alpha}_{H^1(\Omega)} |v|^{\alpha}_{H^2(\Omega)}, \qquad \alpha := \frac{1}{2} + \frac{d}{2}\left(\frac{1}{2} - \frac{1}{p}\right), \quad (1.63)$$

where the first bound follows from [3, Theorem 3] and the second from Poincaré's inequality. The proof of the following Lemma will be given in Section 1.7.

Lemma 1.14 (Discrete Gagliardo–Nirenberg–Poincaré's inequalities)**.** *Under the assumptions of Lemma 1.7, it holds for $p \in [2, +\infty)$ if $d = 2$, $p \in [2, 6]$ if $d = 3$ with $C > 0$ independent of h and α defined as in (1.63),*

$$\forall \underline{v}_h \in \underline{P}^{k+1,k}_{h,0}, \qquad \|\nabla_h v_h\|_{L^p(\Omega)^d} \le C \|\underline{v}_h\|^{1-\alpha}_{1,h} \|\underline{L}^k_h \underline{v}_h\|^{\alpha}_{0,h}. \quad (1.64)$$

Proposition 1.15 (Bound on $\|\underline{z}_h\|_{1,h}$)**.** *With $\underline{z}_h$ defined as in* (1.59)*, the bound* (1.61) *holds.*

Proof. Recalling the definition (1.15) of the $\|\cdot\|_{1,h}$-norm, one has

$$\begin{aligned}\|\underline{z}_h\|_{1,h}^2 &= \|\nabla_h \pi_h^{k+1} Q^n\|^2 + \sum_{T\in\mathcal{T}_h}\sum_{F\in\mathcal{F}_T\cap\mathcal{F}_h^{\mathrm{i}}} h_F^{-1}\|\pi_F^k(\{\{Q^n\}\}_F - \pi_T^{k+1}Q^n)\|_F^2 \\ &:= \mathfrak{T}_1^2 + \mathfrak{T}_2^2.\end{aligned} \tag{1.65}$$

(i) *Bound for $\mathfrak{T}_1$.* Using the H^1-stability (1.7) of π_h^{k+1}, formula (1.41) to infer $Q^n = q^n(c_h^n - c^n)$ with $q^n := (c_h^n)^2 + c_h^n c^n + (c^n)^2 - 1$, the triangle and Hölder inequalities, we get, for all $T \in \mathcal{T}_h$,

$$\begin{aligned}|\mathfrak{T}_1| &\lesssim \|\nabla_h Q^n\| \le \|q^n \nabla_h(c_h^n - c^n)\| + \|(c_h^n - c^n)\nabla_h q^n\| \\ &\lesssim \left(\|c_h^n\|_{L^\infty(\Omega)}^2 + \|c^n\|_{L^\infty(\Omega)}^2 + 1\right)\|\nabla_h(c_h^n - c^n)\| \\ &\quad + \|c_h^n - c^n\|_{L^6(\Omega)}\left(\|c_h^n\|_{L^\infty(\Omega)} + \|c^n\|_{L^\infty(\Omega)}\right)\left(\|\nabla_h c_h^n\|_{L^3(\Omega)^d} + \|\nabla c^n\|_{L^3(\Omega)^d}\right).\end{aligned}$$

Noting the a priori bound (1.44) and the regularity assumption (1.51), both $\|c_h^n\|_{L^\infty(\Omega)}$ and $\|c^n\|_{L^\infty(\Omega)}$ are $\lesssim 1$. Additionally, by the continuous Gagliardo–Nirenberg–Poincaré's inequality (1.63) with $p = 3$ and the regularity assumption (1.51), one has with $\alpha = 1/2 + d/12$, $\|\nabla c^n\|_{L^3(\Omega)^d} \lesssim |c^n|_{H^1(\Omega)}^{1-\alpha}\|c^n\|_{H^2(\Omega)}^{\alpha} \lesssim 1$. Similarly, the discrete Gagliardo–Nirenberg–Poincaré's inequality (1.64) with $p = 3$ combined with the a priori bounds (1.30) and (1.44) yields

$$\|\nabla_h c_h^n\|_{L^3(\Omega)^d} \lesssim \|\underline{c}_h^n\|_{1,h}^{1-\alpha}\|\underline{L}_h^k \underline{c}_h^n\|_{0,h}^{\alpha} \lesssim 1.$$

Then, inserting $\pm(\widehat{c}_h^n - \pi_h^{k+1}c^n)$ and using the triangle inequality,

$$\begin{aligned}|\mathfrak{T}_1| &\lesssim \left(\|\nabla_h e_{c,h}^n\| + \|e_{c,h}^n\|_{L^6(\Omega)}\right) + \left(\|\nabla_h(\widehat{c}_h^n - \pi_h^{k+1}c^n)\| + \|\widehat{c}_h^n - \pi_h^{k+1}c^n\|_{L^6(\Omega)}\right) \\ &\quad + \left(\|\nabla_h(\pi_h^{k+1}c^n - c^n)\| + \|\pi_h^{k+1}c^n - c^n\|_{L^6(\Omega)}\right) \\ &:= \mathfrak{T}_{1,1} + \mathfrak{T}_{1,2} + \mathfrak{T}_{1,3}.\end{aligned} \tag{1.66}$$

Using the discrete Friedrichs' inequality (1.18) with $r = 6$ together with the definition (1.15) of the $\|\cdot\|_{1,h}$-norm and the first inequality in (1.22), it is readily inferred that $\mathfrak{T}_{1,1} \lesssim \|\underline{e}_{c,h}^n\|_{a,h}$. Again the Friedrichs' inequality (1.18) with $r = 6$ followed by the approximation properties (1.48) of $\widehat{c}_h^n$ and the regularity (1.51) yields $\mathfrak{T}_{2,2} \lesssim h^{k+1}\|c^n\|_{H^{k+2}(\Omega)} \lesssim h^{k+1}$. Finally, using the approximation properties (1.8) of π_h^{k+1}, we have $\mathfrak{T}_{1,3} \lesssim h^{k+1}(\|c^n\|_{H^{k+2}(\Omega)} + \|c^n\|_{W^{k+1,6}(\Omega)}) \lesssim h^{k+1}$, where we have used the fact that $H^{k+2}(\Omega) \subset W^{k+1,6}(\Omega)$ for all $k \ge 0$ and $d \in \{2, 3\}$

on domains satisfying the cone condition (cf. [4, Theorem 4.12]). Gathering the previous bounds, we conclude that

$$|\mathfrak{T}_1| \lesssim \|\underline{e}_{c,h}^n\|_{a,h} + h^{k+1}. \tag{1.67}$$

(ii) *Bound for* $\mathfrak{T}_2$. For all interface $F \in \mathcal{F}_{T_1} \cap \mathcal{F}_{T_2}$, we denote by $[\![\cdot]\!]_F$ the usual jump operator such that, for every function φ with a possibly two-valued trace on F, $[\![\varphi]\!]_F := \varphi_{|T_1} - \varphi_{|T_2}$ (the orientation is irrelevant). Let an element $T \in \mathcal{T}_h$ and an interface face $F \in \mathcal{F}_T \cap \mathcal{F}_{T^+}$ be fixed. Using the L^2-stability of π_F^k, inserting $\pm Q_T^n$ (with $Q_T^n := Q^n{}_{|T}$), and using the triangle inequality it holds,

$$\begin{aligned}\|\pi_F^k(\{\{Q^n\}\}_F - \pi_T^{k+1}Q_T^n)\|_F &\le \|\{\{Q^n\}\}_F - \pi_T^{k+1}Q_T^n\|_F \\ &\le \frac{1}{2}\|[\![Q^n]\!]_F\|_F + \|Q_T^n - \pi_T^{k+1}Q_T^n\|_F \\ &\lesssim \|[\![Q^n]\!]_F\|_F + h_T^{\frac{1}{2}}\|\nabla Q_T^n\|_T,\end{aligned} \tag{1.68}$$

where we have used (1.8) for the last term. Let us bound the first term in the right-hand side. Observing that $[\![\Phi'(c^n)]\!]_F = 0$ and recalling (1.41), it is inferred

$$|[\![Q^n]\!]_F| = |[\![\Phi'(c_h^n)]\!]_F| \le |[\![c_h^n]\!]_F| \left(|c_T|^2 + |c_T||c_{T^+}| + |c_{T^+}|^2 + 1\right).$$

Using this relation, and noticing the a priori bound (1.44), we get

$$\|[\![Q^n]\!]_F\|_F \lesssim \left(\|c_h^n\|_{L^\infty(\Omega)}^2 + 1\right)\|[\![c_h^n]\!]_F\|_F \lesssim \|[\![c_h^n]\!]_F\|_F = \|[\![c_h^n - c^n]\!]_F\|_F,$$

where the conclusion follows observing that c^n has zero jumps across interfaces. Inserting $\pm[\![\widehat{c}_h^n - \pi_h^{k+1}c^n]\!]_F$ inside the norm and using the triangle inequality, we obtain

$$\|[\![Q^n]\!]_F\|_F \lesssim \|[\![c_h^n - \widehat{c}_h^n]\!]_F\|_F + \|[\![\widehat{c}_h^n - \pi_h^{k+1}c^n]\!]_F\|_F + \|[\![\pi_h^{k+1}c^n - c^n]\!]_F\|_F. \tag{1.69}$$

Define on $H^1(\mathcal{T}_h)$ the jump seminorm $|v|_{\mathrm{J}}^2 := \sum_{F\in\mathcal{F}_h^{\mathrm{i}}} h_F^{-1}\|[\![v]\!]_F\|_F^2$. Let us prove that

$$\forall \underline{v}_h \in \underline{P}_h^{k+1,k}, \qquad |v_h|_{\mathrm{J}} \lesssim \|\underline{v}_h\|_{1,h} \lesssim \|\underline{v}_h\|_{a,h}. \tag{1.70}$$

Inserting $\pm(\pi_F^k[\![v_h]\!]_F - v_F)$ and using the triangle inequality, it is inferred that

$$|v_h|_{\mathrm{J}}^2 \lesssim \sum_{F\in\mathcal{F}_h^{\mathrm{i}}}\sum_{T\in\mathcal{T}_F} h_F^{-1}\left(\|v_T - \pi_F^k v_T\|_F^2 + \|\pi_F^k(v_T - v_F)\|_F^2\right) \lesssim \|\nabla_h v_h\|^2 + |\underline{v}_h|_{1,h}^2,$$

where we have used (1.9) followed by the discrete trace inequality (1.4) and the fact that $\mathrm{card}(\mathcal{F}_T) \lesssim 1$ by mesh regularity for the first term, and the definition (1.15) of

the $|\cdot|_{1,h}$-seminorm for the second term. This proves the first bound in (1.70). The second bound follows from (1.22).

Multiplying (1.68) by $h_F^{-\frac{1}{2}}$, squaring, summing over $F \in \mathcal{F}_T \cap \mathcal{F}_h^{\mathrm{i}}$ then over $T \in \mathcal{T}_h$, using mesh regularity to infer that $\mathrm{card}(\mathcal{F}_T)$ is bounded uniformly in h, and noticing (1.69) yields

$$\begin{aligned}\mathfrak{T}_2^2 &\lesssim \|\nabla_h Q^n\|^2 + |c_h^n - \widehat{c}_h^n|_{\mathrm{J}}^2 + |\widehat{c}_h^n - \pi_h^{k+1} c^n|_{\mathrm{J}}^2 + |\pi_h^{k+1} c^n - c^n|_{\mathrm{J}}^2 \\ &\lesssim \|\nabla_h Q^n\|^2 + \|\underline{e}_{c,h}^n\|_{a,h}^2 + \|\underline{\widehat{c}}_h^n - \underline{I}_h^k c^n\|_{a,h}^2 + |\pi_h^{k+1} c^n - c^n|_{\mathrm{J}}^2 \\ &\lesssim \|\nabla_h Q^n\|^2 + \|\underline{e}_{c,h}^n\|_{a,h}^2 + \left(h^{k+1}\|c^n\|_{H^{k+2}(\Omega)}\right)^2,\end{aligned} \tag{1.71}$$

where we have used (1.70) to pass to the second line and the approximation properties (1.48) of $\underline{\widehat{c}}_h^n$ and (1.8) of π_h^{k+1} to conclude. Proceeding as in point (i) to bound the first term in the right-hand side of (1.71), and recalling the regularity assumptions (1.51) on c, we conclude

$$|\mathfrak{T}_2| \le \|\underline{e}_{c,h}^n\|_{a,h} + h^{k+1}. \tag{1.72}$$

(iii) *Conclusion.* Using (1.67) and (1.72) in (1.65), the estimate (1.61) follows. □

Remark 1.16 (Polynomial degree for element DOFs). The use of polynomials of degree $(k+1)$ (instead of k) as elements DOFs in the discrete space (1.13) is required to infer an estimate of order h^{k+1} in (1.66) and for the last term in (1.71).

1.6 Numerical results

In this section we provide numerical evidence to confirm the theoretical results.

1.6.1 Convergence

We start by a non-physical numerical test that demonstrates the orders of convergence achieved by our method. We solve the Cahn-Hilliard problem (1.49) on the unit square $\Omega = (0,1)^2$ with $t_F = 1$, order-parameter

$$c(\boldsymbol{x}, t) = t\cos(\pi x_1)\cos(\pi x_2),$$

and chemical potential w inferred from c according to (1.1b). The right-hand side of (1.1a) is also modified by introducing a nonzero source in accordance with the expression of c. The interface parameter γ is taken equal to 1.

We consider the triangular, Cartesian, and (predominantly) hexagonal mesh families of Figure 1.1. The two former mesh families were introduced in the

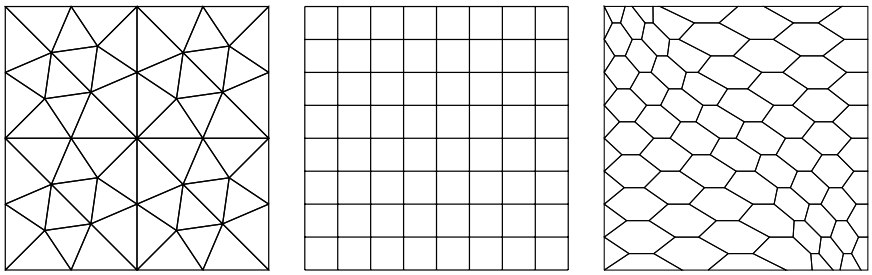

Figure 1.1: Mesh families for the numerical tests

FVCA5 benchmark [111], whereas the latter was introduced in [87]. To march in time, we use the implicit Euler scheme. Since the order-parameter is linear in time, only the spatial component of the discretization error is nonzero and the choice of the time step is irrelevant. The energy errors $\|\underline{c}_h^N - \underline{I}_h^k c^N\|_{a,h}$ and $\|\underline{w}_h^N - \underline{I}_h^k w^N\|_{a,h}$ at final time are depicted in Figure 1.2. For all mesh families, the convergence rate is $(k+1)$, in accordance with Theorem 1.12. For the sake of completeness, we also display in Figure 1.3 the L^2-errors $\|c_h^n - \pi_h^{k+1} c^n\|$ and $\|w_h^n - \pi_h^{k+1} w^n\|$, for which an optimal convergence rate of $(k+2)$ is observed.

1.6.2 Evolution of an elliptic and a cross-shaped interfaces

The numerical examples of this section consist in tracking the evolution of initial data corresponding, respectively, to an elliptic and a cross-shaped interface between phases. For the elliptic interface test case of Figure 1.4, the initial datum is

$$c_0(\boldsymbol{x}) = \begin{cases} 0.95 & \text{if } 81\,(x_1 - 0.5)^2 + 9\,(x_2 - 0.5)^2 < 1, \\ -0.95 & \text{otherwise.} \end{cases}$$

For the cross-shaped interface test case of Figure 1.5, we take

$$c_0(\boldsymbol{x}) = \begin{cases} 0.95 & \text{if } \ 5\left(|(x_2{-}0.5) - \tfrac{2}{5}(x_1{-}0.5)| + |\tfrac{2}{5}(x_1{-}0.5) + (x_2{-}0.5)|\right) < 1 \\ & \text{or } \ 5\left(|(x_1{-}0.5) - \tfrac{2}{5}(x_2{-}0.5)| + |\tfrac{2}{5}(x_2{-}0.5) + (x_1{-}0.5)|\right) < 1, \\ -0.95 & \text{otherwise.} \end{cases}$$

In both cases, the space domain is the unit square $\Omega = (0,1)^2$, and the interface parameter γ is taken to be $1 \cdot 10^{-2}$. We use a 64×64 uniform Cartesian mesh and $k = 1$ with time step $\delta t = \gamma^2/10$.

In the test case of Figure 1.4, we observe evolution of the elliptic interface towards a circular interface and, as expected, mass is well preserved (+0.5% with respect to the initial ellipse). Similar considerations hold for the cross-shaped test case of Figure 1.5, which has the additional difficulty of presenting sharp corners.

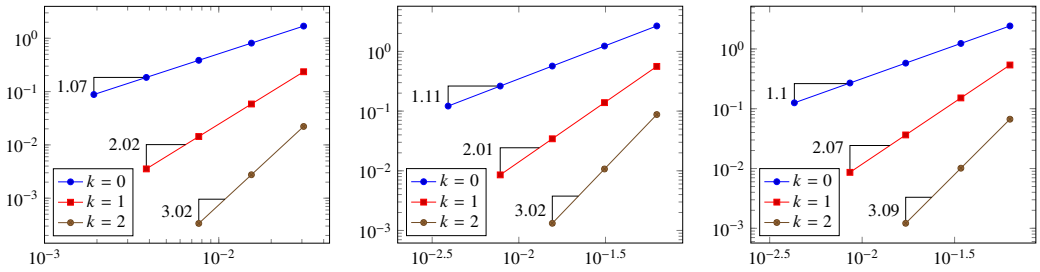

(a) $\|\underline{c}_h^N - \underline{I}_h^k c^N\|_{a,h}$ vs. h

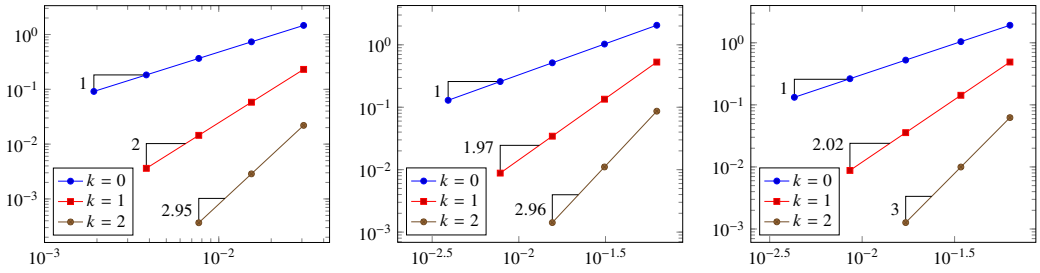

(b) $\|\underline{w}_h^N - \underline{I}_h^k w^N\|_{a,h}$ vs. h

Figure 1.2: Energy-errors at final time vs. h. From left to right: triangular, Cartesian and (predominantly) hexagonal mesh families; cf. Figure 1.1.

1.6.3 Spinodal decomposition

Spinodal decomposition can be observed when a binary alloy is heated to a high temperature for a certain time and then abruptly cooled. As a result, phases are separated in well-defined high concentration areas. In Figure 1.6, we display the numerical solutions obtained on a 128×128 uniform Cartesian mesh for $k = 0$ and on a uniform 64×64 Cartesian mesh for $k = 1$. In both cases, we use the same initial conditions taking random values between -1 and 1 on a 32×32 uniform Cartesian partition of the domain. The interface parameter is $\gamma = 1/100$, and we take $\delta t = \gamma^2/10$. For $k = 0$, the time discretisation is based on the Backward Euler scheme while, for $k = 1$, we use the BDF2 formula to make sure that the spatial and temporal error contributions are equilibrated; cf. Remark 1.13.

The separation of the two components into two distinct phases happens over a very small time; see two leftmost panels of Figure 1.6 corresponding to times 0 and $5 \cdot 10^{-5}$, respectively. Later, the phases gather increasingly slowly until the interfaces develop a constant curvature; see the two rightmost panels of Figure 1.6, corresponding to times $1.25 \cdot 10^{-3}$ and $3.6 \cdot 10^{-2}$, respectively. At the latest stages, we can observe that the solution exhibits a (small) dependence on the mesh and/or the polynomial degree, and the high-concentration regions in Figures 1.6a and 1.6b

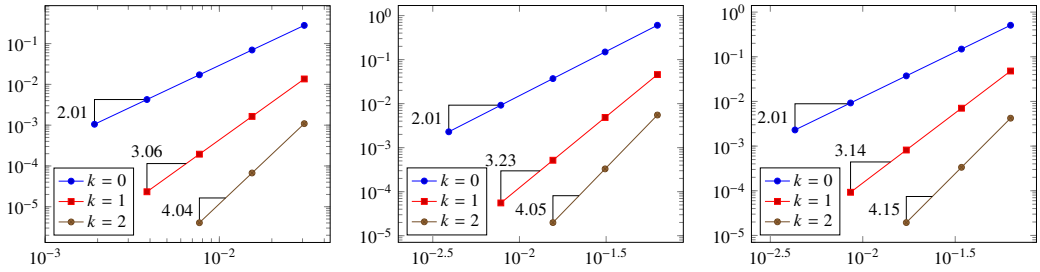

(a) $\|c_h^N - \pi_h^{k+1} c^N\|$ vs. h

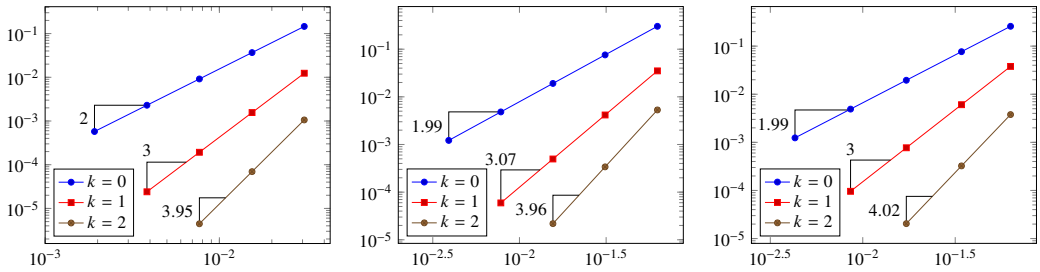

(b) $\|w_h^N - \pi_h^{k+1} w^N\|$ vs. h

Figure 1.3: L^2-errors at final time vs. h. From left to right: triangular, Cartesian and (predominantly) hexagonal mesh families; cf. Figure 1.1.

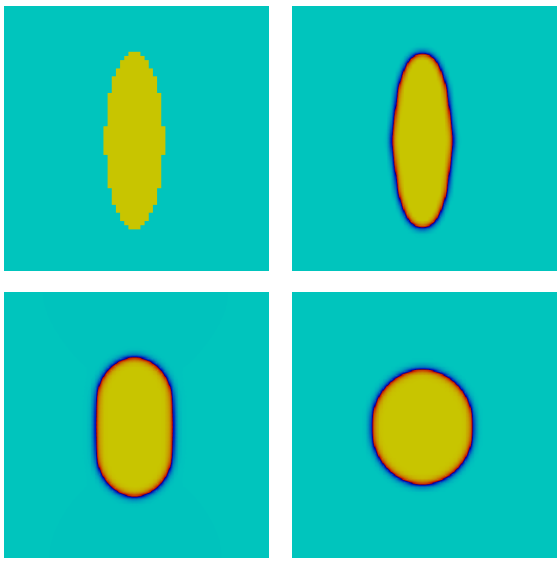

Figure 1.4: Evolution of an elliptic interface (left to right, top to bottom). Displayed times are 0 , $3 \cdot 10^{-3}$, 0.3, 1.

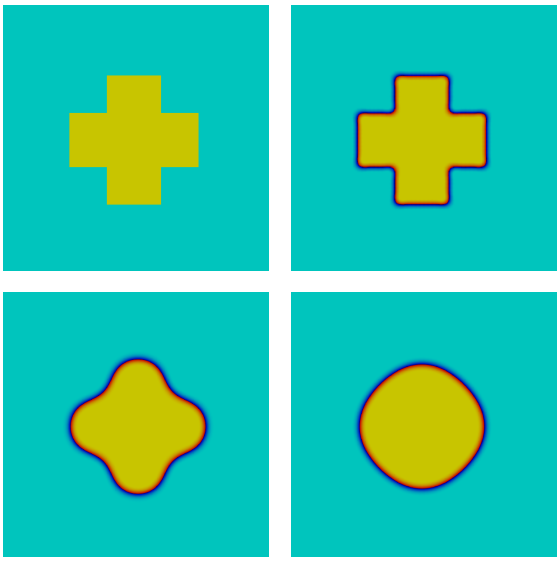

Figure 1.5: Evolution of a cross-shaped interface (left to right, top to bottom). Displayed times are 0, $5 \cdot 10^{-5}$, $1 \cdot 10^{-2}$, $8.17 \cdot 10^{-2}$.

are highly superposable but not identical.

1.7 Proofs of discrete functional analysis results

This section contains the proofs of Lemmas 1.7 and 1.14 preceeded by the required preliminary technical results.

Proposition 1.17 (Estimates for $\underline{L}_h^k$)**.** *Assuming mesh quasi-uniformity* (1.10)*, it holds*

$$\forall \underline{v}_h \in \underline{P}_h^{k+1,k}, \qquad \|\underline{L}_h^k \underline{v}_h\|_{0,h} \lesssim h^{-1} \|\underline{v}_h\|_{1,h}, \tag{1.73}$$

$$\forall \underline{v}_h \in \underline{P}_{h,0}^{k+1,k}, \qquad \|L_h^k \underline{v}_h\|_{H^{-1}(\Omega)} \lesssim \|\underline{v}_h\|_{1,h}. \tag{1.74}$$

Proof. (i) *Proof of* (1.73). Let $\underline{v}_h \in \underline{P}_h^{k+1,k}$. Making $\underline{z}_h = -\underline{L}_h^k \underline{v}_h$ in the definition (1.27) of $\underline{L}_h^k$, we have

$$\|\underline{L}_h^k \underline{v}_h\|_{0,h}^2 = -a_h(\underline{v}_h, \underline{L}_h^k \underline{v}_h) \lesssim \|\underline{v}_h\|_{1,h} \|\underline{L}_h^k \underline{v}_h\|_{1,h} \lesssim \|\underline{v}_h\|_{1,h} h^{-1} \|\underline{L}_h^k \underline{v}_h\|_{0,h},$$

where we have used the continuity of a_h expressed by the second inequality in (1.22) followed by the fact that, for all $\underline{z}_h \in \underline{P}_h^{k+1,k}$, $\|\underline{z}_h\|_{1,h} \lesssim h^{-1} \|\underline{z}_h\|_{0,h}$. This inequality follows from the definition (1.15) of the $\|\cdot\|_{1,h}$-norm using the inverse inequality (1.5) to bound the first term and recalling mesh quasi-uniformity (1.10).

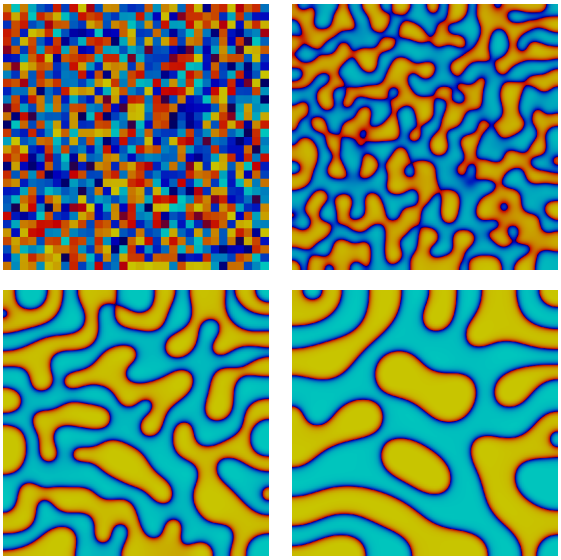

(a) 128×128 uniform Cartesian mesh, $k = 0$, BE

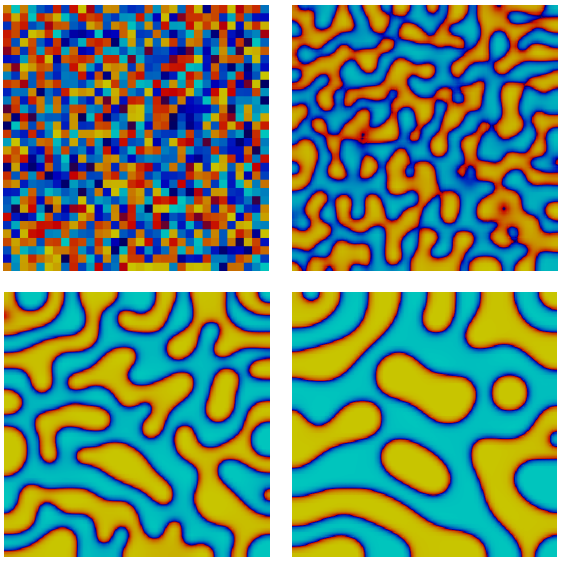

(b) 64×64 uniform Cartesian mesh, $k = 1$, BDF2

Figure 1.6: Spinoidal decomposition (left to right, top to bottom). In both cases, the same random initial condition is used. Displayed times are 0, $5{\cdot}10^{-5}$, $1.25{\cdot}10^{-3}$, $3.6 \cdot 10^{-2}$.

(ii) *Proof of* (1.74). Let $\underline{v}_h \in \underline{P}_{h,0}^{k+1,k}$. Observing that $L_h^k \underline{v}_h$ has zero-average on Ω (cf. Remark 1.6), we have

$$\|L_h^k \underline{v}_h\|_{H^{-1}(\Omega)} = \sup_{\varphi \in H^1(\Omega) \cap L_0^2(\Omega), \|\varphi\|_{H^1(\Omega)}=1} \int_\Omega L_h^k \underline{v}_h \varphi. \tag{1.75}$$

Let now $\underline{\varphi}_h := \underline{I}_h^k \varphi$. Using the fact that $L_h^k \underline{v}_h \in \mathbb{P}^{k+1}(\mathcal{T}_h)$ followed by the definitions (1.27) of $\underline{L}_h^k$ and (1.26) of $(\cdot,\cdot)_{0,h}$, one has

$$\int_\Omega L_h^k \underline{v}_h \varphi = \int_\Omega L_h^k \underline{v}_h \pi_h^{k+1} \varphi = -s_{0,h}(\underline{L}_h^k \underline{v}_h, \underline{\varphi}_h) - a_h(\underline{v}_h, \underline{\varphi}_h).$$

Hence, using the Cauchy–Schwarz inequality we get

$$\begin{aligned} |\int_\Omega L_h^k \underline{v}_h \varphi| &\lesssim |L_h^k \underline{v}_h|_{0,h} |\underline{\varphi}_h|_{0,h} + \|\underline{v}_h\|_{1,h} \|\underline{\varphi}_h\|_{1,h} \\ &\lesssim h^{-1} \|\underline{v}_h\|_{1,h} h |\underline{\varphi}_h|_{1,h} + \|\underline{v}_h\|_{1,h} \|\underline{\varphi}_h\|_{1,h} \\ &\lesssim \|\underline{v}_h\|_{1,h} \|\underline{\varphi}_h\|_{1,h} \lesssim \|\underline{v}_h\|_{1,h} \|\varphi\|_{H^1(\Omega)}, \end{aligned}$$

where we have used the second inequality in (1.22) in the first line, (1.73) together with the fact that $|\underline{z}_h|_{0,h} \le h |\underline{z}_h|_{1,h}$ for all $\underline{z}_h \in \underline{P}_h^{k+1,k}$ to pass to the second line, and the H^1-stability (1.17) of $\underline{I}_h^k$ to conclude. To obtain (1.74), plug the above estimate into the right-hand side of (1.75).

□

We introduce the continuous Green's function $\mathcal{G} : L_0^2(\Omega) \to H^1(\Omega) \cap L_0^2(\Omega)$ such that, for all $\varphi \in L_0^2(\Omega)$,

$$\int_\Omega \nabla \mathcal{G}\varphi \cdot \nabla v = \int_\Omega \varphi v \qquad \forall v \in H^1(\Omega).$$

Owing to elliptic regularity (which holds since Ω is convex), we have $\mathcal{G}\varphi \in H^2(\Omega)$. Its discrete counterpart $\underline{\mathcal{G}}_h^k : \underline{P}_{h,0}^{k+1,k} \to \underline{P}_{h,0}^{k+1,k}$ is defined such that, for all $\underline{\varphi}_h \in \underline{P}_{h,0}^{k+1,k}$,

$$a_h(\underline{\mathcal{G}}_h^k \underline{\varphi}_h, \underline{z}_h) = (\underline{\varphi}_h, \underline{z}_h)_{0,h} \qquad \forall \underline{z}_h \in \underline{P}_{h,0}^{k+1,k}, \tag{1.76}$$

with inner product $(\cdot,\cdot)_{0,h}$ defined by (1.26). We will denote by $\mathcal{G}_h^k \underline{v}_h$ (no underline) the broken polynomial function in $\mathbb{P}^{k+1}(\mathcal{T}_h)$ obtained from element DOFs in $\underline{\mathcal{G}}_h^k \underline{v}_h$. We next show that $-\underline{\mathcal{G}}_h^k$ is the inverse of $\underline{L}_h^k$ restricted to $\underline{P}_{h,0}^{k+1,k} \to \underline{P}_{h,0}^{k+1,k}$. Let $\underline{v}_h \in \underline{P}_{h,0}^{k+1,k}$. Using (1.76) with $\underline{\varphi}_h = \underline{L}_h^k \underline{v}_h$ followed by (1.27), it is inferred, for all $\underline{z}_h \in \underline{P}_{h,0}^{k+1,k}$,

$$a_h(\underline{\mathcal{G}}_h^k \underline{L}_h^k \underline{v}_h, \underline{z}_h) = (\underline{L}_h^k \underline{v}_h, \underline{z}_h)_{0,h} = -a_h(\underline{v}_h, \underline{z}_h) \implies a_h(\underline{v}_h + \underline{\mathcal{G}}_h^k \underline{L}_h^k \underline{v}_h, \underline{z}_h) = 0.$$

Therefore, since $(\underline{v}_h + \underline{\mathcal{G}}_h^k \underline{L}_h^k \underline{v}_h) \in \underline{P}_{h,0}^{k+1,k}$ and a_h is coercive in $\underline{P}_{h,0}^{k+1,k}$ (cf. (1.22) and Proposition 1.3), we conclude

$$\underline{v}_h + \underline{\mathcal{G}}_h^k \underline{L}_h^k \underline{v}_h = \underline{0} \qquad \forall \underline{v}_h \in \underline{P}_{h,0}^{k+1,k}. \tag{1.77}$$

Proposition 1.18 (Estimates for $\underline{\mathcal{G}}_h^k$)**.** *It holds, for all* $\underline{v}_h \in \underline{P}_{h,0}^{k+1,k}$,

$$\|\underline{\mathcal{G}}_h^k \underline{v}_h - \underline{I}_h^k \mathcal{G} v_h\|_{1,h} \lesssim h \left(|\underline{v}_h|_{0,h} + \|\mathcal{G} v_h\|_{H^2(\Omega)} \right) \lesssim h \|\underline{v}_h\|_{0,h}. \tag{1.78}$$

Moreover, using elliptic regularity, we have

$$\|\mathcal{G}_h^k \underline{v}_h - \pi_h^{k+1} \mathcal{G} v_h\| \lesssim h^2 \left(|\underline{v}_h|_{0,h} + \|\mathcal{G} v_h\|_{H^2(\Omega)} \right) \lesssim h^2 \|\underline{v}_h\|_{0,h}. \tag{1.79}$$

Proof. Let $\underline{v}_h \in \underline{P}_{h,0}^{k+1,k}$.

(i) *Proof of* (1.78). For all $\underline{z}_h \in \underline{P}_{h,0}^{k+1,k}$ we have, using the definition (1.76) of $\underline{\mathcal{G}}_h^k \underline{v}_h$ and subtracting the quantity $(v_h + \Delta \mathcal{G} v_h, z_h) = 0$,

$$a_h(\underline{\mathcal{G}}_h^k \underline{v}_h - \underline{I}_h^k \mathcal{G} v_h, \underline{z}_h) = \underbrace{(\underline{v}_h, \underline{z}_h)_{0,h} - \int_\Omega v_h z_h}_{\mathfrak{T}_1} \underbrace{- a_h(\underline{I}_h^k \mathcal{G} v_h, \underline{z}_h) - \int_\Omega \Delta \mathcal{G} v_h z_h}_{\mathfrak{T}_2}. \tag{1.80}$$

Recalling the definition (1.26) of the inner product $(\cdot,\cdot)_{0,h}$, one has

$$|\mathfrak{T}_1| = |s_{0,h}(\underline{v}_h, \underline{z}_h)| \le |\underline{v}_h|_{0,h} |\underline{z}_h|_{0,h} \le h |\underline{v}_h|_{0,h} |\underline{z}_h|_{1,h}. \tag{1.81}$$

On the other hand, the consistency property (1.23) of the bilinear form a_h readily yields

$$|\mathfrak{T}_2| \lesssim h \|\mathcal{G} v_h\|_{H^2(\Omega)} \|\underline{z}_h\|_{1,h}. \tag{1.82}$$

Making $\underline{z}_h = \underline{\mathcal{G}}_h^k \underline{v}_h - \underline{I}_h^k \mathcal{G} v_h$ in (1.80), and using the coercivity of a_h expressed by the first inequality in (1.22) followed by the bounds (1.81)–(1.82), the first bound in (1.78) follows. To prove the second bound in (1.78), use elliptic regularity to estimate $\|\mathcal{G} v_h\|_{H^2(\Omega)} \lesssim \|v_h\|$ and recall the definition of the $\|\cdot\|_{0,h}$-norm.

(ii) *Proof of* (1.79). We follow the ideas of [83, Theorem 10] and [77, Theorem 11], to which we refer for further details. Set, for the sake of brevity, $\underline{\varphi}_h := \underline{\mathcal{G}}_h^k \underline{v}_h - \underline{I}_h^k \mathcal{G} v_h$, and let $z := \mathcal{G} \varphi_h$. By elliptic regularity, $z \in H^2(\Omega)$ and $\|z\|_{H^2(\Omega)} \lesssim \|\varphi_h\|$. Observing that $-\Delta z = \varphi_h$, letting $\widehat{\underline{z}}_h := \underline{I}_h^k z$, and using the definition (1.76) of $\underline{\mathcal{G}}_h^k$, we have

$$\|\varphi_h\|^2 = \underbrace{- \int_\Omega \Delta z \varphi_h - a_h(\underline{\varphi}_h, \widehat{\underline{z}}_h)}_{\mathfrak{T}_1} + \underbrace{\int_\Omega v_h \widehat{z}_h - a_h(\underline{I}_h^k \mathcal{G} v_h, \widehat{\underline{z}}_h)}_{\mathfrak{T}_2} + \underbrace{s_{0,h}(\underline{v}_h, \widehat{\underline{z}}_h)}_{\mathfrak{T}_3}. \tag{1.83}$$

Using the consistency (1.23) of a_h, it is readily inferred for the first term

$$|\mathfrak{T}_1| \lesssim h\|z\|_{H^2(\Omega)}\|\underline{\varphi}_h\|_{1,h} \lesssim h^2\left(|\underline{v}_h|_{0,h} + \|\mathcal{G}v_h\|_{H^2(\Omega)}\right)\|\varphi_h\|, \tag{1.84}$$

where we have used elliptic regularity to infer $\|z\|_{H^2(\Omega)} \lesssim \|\varphi_h\|$ and (1.78) to bound $\|\underline{\varphi}_h\|_{1,h}$. For the second term, upon observing that $\int_\Omega v_h\widehat{z}_h = -\int_\Omega \Delta\mathcal{G}v_h z = \int_\Omega \nabla\mathcal{G}v_h\nabla z$ since, by definition of, $-\Delta\mathcal{G}v_h = v_h \in \mathbb{P}^{k+1}(\mathcal{T}_h)$ and $\widehat{z}_h = \pi_h^{k+1}z$, recalling the definition (1.21) of the bilinear form a_h and using the orthogonality property (1.20) of $(r_T^{k+1}\circ\underline{I}_T^k)$, we have

$$\mathfrak{T}_2 = \sum_{T\in\mathcal{T}_h}\int_T \nabla(r_T^{k+1}\underline{I}_T^k\mathcal{G}v_h - \mathcal{G}v_h)\cdot\nabla(r_T^{k+1}\underline{\widehat{z}}_h - z) + s_{1,h}(\underline{I}_h^k\mathcal{G}v_h, \underline{\widehat{z}}_h).$$

By the approximation properties of $(r_T^{k+1}\circ\underline{I}_T^k)$ and of π_h^{k+1}, and bounding $\|z\|_{H^2(\Omega)}$ and $\|\underline{\varphi}_h\|_{1,h}$ as before, we have

$$|\mathfrak{T}_2| \lesssim h^2\left(|\underline{v}_h|_{0,h} + \|\mathcal{G}v_h\|_{H^2(\Omega)}\right)\|\varphi_h\|. \tag{1.85}$$

Finally, for the last term, we write

$$|\mathfrak{T}_3| \le |\underline{v}_h|_{0,h}|\underline{\widehat{z}}_h|_{0,h} \lesssim |\underline{v}_h|_{0,h}h^2\|z\|_{H^2(\Omega)} \lesssim h^2|\underline{v}_h|_{0,h}\|\varphi_h\|, \tag{1.86}$$

where we have used the Cauchy–Schwarz inequality in the first bound, the approximation properties (1.8) of π_h^{k+1} in the second bound, and elliptic regularity to conclude. Using (1.84)–(1.86) to estimate the right-hand side of (1.83) the first inequality in (1.79) follows. Using elliptic regularity to further bound $\|\mathcal{G}v_h\|_{H^2(\Omega)} \lesssim \|v_h\|$ and recalling the definition of the $\|\cdot\|_{0,h}$-norm yields the second inequality in (1.79).

□

Remark 1.19 (Choice of $s_{0,h}$). The choice (1.26) for the stabilisation bilinear form $s_{0,h}$ is crucial to have the right-hand side of (1.86) scaling as h^2. Penalizing the full difference $(v_F - v_T)$ instead of the lowest-order part $\pi_F^k(v_F - v_T)$ would have lead to a right-hand side only scaling as h.

We are now ready to prove Lemma 1.7.

Proof of Lemma 1.7. Let $\underline{v}_h \in \underline{P}_{h,0}^{k+1,k}$ and set $\underline{\varphi}_h := \underline{L}_h^k\underline{v}_h$. Recalling that, owing to (1.77), $v_h = -\mathcal{G}_h^k\underline{\varphi}_h$, it is inferred using the triangle inequality,

$$\|v_h\|_{L^\infty(\Omega)} \le \|\pi_h^{k+1}\mathcal{G}\varphi_h\|_{L^\infty(\Omega)} + \|\mathcal{G}_h^k\underline{\varphi}_h - \pi_h^{k+1}\mathcal{G}\varphi_h\|_{L^\infty(\Omega)} := \mathfrak{T}_1 + \mathfrak{T}_2. \tag{1.87}$$

The L^∞-stability of π_h^{k+1} (cf. (1.7)) followed by the continuous Agmon's inequality readily yields for the first term

$$\mathfrak{T}_1 \lesssim \|\mathcal{G}\varphi_h\|_{L^\infty(\Omega)} \lesssim \|\mathcal{G}\varphi_h\|_{H^1(\Omega)}^{\frac12}\|\mathcal{G}\varphi_h\|_{H^2(\Omega)}^{\frac12}. \tag{1.88}$$

Using a standard regularity shift (cf., e.g., [108]), recalling that $\varphi_h = L_h^k \underline{v}_h$, and using the H^{-1}-bound (1.74) for $L_h^k \underline{v}_h$, we have

$$\|\mathcal{G}\varphi_h\|_{H^1(\Omega)} \lesssim \|\varphi_h\|_{H^{-1}(\Omega)} \lesssim \|\underline{v}_h\|_{1,h}, \qquad \|\mathcal{G}\varphi_h\|_{H^2(\Omega)} \lesssim \|\varphi_h\| = \|L_h^k \underline{v}_h\|, \tag{1.89}$$

which plugged into (1.88) yields

$$\mathfrak{T}_1 \lesssim \|\underline{v}_h\|_{1,h}^{\frac12}\|L_h^k \underline{v}_h\|^{\frac12}. \tag{1.90}$$

For the second term we have, on the other hand,

$$\begin{aligned}
\mathfrak{T}_2 &\lesssim h^{-\frac{d}{2}}\|\mathcal{G}_h^k \underline{\varphi}_h - \pi_h^{k+1}\mathcal{G}\varphi_h\| \\
&\lesssim h^{\frac{3-d}{2}}(h\|\underline{L}_h^k \underline{v}_h\|_{0,h})^{\frac12}\|\underline{L}_h^k \underline{v}_h\|_{0,h}^{\frac12} \\
&\lesssim h^{\frac{3-d}{2}}\|\underline{v}_h\|_{1,h}^{\frac12}\|\underline{L}_h^k \underline{v}_h\|_{0,h}^{\frac12} \lesssim \|\underline{v}_h\|_{1,h}^{\frac12}\|\underline{L}_h^k \underline{v}_h\|_{0,h}^{\frac12},
\end{aligned} \tag{1.91}$$

where we have used the global inverse inequality (1.12) with $p = 2$ to obtain the first bound, the estimate (1.79) to obtain the second, (1.73) to obtain the third, and the fact that $d \le 3$ together with $h \le h_\Omega \lesssim 1$ (with h_Ω diameter of Ω) to conclude. The conclusion follows plugging (1.90) and (1.91) into (1.87). □

Remark 1.20 (Discrete Agmon's inequality in dimension $d = 2$). When $d = 2$, we have the following sharper form for the discrete Agmon's inequality:

$$\forall \underline{v}_h \in \underline{P}_{h,0}^{k+1,k}, \qquad \|v_h\|_{L^\infty(\Omega)} \lesssim \|\underline{v}_h\|_{0,h}^{\frac12}\|\underline{L}_h^k \underline{v}_h\|_{0,h}^{\frac12}. \tag{1.92}$$

To obtain (1.92), the following modifications are required in the above proof: (i) The term $\mathfrak{T}_1$ is bounded as $\mathfrak{T}_1 \lesssim \|\mathcal{G}\varphi_h\|^{\frac12}\|\mathcal{G}\varphi_h\|_{H^2(\Omega)} \lesssim \|v_h\|^{\frac12}\|L_h^k \underline{v}_h\|^{\frac12}$, where we have used $v_h = -\mathcal{G}\varphi_h$ (cf. (1.77)) for the first factor and (1.89) for the second; (ii) The third line of (1.91) becomes $\mathfrak{T}_2 \lesssim (h\|\underline{v}_h\|_{1,h})^{\frac12}\|\underline{L}_h^k \underline{v}_h\|_{0,h}^{\frac12} \lesssim \|\underline{v}_h\|_{0,h}^{\frac12}\|\underline{L}_h^k \underline{v}_h\|_{0,h}^{\frac12}$, where we have used the inverse inequality (1.5) and mesh quasi-uniformity to bound the first factor.

We next prove the discrete Gagliardo–Nirenberg–Poincaré's inequality of Lemma 1.14.

Proof of Lemma 1.14. Using the same notation as in the proof of Lemma 1.7, we have

$$\|\nabla_h v_h\|_{L^p(\Omega)^d} \le \|\nabla_h \pi_h^{k+1} \mathcal{G}\varphi_h\|_{L^p(\Omega)^d} + \|\nabla_h(\mathcal{G}_h^k \underline{\varphi}_h - \pi_h^{k+1}\mathcal{G}\varphi_h)\|_{L^p(\Omega)^d} := \mathfrak{T}_1 + \mathfrak{T}_2.$$

For the first term, we use the $W^{1,p}$-stability of π_h^{k+1} (cf. (1.7)) followed by the continuous Gagliardo–Nirenberg–Poincaré's inequality (1.63), and (1.89) to infer

$$\mathfrak{T}_1 \lesssim |\mathcal{G}\varphi_h|_{W^{1,p}(\Omega)} \lesssim |\mathcal{G}\varphi_h|_{H^1(\Omega)}^{1-\alpha} \|\mathcal{G}\varphi_h\|_{H^2(\Omega)}^{\alpha} \lesssim \|\underline{v}_h\|_{1,h}^{1-\alpha} \|L_h^k \underline{v}_h\|^{\alpha}.$$

For the second term, on the other hand, we have

$$\begin{aligned}
\mathfrak{T}_2 &\lesssim h^{d\left(\frac{1}{p}-\frac{1}{2}\right)} \|\nabla_h(\mathcal{G}_h^k \underline{\varphi}_h - \pi_h^{k+1}\mathcal{G}\varphi_h)\| \\
&\lesssim h^{d\left(\frac{1}{p}-\frac{1}{2}\right)} \|\underline{\mathcal{G}}_h^k \underline{\varphi}_h - \underline{I}_h^k \mathcal{G}\varphi_h\|_{1,h}^{1-\alpha} \|\underline{\mathcal{G}}_h^k \underline{\varphi}_h - \underline{I}_h^k \mathcal{G}\varphi_h\|_{1,h}^{\alpha} \\
&\lesssim h^{\alpha+d\left(\frac{1}{p}-\frac{1}{2}\right)} (h\|\underline{L}_h^k \underline{v}_h\|_{0,h})^{1-\alpha} \|\underline{L}_h^k \underline{v}_h\|_{0,h}^{\alpha} \\
&\lesssim h^{\alpha+d\left(\frac{1}{p}-\frac{1}{2}\right)} \|\underline{v}_h\|_{1,h}^{1-\alpha} \|\underline{L}_h^k \underline{v}_h\|_{0,h}^{\alpha} \lesssim \|\underline{v}_h\|_{1,h}^{1-\alpha} \|\underline{L}_h^k \underline{v}_h\|_{0,h}^{\alpha},
\end{aligned}$$

where we have used the global reverse Lebesgue inequality (1.11) in the first line, the definition (1.15) of the $\|\cdot\|_{1,h}$-norm to pass to the second line, the estimate (1.78) to pass to the third line, and (1.73) to pass to the fourth line. To obtain the second inequality in the fourth line, we observe that, recalling the definition (1.63) of α and the assumptions on p, it holds for the exponent of h,

$$\alpha + d\left(\frac{1}{p} - \frac{1}{2}\right) = \frac{1}{2} - \frac{d}{2}\left(\frac{1}{2} - \frac{1}{p}\right) \ge 0,$$

and, since $h \le h_\Omega \lesssim 1$, the conclusion follows. □

Remark 1.21 (Validity of the discrete Agmon's and Gagliardo–Niremberg–Poincaré's inequalities). At the discrete level, the fact that the discrete Agmon's inequality (1.28) is valid only up to $d = 3$ and that the Gagliardo–Nirenberg–Poincaré's inequalities (1.64) are valid only for $p \in [2, +\infty)$ if $d = 2$, $p \in [2, 6]$ if $d = 3$ is reflected by the need to have nonnegative powers of h in the estimates of the terms $\mathfrak{T}_2$ to conclude in the corresponding proofs.

Chapter 2

Flows in fractured porous media

This chapter has been published in the following peer-reviewed journal (see [56]):

SIAM Journal on Scientific Computing, 2018.
Volume 40, Issue 2, Pages A1063–A1094.

Contents

2.1 Introduction

In this work we develop a novel Hybrid High-Order (HHO) method for the numerical simulation of steady flows in fractured porous media.

The modelling of flow and transport in fractured porous media, and the correct identification of the fractures as hydraulic barriers or conductors are of utmost importance in several applications. In the context of nuclear waste management, the correct reproduction of flow patterns plays a key role in identifying safe underground storage sites. In petroleum reservoir modelling, accounting for the presence and hydraulic behaviour of the fractures can have a sizeable impact on the identification of drilling sites, as well as on the estimated production rates. In practice, there are several possible ways to incorporate the presence of fractures in porous media models. Our focus is here on the approach developed in [120], where an averaging process is applied, and the fracture is treated as an interface that crosses the bulk region. The fracture is additionally assumed to be filled of debris, so that the flow therein can still be modelled by the Darcy law. To close the problem, interface conditions are enforced that relate the average and jump of the bulk pressure to the normal flux and the fracture pressure. Other works where fractures are treated as interfaces include, e.g., [13, 20, 97].

Several discretization methods for flows in fractured porous media have been proposed in the literature. In [46], the authors consider lowest-order vertex- and face-based Gradient Schemes, and prove convergence in h for the energy-norm of the discretization error; see also [43] and the very recent work [92] on two-phase flows. Extended Finite Element methods (XFEM) are considered in [17, 28] in the context of fracture networks, and their convergence properties are numerically

studied. In [24], the authors compare XFEM with the recently introduced Virtual Element Method (VEM), and numerically observe in both cases convergence in $N_{\mathrm{DOF}}^{1/2}$ for the energy-norm of the discretization error, where N_{DOF} stands for the number of degrees of freedom; see also [23, 25]. Discontinuous Galerkin methods are also considered in [16] for a single-phase flow; see also [15]. Therein, an *hp*-error analysis in the energy norm is carried out on general polygonal/polyhedral meshes possibly including elements with unbounded number of faces, and numerical experiments are presented. A discretization method based on a mixed formulation in the mortar space has also been very recently proposed in [33], where an energy-error estimate in h is proved.

Our focus is here on the Hybrid High-Order (HHO) methods originally introduced in [77] in the context of linear elasticity, and later applied in [5, 78, 82, 83] to anisotropic heterogeneous diffusion problems. HHO methods are based on degrees of freedom (DOFs) that are broken polynomials on the mesh and on its skeleton, and rely on two key ingredients: (i) physics-dependent local reconstructions obtained by solving small, embarassingly parallel problems and (ii) high-order stabilization terms penalizing face residuals. These ingredients are combined to formulate local contributions, which are then assembled as in standard FE methods. In the context of fractured porous media flows, HHO methods display several key advantages, including: (i) the support of general meshes enabling a seamless treatment of nonconforming geometric discretizations of the fractures (see Remark 3.6 below); (ii) the robustness with respect to the heterogeneity and anisotropy of the permeability coefficients (see Remark 2.13 below); (iii) the possibility to increase the approximation order, which can be useful when complex phenomena such as viscous fingering or instabilities linked to thermal convection are present; (iv) the availability of mixed and primal formulations, whose intimate connection is now well-understood [31]; (v) the possibility to obtain efficient implementations thanks to static condensation (see Remark 2.9 below).

The HHO method proposed here hinges on a mixed formulation in the bulk coupled with a primal formulation inside the fracture. To keep the exposition as simple as possible while retaining all the key difficulties, we focus on the two-dimensional case, and we assume that the fracture is a line segment that cuts the bulk region in two. For a given polynomial degree $k \geq 0$, two sets of DOFs are used for the flux in the bulk region: (i) polynomials of total degree up to k on each face (representing the polynomial moments of its normal component) and (ii) fluxes of polynomials of degree up to k inside each mesh element. Combining these DOFs, we locally reconstruct (i) a discrete counterpart of the divergence operator and (ii) an approximation of the flux one degree higher than element-based DOFs. These local reconstructions are used to formulate discrete counterparts of the permeability-weighted product of fluxes and of the bluk flux-pressure coupling

terms. The primal formulation inside the fracture, on the other hand, hinges on fracture pressure DOFs corresponding to (i) polynomial moments of degree up to k inside the fracture edges and (ii) point values at face vertices. From these DOFs, we reconstruct inside each fracture face an approximation of the fracture pressure of degree $(k + 1)$, which is then used to formulate a tangential diffusive bilinear form in the spirit of [83]. Finally, the terms stemming from interface conditions on the fractures are treated using bulk flux DOFs and fracture pressure DOFs on the fracture edges.

A complete theoretical analysis of the method is carried out. In Theorem 2.11 below we prove stability in the form of an inf-sup condition on the global bilinear form collecting the bulk, fracture, and interface contributions. An important intermediate result is the stability of the bulk flux-pressure coupling, whose proof follows the classical Fortin argument based on a commuting property of the divergence reconstruction. In Theorem 2.12 below we prove an optimal error estimate in h^{k+1} for an energy-like norm of the error. The provided error estimate additionally shows that the error on the bulk flux and on the fracture pressure are (i) fully robust with respect to the heterogeneity of the bulk and fracture permeabilities, and (ii) partially robust with respect to the anisotropy of the bulk permeability (with a dependence on the square root of the local anisotropy ratio). These estimates are numerically validated, and the performance of the method is showcased on a comprehensive set of problems. The numerical computations additionally show that the L^2-norm of the errors on the bulk and fracture pressure converge as h^{k+2}.

The rest of the paper is organized as follows. In Section 3.2 we introduce the continuous setting and state the problem along with its weak formulation. In Section 3.3 we define the mesh and the corresponding notation, and recall known results concerning local polynomial spaces and projectors thereon. In Section 3.4 we formulate the HHO approximation: in a first step, we describe the local constructions in the bulk and in the fracture; in a second step, we combine these ingredients to formulate the discrete problem; finally, we state the main theoretical results corresponding to Theorems 2.11 (stability) and 2.12 (error estimate). Section 2.5 contains an extensive numerical validation of the method. Finally, Sections 2.6 and 2.7 contain the proofs of Theorems 2.11 and 2.12, respectively. Readers mainly interested in the numerical recipe and results can skip these sections at first reading.

2.2 Continuous setting

2.2.1 Notation

We consider a porous medium saturated by an incompressible fluid that occupies the space region $\Omega \subset \mathbb{R}^2$ and is crossed by a fracture Γ. We next give precise definitions of these objects. The corresponding notation is illustrated in Figure 3.1. The extension of the following discussion to the three-dimensional case is possible but is not considered here in order to alleviate the exposition; see Remark 2.10 for further details.

From the mathematical point of view, Ω is an open, bounded, connected, polygonal set with Lipschitz boundary $\partial\Omega$, while Γ is an open line segment of nonzero length. We additionally assume that Ω lies on one side of its boundary. The set $\Omega_B := \Omega \setminus \overline{\Gamma}$ represents the bulk region. We assume that the fracture Γ cuts the domain Ω into two disjoint connected polygonal subdomains with Lipschitz boundary, so that the bulk region can be decomposed as $\Omega_B := \Omega_{B,1} \cup \Omega_{B,2}$.

We denote by $\partial\Omega_B := \bigcup_{i=1}^2 \partial\Omega_{B,i} \setminus \overline{\Gamma}$ the external boundary of the bulk region, which is decomposed into two subsets with disjoint interiors: the Dirichlet boundary $\partial\Omega_B^D$, for which we assume strictly positive 1-dimensional Haussdorf measure, and the (possibly empty) Neumann boundary $\partial\Omega_B^N$. We denote by $\boldsymbol{n}_{\partial\Omega}$ the unit normal vector pointing outward Ω_B. For $i \in \{1, 2\}$, the restriction of the boundary $\partial\Omega_B^D$ (respectively, $\partial\Omega_B^N$) to the ith subdomain is denoted by $\partial\Omega_{B,i}^D$ (respectively, $\partial\Omega_{B,i}^N$).

We denote by $\partial\Gamma$ the boundary of the fracture Γ with the corresponding outward unit tangential vector $\boldsymbol{\tau}_{\partial\Gamma}$. $\partial\Gamma$ is also decomposed into two disjoint subsets: the nonempty Dirichlet fracture boundary $\partial\Gamma^D$ and the (possibly empty) Neumann fracture boundary $\partial\Gamma^N$. Notice that this decomposition is completely independent from that of $\partial\Omega_B$. Finally, $\boldsymbol{n}_\Gamma$ and $\boldsymbol{\tau}_\Gamma$ denote, respectively, the unit normal vector to Γ with a fixed orientation and the unit tangential vector on Γ such that $(\boldsymbol{\tau}_\Gamma, \boldsymbol{n}_\Gamma)$ is positively oriented. Without loss of generality, we assume in what follows that the subdomains are numbered so that $\boldsymbol{n}_\Gamma$ points out of $\Omega_{B,1}$.

For any function φ sufficiently regular to admit a (possibly two-valued) trace on Γ, we define the jump and average operators such that

$$[\![\varphi]\!]_\Gamma := \varphi_{|\Omega_{B,1}} - \varphi_{|\Omega_{B,2}}, \qquad \{\{\varphi\}\}_\Gamma := \frac{\varphi_{|\Omega_{B,1}} + \varphi_{|\Omega_{B,2}}}{2}.$$

When applied to vector functions, these operators act component-wise.

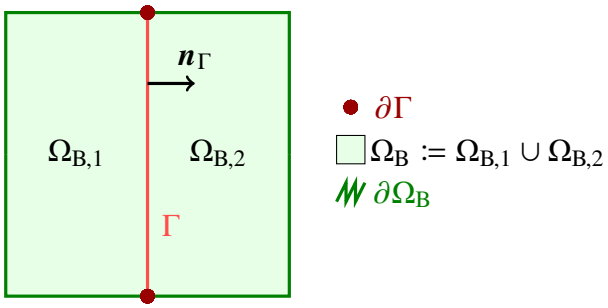

Figure 2.1: Illustration of the notation introduced in Section 3.2.1.

2.2.2 Continuous problem

We discuss in this section the strong formulation of the problem: the governing equations for the bulk region and the fracture, and the interface conditions that relate these subproblems.

2.2.2.1 Bulk region

In the bulk region Ω_B, we model the motion of the incompressible fluid by Darcy's law in mixed form, so that the pressure $p : \Omega_B \to \mathbb{R}$ and the flux $\boldsymbol{u} : \Omega_B \to \mathbb{R}^2$ satisfy

$$\boldsymbol{K}\nabla p + \boldsymbol{u} = 0 \qquad \text{in } \Omega_B, \tag{2.1a}$$
$$\nabla \cdot \boldsymbol{u} = f \qquad \text{in } \Omega_B, \tag{2.1b}$$
$$p = g_B \qquad \text{on } \partial\Omega_B^D, \tag{2.1c}$$
$$\boldsymbol{u} \cdot \boldsymbol{n}_{\partial\Omega} = 0 \qquad \text{on } \partial\Omega_B^N, \tag{2.1d}$$

where $f \in L^2(\Omega_B)$ denotes a volumetric source term, $g_B \in H^{1/2}(\partial\Omega_B^D)$ the boundary pressure, and $\boldsymbol{K} : \Omega_B \to \mathbb{R}^{2\times 2}$ the bulk permeability tensor, which is assumed to be symmetric, piecewise constant on a fixed polygonal partition $\mathcal{P}_B = \{\omega_B\}$ of Ω_B, and uniformly elliptic so that there exist two strictly positive real numbers $\underline{K}_B$ and $\overline{K}_B$ satisfying, for a.e. $\boldsymbol{x} \in \Omega_B$ and all $\boldsymbol{z} \in \mathbb{R}^2$ such that $|\boldsymbol{z}| = 1$,

$$0 < \underline{K}_B \le \boldsymbol{K}(\boldsymbol{x})\boldsymbol{z} \cdot \boldsymbol{z} \le \overline{K}_B.$$

For further use, we define the global anisotropy ratio

$$\varrho_B := \frac{\overline{K}_B}{\underline{K}_B}. \tag{2.2}$$

2.2.2.2 Fracture

Inside the fracture, we consider the motion of the fluid as governed by Darcy's law in primal form, so that the fracture pressure $p_\Gamma : \Gamma \to \mathbb{R}$ satisfies

$$-\nabla_\tau \cdot (K_\Gamma \nabla_\tau p_\Gamma) = \ell_\Gamma f_\Gamma + [\![\boldsymbol{u}]\!]_\Gamma \cdot \boldsymbol{n}_\Gamma \qquad \text{in } \Gamma, \tag{2.3a}$$

$$p_\Gamma = g_\Gamma \qquad \text{on } \partial\Gamma^{\mathrm{D}}, \tag{2.3b}$$

$$-K_\Gamma \nabla_\tau p_\Gamma \cdot \boldsymbol{\tau}_{\partial\Gamma} = 0 \qquad \text{on } \partial\Gamma^{\mathrm{N}}, \tag{2.3c}$$

where $f_\Gamma \in L^2(\Gamma)$ and $K_\Gamma := \kappa_\Gamma^\tau \ell_\Gamma$ with $\kappa_\Gamma^\tau : \Gamma \to \mathbb{R}$ and $\ell_\Gamma : \Gamma \to \mathbb{R}$ denoting the tangential permeability and thickness of the fracture, respectively. The quantities κ_Γ^τ and ℓ_Γ are assumed piecewise constant on a fixed partition $\mathcal{P}_\Gamma = \{\omega_\Gamma\}$ of Γ, and such that there exist strictly positive real numbers $\underline{K}_\Gamma$,$\overline{K}_\Gamma$ such that, for a.e. $\boldsymbol{x} \in \Gamma$,

$$0 < \underline{K}_\Gamma \le K_\Gamma(\boldsymbol{x}) \le \overline{K}_\Gamma.$$

In (2.3), ∇_τ and $\nabla_\tau\cdot$ denote the tangential gradient and divergence operators along Γ, respectively.

Remark 2.1 (Immersed fractures). The Neumann boundary condition (2.3c) has been used for immersed fracture tips. The case where the fracture is fully immersed in the domain Ω can be also considered, and it leads to a homogeneous Neumann boundary condition (2.3c) on the whole fracture boundary; for further details, we refer to [12, Section 2.2.3], [46] or more recently [122].

2.2.2.3 Coupling conditions

The subproblems (2.1) and (2.3) are coupled by the following interface conditions:

$$\begin{aligned} \lambda_\Gamma \{\{\boldsymbol{u}\}\}_\Gamma \cdot \boldsymbol{n}_\Gamma &= [\![p]\!]_\Gamma \qquad \text{on } \Gamma, \\ \lambda_\Gamma^\xi [\![\boldsymbol{u}]\!]_\Gamma \cdot \boldsymbol{n}_\Gamma &= \{\{p\}\}_\Gamma - p_\Gamma \qquad \text{on } \Gamma, \end{aligned} \tag{2.4}$$

where $\xi \in (\frac{1}{2}, 1]$ is a model parameter chosen by the user and we have set

$$\lambda_\Gamma := \frac{\ell_\Gamma}{\kappa_\Gamma^n}, \qquad \lambda_\Gamma^\xi := \lambda_\Gamma \left(\frac{\xi}{2} - \frac{1}{4}\right). \tag{2.5}$$

As above, ℓ_Γ is the fracture thickness, while $\kappa_\Gamma^n : \Gamma \to \mathbb{R}$ represents the normal permeability of the fracture, which is assumed piecewise constant on the partition $\mathcal{P}_\Gamma$ of Γ introduced in Section 2.2.2.2, and such that, for a.e. $\boldsymbol{x} \in \Gamma$,

$$0 < \underline{\lambda}_\Gamma \le \lambda_\Gamma(\boldsymbol{x}) \le \overline{\lambda}_\Gamma, \tag{2.6}$$

for two given strictly positive real numbers $\overline{\lambda}_\Gamma$ and $\underline{\lambda}_\Gamma$.

Remark 2.2 (Coupling condition and choice of the formulation). The coupling conditions (2.4) arise from the averaging process along the normal direction to the fracture, and are necessary to close the problem. They relate the jump and average of the bulk flux to the jump and average of the bulk pressure and the fracture pressure. Using as a starting point the mixed formulation (2.1) in the bulk enables a natural discretization of the coupling conditions, as both the normal flux and the bulk pressure are present as unknowns. On the other hand, the use of the primal formulation (2.3) seems natural in the fracture, since only the fracture pressure appears in (2.4). HHO discretizations using a primal formulation in the bulk as a starting point will make the object of a future work.

Remark 2.3 (Extension to discrete fracture networks). The model could be extended to fracture networks. In this case, additional coupling conditions enforcing the mass conservation and pressure continuity at fracture intersections should be included; see e.g., [44, 46].

2.2.3 Weak formulation

The weak formulation of problem (2.1)–(2.3)–(2.4) hinges on the following function spaces:

$$\begin{aligned} \boldsymbol{U} &\coloneqq \left\{ \boldsymbol{u} \in \boldsymbol{H}(\mathrm{div};\Omega_{\mathrm{B}}) \;:\; \begin{array}{l} \boldsymbol{u}\cdot\boldsymbol{n}_{\partial\Omega} = 0 \text{ on } \partial\Omega_{\mathrm{B}}^{\mathrm{N}} \\ (\boldsymbol{u}_{|\Omega_{\mathrm{B},1}}\cdot\boldsymbol{n}_\Gamma, \boldsymbol{u}_{|\Omega_{\mathrm{B},2}}\cdot\boldsymbol{n}_\Gamma) \in L^2(\Gamma)^2 \end{array} \right\}, \\ P_{\mathrm{B}} &\coloneqq L^2(\Omega_{\mathrm{B}}), \qquad P_\Gamma \coloneqq \left\{ p_\Gamma \in H^1(\Gamma) \;:\; p_\Gamma = 0 \text{ on } \partial\Gamma^{\mathrm{D}} \right\}, \end{aligned}$$

where $\boldsymbol{H}(\mathrm{div};\Omega_{\mathrm{B}})$ is spanned by vector-valued functions on Ω_{B} whose restriction to every bulk subregion $\Omega_{\mathrm{B},i}$, $i \in \{1,2\}$, is in $\boldsymbol{H}(\mathrm{div};\Omega_{\mathrm{B},i})$.

For any $X \subset \overline{\Omega}$, we denote by $(\cdot,\cdot)_X$ and $\|\cdot\|_X$ the usual inner product and norm of $L^2(X)$ or $L^2(X)^2$, according to the context. We define the bilinear forms $a_\xi : \boldsymbol{U}\times\boldsymbol{U} \to \mathbb{R}$, $b : \boldsymbol{U}\times P_{\mathrm{B}} \to \mathbb{R}$, $c : \boldsymbol{U}\times P_\Gamma \to \mathbb{R}$, and $a_\Gamma : P_\Gamma \times P_\Gamma \to \mathbb{R}$ as follows:

$$\begin{aligned} a_\xi(\boldsymbol{u},\boldsymbol{v}) &\coloneqq \int_{\Omega_{\mathrm{B}}} \boldsymbol{K}^{-1}\boldsymbol{u}\cdot\boldsymbol{v} + \int_\Gamma \left(\lambda_\Gamma^\xi [\![\boldsymbol{u}]\!]_\Gamma\cdot\boldsymbol{n}_\Gamma [\![\boldsymbol{v}]\!]_\Gamma\cdot\boldsymbol{n}_\Gamma + \lambda_\Gamma \{\{\boldsymbol{u}\}\}_\Gamma\cdot\boldsymbol{n}_\Gamma \{\{\boldsymbol{v}\}\}_\Gamma\cdot\boldsymbol{n}_\Gamma \right), \\ b(\boldsymbol{u},q) &\coloneqq \int_{\Omega_{\mathrm{B}}} \nabla\cdot\boldsymbol{u}\, q, \\ c(\boldsymbol{u},q_\Gamma) &\coloneqq \int_{\Omega_{\mathrm{B}}} [\![\boldsymbol{u}]\!]_\Gamma\cdot\boldsymbol{n}_\Gamma q_\Gamma, \\ a_\Gamma(p_\Gamma,q_\Gamma) &\coloneqq \int_\Gamma K_\Gamma \nabla_\tau p_\Gamma\cdot\nabla_\tau q_\Gamma. \end{aligned} \tag{2.7}$$

With these spaces and bilinear forms, the weak formulation of problem (2.1)–(2.3)–(2.4) reads: Find $(\boldsymbol{u}, p, p_{\Gamma,0}) \in \boldsymbol{U} \times P_{\mathrm{B}} \times P_{\Gamma}$ such that

$$\begin{aligned} a_{\xi}(\boldsymbol{u},\boldsymbol{v}) - b(\boldsymbol{v},p) + c(\boldsymbol{v},p_{\Gamma,0}) &= -\int_{\partial\Omega_{\mathrm{B}}^{\mathrm{D}}} g_{\mathrm{B}}\boldsymbol{v}\cdot\boldsymbol{n}_{\partial\Omega} && \forall \boldsymbol{v}\in\boldsymbol{U},\\ b(\boldsymbol{u},q) &= \int_{\Omega_{\mathrm{B}}} fq && \forall q\in P_{\mathrm{B}}, \\ -c(\boldsymbol{u},q_{\Gamma}) + a_{\Gamma}(p_{\Gamma,0},q_{\Gamma}) &= \int_{\Gamma} \ell_{\Gamma} f_{\Gamma} q_{\Gamma} - d(p_{\Gamma,\mathrm{D}},q_{\Gamma}) && \forall q_{\Gamma}\in P_{\Gamma}, \end{aligned} \tag{2.8}$$

where $p_{\Gamma,\mathrm{D}} \in H^1(\Gamma)$ is a lifting of the fracture Dirichlet boundary datum such that $(p_{\Gamma,\mathrm{D}})_{|\partial\Gamma^{\mathrm{D}}} = g_{\Gamma}$. The fracture pressure is then computed as $p_{\Gamma} = p_{\Gamma,0} + p_{\Gamma,\mathrm{D}}$. This problem is well-posed; we refer the reader to [17, Proposition 2.4] for a proof.

2.3 Discrete setting

2.3.1 Mesh

The HHO method is built upon a polygonal mesh of the domain Ω defined prescribing a set of mesh elements $\mathcal{T}_h$ and a set of mesh faces $\mathcal{F}_h$.

The set of mesh elements $\mathcal{T}_h$ is a finite collection of open disjoint polygons with nonzero area such that $\overline{\Omega} = \bigcup_{T\in\mathcal{T}_h} \overline{T}$ and $h = \max_{T\in\mathcal{T}_h} h_T$, with h_T denoting the diameter of T. We also denote by ∂T the boundary of a mesh element $T \in \mathcal{T}_h$. The set of mesh faces $\mathcal{F}_h$ is a finite collection of open disjoint line segments in $\overline{\Omega}$ with nonzero length such that, for all $F \in \mathcal{F}_h$, (i) either there exist two distinct mesh elements $T_1, T_2 \in \mathcal{T}_h$ such that $F \subset \partial T_1 \cap \partial T_2$ (and F is called an interface) or (ii) there exist a (unique) mesh element $T \in \mathcal{T}_h$ such that $F \subset \partial T \cap \partial\Omega$ (and F is called a boundary face). We assume that $\mathcal{F}_h$ is a partition of the mesh skeleton in the sense that $\bigcup_{T\in\mathcal{T}_h} \partial T = \bigcup_{F\in\mathcal{F}_h} \overline{F}$.

Remark 2.4 (Mesh faces). Despite working in two space dimensions, we have preferred the terminology "face" over "edge" in order to (i) be consistent with the standard HHO nomenclature and (ii) stress the fact that faces *need not* coincide with polygonal edges (but can be subsets thereof); see also Remark 3.6 on this point.

We denote by $\mathcal{F}_h^{\mathrm{i}}$ the set of all interfaces and by $\mathcal{F}_h^{\mathrm{b}}$ the set of all boundary faces, so that $\mathcal{F}_h = \mathcal{F}_h^{\mathrm{i}} \cup \mathcal{F}_h^{\mathrm{b}}$. The length of a face $F \in \mathcal{F}_h$ is denoted by h_F. For any mesh element $T \in \mathcal{T}_h$, $\mathcal{F}_T$ is the set of faces that lie on ∂T and, for any $F \in \mathcal{F}_T$, $\boldsymbol{n}_{TF}$ is the unit normal to F pointing out of T. Symmetrically, for any $F \in \mathcal{F}_h$, $\mathcal{T}_F$ is the set containing the mesh elements sharing the face F (two if F is an interface, one if F is a boundary face).

To account for the presence of the fracture, we make the following

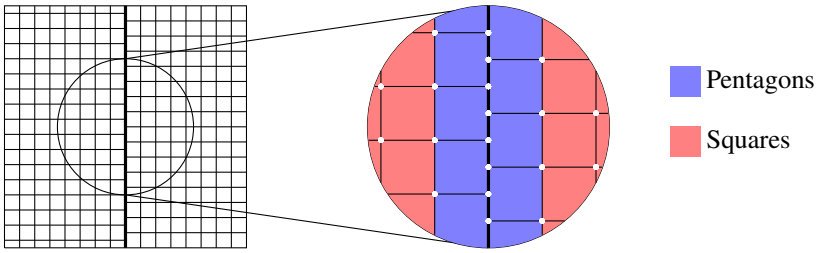

Figure 2.2: Treatment of nonconforming fracture discretizations.

Assumption 2.5 (Geometric compliance with the fracture)**.** The mesh is compliant with the fracture, i.e., there exists a subset $\mathcal{F}_h^\Gamma \subset \mathcal{F}_h^{\mathrm{i}}$ such that $\overline{\Gamma} = \bigcup_{F\in\mathcal{F}_h^\Gamma} \overline{F}$. As a result, $\mathcal{F}_h^\Gamma$ is a (1-dimensional) mesh of the fracture.

Remark 2.6 (Polygonal meshes and geometric compliance with the fracture). Fulfilling Assumption 3.5 does not pose particular problems in the context of polygonal methods, even when the fracture discretization is nonconforming in the classical sense. Consider, e.g., the situation illustrated in Figure 3.2, where the fracture lies at the intersection of two nonmatching Cartesian submeshes. In this case, no special treatment is required provided the mesh elements in contact with the fracture are treated as pentagons with two coplanar faces instead of rectangles. This is possible since, as already pointed out, the set of mesh faces $\mathcal{F}_h$ need not coincide with the set of polygonal edges of $\mathcal{T}_h$.

The set of vertices of the fracture is denoted by $\mathcal{V}_h$ and, for all $F \in \mathcal{F}_h^\Gamma$, we denote by $\mathcal{V}_F$ the vertices of F. For all $F \in \mathcal{F}_h^\Gamma$ and all $V \in \mathcal{V}_F$, $\boldsymbol{\tau}_{FV}$ denotes the unit vector tangent to the fracture and oriented so that it points out of F. Finally, $\mathcal{V}_h^{\mathrm{D}}$ is the set containing the points in $\partial\Gamma^{\mathrm{D}}$.

To avoid dealing with jumps of the problem data inside mesh elements, as well as on boundary and fracture faces, we additionally make the following

Assumption 2.7 (Compliance with the problem data)**.** The mesh is compliant with the data, i.e., the following conditions hold:

(i) *Compliance with the bulk permeability.* For each mesh element $T \in \mathcal{T}_h$, there exists a unique sudomain $\omega_{\mathrm{B}} \in \mathcal{P}_{\mathrm{B}}$ (with $\mathcal{P}_{\mathrm{B}}$ partition introduced in Section 2.2.2.1) such that $T \subset \omega_{\mathrm{B}}$;

(ii) *Compliance with the fracture thickness, normal, and tangential permeabilities.* For each fracture face $F \in \mathcal{F}_h^\Gamma$, there is a unique subdomain $\omega_\Gamma \in \mathcal{P}_\Gamma$ (with $\mathcal{P}_\Gamma$ partition introduced in Section 2.2.2.2) such that $F \subset \omega_\Gamma$;

(iii) *Compliance with the boundary conditions.* There exist subsets $\mathcal{F}_h^{\mathrm{D}}$ and $\mathcal{F}_h^{\mathrm{N}}$ of $\mathcal{F}_h^{\mathrm{b}}$ such that $\overline{\partial\Omega_{\mathrm{B}}^{\mathrm{N}}} = \bigcup_{F\in\mathcal{F}_h^{\mathrm{N}}} \overline{F}$ and $\overline{\partial\Omega_{\mathrm{B}}^{\mathrm{D}}} = \bigcup_{F\in\mathcal{F}_h^{\mathrm{D}}} \overline{F}$.

For the h-convergence analysis, one needs to make assumptions on how the mesh is refined. The notion of geometric regularity for polygonal meshes is, however, more subtle than for standard meshes. To formulate it, we assume the existence of a matching simplicial submesh, meaning that there is a conforming triangulation $\mathfrak{T}_h$ of the domain such that each mesh element $T \in \mathcal{T}_h$ is decomposed into a finite number of triangles from $\mathfrak{T}_h$, and each mesh face $F \in \mathcal{F}_h$ is decomposed into a finite number of edges from the skeleton of $\mathfrak{T}_h$. We denote by $\varrho \in (0,1)$ the regularity parameter such that (i) for any triangle $S \in \mathfrak{T}_h$ of diameter h_S and inradius r_S, $\varrho h_S \le r_S$ and (ii) for any mesh element $T \in \mathcal{T}_h$ and any triangle $S \in \mathfrak{T}_h$ such that $S \subset T$, $\varrho h_T \le h_S$. When considering h-refined mesh sequences, ϱ should remain uniformly bounded away from zero. We stress that the matching triangular submesh is merely a theoretical tool, and need not be constructed in practice.

2.3.2 Local polynomial spaces and projectors

Let an integer $l \ge 0$ be fixed, and let X be a mesh element or face. We denote by $\mathbb{P}^l(X)$ the space spanned by the restriction to X of two-variate polynomials of total degree up to l, and define the L^2-orthogonal projector $\pi_X^l : L^1(X) \to \mathbb{P}^l(X)$ such that, for all $v \in L^1(X)$, $\pi_X^l v$ solves

$$\int_X (\pi_X^l v - v) w = 0 \qquad \forall w \in \mathbb{P}^l(X). \tag{2.9}$$

By the Riesz representation theorem in $\mathbb{P}^l(X)$ for the L^2-inner product, this defines $\pi_X^l v$ uniquely.

It has been proved in [81, Lemmas 1.58 and 1.59] that the L^2-orthogonal projector on mesh elements has optimal approximation properties: For all $s \in \{0, \dots, l+1\}$, all $T \in \mathcal{T}_h$, and all $v \in H^s(T)$,

$$|v - \pi_T^l v|_{H^m(T)} \le C h_T^{s-m} |v|_{H^s(T)} \qquad \forall m \in \{0, \dots, s\}, \tag{2.10a}$$

and, if $s \ge 1$,

$$|v - \pi_T^l v|_{H^m(\mathcal{F}_T)} \le C h_T^{s-m-1/2} |v|_{H^s(T)} \qquad \forall m \in \{0, \dots, s-1\}, \tag{2.10b}$$

with real number $C > 0$ only depending on ϱ, l, s, and m, and $H^m(\mathcal{F}_T)$ spanned by the functions on ∂T that are in $H^m(F)$ for all $F \in \mathcal{F}_T$. More general $W^{s,p}$-approximation results for the L^2-orthogonal projector can be found in [74]; see also [73] concerning projectors on local polynomial spaces.

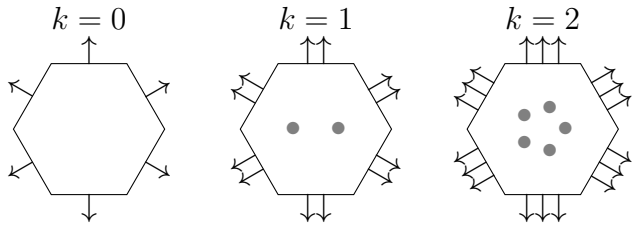

Figure 2.3: Local DOF space $\underline{\boldsymbol{U}}_T^k$ for a hexagonal mesh element and $k \in \{0, 1, 2\}$.

2.4 The Hybrid High-Order method

In this section we illustrate the local constructions in the bulk and in the fracture on which the HHO method hinges, formulate the discrete problem, and state the main results.

2.4.1 Local construction in the bulk

We present here the key ingredients to discretize the bulk-based terms in problem (2.8). First, we introduce the local DOF spaces for the bulk-based flux and pressure unknowns. Then, we define local divergence and flux reconstruction operators obtained from local DOFs.

In this section, we work on a fixed mesh element $T \in \mathcal{T}_h$, and denote by $\boldsymbol{K}_T := \boldsymbol{K}_{|T} \in \mathbb{P}^0(T)^{2\times 2}$ the (constant) restriction of the bulk permeability tensor to the element T. We also introduce the local anisotropy ratio

$$\varrho_{\mathrm{B},T} := \frac{\overline{K}_{\mathrm{B},T}}{\underline{K}_{\mathrm{B},T}}, \tag{2.11}$$

where $\overline{K}_{\mathrm{B},T}$ and $\underline{K}_{\mathrm{B},T}$ denote, respectively, the largest and smallest eigenvalue of $\boldsymbol{K}_T$. In the error estimate of Theorem 2.12, we will explicitly track the dependence of the constants on $\rho_{\mathrm{B},T}$ in order to assess the robustness of our method with respect to the anisotropy of the diffusion coefficient.

2.4.1.1 Local bulk unknowns

For any integer $l \geq 0$, set $\boldsymbol{U}_T^l := \boldsymbol{K}_T \nabla \mathbb{P}^l(T)$. The local DOF spaces for the bulk flux and pressure are given by (see Figure 2.3)

$$\underline{\boldsymbol{U}}_T^k := \boldsymbol{U}_T^k \times \left(\bigtimes_{F\in\mathcal{F}_T} \mathbb{P}^k(F) \right), \qquad P_{\mathrm{B},T}^k := \mathbb{P}^k(T). \tag{2.12}$$

Notice that, for $k = 0$, we have $\boldsymbol{U}_T^0 = \boldsymbol{K}_T\nabla\mathbb{P}^0(T) = \{\boldsymbol{0}\}$, expressing the fact that element-based flux DOFs are not needed. A generic element $\underline{\boldsymbol{v}}_T \in \underline{\boldsymbol{U}}_T^k$ is decomposed as $\underline{\boldsymbol{v}}_T = (\boldsymbol{v}_T, (v_{TF})_{F\in\mathcal{F}_T})$. We define on $\underline{\boldsymbol{U}}_T^k$ and on $P_{\mathrm{B},T}^k$, respectively, the norms $\|\cdot\|_{U,T}$ and $\|\cdot\|_{\mathrm{B},T}$ such that, for all $\underline{\boldsymbol{v}}_T \in \underline{\boldsymbol{U}}_T^k$ and all $q_T \in P_{\mathrm{B},T}^k$,

$$\|\underline{\boldsymbol{v}}_T\|_{U,T}^2 \coloneqq (\overline{K}_{\mathrm{B},T})^{-1}\left(\|\boldsymbol{v}_T\|_T^2 + \sum_{F\in\mathcal{F}_T} h_F\|v_{TF}\|_F^2\right), \qquad \|q_T\|_{\mathrm{B},T} \coloneqq \|q_T\|_T, \quad (2.13)$$

where we remind the reader that $\overline{K}_{\mathrm{B},T}$ denotes the largest eigenvalue of the two-by-two matrix $\boldsymbol{K}_T$, see Section 2.4.1. We define the local interpolation operator $\underline{\boldsymbol{I}}_T^k : H^1(T)^2 \to \underline{\boldsymbol{U}}_T^k$ such that, for all $\boldsymbol{v} \in H^1(T)^2$,

$$\underline{\boldsymbol{I}}_T^k\boldsymbol{v} \coloneqq (\boldsymbol{K}_T\nabla y_T, (\pi_F^k(\boldsymbol{v}\cdot\boldsymbol{n}_{TF}))_{F\in\mathcal{F}_T}), \quad (2.14)$$

where $y_T \in \mathbb{P}^k(T)$ is the solution (defined up to an additive constant) of the following Neumann problem:

$$\int_T \boldsymbol{K}_T\nabla y_T\cdot\nabla q_T = \int_T \boldsymbol{v}\cdot\nabla q_T \qquad \forall q_T \in \mathbb{P}^k(T). \quad (2.15)$$

Remark 2.8 (Domain of the interpolator). The regularity in $H^1(T)^2$ beyond $\boldsymbol{H}(\mathrm{div};T)$ is classically needed for the face interpolators to be well-defined; see, e.g., [30, Section 2.5.1] for further insight into this point.

2.4.1.2 Local divergence reconstruction operator

We define the local divergence reconstruction operator $D_T^k : \underline{\boldsymbol{U}}_T^k \to P_{\mathrm{B},T}^k$ such that, for all $\underline{\boldsymbol{v}}_T = (\boldsymbol{v}_T, (v_{TF})_{F\in\mathcal{F}_T}) \in \underline{\boldsymbol{U}}_T^k$, $D_T^k\underline{\boldsymbol{v}}_T$ solves

$$\int_T D_T^k\underline{\boldsymbol{v}}_T q_T = -\int_T \boldsymbol{v}_T\cdot\nabla q_T + \sum_{F\in\mathcal{F}_T}\int_F v_{TF}q_T \qquad \forall q_T \in P_{\mathrm{B},T}^k. \quad (2.16)$$

By the Riesz representation theorem in $P_{\mathrm{B},T}^k$ for the L^2-inner product, this defines the divergence reconstruction uniquely. The right-hand side of (2.16) is designed to resemble an integration by parts formula where the role of the function represented by $\underline{\boldsymbol{v}}_T$ is played by element-based DOFs in volumetric terms and face-based DOFs in boundary terms. With this choice, the following commuting property holds (see [78, Lemma 2]): For all $\boldsymbol{v} \in H^1(T)^2$,

$$D_T^k\underline{\boldsymbol{I}}_T^k\boldsymbol{v} = \pi_T^k(\nabla\cdot\boldsymbol{v}). \quad (2.17)$$

We also note the following inverse inequality, obtained from (2.16) setting $q_T = D_T^k \underline{\boldsymbol{v}}_T$ and using Cauchy–Schwarz and discrete inverse and trace inequalities (see [78, Lemma 8] for further details): There is a real number $C > 0$ independent of h and of T, but depending on ϱ and k, such that, for all $\underline{\boldsymbol{v}}_T \in \underline{\boldsymbol{U}}_T^k$,

$$h_T \|D_T^k \underline{\boldsymbol{v}}_T\|_T \le C \overline{K}_{\mathrm{B},T}^{1/2} \|\underline{\boldsymbol{v}}_T\|_{U,T}. \tag{2.18}$$

2.4.1.3 Local flux reconstruction operator and permeability-weighted local product

We next define the local discrete flux operator $\boldsymbol{F}_T^{k+1} : \underline{\boldsymbol{U}}_T^k \to \boldsymbol{U}_T^{k+1}$ such that, for all $\underline{\boldsymbol{v}}_T = (\boldsymbol{v}_T, (v_{TF})_{F\in\mathcal{F}_T}) \in \underline{\boldsymbol{U}}_T^k$, $\boldsymbol{F}_T^{k+1}\underline{\boldsymbol{v}}_T$ solves

$$\int_T \boldsymbol{F}_T^{k+1}\underline{\boldsymbol{v}}_T \cdot \nabla w_T = -\int_T D_T^k \underline{\boldsymbol{v}}_T w_T + \sum_{F\in\mathcal{F}_T} \int_F v_{TF} w_T \qquad \forall w_T \in \mathbb{P}^{k+1}(T). \tag{2.19}$$

By the Riesz representation theorem in $\boldsymbol{U}_T^{k+1}$ for the $(\boldsymbol{K}_T^{-1}\cdot,\cdot)_T$-inner product, this defines the flux reconstruction uniquely. Also in this case, the right-hand side is designed so as to resemble an integration by parts formula where the role of the divergence of the function represented by $\underline{\boldsymbol{v}}_T$ is played by $D_T^k\underline{\boldsymbol{v}}_T$, while its normal traces are replaced by boundary DOFs.

We now have all the ingredients required to define the permeability-weighted local product $m_T : \underline{\boldsymbol{U}}_T^k \times \underline{\boldsymbol{U}}_T^k \to \mathbb{R}$ such that

$$m_T(\underline{\boldsymbol{u}}_T, \underline{\boldsymbol{v}}_T) \coloneqq \int_T \boldsymbol{K}_T^{-1}\boldsymbol{F}_T^{k+1}\underline{\boldsymbol{u}}_T \cdot \boldsymbol{F}_T^{k+1}\underline{\boldsymbol{v}}_T + J_T(\underline{\boldsymbol{u}}_T, \underline{\boldsymbol{v}}_T), \tag{2.20}$$

where the first term is the usual Galerkin contribution responsible for consistency, while $J_T : \underline{\boldsymbol{U}}_T^k \times \underline{\boldsymbol{U}}_T^k \to \mathbb{R}$ is a stabilization bilinear form such that, letting $\mu_{TF} \coloneqq \boldsymbol{K}_T\boldsymbol{n}_{TF}\cdot\boldsymbol{n}_{TF}$ for all $F \in \mathcal{F}_T$,

$$J_T(\underline{\boldsymbol{u}}_T, \underline{\boldsymbol{v}}_T) \coloneqq \sum_{F\in\mathcal{F}_T} \frac{h_F}{\mu_{TF}} \int_F (\boldsymbol{F}_T^{k+1}\underline{\boldsymbol{u}}_T\cdot\boldsymbol{n}_{TF} - u_{TF})(\boldsymbol{F}_T^{k+1}\underline{\boldsymbol{v}}_T\cdot\boldsymbol{n}_{TF} - v_{TF}).$$

The role of J_T is to ensure the existence of a real number $\eta_m > 0$ independent of h, T, and $\boldsymbol{K}_T$, but possibly depending on ϱ and k, such that, for all $\underline{\boldsymbol{v}}_T \in \underline{\boldsymbol{U}}_T^k$,

$$\eta_m^{-1}\|\underline{\boldsymbol{v}}_T\|_{U,T}^2 \le \|\underline{\boldsymbol{v}}_T\|_{m,T}^2 \coloneqq m_T(\underline{\boldsymbol{v}}_T, \underline{\boldsymbol{v}}_T) \le \eta_m \rho_{\mathrm{B},T}\|\underline{\boldsymbol{v}}_T\|_{U,T}^2, \tag{2.21}$$

with norm $\|\cdot\|_{U,T}$ defined by (2.13); see [78, Lemma 4] for a proof. Additionally, we note the following consistency property for J_T proved in [78, Lemma 9]: There is a real number $C > 0$ independent of h, T, and $\boldsymbol{K}_T$, but possibly depending on ϱ and k, such that, for all $\boldsymbol{v} = \boldsymbol{K}_T\nabla q$ with $q \in H^{k+2}(T)$,

$$J_T(\underline{\boldsymbol{I}}_T^k\boldsymbol{v}, \underline{\boldsymbol{I}}_T^k\boldsymbol{v})^{1/2} \le C\varrho_{\mathrm{B},T}^{1/2}\overline{K}_{\mathrm{B}}^{s1/2} h_T^{k+1}|q|_{H^{k+2}(T)}. \tag{2.22}$$

2.4.2 Local construction in the fracture

We now focus on the discretization of the fracture-based terms in problem (2.8). First, we define the local space of fracture pressure DOFs, then a local pressure reconstruction operator inspired by a local integration by parts formula. Based on this operator, we formulate a local discrete tangential diffusive bilinear form. Throughout this section, we work on a fixed fracture face $F \in \mathcal{F}_h^\Gamma$ and we let, for the sake of brevity, $K_F \coloneqq (K_\Gamma)_{|F} \in \mathbb{P}^0(F)$ with K_Γ defined in Section 2.2.2.2.

2.4.2.1 Local fracture unknowns

Set $\mathbb{P}(V) \coloneqq \mathrm{span}\{1\}$ for all $V \in \mathcal{V}_F$. The local space of DOFs for the fracture pressure is

$$\underline{P}^k_{\Gamma,F} \coloneqq \mathbb{P}(F)^k \times \left(\bigtimes_{V\in\mathcal{V}_F} \mathbb{P}(V) \right).$$

In what follows, a generic element $\underline{q}^\Gamma_F \in \underline{P}^k_{\Gamma,F}$ is decomposed as $\underline{q}^\Gamma_F = (q^\Gamma_F, (q^\Gamma_V)_{V\in\mathcal{V}_F})$. We define on $\underline{P}^k_{\Gamma,F}$ the seminorm $\|\cdot\|_{\Gamma,F}$ such that, for all $\underline{q}^\Gamma_F \in \underline{P}^k_{\Gamma,F}$,

$$\|\underline{q}^\Gamma_F\|^2_{\Gamma,F} \coloneqq \|K_F^{1/2}\nabla_\tau q^\Gamma_F\|^2_F + \sum_{V\in\mathcal{V}_F} \frac{K_F}{h_F}(q_F - q_V)^2(V).$$

We also introduce the local interpolation operator $\underline{I}^k_F : H^1(F) \to \underline{P}^k_{\Gamma,F}$ such that, for all $q \in H^1(F)$,

$$\underline{I}^k_F q \coloneqq (\pi^k_F q, (q(V))_{V\in\mathcal{V}_F}).$$

2.4.2.2 Local pressure reconstruction operator and local tangential diffusive bilinear form

We define the local pressure reconstruction operator $r^{k+1}_F : \underline{P}^k_{\Gamma,F} \to \mathbb{P}^{k+1}(F)$ such that, for all $\underline{q}^\Gamma_F = (q^\Gamma_F, (q^\Gamma_V)_{V\in\mathcal{V}_F}) \in \underline{P}^k_{\Gamma,F}$, $r^{k+1}_F \underline{q}^\Gamma_F$ solves

$$\int_F K_F\nabla_\tau r^{k+1}_F \underline{q}^\Gamma_F \cdot \nabla_\tau w^\Gamma_F = -\int_F q^\Gamma_F \nabla_\tau \cdot (K_F\nabla_\tau w^\Gamma_F) + \sum_{V\in\mathcal{V}_F} q^\Gamma_V (K_F\nabla_\tau w^\Gamma_F \cdot \boldsymbol{\tau}_{FV})(V),$$

for all $w^\Gamma_F \in \mathbb{P}^{k+1}(F)$. By the Riesz representation theorem in $\nabla\mathbb{P}^{k+1}(F)$ for the $(K_F\cdot,\cdot)_F$-inner product, this relation defines a unique element $\nabla_\tau r^{k+1}_F \underline{q}^\Gamma_F$, hence a

polynomial $r_F^{k+1}\underline{q}_F^\Gamma \in \mathbb{P}^{k+1}(F)$ up to an additive constant. This constant is fixed by additionally imposing that

$$\int_F (r_F^{k+1}\underline{q}_F^\Gamma - q_F^\Gamma) = 0.$$

We can now define the local tangential diffusive bilinear form $d_F : \underline{P}_{\Gamma,F}^k \times \underline{P}_{\Gamma,F}^k \to \mathbb{R}$ such that

$$d_F(\underline{p}_F^\Gamma, \underline{q}_F^\Gamma) \coloneqq \int_F K_F \nabla_\tau r_F^{k+1}\underline{p}_F^\Gamma \cdot \nabla_\tau r_F^{k+1}\underline{q}_F^\Gamma + j_F(\underline{p}_F^\Gamma, \underline{q}_F^\Gamma),$$

where the first term is the standard Galerkin contribution responsible for consistency, while $j_F : \underline{P}_{\Gamma,F}^k \times \underline{P}_{\Gamma,F}^k \to \mathbb{R}$ is the stabilization bilinear form such that

$$j_F(\underline{p}_F^\Gamma, \underline{q}_F^\Gamma) \coloneqq \sum_{V\in\mathcal{V}_F} \frac{K_F}{h_F}(R_F^{k+1}\underline{p}_F^\Gamma(V) - p_V^\Gamma)(R_F^{k+1}\underline{q}_F^\Gamma(V) - q_V^\Gamma),$$

with $R_F^{k+1} : \underline{P}_{\Gamma,F}^k \to \mathbb{P}^{k+1}(F)$ such that, for all $\underline{q}_F^\Gamma \in \underline{P}_{\Gamma,F}^k$, $R_F^{k+1}\underline{q}_F^\Gamma \coloneqq q_F^\Gamma + (r_F^{k+1}\underline{q}_F^\Gamma - \pi_F^k r_F^{k+1}\underline{q}_F^\Gamma)$. The role of j_T is to ensure stability and boundedness, expressed by the existence of a real number $\eta_d > 0$ independent of h, F, and of K_F, but possibly depending on k and ϱ, such that, for all $\underline{q}_F^\Gamma \in \underline{P}_{\Gamma,F}^k$, the following holds (see [83, Lemma 4]):

$$\eta_d^{-1}\|\underline{q}_F^\Gamma\|_{\Gamma,F}^2 \le d_F(\underline{q}_F^\Gamma, \underline{q}_F^\Gamma) \le \eta_d\|\underline{q}_F^\Gamma\|_{\Gamma,F}^2. \tag{2.23}$$

2.4.3 The discrete problem

We define the global discrete spaces together with the corresponding interpolators and norms, formulate the discrete problem, and state the main results.

2.4.3.1 Global discrete spaces

We define the following global spaces of fully discontinuous bulk flux and pressure DOFs:

$$\widetilde{\underline{\boldsymbol{U}}}_h^k \coloneqq \bigtimes_{T\in\mathcal{T}_h} \underline{\boldsymbol{U}}_T^k, \qquad P_{\mathrm{B},h}^k \coloneqq \bigtimes_{T\in\mathcal{T}_h} P_{\mathrm{B},T}^k,$$

with local spaces $\underline{\boldsymbol{U}}_T^k$ and $P_{\mathrm{B},T}^k$ defined by (2.12). We will also need the following subspace of $\widetilde{\underline{\boldsymbol{U}}}_h^k$ that incorporates (i) the continuity of flux unknowns at each interface $F \in \mathcal{F}_h^{\mathrm{i}} \setminus \mathcal{F}_h^\Gamma$ not included in the fracture and (ii) the strongly enforced homogeneous Neumann boundary condition on $\partial\Omega_{\mathrm{B}}^{\mathrm{N}}$:

$$\underline{\boldsymbol{U}}_{h,0}^k \coloneqq \{\underline{\boldsymbol{v}}_h \in \widetilde{\underline{\boldsymbol{U}}}_h^k \mid [\![\underline{\boldsymbol{v}}_h]\!]_F = 0 \ \forall F \in \mathcal{F}_h^{\mathrm{i}} \setminus \mathcal{F}_h^\Gamma \text{ and } v_F = 0 \ \forall F \in \mathcal{F}_h^{\mathrm{N}}\}, \tag{2.24}$$

where, for all $F \in \mathcal{F}_h^{\mathrm{b}}$, we have set $v_F \coloneqq v_{TF}$ with T denoting the unique mesh element such that $F \in \mathcal{F}_T$, while, for all $F \in \mathcal{F}_h^{\mathrm{i}}$ with $F \subset \partial T_1 \cap \partial T_2$ for distinct mesh elements $T_1, T_2 \in \mathcal{T}_h$, the jump operator is such that

$$[\![\underline{\boldsymbol{v}}_h]\!]_F \coloneqq v_{T_1F} + v_{T_2F}.$$

Notice that this quantity is the discrete counterpart of the jump of the normal flux component since, for $i \in \{1,2\}$, v_{T_iF} can be interpreted as the normal flux exiting T_i.

We also define the global space of fracture-based pressure unknowns and its subspace with strongly enforced homogeneous Dirichlet boundary condition on $\partial\Gamma^{\mathrm{D}}$ as follows:

$$\underline{P}_{\Gamma,h}^k \coloneqq \left(\bigtimes_{F\in\mathcal{F}_h^\Gamma} \mathbb{P}^k(F)\right) \times \left(\bigtimes_{V\in\mathcal{V}_h} \mathbb{P}(V)\right), \quad \underline{P}_{\Gamma,h,0}^k \coloneqq \left\{\underline{q}_h^\Gamma \in \underline{P}_{\Gamma,h}^k \mid q_V^\Gamma = 0 \ \forall V \in \mathcal{V}_h^{\mathrm{D}}\right\}.$$

A generic element $\underline{q}_h^\Gamma$ of $\underline{P}_{\Gamma,h}^k$ is decomposed as $\underline{q}_h^\Gamma = ((q_F)_{F\in\mathcal{F}_h^\Gamma}, (q_V)_{V\in\mathcal{V}_h})$ and, for all $F \in \mathcal{F}_h^\Gamma$, we denote by $\underline{q}_F^\Gamma = (q_F^\Gamma, (q_V^\Gamma)_{v\in\mathcal{V}_F})$ its restriction to $\underline{P}_{\Gamma,F}^k$.

2.4.3.2 Discrete norms and interpolators

We equip the DOF spaces $\widetilde{\underline{\boldsymbol{U}}}_h^k$, $P_{\mathrm{B},h}^k$, and $\underline{P}_{\Gamma,h}^k$ respectively, with the norms $\|\cdot\|_{\boldsymbol{U},\xi,h}$ and $\|\cdot\|_{\mathrm{B},h}$, and the seminorm $\|\cdot\|_{\Gamma,h}$ such that for all $\underline{\boldsymbol{v}}_h \in \underline{\boldsymbol{U}}_h^k$, all $q_h \in P_{\mathrm{B},h}^k$, and all $\underline{q}_h^\Gamma \in \underline{P}_{\Gamma,h}^k$,

$$\|\underline{\boldsymbol{v}}_h\|_{\boldsymbol{U},\xi,h}^2 \coloneqq \sum_{T\in\mathcal{T}_h} \|\underline{\boldsymbol{v}}_T\|_{\boldsymbol{U},T}^2 + |\underline{\boldsymbol{v}}_h|_{\xi,h}^2, \quad |\underline{\boldsymbol{v}}_h|_{\xi,h}^2 \coloneqq \sum_{F\in\mathcal{F}_h^\Gamma} \left(\lambda_F^\xi \|[\![\underline{\boldsymbol{v}}_h]\!]_F\|_F^2 + \lambda_F \|\{\{\underline{\boldsymbol{v}}_h\}\}_F\|_F^2\right),$$
$$\|q_h\|_{\mathrm{B},h}^2 \coloneqq \sum_{T\in\mathcal{T}_h} \|q_T\|_{\mathrm{B},T}^2, \quad \|\underline{q}_h^\Gamma\|_{\Gamma,h}^2 \coloneqq \sum_{F\in\mathcal{F}_h^\Gamma} \|\underline{q}_F^\Gamma\|_{\Gamma,F}^2,$$

where, for the sake of brevity, we have set $\lambda_F \coloneqq (\lambda_\Gamma)_{|F}$ and $\lambda_F^\xi \coloneqq (\lambda_\Gamma^\xi)_{|F}$ (see (2.5) for the definition of λ_Γ and λ_Γ^ξ), and we have defined the average operator such that, for all $F \in \mathcal{F}_h^\Gamma$ and all $\underline{\boldsymbol{v}}_h \in \widetilde{\underline{\boldsymbol{U}}}_h^k$,

$$\{\{\underline{\boldsymbol{v}}_h\}\}_F \coloneqq \frac{1}{2} \sum_{T\in\mathcal{T}_F} v_{TF}(\boldsymbol{n}_{TF} \cdot \boldsymbol{n}_\Gamma).$$

Using the arguments of [77, Proposition 5], it can be proved that $\|\cdot\|_{\Gamma,h}$ is a norm on $\underline{P}_{\Gamma,h,0}^k$.

Let now $H^1(\mathcal{T}_h)^2$ denote the space spanned by vector-valued functions whose restriction to each mesh element $T \in \mathcal{T}_h$ lies in $H^1(T)^2$. We define the global interpolators $\underline{\boldsymbol{I}}_h^k : H^1(\mathcal{T}_h)^2 \to \underline{\boldsymbol{U}}_h^k$ and $\underline{I}_h^k : H^1(\Gamma) \to \underline{P}_{\Gamma,h}^k$ such that, for all $\boldsymbol{v} \in H^1(\mathcal{T}_h)^2$ and all $q \in H^1(\Gamma)$,

$$\underline{\boldsymbol{I}}_h^k \boldsymbol{v} \coloneqq \big(\underline{\boldsymbol{I}}_T^k \boldsymbol{v}_{|T}\big)_{T\in\mathcal{T}_h}, \qquad \underline{I}_h^k q \coloneqq \big((\pi_F^k q)_{F\in\mathcal{F}_h^\Gamma}, (q(V))_{V\in\mathcal{V}_h}\big), \tag{2.25}$$

where, for all $T \in \mathcal{T}_h$, the local interpolator $\underline{\boldsymbol{I}}_T^k$ is defined by (2.14). We also denote by π_h^k the global L^2-orthogonal projector on $P_{\mathrm{B},h}^k$ such that, for all $q \in L^1(\Omega_\mathrm{B})$,

$$(\pi_h^k q)_{|T} \coloneqq \pi_T^k q_{|T} \qquad \forall T \in \mathcal{T}_h.$$

2.4.3.3 Discrete problem

At the discrete level, the counterparts of the continuous bilinear forms defined in Section 2.2.3 are the bilinear forms $a_h^\xi : \underline{\boldsymbol{U}}_h^k \times \underline{\boldsymbol{U}}_h^k \to \mathbb{R}$, $b_h : \underline{\boldsymbol{U}}_h^k \times P_{\mathrm{B},h}^k \to \mathbb{R}$, $c_h : \underline{\boldsymbol{U}}_h^k \times \underline{P}_{\Gamma,h}^k \to \mathbb{R}$, and $d_h : \underline{P}_{\Gamma,h}^k \times \underline{P}_{\Gamma,h}^k \to \mathbb{R}$ such that

$$\begin{aligned} a_h^\xi(\underline{\boldsymbol{u}}_h, \underline{\boldsymbol{v}}_h) \coloneqq &\sum_{T\in\mathcal{T}_h} m_T(\underline{\boldsymbol{u}}_T, \underline{\boldsymbol{v}}_T) \\ &+ \sum_{F\in\mathcal{F}_h^\Gamma} \int_F \Big(\lambda_F^\xi [\![\underline{\boldsymbol{u}}_h]\!]_F [\![\underline{\boldsymbol{v}}_h]\!]_F + \lambda_F \{\{\underline{\boldsymbol{u}}_h\}\}_F \{\{\underline{\boldsymbol{v}}_h\}\}_F\Big), \end{aligned} \tag{2.26}$$

$$b_h(\underline{\boldsymbol{u}}_h, p_h) \coloneqq \sum_{T\in\mathcal{T}_h} \int_T D_T^k \underline{\boldsymbol{u}}_T p_T, \tag{2.27}$$

$$c_h(\underline{\boldsymbol{u}}_h, \underline{p}_h^\Gamma) \coloneqq \sum_{F\in\mathcal{F}_h^\Gamma} \int_F [\![\underline{\boldsymbol{u}}_h]\!]_F p_F^\Gamma, \tag{2.28}$$

$$d_h(\underline{p}_h^\Gamma, \underline{q}_h^\Gamma) \coloneqq \sum_{F\in\mathcal{F}_h^\Gamma} d_F(\underline{p}_F^\Gamma, \underline{q}_F^\Gamma). \tag{2.29}$$

The HHO discretization of problem (2.8) reads : Find $(\underline{\boldsymbol{u}}_h, p_h, \underline{p}_{h,0}^\Gamma) \in \underline{\boldsymbol{U}}_{h,0}^k \times P_{\mathrm{B},h}^k \times \underline{P}_{\Gamma,h,0}^k$ such that, for all $(\underline{\boldsymbol{v}}_h, q_h, \underline{q}_h^\Gamma) \in \underline{\boldsymbol{U}}_{h,0}^k \times P_{\mathrm{B},h}^k \times \underline{P}_{\Gamma,h,0}^k$,

$$a_h^\xi(\underline{\boldsymbol{u}}_h, \underline{\boldsymbol{v}}_h) - b_h(\underline{\boldsymbol{v}}_h, p_h) + c_h(\underline{\boldsymbol{v}}_h, \underline{p}_{h,0}^\Gamma) = -\sum_{F\in\mathcal{F}_h^\mathrm{D}} \int_F g_\mathrm{B} v_F, \tag{2.30a}$$

$$b_h(\underline{\boldsymbol{u}}_h, q_h) = \sum_{T\in\mathcal{T}_h} \int_T f q_T, \tag{2.30b}$$

$$-c_h(\underline{\boldsymbol{u}}_h, \underline{q}_h^\Gamma) + d_h(\underline{p}_{h,0}^\Gamma, \underline{q}_h^\Gamma) = \sum_{F\in\mathcal{F}_h^\Gamma} \int_F \ell_F f_\Gamma q_F^\Gamma - d_h(\underline{p}_{\mathrm{D},h}^\Gamma, \underline{q}_h^\Gamma), \tag{2.30c}$$

where, for all $F \in \mathcal{F}_h^{\mathrm{D}}$, we have set $v_F := v_{TF}$ with $T \in \mathcal{T}_h$ unique element such that $F \subset \partial T \cap \partial\Omega$ in (2.30a), while $\underline{p}_{\mathrm{D},h}^{\Gamma} = \big((p_{\mathrm{D},F}^{\Gamma})_{F\in\mathcal{F}_h^{\Gamma}}, (p_{\mathrm{D},V}^{\Gamma})_{V\in\mathcal{V}_h}\big) \in \underline{P}_{\Gamma,h}^{k}$ is such that

$$p_{\mathrm{D},F}^{\Gamma} \equiv 0 \quad \forall F \in \mathcal{F}_h^{\Gamma}, \quad p_{\mathrm{D},V}^{\Gamma} = g_{\Gamma}(V) \quad \forall V \in \mathcal{V}_h^{\mathrm{D}}, \quad p_{\mathrm{D},V}^{\Gamma} = 0 \quad \forall V \in \mathcal{V}_h \setminus \mathcal{V}_h^{\mathrm{D}}.$$

The discrete fracture pressure $\underline{p}_h^{\Gamma} \in \underline{P}_{\Gamma,h}^{k}$ is finally computed as $\underline{p}_h^{\Gamma} = \underline{p}_{h,0}^{\Gamma} + \underline{p}_{\mathrm{D},h}^{\Gamma}$.

Remark 2.9 (Implementation). In the practical implementation, all bulk flux DOFs and all bulk pressure DOFs up to one constant value per element can be statically condensed by solving small saddle point problems inside each element. This corresponds to the first static condensation procedure discussed in [78, Section 3.4], to which we refer the reader for further details.

We next write a more compact equivalent reformulation of problem (2.30). Define the Cartesian product space $\underline{\boldsymbol{X}}_h^k := \underline{\boldsymbol{U}}_{h,0}^k \times P_{\mathrm{B},h}^k \times \underline{P}_{\Gamma,h,0}^k$ as well as the bilinear form $\mathcal{A}_h^{\xi} : \underline{\boldsymbol{X}}_h^k \times \underline{\boldsymbol{X}}_h^k \to \mathbb{R}$ such that

$$\begin{aligned}\mathcal{A}_h^{\xi}((\underline{\boldsymbol{u}}_h, p_h, \underline{p}_h^{\Gamma}), (\underline{\boldsymbol{v}}_h, q_h, \underline{q}_h^{\Gamma})) := a_h^{\xi}(\underline{\boldsymbol{u}}_h, \underline{\boldsymbol{v}}_h) + b_h(\underline{\boldsymbol{u}}_h, q_h) - b_h(\underline{\boldsymbol{v}}_h, p_h) \\ + c_h(\underline{\boldsymbol{v}}_h, \underline{p}_h^{\Gamma}) - c_h(\underline{\boldsymbol{u}}_h, \underline{q}_h^{\Gamma}) + d_h(\underline{p}_h^{\Gamma}, \underline{q}_h^{\Gamma}).\end{aligned} \tag{2.31}$$

Then, problem (2.30) is equivalent to: Find $(\underline{\boldsymbol{u}}_h, p_h, \underline{p}_{h,0}^{\Gamma}) \in \underline{\boldsymbol{X}}_h^k$ such that, for all $(\underline{\boldsymbol{v}}_h, q_h, \underline{q}_h^{\Gamma}) \in \underline{\boldsymbol{X}}_h^k$,

$$\begin{aligned}\mathcal{A}_h^{\xi}((\underline{\boldsymbol{u}}_h, p_h, \underline{p}_{h,0}^{\Gamma}), (\underline{\boldsymbol{v}}_h, q_h, \underline{q}_h^{\Gamma})) = \sum_{T\in\mathcal{T}_h}\int_F f q_T + \sum_{F\in\mathcal{F}_h^{\Gamma}}\int_F \ell_F f_{\Gamma} q_F^{\Gamma} \\ - \sum_{F\in\mathcal{F}_h^{\mathrm{D}}}\int_F g_{\mathrm{B}} v_F - d_h(\underline{p}_{\mathrm{D},h}^{\Gamma}, \underline{q}_h^{\Gamma}).\end{aligned} \tag{2.32}$$

Remark 2.10 (Extension to three space dimensions). The proposed method can be extended to the case of a three-dimensional domain with fracture corresponding to the intersection of the domain with a plane. The main differences are linked to the fracture terms, and can be summarized as follows: (i) the tangential permeability of the fracture is a uniformly elliptic, 2×2 matrix-valued field instead of a scalar; (ii) the fracture is discretized by means of a two-dimensional mesh $\mathcal{F}_h^{\Gamma}$ composed of element faces, and vertex-based DOFs are replaced by discontinuous polynomials of degree up to k on the skeleton (i.e., the union of the edges) of $\mathcal{F}_h^{\Gamma}$; (iii) all the terms involving pointwise evaluations at vertices are replaced by integrals on the edges of $\mathcal{F}_h^{\Gamma}$. Similar stability and error estimates as in the two-dimensional case can be proved in three space dimensions. A difference is that the right-hand side of the error estimate will additionally depend on the local anisotropy ratio of the tangential permeability of the fracture, arguably with a power of $1/2$.

2.4.4 Main results

In this section we report the main results of the analysis of our method, postponing the details of the proofs to Section 2.6. For the sake of simplicity, we will assume that

$$\partial\Omega_{\mathrm{B}}^{\mathrm{N}} = \emptyset, \quad g_{\mathrm{B}} \equiv 0, \qquad\qquad \partial\Gamma^{\mathrm{N}} = \emptyset, \quad g_{\Gamma} \equiv 0 \tag{2.33}$$

which means that homogeneous Dirichlet boundary conditions on the pressure are enforced on both the external boundary of the bulk region and on the boundary of the fracture. This corresponds to the situation when the motion of the fluid is driven by the volumetric source terms f in the bulk region and f_Γ in the fracture. The results illustrated below and in Section 2.6 can be adapted to more general boundary conditions at the price of heavier notations and technicalities that we want to avoid here.

In the error estimate of Theorem 2.12 below, we track explicitly the dependence of the multiplicative constants on the following quantites and bounds thereof: the bulk permeability $\boldsymbol{K}$, the tangential fracture permeability κ_Γ^τ, the normal fracture permeability κ_Γ^n, and the fracture thickness ℓ_Γ, which we collectively refer to in the following as the *problem data*.

We equip the space $\underline{\boldsymbol{X}}_h^k$ with the norm $\|\cdot\|_{\boldsymbol{X},h}$ such that, for all $(\underline{\boldsymbol{v}}_h, q_h, \underline{q}_h^\Gamma) \in \underline{\boldsymbol{X}}_h^k$,

$$\|(\underline{\boldsymbol{v}}_h, q_h, \underline{q}_h^\Gamma)\|_{\boldsymbol{X},h}^2 \coloneqq \|\underline{\boldsymbol{v}}_h\|_{\boldsymbol{U},\xi,h}^2 + \|q_h\|_{\mathrm{B},h}^2 + \|\underline{q}_h^\Gamma\|_{\Gamma,h}^2. \tag{2.34}$$

Theorem 2.11 (Stability)**.** *Assume* (2.33)*. Then, there exists a real number $\gamma > 0$ independent of h, but possibly depending on the problem geometry, on ϱ, k, and on the problem data, such that, for all $\underline{\boldsymbol{z}}_h \in \underline{\boldsymbol{X}}_h^k$,*

$$\|\underline{\boldsymbol{z}}_h\|_{\boldsymbol{X},h} \le \gamma \sup_{\underline{\boldsymbol{y}}_h \in \underline{\boldsymbol{X}}_h^k, \|\underline{\boldsymbol{y}}_h\|_{\boldsymbol{X},h}=1} \mathcal{A}_h^\xi(\underline{\boldsymbol{z}}_h, \underline{\boldsymbol{y}}_h). \tag{2.35}$$

Consequently, problem (2.32) *admits a unique solution.*

Proof. See Section 2.6. □

We next provide an a priori estimate of the discretization error. Let $(\boldsymbol{u}, p, p_\Gamma) \in \boldsymbol{U} \times P_{\mathrm{B}} \times P_\Gamma$ and $(\underline{\boldsymbol{u}}_h, p_h, \underline{p}_h^\Gamma) \in \underline{\boldsymbol{X}}_h$ denote, respectively, the unique solutions to problems (2.8) and (2.30) (recall that, owing to (2.33), $p_\Gamma = p_{\Gamma,0}$ and $\underline{p}_h^\Gamma = \underline{p}_{h,0}^\Gamma$). We further assume that $\boldsymbol{u} \in H^1(\mathcal{T}_h)^2$, and we estimate the error defined as the difference between the discrete solution $(\underline{\boldsymbol{u}}_h, p_h, \underline{p}_h^\Gamma)$ and the following projection of the exact solution:

$$(\widehat{\underline{\boldsymbol{u}}}_h, \widehat{p}_h, \widehat{\underline{p}}_h^\Gamma) \coloneqq (\underline{\boldsymbol{I}}_h^k \boldsymbol{u}, \pi_h^k p, \underline{I}_h^k p_\Gamma) \in \underline{\boldsymbol{X}}_h. \tag{2.36}$$

Theorem 2.12 (Error estimate)**.** *Let* (2.33) *hold true, and denote by* $(\boldsymbol{u}, p, p_\Gamma) \in \boldsymbol{U}\times P_{\mathrm{B}}\times P_\Gamma$ *and* $(\underline{\boldsymbol{u}}_h, p_h, \underline{p}_h^\Gamma) \in \underline{\boldsymbol{X}}_h^k$ *the unique solutions to problems* (2.8) *and* (2.30)*, respectively. Assume the additional regularity* $p_{|T} \in H^{k+2}(T)$ *for all* $T \in \mathcal{T}_h$ *and* $(p_\Gamma)_{|F} \in H^{k+2}(F)$ *for all* $F \in \mathcal{F}_h^\Gamma$*. Then, there exist a real number* $C > 0$ *independent of* h *and of the problem data, but possibly depending on* ϱ *and* k*, such that*

$$\begin{aligned}&\|\underline{\boldsymbol{u}}_h - \widehat{\underline{\boldsymbol{u}}}_h\|_{U,\xi,h} + \|\underline{p}_h^\Gamma - \widehat{\underline{p}}_h^\Gamma\|_{\Gamma,h} + \chi\|p_h - \widehat{p}_h\|_{B,h}\\ &\quad\le C\left(\sum_{T\in\mathcal{T}_h}\varrho_{\mathrm{B},T}\overline{K}_{\mathrm{B},T}h_T^{2(k+1)}\|p\|_{H^{k+2}(T)}^2 + \sum_{F\in\mathcal{F}_h^\Gamma}K_F h_F^{2(k+1)}\|p_\Gamma\|_{H^{k+2}(F)}^2\right)^{1/2},\end{aligned} \tag{2.37}$$

with $\chi > 0$ *independent of* h *but possibly depending on* ϱ*,* k*, and on the problem geometry and data.*

Proof. See Section 2.6. □

Remark 2.13 (Error norm and robustness). The error norm in the left-hand side of (2.37) is selected so as to prevent the right-hand side from depending on the global bulk anisotropy ratio ϱ_{B} (see (2.2)). As a result, for both the error on the bulk flux measured by $\|\underline{\boldsymbol{u}}_h - \widehat{\underline{\boldsymbol{u}}}_h\|_{U,\xi,h}$ and the error on the fracture pressure measured by $\|\underline{p}_h^\Gamma - \widehat{\underline{p}}_h^\Gamma\|_{\Gamma,h}$, we have: (i) as in more standard discretizations, full robustness with respect to the heterogeneity of $\boldsymbol{K}$ and K_Γ, meaning that the right-hand side does not depend on the jumps of these quantities; (ii) partial robustness with respect to the anisotropy of the bulk permeability, with a mild dependence on the square root of $\varrho_{\mathrm{B},T}$ (see (2.11)). As expected, robustness is not obtained for the L^2-error on the pressure in the bulk, which is multiplied by a data-dependent real number χ.

In the context of primal HHO methods, more general, possibly nonlinear diffusion terms including, as a special case, variable diffusion tensors inside the mesh elements have been recently considered in [73, 74]. In this case, one can expect the error estimate to depend on the square root of the ratio of the Lipschitz module and the coercivity constant of the diffusion field; see [73, Eq. (3.1)]. The extension to the mixed HHO formulation considered here for the bulk region can be reasonably expected to behave in a similar way. The details are postponed to a future work.

Remark 2.14 (L^2-supercloseness of bulk and fracture pressures). Using arguments based on the Aubin–Nitsche trick, one could prove under further regularity assumptions on the problem geometry that the L^2-errors $\|p_h - \widehat{p}_h\|_{\mathrm{B},h}$ and $\|p_h^\Gamma - \widehat{p}_h^\Gamma\|_{\Gamma,h}$ converge as h^{k+2}, where we have denoted by p_h^Γ and $\widehat{p}_h^\Gamma$ the broken polynomial

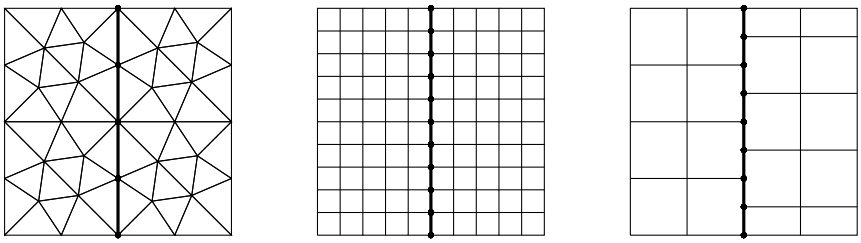

(a) Triangular (b) Cartesian (c) Nonconforming

Figure 2.4: Mesh families for the numerical tests

functions on Γ such that $(p_h^\Gamma)_{|F} \coloneqq p_F^\Gamma$ and $(\widehat{p}_h^\Gamma) \coloneqq \widehat{p}_F^\Gamma$ for all $F \in \mathcal{F}_h^\Gamma$. This supercloseness behaviour is typical of HHO methods (cf., e.g., [78, Theorem 7] and [83, Theorem 10]), and is confirmed by the numerical example of Section 2.5.1; see, in particular, Figures 2.5 and 2.6.

2.5 Numerical results

We provide an extensive numerical validation of the method on a set of model problems.

2.5.1 Convergence

We start by a non physical numerical test that demonstrates the convergence properties of the method. We approximate problem (2.30) on the square domain $\Omega = (0,1)^2$ crossed by the fracture $\Gamma = \{\boldsymbol{x} \in \Omega \mid x_1 = 0.5\}$ with $\partial\Omega_{\mathrm{B}}^{\mathrm{N}} = \partial\Gamma^{\mathrm{N}} = \emptyset$. We consider the exact solution corresponding to the bulk and fracture pressures

$$p(\boldsymbol{x}) = \begin{cases} \sin(4x_1)\cos(\pi x_2) & \text{if } x_1 < 0.5 \\ \cos(4x_1)\cos(\pi x_2) & \text{if } x_1 > 0.5 \end{cases}, \quad p_\Gamma(\boldsymbol{x}) = \xi(\cos(2) + \sin(2))\cos(\pi x_2),$$

and let $\boldsymbol{u}_{|\Omega_{\mathrm{B},i}} = -\boldsymbol{K}\nabla p_{|\Omega_{\mathrm{B},i}}$ for $i \in \{1,2\}$. We take here $\xi = 3/4$, $\kappa_\Gamma^\tau = 1$, $\ell_\Gamma = 0.01$ and

$$\boldsymbol{K} \coloneqq \begin{bmatrix} \kappa_\Gamma^n/(2\ell_\Gamma) & 0 \\ 0 & 1 \end{bmatrix}, \tag{2.38}$$

where $\kappa_\Gamma^n > 0$ is the normal permeability of the fracture. The expression of the source terms f, f_Γ, and of the Dirichlet data g_{B} and g_Γ are inferred from (2.30). It can be checked that, with this choice, the quantities $[\![p]\!]_\Gamma$, $[\![\boldsymbol{u}]\!]_\Gamma$, and $\{\{\boldsymbol{u}\}\}_\Gamma$ are not identically zero on the fracture. We consider the triangular, Cartesian, and

nonconforming mesh families of Figure 3.3 and monitor the following errors:

$$\underline{\boldsymbol{e}}_h \coloneqq \underline{\boldsymbol{u}}_h - \widehat{\underline{\boldsymbol{u}}}_h, \quad \epsilon_h \coloneqq p_h - \widehat{p}_h, \quad \underline{\epsilon}_h^\Gamma \coloneqq \underline{p}_h^\Gamma - \widehat{\underline{p}}_h^\Gamma, \quad \epsilon_h^\Gamma \coloneqq p_h^\Gamma - \widehat{p}_h^\Gamma, \tag{2.39}$$

where $\widehat{\underline{\boldsymbol{u}}}_h$, $\widehat{p}_h$, and $\widehat{\underline{p}}_h^\Gamma$ are the broken fracture pressures defined by (2.36), while p_h^Γ and $\widehat{p}_h^\Gamma$ are defined as in Remark 2.14. Notice that, while the triangular and Cartesian mesh families can be handled by standard finite element discretizations, this is not the case for the nonconforming mesh. This kind of nonconforming meshes appear, e.g., when the fracture occurs between two plates, and the mesh of each bulk subdomain is designed to be compliant with the permeability values therein.

We display in Figure 2.5 and 2.6 various error norms as a function of the meshsize, obtained with different values of the normal fracture permeability $\kappa_\Gamma^n \in \{2\ell_\Gamma, 1\}$ in order to show (i) the convergence rates, and (ii) the influence of the global anisotropy ratio ϱ_B on the value of the error, both predicted by Theorem 2.12. By choosing $\kappa_\Gamma^n = 2\ell_\Gamma$, we obtain an homogeneous bulk permeability tensor $\boldsymbol{K} = \boldsymbol{I}_2$ so the value of the error is not impacted by the global anisotropy ratio ϱ_B (since it is equal to 1 in that case); see Figure 2.5. On the other hand, letting $\kappa_\Gamma^n = 1$, we obtain a global anisotropy ratio $\varrho_\mathrm{B} = 50$ and we can clearly see the impact on the value of the error $\|\underline{\boldsymbol{e}}_h\|_{U,\xi,h}$ in Figure 2.6. For both configurations, the orders of convergence predicted by Theorem 2.12 are confirmed numerically for $\|\underline{\boldsymbol{e}}_h\|_{U,\xi,h}$ and $\|\underline{\epsilon}_h^\Gamma\|_{\Gamma,h}$ (and even a slightly better convergence rate on Cartesian and nonconforming meshes). Moreover, convergence in h^{k+2} is observed for the L^2-norms of the bulk and fracture pressures, corresponding to $\|\epsilon_h\|_{\mathrm{B},h}$ and $\|\epsilon_h^\Gamma\|_\Gamma$, respectively; see Remark 2.14 on this point.

2.5.2 Quarter five-spot problem

The five-spot pattern is a standard configuration in petroleum engineering used to displace and extract the oil in the basement by injecting water, steam, or gas; see, e.g., [66, 125]. The injection well sits in the center of a square, and four production wells are located at the corners. Due to the symmetry of the problem, we consider here only a quarter five-spot pattern on $\Omega = (0,1)^2$ with injection and production wells located in $(0,0)$ and $(1,1)$, respectively, and modelled by the source term $f : \Omega_\mathrm{B} \to \mathbb{R}$ such that

$$f(\boldsymbol{x}) = 200\Big(\tanh\big(200(0.025 - (x_1^2 + x_2^2)^{1/2})\big) - \tanh\big(200(0.025 - ((x_1-1)^2 + (x_2-1)^2)^{1/2})\big)\Big).$$

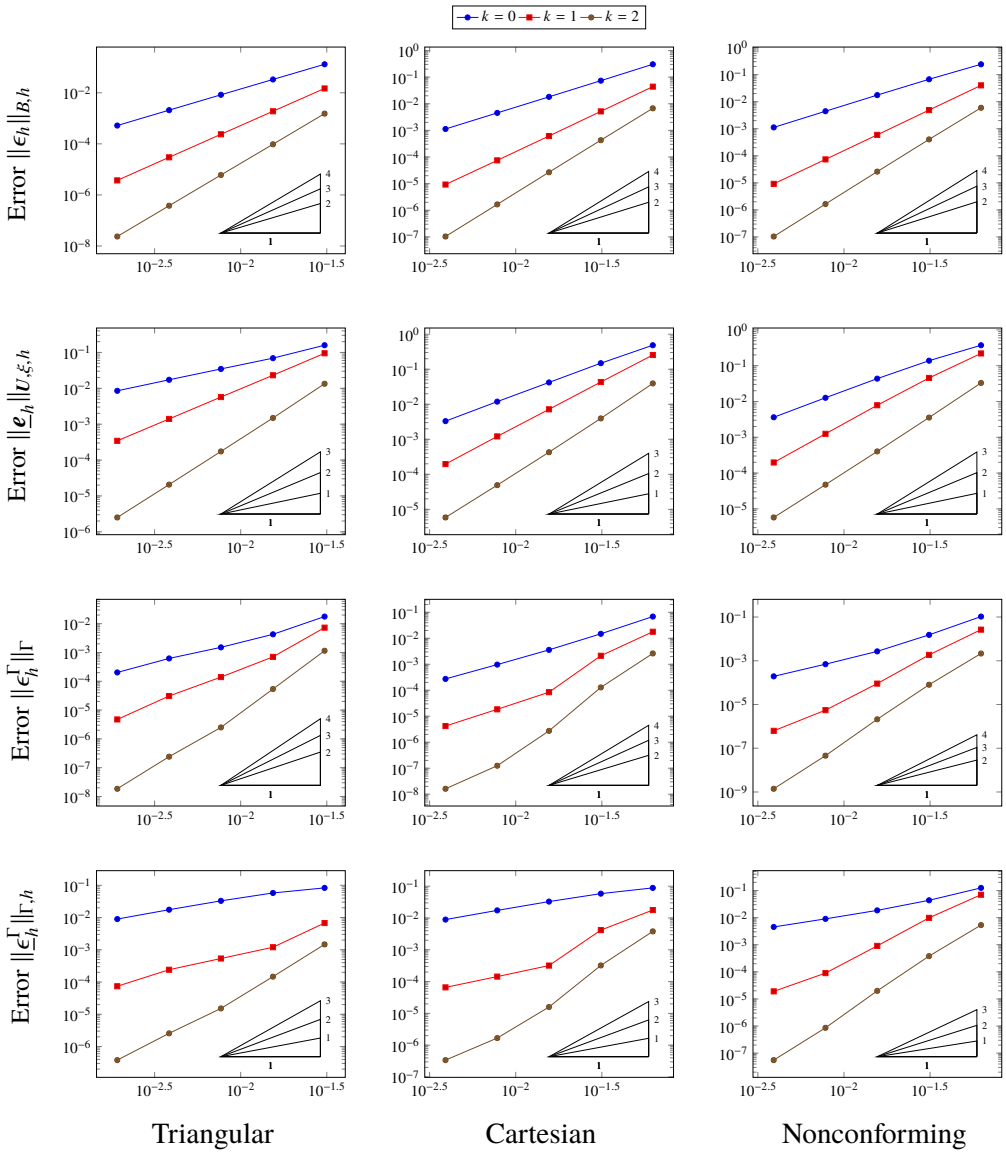

Figure 2.5: Errors vs. h for the test case of Section 2.5.1 on the mesh families introduced in Figure 3.3 with $\kappa_\Gamma^n = 2\ell_\Gamma$

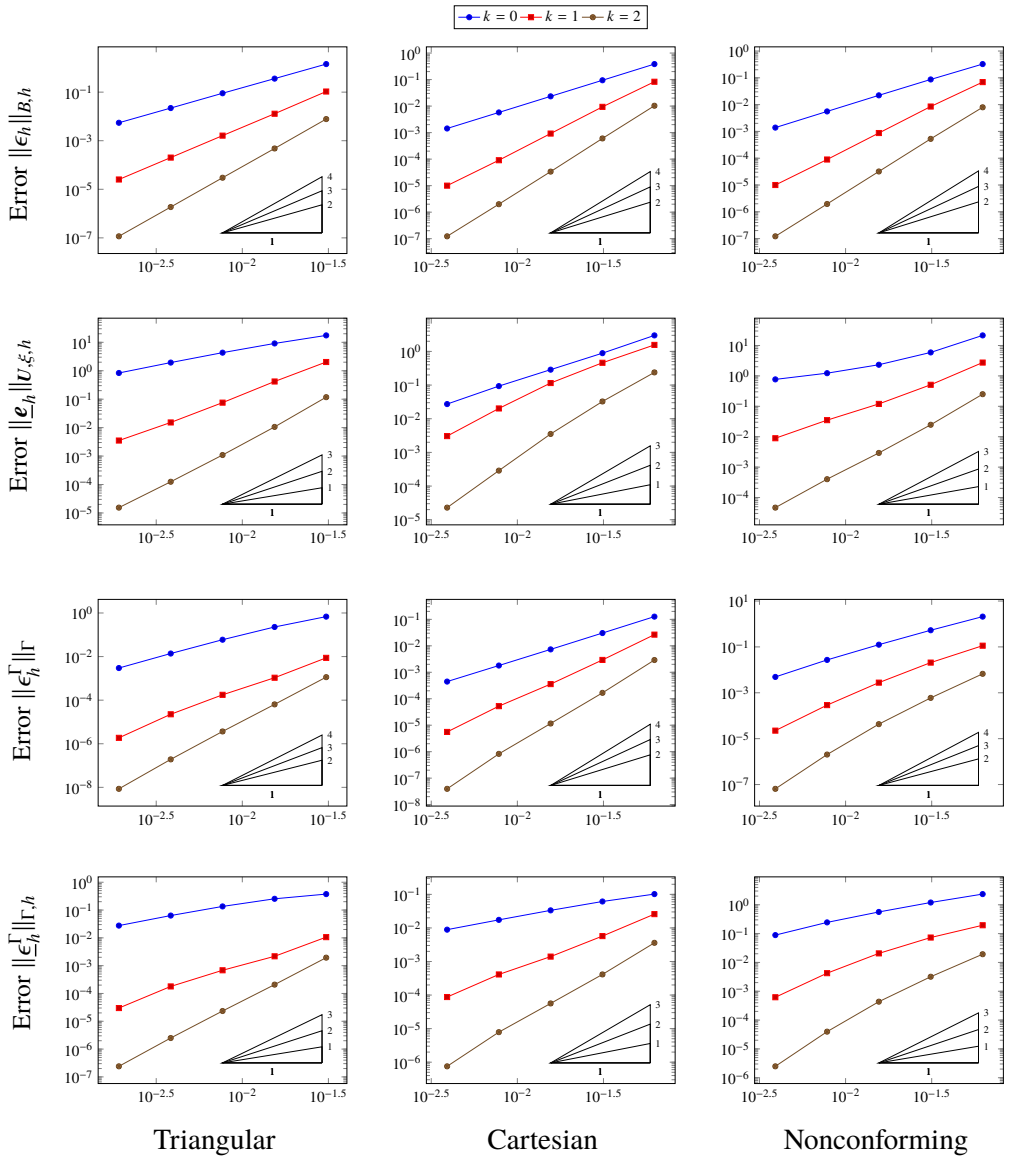

Figure 2.6: Errors vs. h for the test case of Section 2.5.1 on the mesh families introduced in Figure 3.3 with $\kappa_\Gamma^n = 1$

Test 1: No fracture In Figure 2.7a, we display the pressure distribution when the domain Ω contains no fracture, i.e. $\Omega_B = \Omega$; see Figure 2.8a. The bulk tensor is given by $\boldsymbol{K} = \boldsymbol{I}_2$, and we enforce homogeneous Neumann and Dirichlet boundary conditions, respectively, on (see Figure 2.8a)

$$\partial\Omega_B^N = \{\boldsymbol{x} \in \partial\Omega_B \mid x_1 = 0 \text{ or } x_2 = 0 \text{ or } (x_1 > 3/4 \text{ and } x_2 > 3/4)\},$$
$$\partial\Omega_B^D = \{\boldsymbol{x} \in \partial\Omega_B \mid (x_1 = 1 \text{ and } x_2 \leq 3/4) \text{ or } (x_2 = 1 \text{ and } x_1 \leq 3/4)\}.$$

Since the bulk permeability is the identity matrix and there is no fracture inside the domain, the pressure decreases continuously moving from the injection well towards the production well.

Test 2: Permeable fracture We now let the domain Ω be crossed by the fracture $\Gamma = \{\boldsymbol{x} \in \Omega \mid x_2 = 1 - x_1\}$ of constant thickness $\ell_\Gamma = 10^{-2}$, and we let $f_\Gamma \equiv 0$. In addition to the bulk boundary conditions described in **Test 1**, we enforce homogeneous Dirichlet boundary conditions on $\partial\Gamma^D = \partial\Gamma$; see Figure 2.8a. The bulk and fracture permeability parameters are such that

$$\boldsymbol{K} = \boldsymbol{I}_2 \qquad \kappa_\Gamma^n = 1, \qquad \kappa_\Gamma^\tau = 100,$$

and are chosen in such a way that the fracture is permeable, which means that the fluid should be attracted by it. The bulk pressure corresponding to this configuration is depicted in Figure 2.7b. As shown in Figure 2.8b, we remark that (i) in $\Omega_{B,1}$, we have a lower pressure, and that the pressure decreases more slowly than in **Test 1** going from the injection well towards the fracture and (ii) in $\Omega_{B,2}$, the flow caused by the production well attracts, less significantly than in **Test 1**, the flow outside the fracture.

Test 3: Impermeable fracture We next consider the case of an impermeable fracture: we keep the same domain configuration as before, but we let

$$\kappa_\Gamma^n = 10^{-2}, \qquad \kappa_\Gamma^\tau = 1.$$

Unlike before, we observe in this case a significant jump of the bulk pressure across the fracture Γ, see Figure 2.7c. This can be better appreciated in Figure 2.8b, which contains the plots of the bulk pressure over the line $x_1 = x_2$ for the various configurations considered.

Flow across the fracture Since an exact solution is not available for the previous test cases, we provide a quantitative assessment of the convergence by monitoring the quantity

$$M_{p/i}^{k,h} := \sum_{F \in \mathcal{F}_h^\Gamma} \int_F [\![\underline{\boldsymbol{u}}_h]\!]_F,$$

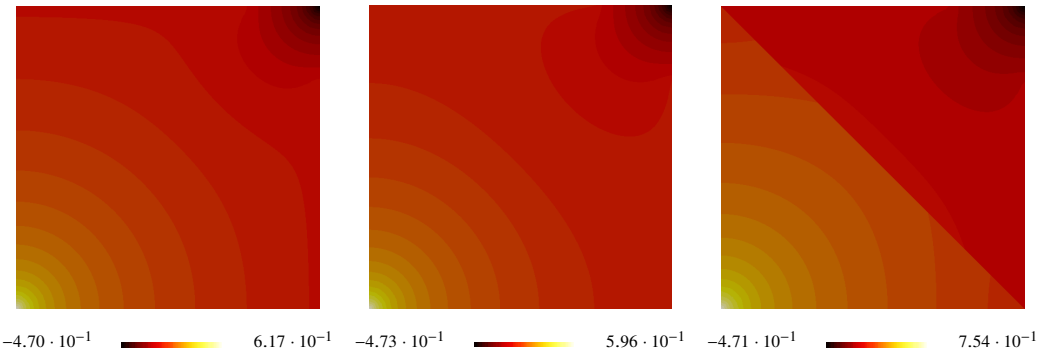

(a) No fracture (b) Permeable fracture (c) Impermeable fracture

Figure 2.7: Bulk pressure for the test cases of Section 2.5.2 on a triangular mesh ($h = 7.68 \cdot 10^{-3}$) with $k = 2$

which corresponds to the global flux entering the fracture for the permeable (subscript p) and impermeable (subscript i) fractured test cases. The index k refers to the polynomial degree $k \in \{0, 1, 2\}$, and the index h to the meshsize. Five refinement levels of the triangular mesh depicted in Figure 3.3a are considered. We plot in Figure 2.8c and 2.8d the errors $\epsilon_{\mathrm{p/i}} := |\mathrm{M}^{\mathrm{r}}_{\mathrm{p/i}} - \mathrm{M}^{k,h}_{\mathrm{p/i}}|$ for the permeable or impermeable case (p/i), where $\mathrm{M}^{r}_{\mathrm{p/i}}$ denotes the reference value obtained with $k = 2$ on the fifth mesh refinement corresponding to $h = 9.60 \cdot 10^{-4}$. In both cases we have convergence, with respect to the polynomial degree and the meshsize, to the reference values $\mathrm{M}^{r}_{\mathrm{p}} = 9.96242 \cdot 10^{-2}$ and $\mathrm{M}^{r}_{\mathrm{i}} = 3.19922 \cdot 10^{-2}$. For the permeable test case depicted in Figure 2.8c, after the second refinement, increasing the polynomial degree only modestly affect the error decay, which suggests that convergence may be limited by the local regularity of the exact solution. For the impermeable test case depicted in Figure 2.8d, on the other hand, the local regularity of the exact solution seems sufficient to benefit from the increase of the approximation order.

2.5.3 Porous medium with random permeability

To show the influence of the bulk permeability tensor on the solution, we consider two piecewise constants functions $\mu_1, \mu_2 : \Omega_{\mathrm{B}} \to (0, 2)$ and the heterogeneous and possibly anisotropic bulk tensor $\boldsymbol{K}$ given by

$$\boldsymbol{K} := \begin{bmatrix} \mu_1 & 0 \\ 0 & \mu_2 \end{bmatrix}.$$

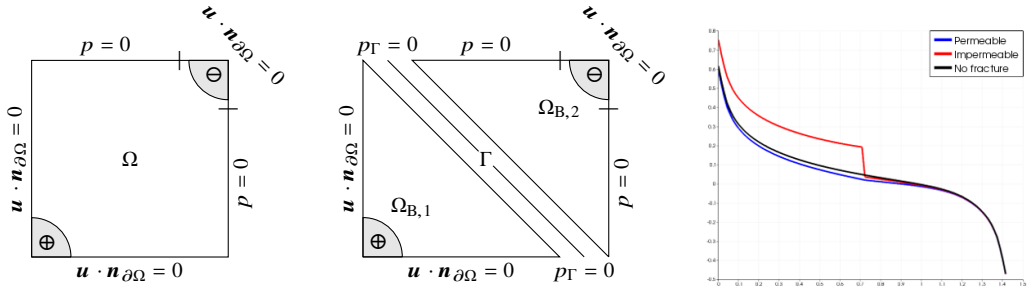

(a) Domain configurations without (left) and with (right) fracture (b) Bulk pressure over $x_1 = x_2$

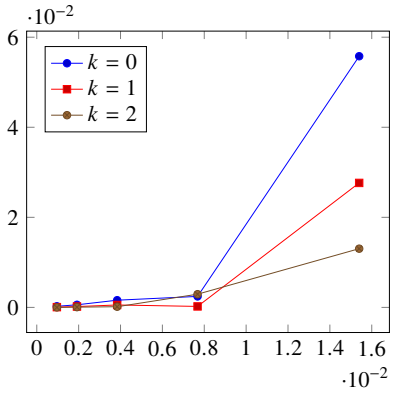

(c) ϵ_p vs. h

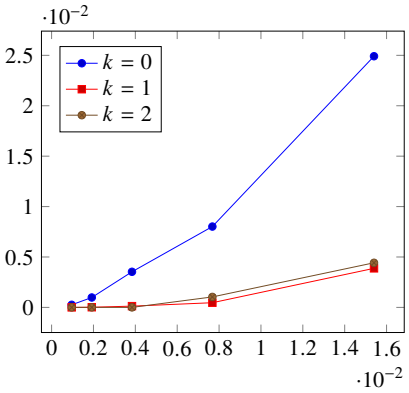

(d) ϵ_i vs. h

Figure 2.8: Domain configurations, pressure along the line $x_1 = x_2$, and errors on the flow across the fracture vs. h for the test cases of Section 2.5.2.

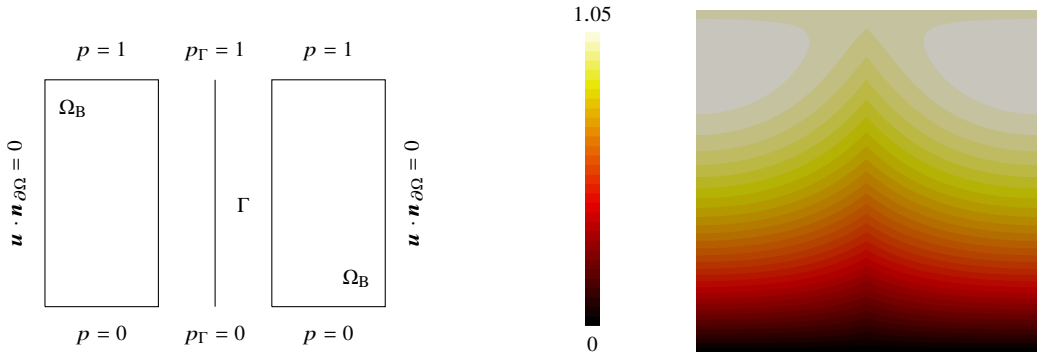

(a) Domain configuration (b) Bulk pressure p

Figure 2.9: Bulk pressure for the first test case of Section 2.5.3 (homogeneous permeability).

For the following tests, we use a 64×64 uniform Cartesian mesh ($h = 3.91 \cdot 10^{-3}$) and $k = 2$. The domain $\Omega := (0,1)^2$ is crossed by a fracture $\Gamma := \{0.5\} \times (0,1)$ of constant thickness $\ell_\Gamma := 10^{-2}$. We set the fracture permeability parameters $\kappa_\Gamma^n := 1$ and $\kappa_\Gamma^\tau := 100$, corresponding to a permeable fracture. The source terms are constant and such that $f \equiv 4$ and $f_\Gamma \equiv 4$. We enforce homogeneous Neumann boundary conditions on $\partial\Omega_B^N := \{\boldsymbol{x} \in \partial\Omega_B \mid x_1 \in \{0,1\}\}$ and Dirichlet boundary conditions on $\partial\Omega_B^D := \{\boldsymbol{x} \in \partial\Omega_B \mid x_2 \in \{0,1\}\}$ and $\partial\Gamma^D := \partial\Gamma$ with

$$g_B(\boldsymbol{x}) := x_2 \quad \forall \boldsymbol{x} \in \partial\Omega_B^D, \qquad g_\Gamma(\boldsymbol{x}) := x_2 \quad \forall \boldsymbol{x} \in \partial\Gamma^D.$$

Test 1: Homogeneous permeability In Figure 2.9, we depict the bulk pressure distribution corresponding to $\mu_1 = \mu_2 := 1$. As expected, the flow is moving towards the fracture but less and less significantly as we approach the bottom of the domain since the pressure decreases with respect to the boundary conditions.

Test 2: Random permeability We next define inside the bulk region Ω_B horizontal layers of random permeabilities which are separated by the fracture, and let the functions μ_1 and μ_2 take, inside each element, a random value between 0 and 1 on one side of each layer, and between 1 and 2 on the other side; see Figure 2.10a. High permeability zones are prone to let the fluid flow towards the fracture, in contrast to the low permeability zones in which the pressure variations are larger; see Figure 2.10b, where dashed lines represent the different layers described above. This qualitative behaviour is well captured by the numerical solution.

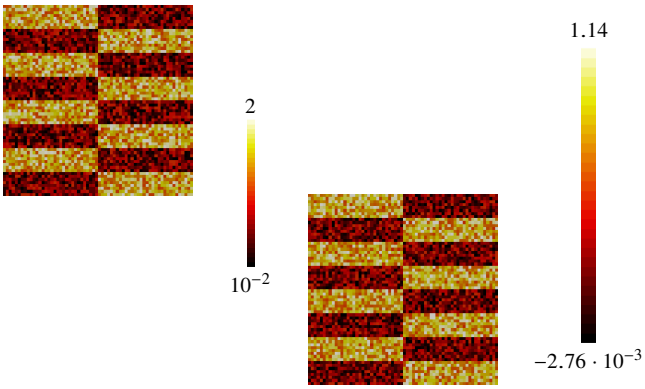

(a) Values of μ_1 (left) and μ_2 (right)

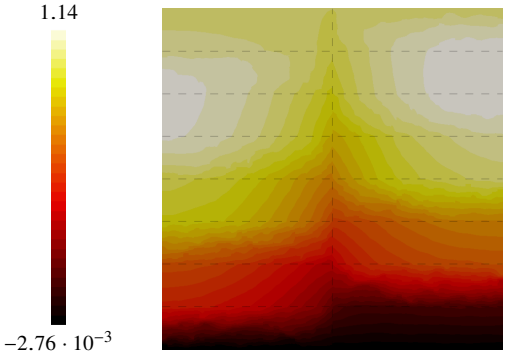

(b) Bulk pressure p

Figure 2.10: Permeability components distribution and bulk pressure for the second test case of Section 2.5.3 (random permeability).

2.6 Stability analysis

This section contains the proof of Theorem 2.11 preceeded by the required preliminary results. We recall that, for the sake of simplicity, we work here under the assumption that homogeneous Dirichlet boundary conditions are enforced on both the bulk and the fracture pressures; see (2.33). This simplifies the arguments of Lemma 2.15 below.

Recalling the definition (2.26) of a_h^ξ, and using (2.21) together with Cauchy–Schwarz inequalities, we infer the existence of a real number $\eta_a > 0$ independent of h and of the problem data such that, for all $\underline{\boldsymbol{v}}_h \in \underline{\widetilde{\boldsymbol{U}}}_h^k$,

$$\eta_a^{-1} \|\underline{\boldsymbol{v}}_h\|_{U,\xi,h}^2 \le \|\underline{\boldsymbol{v}}_h\|_{a,\xi,h}^2 := a_h^\xi(\underline{\boldsymbol{v}}_h, \underline{\boldsymbol{v}}_h) \le \eta_a \varrho_{\mathrm{B}} \|\underline{\boldsymbol{v}}_h\|_{U,\xi,h}^2, \tag{2.40}$$

with global bulk anisotropy ratio ϱ_{B} defined by (2.2). Similarly, summing (2.23) over $F \in \mathcal{F}_h^\Gamma$, it is readily inferred that it holds, for all $\underline{q}_h^\Gamma \in \underline{P}_{\Gamma,h}^k$,

$$\eta_d^{-1} \|\underline{q}_h^\Gamma\|_{\Gamma,h}^2 \le d_h(\underline{q}_h^\Gamma, \underline{q}_h^\Gamma) \le \eta_d \|\underline{q}_h^\Gamma\|_{\Gamma,h}^2. \tag{2.41}$$

The following lemma contains a stability result for the bilinear form b_h.

Lemma 2.15 (Inf-sup stability of b_h)**.** *There is a real number $\beta > 0$ independent of h, but possibly depending on ϱ, k, and on the problem geometry and data, such that, for all $q_h \in P_{\mathrm{B},h}^k$,*

$$\|q_h\|_{\mathrm{B},h} \le \beta \sup_{\underline{\boldsymbol{w}}_h \in \underline{\boldsymbol{U}}_{h,0}^k, \|\underline{\boldsymbol{w}}_h\|_{U,\xi,h}=1} b_h(\underline{\boldsymbol{w}}_h, q_h). \tag{2.42}$$

Proof. We use the standard Fortin argument relying on the continuous inf-sup condition. In what follows, $a \lesssim b$ stands for the inequality $a \le Cb$ with real number $C > 0$ having the same dependencies as β in (2.42). Let $q_h \in P^k_{\mathrm{B},h}$. For each $i \in \{1,2\}$, the surjectivity of the continuous divergence operator from $\boldsymbol{H}(\mathrm{div};\Omega_{\mathrm{B},i})$ onto $L^2(\Omega_{\mathrm{B},i})$ (see, e.g., [106, Section 2.4.1]) yields the existence of $\boldsymbol{v}_i \in \boldsymbol{H}(\mathrm{div};\Omega_{\mathrm{B},i})$ such that

$$\nabla\cdot\boldsymbol{v}_i = q_h \text{ in } \Omega_{\mathrm{B},i} \text{ and } \|\boldsymbol{v}_i\|_{\boldsymbol{H}(\mathrm{div};\Omega_{\mathrm{B},i})} \lesssim \|q_h\|_{\Omega_{\mathrm{B},i}}, \tag{2.43}$$

with hidden multiplicative constant depending on $\Omega_{\mathrm{B},i}$. Let $\boldsymbol{v}:\Omega_{\mathrm{B}}\to\mathbb{R}^2$ be such that $\boldsymbol{v}_{|\Omega_{\mathrm{B},i}} = \boldsymbol{v}_i$ for $i\in\{1,2\}$. This function cannot be interpolated through $\underline{\boldsymbol{I}}^k_h$, as it does not belong to the space $H^1(\mathcal{T}_h)^2$ introduced in Section 2.4.3.2; see also Remark 2.8 on this point. However, since we have assumed Dirichlet boundary conditions (cf. (2.33)), following the procedure described in [106, Section 4.1] one can construct smoothings $\tilde{\boldsymbol{v}}_i \in H^1(\Omega_{\mathrm{B},i})^2$, $i\in\{1,2\}$, such that

$$\nabla\cdot\tilde{\boldsymbol{v}}_i = \nabla\cdot\boldsymbol{v}_i \text{ in } \Omega_{\mathrm{B},i} \text{ and } \|\tilde{\boldsymbol{v}}_i\|_{H^1(\Omega_{\mathrm{B},i})^2} \lesssim \|\boldsymbol{v}_i\|_{\boldsymbol{H}(\mathrm{div};\Omega_{\mathrm{B},i})}. \tag{2.44}$$

Let now $\tilde{\boldsymbol{v}}:\Omega_{\mathrm{B}}\to\mathbb{R}^2$ be such that $\tilde{\boldsymbol{v}}_{|\Omega_{\mathrm{B},i}} = \tilde{\boldsymbol{v}}_i$ for $i\in\{1,2\}$. The function $\tilde{\boldsymbol{v}}$ belongs to $\boldsymbol{U}\cap H^1(\mathcal{T}_h)^2$, and it can be easily checked that $\underline{\boldsymbol{I}}^k_h\tilde{\boldsymbol{v}}\in\underline{\boldsymbol{U}}^k_{h,0}$. Recalling the definition (2.13) of the $\|\cdot\|_{U,T}$-norm and using the boundedness of the L^2-orthogonal projector in the corresponding L^2-norm together with local continuous trace inequalities (see, e.g., [81, Lemma 1.49]), one has that

$$\sum_{T\in\mathcal{T}_h}\|\underline{\boldsymbol{I}}^k_T\tilde{\boldsymbol{v}}\|^2_{\boldsymbol{U},T} \lesssim \sum_{i=1}^2\|\tilde{\boldsymbol{v}}_i\|^2_{H^1(\Omega_{\mathrm{B},i})^2} \lesssim \sum_{i=1}^2\|\boldsymbol{v}_i\|^2_{\boldsymbol{H}(\mathrm{div};\Omega_{\mathrm{B},i})} \lesssim \|q_h\|^2_{\mathrm{B},h}, \tag{2.45}$$

where we have used (2.44) in the second inequality and (2.43) in the third. The hidden constant depends here on $\underline{K}_{\mathrm{B}}^{-1}$. Moreover, using a triangle inequality, the fact that $\lambda^\xi_F \le \lambda_F = (\lambda_\Gamma)_{|F} \le \overline{\lambda}_\Gamma$ (see (2.6)) for all $F\in\mathcal{F}^\Gamma_h$, the boundedness of the L^2-orthogonal projector, and a global continuous trace inequality in each bulk subdomain $\Omega_{\mathrm{B},i}$, $i\in\{1,2\}$, we get

$$|\underline{\boldsymbol{I}}^k_h\tilde{\boldsymbol{v}}|^2_{\xi,h} \lesssim \sum_{i=1}^2\|(\tilde{\boldsymbol{v}}_i)_{|\Gamma}\cdot\boldsymbol{n}_\Gamma\|^2_\Gamma \lesssim \sum_{i=1}^2\|\tilde{\boldsymbol{v}}_i\|^2_{H^1(\Omega_{\mathrm{B},i})^2} \lesssim \|q_h\|^2_{\mathrm{B},h}, \tag{2.46}$$

where we have used (2.44) and (2.43) in the third inequality. The hidden constant depends here on $\overline{\lambda}_\Gamma$ and on the inverse of the diameters of the bulk subdomains. Combining (2.45) and (2.46), and naming β the hidden constant, we conclude that

$$\|\underline{\boldsymbol{I}}^k_h\tilde{\boldsymbol{v}}\|_{\boldsymbol{U},\xi,h} \le \beta\|q_h\|_{\mathrm{B},h}. \tag{2.47}$$

Finally, (2.44) together with the commuting property (2.17) of the local divergence reconstruction operator gives

$$\pi_T^k(\nabla\cdot\boldsymbol{v}) = \pi_T^k(\nabla\cdot\tilde{\boldsymbol{v}}) = D_T^k\underline{\boldsymbol{I}}_T^k\tilde{\boldsymbol{v}}_{|T} \qquad \forall T\in\mathcal{T}_h. \tag{2.48}$$

Gathering all of the above properties, we infer that

$$\|q_h\|_{\mathrm{B},h}^2 = b(\boldsymbol{v},q_h) = b(\tilde{\boldsymbol{v}},q_h) = b_h(\underline{\boldsymbol{I}}_h^k\tilde{\boldsymbol{v}},q_h),$$

where we have used (2.43) together with the definition (2.7) of b in the first equality, (2.44) in the second, and (2.48) along with the definition (2.30b) of b_h to conclude. Finally, factoring $\|\underline{\boldsymbol{I}}_h^k\tilde{\boldsymbol{v}}\|_{U,\xi,h}$, using the linearity of b_h in its first argument, and denoting by \$ the supremum in (2.42), we get

$$\|q_h\|_{\mathrm{B},h}^2 \le \$\|\underline{\boldsymbol{I}}_h^k\tilde{\boldsymbol{v}}\|_{U,\xi,h} \le \beta\$\|q_h\|_{\mathrm{B},h},$$

where the conclusion follows from (2.47). This proves (2.42). □

We next recall the following Poincaré inequality, which is a special case of the discrete Sobolev embeddings proved in [74, Proposition 5.4]: There exist a real number $C_{\mathrm{P}}>0$ independent of h and of the problem data (but possibly depending on Γ and k) such that, for all $\underline{q}_h^\Gamma = ((q_F^\Gamma)_{F\in\mathcal{F}_h^\Gamma},(q_V^\Gamma)_{V\in\mathcal{V}_h}) \in \underline{P}_{\Gamma,h,0}^k$,

$$\|q_h^\Gamma\|_\Gamma \le C_{\mathrm{P}}\underline{K}_\Gamma^{-1/2}\|\underline{q}_h^\Gamma\|_{\Gamma,h}, \tag{2.49}$$

where q_h^Γ is the piecewise polynomial function on Γ such that $(q_h^\Gamma)_{|F} = q_F^\Gamma$ for all $F\in\mathcal{F}_h^\Gamma$.

Using the Cauchy–Schwarz inequality together with the fact that $\lambda_F^\xi = (\lambda_\Gamma^\xi)_{|F} \ge \underline{\lambda}_\Gamma\left(\frac{\xi}{2}-\frac{1}{4}\right)$ for all $F\in\mathcal{F}_h^\Gamma$ (see (2.5) and and (2.6)) and the Poincaré inequality (2.49), we can prove the following boundedness property for the bilinear form c_h defined by (2.28): For all $\underline{\boldsymbol{v}}_h\in\underline{\boldsymbol{U}}_{h,0}^k$ and all $\underline{q}_h^\Gamma\in\underline{P}_{\Gamma,h,0}^k$, it holds that

$$|c_h(\underline{\boldsymbol{v}}_h,\underline{q}_h^\Gamma)| \le \eta_c\underline{\lambda}_\Gamma^{-1/2}|\underline{\boldsymbol{v}}_h|_{\xi,h}\|\underline{q}_h^\Gamma\|_{\Gamma,h}, \qquad \eta_c \coloneqq C_{\mathrm{P}}\left(\frac{\xi}{2}-\frac{1}{4}\right)^{-1/2}. \tag{2.50}$$

We are now ready to prove Theorem 2.11.

Proof of Theorem 2.11. Let $\underline{\boldsymbol{z}}_h \coloneqq (\underline{\boldsymbol{w}}_h,r_h,\underline{r}_h^\Gamma)\in\underline{\boldsymbol{X}}_h^k$. In the spirit of [95, Lemma 4.38], the proof proceeds in three steps.

Step 1: Control of the flux in the bulk and of the pressure in the fracture Using the coercivity (2.40) of the bilinear form a_h^ξ and (2.41) of the bilinear form d_h, it is inferred that

$$\mathcal{A}_h^\xi(\underline{\boldsymbol{z}}_h,\underline{\boldsymbol{z}}_h) \ge \eta_a^{-1}\|\underline{\boldsymbol{w}}_h\|_{U,\xi,h}^2 + \eta_d^{-1}\|\underline{r}_h^\Gamma\|_{\Gamma,h}^2. \tag{2.51}$$

Step 2: Control of the pressure in the bulk The inf-sup condition (2.42) on the bilinear form b_h gives the existence of $\underline{\boldsymbol{v}}_h \in \underline{\boldsymbol{U}}_{h,0}^k$ such that

$$\|r_h\|_{\mathrm{B},h}^2 = -b_h(\underline{\boldsymbol{v}}_h, r_h) \text{ and } \|\underline{\boldsymbol{v}}_h\|_{U,\xi,h} \le \beta \|r_h\|_{\mathrm{B},h}. \tag{2.52}$$

Using the definition (2.31) of $\mathcal{A}_h^\xi$, it is readily inferred that

$$\begin{aligned} \mathcal{A}_h^\xi(\underline{\boldsymbol{z}}_h, (\underline{\boldsymbol{v}}_h, 0, \underline{0})) &= \|r_h\|_{\mathrm{B},h}^2 + a_h^\xi(\underline{\boldsymbol{w}}_h, \underline{\boldsymbol{v}}_h) + c_h(\underline{\boldsymbol{v}}_h, \underline{r}_h^\Gamma) \\ &\ge \|r_h\|_{\mathrm{B},h}^2 - |a_h^\xi(\underline{\boldsymbol{w}}_h, \underline{\boldsymbol{v}}_h)| - |c_h(\underline{\boldsymbol{v}}_h, \underline{r}_h^\Gamma)|. \end{aligned} \tag{2.53}$$

Using the continuity of a_h^ξ expressed by the second inequality in (2.40) followed by Young's inequality, we infer that it holds, for all $\epsilon > 0$,

$$\begin{aligned} |a_h^\xi(\underline{\boldsymbol{w}}_h, \underline{\boldsymbol{v}}_h)| &\le \eta_a \varrho_{\mathrm{B}} \|\underline{\boldsymbol{w}}_h\|_{U,\xi,h} \|\underline{\boldsymbol{v}}_h\|_{U,\xi,h} \\ &\le \frac{\epsilon}{4} \|\underline{\boldsymbol{v}}_h\|_{U,\xi,h}^2 + \frac{(\eta_a \varrho_{\mathrm{B}})^2}{\epsilon} \|\underline{\boldsymbol{w}}_h\|_{U,\xi,h}^2. \end{aligned} \tag{2.54}$$

Similarly, the boundedness (2.50) of c_h followed by Young's inequality gives

$$|c_h(\underline{\boldsymbol{v}}_h, \underline{r}_h^\Gamma)| \le \eta_c \underline{\lambda}_\Gamma^{-1/2} \|\underline{\boldsymbol{v}}_h\|_{U,\xi,h} \|\underline{r}_h^\Gamma\|_{\Gamma,h} \le \frac{\epsilon}{4} \|\underline{\boldsymbol{v}}_h\|_{U,\xi,h}^2 + \frac{\eta_c^2}{\epsilon \underline{\lambda}_\Gamma} \|\underline{r}_h^\Gamma\|_{\Gamma,h}^2. \tag{2.55}$$

Plugging (2.54) and (2.55) into (2.53), selecting $\epsilon = \beta^{-2}$, and using the bound in (2.52), we arrive at

$$\mathcal{A}_h^\xi(\underline{\boldsymbol{z}}_h, (\underline{\boldsymbol{v}}_h, 0, \underline{0})) \ge \frac{1}{2} \|r_h\|_{\mathrm{B},h}^2 - C_1 \|\underline{\boldsymbol{w}}_h\|_{U,\xi,h}^2 - C_2 \|\underline{r}_h^\Gamma\|_{\Gamma,h}^2, \tag{2.56}$$

with $C_1 := (\eta_a \beta \varrho_{\mathrm{B}})^2$ and $C_2 := (\eta_c \beta)^2 / \underline{\lambda}_\Gamma$.

Step 3: Conclusion Setting $\alpha := (1 + C_1\eta_a + C_2\eta_d)^{-1}/2$ and combining (2.51) with (2.56), we infer that

$$\begin{aligned} \mathcal{A}_h^\xi(\underline{\boldsymbol{z}}_h, (1-\alpha)\underline{\boldsymbol{z}}_h + \alpha(\underline{\boldsymbol{v}}_h, 0, \underline{0})) \ge \frac{\alpha}{2} \|r_h\|_{\mathrm{B},h}^2 &+ \eta_a^{-1} (1 - \alpha(1 + C_1\eta_a)) \|\underline{\boldsymbol{w}}_h\|_{U,\xi,h}^2 \\ &+ \eta_d^{-1} (1 - \alpha(1 + C_2\eta_d)) \|\underline{r}_h^\Gamma\|_{\Gamma,h}^2. \end{aligned}$$

Denoting by \$ the supremum in the right-hand side of (2.35), we infer from the previous inequality that

$$C_3 \|\underline{\boldsymbol{z}}_h\|_{\boldsymbol{X},h}^2 \le \mathcal{A}_h^\xi(\underline{\boldsymbol{z}}_h, (1-\alpha)\underline{\boldsymbol{z}}_h + \alpha(\underline{\boldsymbol{v}}_h, 0, \underline{0})) \le \$ \|(1-\alpha)\underline{\boldsymbol{z}}_h + \alpha(\underline{\boldsymbol{v}}_h, 0, \underline{0})\|_{\boldsymbol{X},h}, \tag{2.57}$$

with $C_3 := \min\left(\alpha/2, \eta_a^{-1}(1 - \alpha(1 + C_1\eta_a)), \eta_d^{-1}(1 - \alpha(1 + C_2\eta_d))\right) > 0$. Finally, observing that, by the definition (2.34) of the $\|\cdot\|_{\boldsymbol{X},h}$-norm together with (2.52), it holds that $\|(\underline{\boldsymbol{v}}_h, 0, \underline{0})\|_{\boldsymbol{X},h} \le \beta \|r_h\|_{\mathrm{B},h} \le \beta \|\underline{\boldsymbol{z}}_h\|_{\boldsymbol{X},h}$, (2.57) gives (2.35) with $\gamma = C_3^{-1}(1 + \beta)$. □

2.7 Error analysis

This section contains the proof of Theorem 2.12 preceeded by the required preliminary results. As in the previous section, we work under the assumption that homogeneous Dirichlet boundary conditions are enforced on both the bulk and the fracture pressures; see (2.33). In what follows, $a \lesssim b$ means $a \le Cb$ with real number $C > 0$ independent of h and of the problem data, but possibly depending on ϱ, k, and on the problem geometry.

For all $T \in \mathcal{T}_h$, we define the local elliptic projection $\breve{p}_T \in \mathbb{P}^{k+1}(T)$ of the bulk pressure p such that

$$\int_T \boldsymbol{K}_T \nabla(\breve{p}_T - p) \cdot \nabla w = 0 \text{ for all } w \in \mathbb{P}^{k+1}(T) \text{ and } \int_T (\breve{p}_T - p) = 0. \tag{2.58}$$

Adapting the results of [83, Lemma 3], it can be proved that the following approximation properties hold for all $T \in \mathcal{T}_h$ provided that $p_{|T} \in H^{k+2}(T)$:

$$\begin{aligned} &\|\boldsymbol{K}_T^{1/2}\nabla(p - \breve{p}_T)\|_T + h_T^{1/2}\|\boldsymbol{K}_T^{1/2}\nabla(p_{|T} - \breve{p}_T)\|_{\partial T} \\ &+ \underline{K}_{\mathrm{B},T}^{1/2} h_T^{-1}\|p - \breve{p}_T\|_T + \underline{K}_{\mathrm{B},T}^{1/2} h_T^{-1/2}\|p_{|T} - \breve{p}_T\|_{\partial T} \lesssim \overline{K}_{\mathrm{B},T}^{1/2} h_T^{k+1}\|p\|_{H^{k+2}(T)}. \end{aligned} \tag{2.59}$$

Note that we need to specify that the trace of p and of the corresponding flux are taken from the side of T in boundary norms, since these quantities are possibly two-valued on fracture faces. We also introduce the broken polynomial function $\breve{p}_h$ such that

$$(\breve{p}_h)_{|T} = \breve{p}_T \qquad \forall T \in \mathcal{T}_h.$$

The following boundedness result for the bilinear form b_h defined by (2.27) can be proved using (2.18): For all $\underline{\boldsymbol{v}}_h \in \underline{\breve{\boldsymbol{U}}}_h^k$ and all $q_h \in P_{\mathrm{B},h}^k$,

$$\begin{aligned} |b_h(\underline{\boldsymbol{v}}_h, q_h)| &\lesssim \left(\sum_{T\in\mathcal{T}_h} \|\underline{\boldsymbol{v}}_T\|_{U,T}^2\right)^{1/2} \times \left(\sum_{T\in\mathcal{T}_h} \overline{K}_{\mathrm{B},T} h_T^{-2}\|q_T\|_T^2\right)^{1/2} \\ &\lesssim \|\underline{\boldsymbol{v}}_h\|_{m,h}\left(\sum_{T\in\mathcal{T}_h} \overline{K}_{\mathrm{B},T} h_T^{-2}\|q_T\|_T^2\right)^{1/2}, \end{aligned} \tag{2.60}$$

where, to obtain the second inequality, we have used the first bound in (2.21) and summed over $T \in \mathcal{T}_h$ to infer

$$\sum_{T\in\mathcal{T}_h} \|\underline{\boldsymbol{v}}_T\|_{U,T}^2 \lesssim \|\underline{\boldsymbol{v}}_h\|_{m,h}^2 \coloneqq \sum_{T\in\mathcal{T}_h} \|\underline{\boldsymbol{v}}_T\|_{m,T}^2.$$

Finally, we note the following consistency property for the bilinear form d_h defined by (2.29), which can be inferred from [83, Theorem 8]: For all $q \in H^1_0(\Gamma)$ such that $q \in H^{k+2}(F)$ for all $F \in \mathcal{F}_h^\Gamma$,

$$\sup_{\underline{r}_h^\Gamma \in \underline{P}^k_{\Gamma,h,0}, \|\underline{r}_h^\Gamma\|_{\Gamma,h}=1} \left(\sum_{F\in\mathcal{F}_h^\Gamma} \int_F \nabla_\tau\cdot(K_F\nabla_\tau q) r_F^\Gamma + d_h(\underline{I}_h^k q, \underline{r}_h^\Gamma) \right) \lesssim \left(\sum_{F\in\mathcal{F}_h^\Gamma} K_F h_F^{2(k+1)} \|q\|^2_{H^{k+2}(F)} \right)^{1/2}. \tag{2.61}$$

We are now ready to prove the error estimate.

Proof of Theorem 2.12. The proof proceeds in five steps: in **Step 1** we derive an estimate for the discretization error measured by the left-hand side of (2.37) in terms of a conformity error; in **Step 2** we bound the different components of the conformity error; in **Step 3** we combine the previous results to obtain (2.37). **Steps 4-5** contain the proofs of technical results used in **Step 2**.

Remark 2.16 (Role of **Step 1**). The discretization error in the left-hand side of (2.37) can be clearly estimated in terms of a conformity error using the inf-sup condition on $\mathcal{A}_h^\xi$ proved in Theorem 2.11. Proceeding this way, however, we would end up with constants depending on the problem data (and, in particular, on the global bulk anisotropy ratio ϱ_B defined by (2.2)) in the right-hand side of (2.37). This is to be avoided if one wants to have a sharp indication of the behaviour of the method for strongly anisotropic bulk permeability tensors.

In what follows, we use the shortcut notation for the error components introduced in (2.39).

Step 1: Basic error estimate Recalling the definitions (2.31) of $\mathcal{A}_h^\xi$ and (2.40) of the norm $\|\cdot\|_{a,\xi,h}$, and using the coercivity of d_h expressed by the first inequality in (2.41), we have that

$$\begin{aligned} \|\underline{\boldsymbol{e}}_h\|^2_{a,\xi,h} + \|\underline{\epsilon}_h^\Gamma\|^2_{\Gamma,h} &\lesssim \mathcal{A}_h^\xi((\underline{\boldsymbol{e}}_h, \epsilon_h, \underline{\epsilon}_h^\Gamma), (\underline{\boldsymbol{e}}_h, \epsilon_h, \underline{\epsilon}_h^\Gamma)) \\ &= \mathcal{E}_{h,1}(\underline{\boldsymbol{e}}_h) + \mathcal{E}_{h,2}(\epsilon_h) + \mathcal{E}_{h,3}(\underline{\epsilon}_h^\Gamma), \end{aligned} \tag{2.62}$$

where the linear forms $\mathcal{E}_{h,1} : \underline{\boldsymbol{U}}_{h,0}^k \to \mathbb{R}$, $\mathcal{E}_{h,2} : P_{\mathrm{B},h}^k \to \mathbb{R}$, and $\mathcal{E}_{h,3} : \underline{P}_{\Gamma,h,0}^k \to \mathbb{R}$ correspond to the components of the conformity error and are defined such that

$$\mathcal{E}_{h,1}(\underline{\boldsymbol{v}}_h) \coloneqq -a_h^\xi(\widehat{\underline{\boldsymbol{u}}}_h, \underline{\boldsymbol{v}}_h) + b_h(\underline{\boldsymbol{v}}_h, \widehat{p}_h) - c_h(\underline{\boldsymbol{v}}_h, \widehat{\underline{p}}_h^\Gamma), \tag{2.63a}$$

$$\mathcal{E}_{h,2}(q_h) \coloneqq \sum_{T\in\mathcal{T}_h} \int_T f q_T - b_h(\widehat{\underline{\boldsymbol{u}}}_h, q_h), \tag{2.63b}$$

$$\mathcal{E}_{h,3}(\underline{q}_h^\Gamma) \coloneqq \sum_{F\in\mathcal{F}_h^\Gamma} \int_F \ell_F f_\Gamma q_F^\Gamma + c_h(\widehat{\underline{\boldsymbol{u}}}_h, \underline{q}_h^\Gamma) - d_h(\widehat{\underline{p}}_h^\Gamma, \underline{q}_h^\Gamma). \tag{2.63c}$$

We next estimate the error ϵ_h on the bulk pressure. The inf-sup condition (2.42) yields the existence of $\underline{\boldsymbol{v}}_h \in \underline{\boldsymbol{U}}_{h,0}^k$ such that

$$\|\epsilon_h\|_{\mathrm{B},h}^2 = -b_h(\underline{\boldsymbol{v}}_h, \epsilon_h) \text{ and } \|\underline{\boldsymbol{v}}_h\|_{\boldsymbol{U},\xi,h} \le \beta\|\epsilon_h\|_{\mathrm{B},h}. \tag{2.64}$$

Hence,

$$\begin{aligned}\|\epsilon_h\|_{\mathrm{B},h}^2 &= b_h(\underline{\boldsymbol{v}}_h, p_h) - b_h(\underline{\boldsymbol{v}}_h, \widehat{p}_h)\\ &= a_h^\xi(\underline{\boldsymbol{u}}_h, \underline{\boldsymbol{v}}_h) + c_h(\underline{\boldsymbol{v}}_h, \underline{p}_h^\Gamma) - b_h(\underline{\boldsymbol{v}}_h, \widehat{p}_h)\\ &= a_h^\xi(\underline{\boldsymbol{e}}_h, \underline{\boldsymbol{v}}_h) + c_h(\underline{\boldsymbol{v}}_h, \underline{\epsilon}_h^\Gamma) - \mathcal{E}_{h,1}(\underline{\boldsymbol{v}}_h),\end{aligned}$$

where we have used the linearity of b_h in its second argument in the first line, (2.30a) in the second line (recall that $g_\mathrm{B} \equiv 0$ owing to (2.33)), and we have inserted $\pm\big(a_h^\xi(\widehat{\underline{\boldsymbol{u}}}_h, \underline{\boldsymbol{v}}_h) + c_h(\underline{\boldsymbol{v}}_h, \widehat{\underline{p}}_h^\Gamma)\big)$ to conclude. Using the Cauchy–Schwarz inequality together with (2.40) for the first term, the boundedness (2.50) of the second, and the linearity of $\mathcal{E}_{h,1}$ together with the second bound in (2.40) for the third, we get

$$\|\epsilon_h\|_{\mathrm{B},h}^2 \lesssim \Big(\varrho_\mathrm{B}^{1/2}\|\underline{\boldsymbol{e}}_h\|_{a,\xi,h} + \underline{\lambda}_\Gamma^{-1/2}\|\underline{\epsilon}_h^\Gamma\|_{\Gamma,h} + \varrho_\mathrm{B}^{1/2}\mathcal{E}_{h,1}(\underline{\boldsymbol{v}}_h/\|\underline{\boldsymbol{v}}_h\|_{a,\xi,h})\Big)\,\|\underline{\boldsymbol{v}}_h\|_{\boldsymbol{U},\xi,h}.$$

Using the inequality in (2.64) to bound the second factor, and naming χ the hidden constant, we arrive at

$$\chi\|\epsilon_h\|_{\mathrm{B},h} \le \|\underline{\boldsymbol{e}}_h\|_{a,\xi,h} + \|\underline{\epsilon}_h^\Gamma\|_{\Gamma,h} + \mathcal{E}_{h,1}(\underline{\boldsymbol{v}}_h/\|\underline{\boldsymbol{v}}_h\|_{\boldsymbol{U},\xi,h}). \tag{2.65}$$

Step 2: Bound of the conformity error components We proceed to bound the conformity error components for a generic $(\underline{\boldsymbol{v}}_h, q_h, \underline{q}_h^\Gamma) \in \underline{\boldsymbol{X}}_h$.

To bound $\mathcal{E}_{h,1}$, we use the following reformulations of the first and second

contribution, whose proofs are given in **Steps 4-5** below:

$$\begin{aligned} a_h^\xi(\widehat{\underline{\boldsymbol{u}}}_h, \underline{\boldsymbol{v}}_h) = &\sum_{F\in\mathcal{F}_h^\Gamma}\int_F \left(\lambda_F^\xi [\![\boldsymbol{u}]\!]_\Gamma\cdot\boldsymbol{n}_\Gamma[\![\underline{\boldsymbol{v}}_h]\!]_F + \lambda_F\{\{\boldsymbol{u}\}\}_\Gamma\cdot\boldsymbol{n}_\Gamma\{\{\underline{\boldsymbol{v}}_h\}\}_F\right)\\ &+\sum_{T\in\mathcal{T}_h}\sum_{F\in\mathcal{F}_T}\int_F \boldsymbol{K}_T\nabla(\breve{p}_T - p_{|T})\cdot\boldsymbol{n}_{TF}(\pi_F^k w_T - \pi_T^k w_T)\\ &-\sum_{T\in\mathcal{T}_h}\int_T \nabla p\cdot\boldsymbol{F}_T^{k+1}\underline{\boldsymbol{v}}_T - \sum_{T\in\mathcal{T}_h} J_T(\widehat{\underline{\boldsymbol{u}}}_T, \underline{\boldsymbol{v}}_T), \end{aligned} \tag{2.66}$$

where, for all $T\in\mathcal{T}_h$, $w_T\in\mathbb{P}^{k+1}(T)$ is such that $\boldsymbol{F}_T^{k+1}\underline{\boldsymbol{v}}_T = \boldsymbol{K}_T\nabla w_T$ and

$$\begin{aligned} b_h(\underline{\boldsymbol{v}}_h, \widehat{p}_h) = &\, b_h(\underline{\boldsymbol{v}}_h, \pi_h^k(p-\breve{p}_h)) + \sum_{T\in\mathcal{T}_h}\sum_{F\in\mathcal{F}_T}\int_F(\breve{p}_T - p_{|T})v_{TF} + c_h(\underline{\boldsymbol{v}}_h, \widehat{p}_h^\Gamma)\\ &+\sum_{F\in\mathcal{F}_h^\Gamma}\int_F\left(\lambda_F^\xi[\![\boldsymbol{u}]\!]_\Gamma\cdot\boldsymbol{n}_\Gamma[\![\underline{\boldsymbol{v}}_h]\!]_F + \lambda_F\{\{\boldsymbol{u}\}\}_\Gamma\cdot\boldsymbol{n}_\Gamma\{\{\underline{\boldsymbol{v}}_h\}\}_F\right)\\ &-\sum_{T\in\mathcal{T}_h}\int_T\nabla p\cdot\boldsymbol{F}_T^{k+1}\underline{\boldsymbol{v}}_T. \end{aligned} \tag{2.67}$$

Using (2.66) and (2.67) in (2.63a), we infer that

$$\begin{aligned} \mathcal{E}_{h,1}(\underline{\boldsymbol{v}}_h) = &\, b_h(\underline{\boldsymbol{v}}_h, \pi_h^k(p-\breve{p}_h)) + \sum_{T\in\mathcal{T}_h}\sum_{F\in\mathcal{F}_T}\int_F(\breve{p}_T - p_{|T})v_{TF}\\ &-\sum_{T\in\mathcal{T}_h}\sum_{F\in\mathcal{F}_T}\int_F\boldsymbol{K}_T\nabla(\breve{p}_T - p_{|T})\cdot\boldsymbol{n}_{TF}(\pi_F^k w_T - \pi_T^k w_T) + \sum_{T\in\mathcal{T}_h} J_T(\widehat{\underline{\boldsymbol{u}}}_T, \underline{\boldsymbol{v}}_T). \end{aligned}$$

Using the boundedness (2.60) of b_h together with the third bound in (2.59) to estimate the first term, Cauchy–Schwarz inequalities together with the fourth bound in (2.59) and the first bound in (2.21) to estimate the second term, Cauchy–Schwarz inequalities together with the fact that $h_T^{-1/2}\|\pi_F^k w_T - \pi_T^k w_T\|_F \lesssim h_T^{-1}\|w_T - \pi_T^k w_T\|_T \lesssim \underline{K}_{\mathrm{B},T}^{-1/2}\|\boldsymbol{F}_T^{k+1}\underline{\boldsymbol{v}}_T\|_T$ (a consequence of the $L^2(F)$-boundedness of π_F^k and (2.10b) with $l = k+1$, $m = 0$, and $s = 1$) to estimate the third term, and (2.22) to estimate the fourth term, we infer that

$$|\mathcal{E}_{h,1}(\underline{\boldsymbol{v}}_h)| \lesssim \left(\sum_{T\in\mathcal{T}_h}\varrho_{\mathrm{B},T}\overline{K}_{\mathrm{B},T}h_T^{2(k+1)}\|p\|_{H^{k+2}(T)}^2\right)^{1/2}\|\underline{\boldsymbol{v}}_h\|_{m,h}. \tag{2.68}$$

For the second error component, using (2.1b), the definition (2.27) of the bilinear form b_h, and the commuting property (2.17) of the local divergence

reconstruction, we get

$$\mathcal{E}_{h,2}(\underline{\boldsymbol{v}}_h) = \sum_{T\in\mathcal{T}_h}\int_T(\nabla\cdot\boldsymbol{u} - \pi_T^k(\nabla\cdot\boldsymbol{u}))q_T = 0, \tag{2.69}$$

where we have used the fact that $q_T \in \mathbb{P}^k(T)$ and the definition (2.9) of π_T^k to conclude.

We next observe that, for all $F \in \mathcal{F}_T^\Gamma$ such that $F \subset \partial T_1 \cap \partial T_2$ for distinct mesh elements $T_1, T_2 \in \mathcal{T}_h$,

$$[\![\widehat{\underline{\boldsymbol{u}}}_h]\!]_F = \pi_F^k\left(\boldsymbol{u}_{|T_1}\cdot\boldsymbol{n}_{T_1F} + \boldsymbol{u}_{|T_2}\cdot\boldsymbol{n}_{T_2F}\right) = \pi_F^k\left([\![\boldsymbol{u}]\!]\cdot\boldsymbol{n}_\Gamma\right), \tag{2.70a}$$

$$\{\{\widehat{\underline{\boldsymbol{u}}}_h\}\}_F = \frac{1}{2}\pi_F^k\left(\boldsymbol{u}_{|T_1}\cdot\boldsymbol{n}_\Gamma + \boldsymbol{u}_{|T_2}\cdot\boldsymbol{n}_\Gamma\right) = \pi_F^k\left(\{\{\boldsymbol{u}\}\}\cdot\boldsymbol{n}_\Gamma\right). \tag{2.70b}$$

For the third error component, we can then write

$$\begin{aligned}\mathcal{E}_{h,3}(q_h) &= \sum_{F\in\mathcal{F}_h^\Gamma}\int_F(\ell_F f_\Gamma + [\![\widehat{\underline{\boldsymbol{u}}}_h]\!]_F)q_F^\Gamma - d_h(\widehat{\underline{p}}_h^\Gamma, \underline{q}_h^\Gamma)\\ &= \sum_{F\in\mathcal{F}_h^\Gamma}\int_F(\ell_F f_\Gamma + [\![\boldsymbol{u}]\!]_\Gamma\cdot\boldsymbol{n}_\Gamma)q_F^\Gamma - d_h(\widehat{\underline{p}}_h^\Gamma, \underline{q}_h^\Gamma)\\ &= -\sum_{F\in\mathcal{F}_h^\Gamma}\int_F\nabla_\tau\cdot(K_F\nabla_\tau p_\Gamma)q_F^\Gamma - d_h(\widehat{\underline{p}}_h^\Gamma, \underline{q}_h^\Gamma),\end{aligned}$$

where we have expanded the bilinear form c_h according to its definition (2.28) in the first line, we have used (2.70a) followed by (2.9) and the fact that $q_F^\Gamma \in \mathbb{P}^k(F)$ to remove π_F^k in the second line, and we have concluded invoking (2.3a). The consistency property (2.61) then gives

$$|\mathcal{E}_{h,3}(q_h)| \lesssim \left(\sum_{F\in\mathcal{F}_h^\Gamma}K_F h_F^{2(k+1)}\|p_\Gamma\|^2_{H^{k+2}(F)}\right)\|\underline{q}_h^\Gamma\|_{\Gamma,h}. \tag{2.71}$$

Step 3: Conclusion Using (2.68), (2.69), and (2.71) with $(\underline{\boldsymbol{v}}_h, q_h, \underline{q}_h^\Gamma) = (\underline{\boldsymbol{e}}_h, \epsilon_h, \underline{\epsilon}_h^\Gamma)$ to estimate the right-hand side of (2.62), and recalling that $\|\underline{\boldsymbol{e}}_h\|_{m,h} \le \|\underline{\boldsymbol{e}}_h\|_{a,\xi,h}$, we infer that

$$\begin{aligned}\|\underline{\boldsymbol{e}}_h\|_{a,\xi,h} + \|\underline{\epsilon}_h^\Gamma\|_{\Gamma,h} \lesssim \Bigg(&\sum_{T\in\mathcal{T}_h}\varrho_{\mathrm{B},T}\overline{K}_{\mathrm{B},T}h_T^{2(k+1)}\|p\|^2_{H^{k+2}(T)}\\ &+\sum_{F\in\mathcal{F}_h^\Gamma}K_F h_F^{2(k+1)}\|p_\Gamma\|^2_{H^{k+2}(F)}\Bigg)^{1/2},\end{aligned} \tag{2.72}$$

which, in view of the first inequality in (2.40), gives the bounds on the first and second term in the left-hand side of (2.37). Plugging (2.72) and (2.68) into (2.65), and recalling that $\|\underline{\boldsymbol{v}}_h\|_{m,h} \le \|\underline{\boldsymbol{v}}_h\|_{a,\xi,h}$ gives the estimate for the third term in the left-hand side of (2.37).

Step 4: Proof of (2.66) For every mesh element $T \in \mathcal{T}_h$, we have that

$$\begin{aligned}
\int_T \boldsymbol{K}_T^{-1}\boldsymbol{F}_T^{k+1}\widehat{\underline{\boldsymbol{u}}}_T\cdot\boldsymbol{F}_T^{k+1}\underline{\boldsymbol{v}}_T &= \int_T \boldsymbol{F}_T^{k+1}\widehat{\underline{\boldsymbol{u}}}_T\cdot\nabla w_T\\
&= -\int_T D_T^k\widehat{\underline{\boldsymbol{u}}}_T w_T + \sum_{f\in\mathcal{F}_T}\int_F \widehat{u}_{TF}w_T\\
&= -\int_T \pi_T^k(\nabla\cdot\boldsymbol{u})w_T + \sum_{f\in\mathcal{F}_T}\int_F \pi_F^k(\boldsymbol{u}\cdot\boldsymbol{n}_{TF})w_T\\
&= -\int_T \nabla\cdot\boldsymbol{u}\pi_T^k w_T + \sum_{f\in\mathcal{F}_T}\int_F \boldsymbol{u}\cdot\boldsymbol{n}_{TF}\pi_F^k w_T\\
&= \int_T \boldsymbol{u}\cdot\nabla\pi_T^k w_T + \sum_{f\in\mathcal{F}_T}\int_F \boldsymbol{u}\cdot\boldsymbol{n}_{TF}(\pi_F^k w_T - \pi_T^k w_T),
\end{aligned} \tag{2.73}$$

where we have used the fact that $\boldsymbol{F}_T^{k+1}\underline{\boldsymbol{v}}_T = \boldsymbol{K}_T\nabla w_T$ in the first line, the definition (2.19) of $\boldsymbol{F}_T^{k+1}\widehat{\underline{\boldsymbol{u}}}_T$ in the second line, the commuting property (2.17) together with the definition (2.25) of $\underline{\boldsymbol{I}}_h^k$ in the third line, the definition (2.9) of the L^2-orthogonal projectors π_T^k and π_F^k to pass to the fourth line, and an integration by parts to conclude.

On the other hand, recalling again that $\boldsymbol{F}_T^{k+1}\underline{\boldsymbol{v}}_T = \boldsymbol{K}_T\nabla w_T$ and using the definition (2.58) of the local elliptic projection, we have that

$$\begin{aligned}
\int_T \nabla p\cdot\boldsymbol{F}_T^{k+1}\underline{\boldsymbol{v}}_T &= \int_T \boldsymbol{K}_T\nabla p\cdot\nabla w_T = \int_T \boldsymbol{K}_T\nabla\breve{p}_T\cdot\nabla w_T\\
&= -\int_T \nabla\cdot(\boldsymbol{K}_T\nabla\breve{p}_T)w_T + \sum_{F\in\mathcal{F}_T}\int_F \boldsymbol{K}_T\nabla\breve{p}_T\cdot\boldsymbol{n}_{TF}w_T\\
&= -\int_T \nabla\cdot(\boldsymbol{K}_T\nabla\breve{p}_T)\pi_T^k w_T + \sum_{F\in\mathcal{F}_T}\int_F \boldsymbol{K}_T\nabla\breve{p}_T\cdot\boldsymbol{n}_{TF}\pi_F^k w_T\\
&= \int_T \boldsymbol{K}_T\nabla p\cdot\nabla\pi_T^k w_T + \sum_{F\in\mathcal{F}_T}\int_F \boldsymbol{K}_T\nabla\breve{p}_T\cdot\boldsymbol{n}_{TF}(\pi_F^k w_T - \pi_T^k w_T),
\end{aligned} \tag{2.74}$$

where we have used an integration by parts to pass to the second line, the definition (2.9) of the L^2-orthogonal projectors π_T^k and π_F^k together with the fact that $\nabla\cdot(\boldsymbol{K}_T\nabla\breve{p}_T) \in \mathbb{P}^{k-1}(T) \subset \mathbb{P}^k(T)$ and $(\boldsymbol{K}_T\nabla\breve{p}_T)_{|F}\cdot\boldsymbol{n}_{TF} \in \mathbb{P}^k(F)$ for all $F \in \mathcal{F}_T$ (since

$w_T \in \mathbb{P}^{k+1}(T)$ and $\boldsymbol{K}_T \in \mathbb{P}^0(T)^{2\times 2}$) in the second line, and again an integration by parts together with the definition (2.58) to replace $\breve{p}_T$ by p in the first term and conclude.

Summing (2.73) and (2.74), using (2.1a) to replace $\boldsymbol{u}$ by $-\boldsymbol{K}\nabla p$, and rearranging the terms, we finally obtain

$$\int_T \boldsymbol{K}_T^{-1}\boldsymbol{F}_T^{k+1}\widehat{\underline{\boldsymbol{u}}}_T\cdot\boldsymbol{F}_T^{k+1}\underline{\boldsymbol{v}}_T = -\int_T \nabla p\cdot\boldsymbol{F}_T^{k+1}\underline{\boldsymbol{v}}_T + \sum_{F\in\mathcal{F}_T}\int_F \boldsymbol{K}_T\nabla(\breve{p}_T-p)\cdot\boldsymbol{n}_{TF}(\pi_F^k w_T-\pi_T^k w_T). \tag{2.75}$$

Using (2.75) for the consistency term in $m_T(\widehat{\underline{\boldsymbol{u}}}_T,\underline{\boldsymbol{v}}_T)$ (see (2.20)), plugging the resulting relation into the expression of $a_h^\xi(\widehat{\underline{\boldsymbol{u}}}_h,\underline{\boldsymbol{v}}_h)$ (see (2.26)), and accounting for (2.70) in the fracture terms of $a_h^\xi(\widehat{\underline{\boldsymbol{u}}}_h,\underline{\boldsymbol{v}}_h)$ (where π_F^k can be cancelled using (2.9) after observing that $\lambda_F^\xi[\![\underline{\boldsymbol{v}}_h]\!]_F\in\mathbb{P}^k(F)$ and $\lambda_F[\![\underline{\boldsymbol{v}}_h]\!]_F\in\mathbb{P}^k(F)$ for all $F\in\mathcal{F}_h^\Gamma$) gives (2.66).

Step 5: Proof of (2.67) We have that

$$\begin{aligned}
b_h(\underline{\boldsymbol{v}}_h,\widehat{p}_h) &= b_h(\underline{\boldsymbol{v}}_h,\pi_h^k(p-\breve{p}_h)) + b_h(\underline{\boldsymbol{v}}_h,\pi_h^k\breve{p}_h)\\
&= b_h(\underline{\boldsymbol{v}}_h,\pi_h^k(p-\breve{p}_h)) + \sum_{T\in\mathcal{T}_h}\int_T \breve{p}_T D_T^k\underline{\boldsymbol{v}}_T\\
&= b_h(\underline{\boldsymbol{v}}_h,\pi_h^k(p-\breve{p}_h)) + \sum_{T\in\mathcal{T}_h}\left(\sum_{F\in\mathcal{F}_T}\int_F \breve{p}_T v_{TF} - \int_T\nabla\breve{p}_T\cdot\boldsymbol{F}_T^{k+1}\underline{\boldsymbol{v}}_T\right)\\
&= b_h(\underline{\boldsymbol{v}}_h,\pi_h^k(p-\breve{p}_h)) + \sum_{T\in\mathcal{T}_h}\sum_{F\in\mathcal{F}_T}\int_F(\breve{p}_T-p_{|T})v_{TF} - \sum_{T\in\mathcal{T}_h}\int_T\nabla p\cdot\boldsymbol{F}_T^{k+1}\underline{\boldsymbol{v}}_T\\
&\quad + \sum_{T\in\mathcal{T}_h}\sum_{F\in\mathcal{F}_T}\int_F p_{|T}v_{TF},
\end{aligned} \tag{2.76}$$

where we have inserted $\pm\pi_h^k\breve{p}_h$ into the second argument of b_h and used its linearity in the first line, expanded the second term according to its definition (2.27) and cancelled the projector since $D_T^k\underline{\boldsymbol{v}}_T\in\mathbb{P}^k(T)$ for all $T\in\mathcal{T}_h$ in the second line, used the definition (2.19) of $\boldsymbol{F}_T^{k+1}\underline{\boldsymbol{v}}_T$ (with $w_T=\breve{p}_T$) in the third line, and we have inserted $\pm\sum_{T\in\mathcal{T}_h}\sum_{F\in\mathcal{F}_T}\int_F p_{|T}v_{TF}$ to pass to the fourth line, where (2.58) was also used to write p instead of $\breve{p}_T$ in the third term.

Let us consider the last term in (2.76). Rearranging the sums and using the

fact that $p = 0$ on every boundary face $F \in \mathcal{F}_h^{\mathrm{b}}$ owing to (2.33), it is inferred that

$$\sum_{T\in\mathcal{T}_h}\sum_{F\in\mathcal{F}_T}\int_F p_{|T}v_{TF} = \sum_{F\in\mathcal{F}_h}\sum_{T\in\mathcal{T}_F}\int_F p_{|T}v_{TF} = \sum_{\substack{F\in\mathcal{F}_h^{\mathrm{i}}\\ F\subset\partial T_1\cap\partial T_2}}\int_F \left(p_{|T_1}v_{T_1F} + p_{|T_2}v_{T_2F}\right).$$

If $F \in \mathcal{F}_h^{\mathrm{i}}\backslash\mathcal{F}_h^{\Gamma}$, the integrand vanishes since $v_{T_1F}+v_{T_2F} = 0$ (see the definition (2.24) of $\underline{\boldsymbol{U}}_{h,0}^k$) and $p_{|T_1} - p_{|T_2} = 0$ since the jumps of the bulk pressure vanish across interfaces in the bulk region. If, on the other hand, $F \in \mathcal{F}_h^{\Gamma}$, assuming without loss of generality that $T_i \subset \Omega_{\mathrm{B},i}$ for $i \in \{1,2\}$, it can be checked that $p_{|T_1}v_{T_1F}+p_{|T_2}v_{T_2F} = [\![p]\!]_\Gamma\{\{\underline{\boldsymbol{v}}_h\}\}_F + \{\{p\}\}_\Gamma[\![\underline{\boldsymbol{v}}_h]\!]_F$. In conclusion, we have that

$$\int_F \left(p_{|T_1}v_{T_1F} + p_{|T_2}v_{T_2F}\right) = \begin{cases} 0 & \text{if } F \in \mathcal{F}_h^{\mathrm{i}}\setminus\mathcal{F}_h^{\Gamma},\\ \int_F \left([\![p]\!]_\Gamma\{\{\underline{\boldsymbol{v}}_h\}\}_F + \{\{p\}\}_\Gamma[\![\underline{\boldsymbol{v}}_h]\!]_F\right) & \text{if } F \in \mathcal{F}_h^{\Gamma}. \end{cases} \tag{2.77}$$

Plugging (2.77) into (2.76), and using (2.4) to replace $[\![p]\!]_\Gamma$ and $\{\{p\}\}_\Gamma$, (2.67) follows. □

Chapter 3

Passive transport in fractured porous media

This chapter has been submitted in the following peer-reviewed journal (see [57]):

International Journal on Geomathematics, 2018.

Contents

3.1 Introduction

Over the last decades, the research on fluid flows in fractured porous media has received a great amount of attention because of its relevance in many areas of the geosciences, ranging from ground-water hydrology to hydrocarbon exploitation. Fractures in the subsurface are indeed ubiquitous, and can be caused by tectonic forces, changes of temperature, drying processes, by leaching in the plane of stratification, or by schistosity. Depending on the material that has accumulated within the fractures, they may act as conduits or barriers, and thus affect the flow patterns in a substantial way. For instance, it has been observed that fractures near boreholes tend to increase the productivity of wells during oil recovery. In the context of geological isolation of radioactive waste, the presence of fractures in the disposal areas due to, for example, tunnel excavation, can drastically accelerate the migration process of radionuclides.

A common feature of fractures in porous media is the variety of length scales. While the presence of smaller fractures may be accounted for by using

homogenization or other upscaling techniques, fractures with larger extension have to be modelled explicitly, and there are several possible ways to incorporate their presence. Our focus is here on the approach developed in [120], where a reduced model for the flow in the fracture is obtained by an averaging process, and the fracture is treated as an interface inside the bulk region. The fracture is assumed to be filled of debris, so that the flow therein can still be modelled by Darcy's law. The problem is closed by interface conditions that relate the average and jump of the bulk pressure to the normal flux and pressure in the fracture. In [56] we have designed and analysed a Hybrid High-Order (HHO) method to discretize this model, and proved stability and order $O(h^{k+1})$ convergence of the discretization error measured in an energy-like norm, with h denoting the meshsize and $k \geq 0$ the polynomial degree. Several other discretization schemes have been proposed for this type of models; see, e.g., [12, 16, 24, 26, 33, 45, 71, 102, 122] and references therein. Other works where fractures are treated as interfaces include [13, 20, 97].

The literature on passive transport in fractured porous media and related problems is, however, more scarce. In [109], the authors study a system of advection-diffusion equations where the jump of the diffusive bulk flux acts as a source term inside the fracture. In the coupling conditions, only the diffusive part of the total bulk flux is considered. The discretization is based on the Unfitted Finite Element method, for which well-posedness and $O(h^k)$ convergence in the energy-norm are proved. In [62], a Finite Volume method is combined to a Trace Finite Element method to solve a transport problem in the bulk region and inside the fracture, with the jump of the total bulk flux acting as a source term in the surface problem and under the assumption that the concentration is continuous at the interface. Convergence in $O(h)$ is numerically observed for the energy-norm of the discretization error. A similar problem is studied in [10]. In [103], the authors use an averaging technique similar to [120] in order to derive coupling conditions for a transport problem which allow the concentration to jump across the fracture. This enables them to model high concentration gradients near the fracture resulting from highly heterogeneous diffusivity. The problem is discretized by eXtended Finite Elements (XFEM), and numerical evidence is provided. Another approach can be to consider Discrete Fracture Networks (DFNs) models, where the bulk surrounding fractures is considered as impervious so that the flow can only occur through the fracture planes and across their intersections; see, e.g., [27], where authors propose a system of unsteady advection-diffusion in DFNs.

In this work, we consider the passive transport of a solute driven by a velocity field solution of a (decoupled) Darcy problem. We present two novel contributions:

(i) first, we propose new coupling conditions between the bulk region and fracture inspired by energy-based arguments, following the general ideas developed by [100] in a different context. Crucially, these transmission

conditions allow the solute concentration to jump across the fracture;

(ii) second, we propose a novel HHO discretization of this new model where the Darcy velocity field results from an HHO approximation of the flow problem in the spirit of [56]. The discretization is designed to incorporate the new transmission conditions and to reproduce at the discrete level the energy argument from which they originate.

The main source of inspiration for the discretization of the advection terms in the bulk region and inside the fracture is [75], where the authors develop an HHO method that is robust across the entire range of Péclet numbers and supports locally degenerate diffusion. Concerning the coupling of the flow and transport problems, we take inspiration from [11], where an HHO discretization of miscible displacements in non-fractured porous media described by the Peaceman model is considered. Therein, in order to obtain a well-posed discrete problem, the flow problem has to be solved using polynomials of degree twice as high as the transport problem. In our work, we find that a similar condition is required to prove the coercivity of the transport bilinear form; see Remark 3.10 for further details. A thorough numerical investigation is carried out to demonstrate the order of convergence of the method and showcase its performance on physical test cases.

The material is organized as follows. In Section 3.2 we describe the equations that govern the model along with their weak formulation. In Section 3.3 we discuss the discrete setting and, in Section 3.4, we formulate the HHO approximation. Section 3.5 is devoted to the numerical tests, including a numerical study of the convergence properties of the method.

3.2 The differential model

In this section we introduce the strong and weak formulations of the flow and passive transport problems. For the sake of simplicity, the presentation focuses on the two-dimensional case with a single fracture. The extension to the three-dimensional case and to fracture networks is possible (and, actually, quite straightforward), but requires heavier notations which we want to avoid here.

3.2.1 Notation

We consider a porous medium saturated by an incompressible fluid that occupies a space region $\Omega \subset \mathbb{R}^2$ traversed by a fracture Γ. We assume that Ω is an open, bounded, connected, polygonal set with Lipschitz boundary $\partial\Omega$. The fracture Γ is represented by an open line segment of nonzero length which cuts Ω into two disjoint connected polygonal subdomains $\Omega_{B,1}$ and $\Omega_{B,2}$ with Lipschitz boundary.

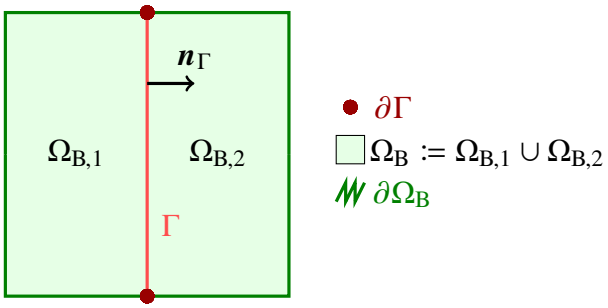

Figure 3.1: Illustration of the notation introduced in Section 3.2.1.

The set $\Omega_B := \Omega \setminus \overline{\Gamma} = \Omega_{B,1} \cup \Omega_{B,2}$ corresponds to the bulk region. We denote by $\partial\Omega_B := \bigcup_{i=1}^{2}(\partial\Omega_{B,i} \setminus \overline{\Gamma})$ the external boundary of the bulk region and by $\boldsymbol{n}_{\partial\Omega}$ the unit normal vector on $\partial\Omega_B$ pointing out of Ω_B. For $i \in \{1,2\}$, we let $\partial\Omega_{B,i} := \partial\Omega_B \cap \overline{\Omega_{B,i}}$ denote the external boundary of the subdomain $\Omega_{B,i}$. The boundary of the fracture Γ is denoted by $\partial\Gamma$, and the corresponding outward unit tangential vector is $\boldsymbol{\tau}_{\partial\Gamma}$. Finally, $\boldsymbol{n}_\Gamma$ denotes the unit normal vector to Γ pointing out of $\Omega_{B,1}$. This notation is illustrated in Figure 3.1.

For any function φ sufficiently regular to admit a (possibly two-valued) trace on Γ, we define the jump and average operators such that

$$[\![\varphi]\!]_\Gamma := \varphi_1 - \varphi_2, \qquad \{\{\varphi\}\}_\Gamma := \frac{\varphi_1 + \varphi_2}{2},$$

where $\varphi_i := \varphi_{|\Omega_{B,i}}$ denotes the restriction of φ to the subdomain $\Omega_{B,i} \subset \Omega_B$. When applied to vector-valued functions, these operators act component-wise.

Finally, for any $X \subset \overline{\Omega}$, we denote by $(\cdot,\cdot)_X$ and $\|\cdot\|_X$ the usual inner product and norm of $L^2(X)$ or $L^2(X)^2$, according to the context.

3.2.2 Darcy flow

We now formulate the equations that govern the flow in the saturated, fractured porous medium and discuss a weak formulation inspired by [17, 72].

3.2.2.1 Governing equations

In the bulk region Ω_B and in the fracture Γ, we model the fluid flow by Darcy's law in mixed and primal form, respectively, so that the bulk Darcy velocity $\boldsymbol{u} : \Omega_B \to \mathbb{R}^2$, the bulk pressure pressure $p : \Omega_B \to \mathbb{R}$, and the fracture pressure $p_\Gamma : \Gamma \to \mathbb{R}$

satisfy

$$\begin{aligned}
\boldsymbol{u} + \boldsymbol{K}\nabla p &= 0 && \text{in } \Omega_{\mathrm{B}}, && (3.1a)\\
\nabla \cdot \boldsymbol{u} &= f && \text{in } \Omega_{\mathrm{B}}, && (3.1b)\\
-\nabla_\tau \cdot (K_\Gamma \nabla_\tau p_\Gamma) &= \ell_\Gamma f_\Gamma + [\![\boldsymbol{u}]\!]_\Gamma \cdot \boldsymbol{n}_\Gamma && \text{in } \Gamma, && (3.1c)\\
\boldsymbol{u} \cdot \boldsymbol{n}_{\partial\Omega} &= 0 && \text{on } \partial\Omega_{\mathrm{B}}, && (3.1d)\\
-K_\Gamma \nabla_\tau p_\Gamma \cdot \boldsymbol{\tau}_{\partial\Gamma} &= 0 && \text{on } \partial\Gamma, && (3.1e)\\
\int_\Gamma p_\Gamma &= 0, && && (3.1f)
\end{aligned}$$

where $f \in L^2(\Omega_{\mathrm{B}})$ and $f_\Gamma \in L^2(\Gamma)$ denote source or sink terms, $\boldsymbol{K} : \Omega_{\mathrm{B}} \to \mathbb{R}^{2\times 2}$ the bulk permeability tensor, and we have set $K_\Gamma \coloneqq \kappa_\Gamma^\tau \ell_\Gamma$, with $\kappa_\Gamma^\tau : \Gamma \to \mathbb{R}$ denoting the tangential permeability inside the fracture and $\ell_\Gamma : \Gamma \to \mathbb{R}$ the fracture thickness. In (3.1c) and (3.1e), ∇_τ and $\nabla_\tau\cdot$ denote the tangential gradient and divergence operators along Γ, respectively. We assume that $\boldsymbol{K}$ is symmetric, piecewise constant on a finite polygonal partition

$$\mathcal{P}_{\mathrm{B}} = \{\omega_{\mathrm{B},i} \ : \ i \in I_{\mathrm{B}}\} \tag{3.2}$$

of Ω_{B}, and uniformly elliptic so that there exist two strictly positive real numbers $\underline{K}_{\mathrm{B}}$ and $\overline{K}_{\mathrm{B}}$ such that, for almost every $\boldsymbol{x} \in \Omega_{\mathrm{B}}$ and all $\boldsymbol{z} \in \mathbb{R}^2$ with $|\boldsymbol{z}| = 1$,

$$0 < \underline{K}_{\mathrm{B}} \le \boldsymbol{K}(\boldsymbol{x})\boldsymbol{z} \cdot \boldsymbol{z} \le \overline{K}_{\mathrm{B}}.$$

The quantities κ_Γ^τ and ℓ_Γ are also assumed piecewise constant on a finite partition

$$\mathcal{P}_\Gamma = \{\omega_{\Gamma,i} \ : \ i \in I_\Gamma\} \tag{3.3}$$

of Γ, and such that there exist strictly positive real numbers $\underline{\ell}_\Gamma$,$\overline{\ell}_\Gamma$ $\underline{K}_\Gamma$,$\overline{K}_\Gamma$ such that, for almost every $\boldsymbol{x} \in \Gamma$,

$$0 < \underline{\ell}_\Gamma \le \ell_\Gamma(\boldsymbol{x}) \le \overline{\ell}_\Gamma, \qquad 0 < \underline{K}_\Gamma \le K_\Gamma(\boldsymbol{x}) \le \overline{K}_\Gamma.$$

To close the problem, we add the following transmission conditions across the fracture:

$$\begin{aligned}
\lambda_\Gamma \{\{\boldsymbol{u}\}\}_\Gamma \cdot \boldsymbol{n}_\Gamma &= [\![p]\!]_\Gamma && \text{on } \Gamma,\\
\lambda_\Gamma^\xi [\![\boldsymbol{u}]\!]_\Gamma \cdot \boldsymbol{n}_\Gamma &= \{\{p\}\}_\Gamma - p_\Gamma && \text{on } \Gamma,
\end{aligned} \tag{3.4}$$

where, denoting by $\xi \in (\frac{1}{2}, 1]$ a user-dependent model parameter, we have set

$$\lambda_\Gamma \coloneqq \frac{\ell_\Gamma}{\kappa_\Gamma^n}, \qquad \lambda_\Gamma^\xi \coloneqq \lambda_\Gamma \left(\frac{\xi}{2} - \frac{1}{4}\right).$$

Here, $\kappa_\Gamma^n : \Gamma \to \mathbb{R}$ represents the normal permeability inside the fracture, which is assumed piecewise constant on the partition $\mathcal{P}_\Gamma$ of Γ and such that, for almost every $\boldsymbol{x} \in \Gamma$,

$$0 < \underline{\lambda}_\Gamma \le \lambda_\Gamma(\boldsymbol{x}) \le \overline{\lambda}_\Gamma,$$

for two given strictly positive real numbers $\underline{\lambda}_\Gamma$ and $\overline{\lambda}_\Gamma$.

Remark 3.1 (Compatibility condition). Since homogeneous Neumann boundary conditions are considered on both the bulk and fracture boundaries (cf. (3.1d) and (3.1e)), the flow through the porous medium is entirely driven by the source terms f and f_Γ, which typically model injection or production wells according to their sign. Decomposing f and f_Γ into their positive and negative parts, i.e., writing $f = f^+ - f^-$ and $f_\Gamma = f_\Gamma^+ - f_\Gamma^-$ with $f^\pm := \frac{|f| \pm f}{2}$ and $f_\Gamma^\pm := \frac{|f_\Gamma| \pm f_\Gamma}{2}$, we need to further assume the following compatibility condition in order to ensure that a global mass balance is satisfied:

$$\int_{\Omega_B} f^+ + \int_\Gamma \ell_\Gamma f_\Gamma^+ = \int_{\Omega_B} f^- + \int_\Gamma \ell_\Gamma f_\Gamma^-, \tag{3.5}$$

which translates the fact that all the fluid that enters the domain through injection wells must exit the domain through production wells. In this configuration, the fracture pressure p_Γ is defined up to a constant that is fixed by the zero-average constraint (3.1f). The bulk pressure, on the other hand, is uniquely defined without additional conditions owing to the coupling conditions (3.4).

3.2.2.2 Weak formulation

We define the space $\boldsymbol{H}(\mathrm{div}; \Omega_B)$, spanned by vector-valued functions on Ω_B whose restriction to every bulk subregion $\Omega_{B,i}$, $i \in \{1, 2\}$, is in $\boldsymbol{H}(\mathrm{div}; \Omega_{B,i})$. The Darcy velocity space is

$$\boldsymbol{U} := \left\{ \boldsymbol{u} \in \boldsymbol{H}(\mathrm{div}; \Omega_B) \ : \ \boldsymbol{u} \cdot \boldsymbol{n}_{\partial\Omega} = 0 \text{ on } \partial\Omega_B \text{ and } (\boldsymbol{u}_1 \cdot \boldsymbol{n}_\Gamma, \boldsymbol{u}_2 \cdot \boldsymbol{n}_\Gamma) \in L^2(\Gamma)^2 \right\}.$$

The fracture pressure space is $P_\Gamma := H^1(\Gamma) \cap L_0^2(\Gamma)$, with $L_0^2(\Gamma)$ spanned by square-integrable functions with zero mean value on Γ. We define the bilinear forms $a_K^\xi : \boldsymbol{U} \times \boldsymbol{U} \to \mathbb{R}$, $a_K^\Gamma : H^1(\Gamma) \times H^1(\Gamma) \to \mathbb{R}$, $b : \boldsymbol{U} \times L^2(\Omega_B) \to \mathbb{R}$ and $d : \boldsymbol{U} \times L^2(\Gamma) \to \mathbb{R}$ such that

$$a_K^\xi(\boldsymbol{u}, \boldsymbol{q}) := \int_{\Omega_B} \boldsymbol{K}^{-1} \boldsymbol{u} \cdot \boldsymbol{q} + \int_\Gamma \left(\lambda_\Gamma^\xi [\![\boldsymbol{u}]\!]_\Gamma \cdot \boldsymbol{n}_\Gamma [\![\boldsymbol{q}]\!]_\Gamma \cdot \boldsymbol{n}_\Gamma + \lambda_\Gamma \{\{\boldsymbol{u}\}\}_\Gamma \cdot \boldsymbol{n}_\Gamma \{\{\boldsymbol{q}\}\}_\Gamma \cdot \boldsymbol{n}_\Gamma \right),$$

$$a_K^\Gamma(p_\Gamma, z_\Gamma) := \int_\Gamma K_\Gamma \nabla_\tau p_\Gamma \cdot \nabla_\tau z_\Gamma, \quad b(\boldsymbol{u}, z) := \int_{\Omega_B} \nabla \cdot \boldsymbol{u} z, \quad d(\boldsymbol{u}, z_\Gamma) := \int_\Gamma [\![\boldsymbol{u}]\!]_\Gamma \cdot \boldsymbol{n}_\Gamma z_\Gamma,$$

as well as the global bilinear form $\mathcal{A}_\xi^{\mathrm{flow}} : (\boldsymbol{U} \times L^2(\Omega_\mathrm{B}) \times H^1(\Gamma)) \times (\boldsymbol{U} \times L^2(\Omega_\mathrm{B}) \times H^1(\Gamma)) \to \mathbb{R}$ such that

$$\mathcal{A}_\xi^{\mathrm{flow}}((\boldsymbol{u}, p, p_\Gamma), (\boldsymbol{q}, z, z_\Gamma)) \coloneqq a_K^\xi(\boldsymbol{u}, \boldsymbol{q}) + b(\boldsymbol{u}, z) - b(\boldsymbol{q}, p) + d(\boldsymbol{q}, p_\Gamma) - d(\boldsymbol{u}, z_\Gamma) + a_K^\Gamma(p_\Gamma, z_\Gamma).$$

With these spaces and bilinear forms, the weak formulation of problem (3.1)–(3.4) reads: Find $(\boldsymbol{u}, p, p_\Gamma) \in \boldsymbol{U} \times L^2(\Omega_\mathrm{B}) \times P_\Gamma$ such that, for all $(\boldsymbol{q}, z, z_\Gamma) \in \boldsymbol{U} \times L^2(\Omega_\mathrm{B}) \times H^1(\Gamma)$,

$$\mathcal{A}_\xi^{\mathrm{flow}}((\boldsymbol{u}, p, p_\Gamma), (\boldsymbol{q}, z, z_\Gamma)) = \int_{\Omega_\mathrm{B}} f z + \int_\Gamma \ell_\Gamma f_\Gamma z_\Gamma. \tag{3.6}$$

The well-posedness of problem (3.6) with mixed boundary conditions is studied in [17]; cf. also [72, 122] and references therein.

3.2.3 Passive transport

We next formulate the equations that govern the passive transport of a solute by the Darcy flow solution of problem (3.1)–(3.4). For the sake of simplicity, we focus on the case where the transport problem is fully decoupled. This section contains the first main contribution of this paper, namely novel transmission conditions that enable the treatment of discontinuous solute concentrations across the fracture.

3.2.3.1 Bulk region

Denoting by $c : \Omega_\mathrm{B} \to \mathbb{R}$ the concentration of the solute in the bulk and by $\boldsymbol{D} : \Omega_\mathrm{B} \to \mathbb{R}^{2\times 2}$ the symmetric, uniformly elliptic bulk diffusion-dispersion tensor, the passive transport of the solute in the bulk region is governed by the following equations:

$$\nabla \cdot (\boldsymbol{u} c - \boldsymbol{D}\nabla c) + f^- c = f^+ \widehat{c} \qquad \text{in } \Omega_\mathrm{B}, \tag{3.7a}$$

$$-\boldsymbol{D}\nabla c \cdot \boldsymbol{n}_{\partial\Omega} = 0 \qquad \text{on } \partial\Omega_\mathrm{B}, \tag{3.7b}$$

where the term $f^- c$ acts as a sink, while the term $f^+\widehat{c}$, with $\widehat{c} : \Omega_\mathrm{B} \to \mathbb{R}$ denoting the concentration of solute as it is injected, acts as a source. We assume that both $\boldsymbol{D}$ and $\widehat{c}$ are piecewise constant on the polygonal partition $\mathcal{P}_\mathrm{B}$ of Ω_B (see (3.2)), and that there exist two strictly positive real numbers $\underline{D}_\mathrm{B}$ and $\overline{D}_\mathrm{B}$ such that, for almost every $\boldsymbol{x} \in \Omega_\mathrm{B}$ and all $\boldsymbol{z} \in \mathbb{R}^2$ such that $|\boldsymbol{z}| = 1$,

$$0 \le \widehat{c}(\boldsymbol{x}) \le 1, \qquad 0 < \underline{D}_\mathrm{B} \le \boldsymbol{D}(\boldsymbol{x})\boldsymbol{z} \cdot \boldsymbol{z} \le \overline{D}_\mathrm{B}.$$

More generally $\boldsymbol{D}$ can depend on $\boldsymbol{u}$. While the theoretical focus on the case of $\boldsymbol{D}$ independent from $\boldsymbol{u}$, this dependence has been considered in some numerical experiments presented in section 3.5.

3.2.3.2 Fracture

We define the Darcy velocity $\boldsymbol{u}_\Gamma : \Gamma \to \mathbb{R}^2$ inside the fracture such that $\boldsymbol{u}_\Gamma \coloneqq -K_\Gamma \nabla_\tau p_\Gamma$ where $p_\Gamma : \Gamma \to \mathbb{R}$ is the fracture pressure solution of problem (3.1)–(3.4). Denoting by $c_\Gamma : \Gamma \to \mathbb{R}$ the concentration of the solute inside the fracture, and letting $D_\Gamma \coloneqq \mathcal{D}_\Gamma^\tau \ell_\Gamma$ with $\mathcal{D}_\Gamma^\tau : \Gamma \to \mathbb{R}$ denoting the (strictly positive almost everywhere) tangential diffusion-dispersion coefficient of the fracture, the governing equations for the transport problem inside the fracture are:

$$\nabla_\tau \cdot (\boldsymbol{u}_\Gamma c_\Gamma - D_\Gamma \nabla_\tau c_\Gamma) + \ell_\Gamma f_\Gamma^- c_\Gamma = \ell_\Gamma f_\Gamma^+ \widehat{c_\Gamma} + [\![\boldsymbol{u} c - \boldsymbol{D} \nabla c]\!]_\Gamma \cdot \boldsymbol{n}_\Gamma \quad \text{in } \Gamma, \tag{3.8a}$$

$$-D_\Gamma \nabla_\tau c_\Gamma \cdot \boldsymbol{\tau}_{\partial\Gamma} = 0 \quad \text{on } \partial\Gamma, \tag{3.8b}$$

where again $f_\Gamma^- c$ acts as a sink term while $f_\Gamma^+ \widehat{c_\Gamma}$ acts as a source, with $\widehat{c_\Gamma} : \Gamma \to \mathbb{R}$ denoting the concentration of solute as it is injected in the fracture. For the sake of simplicity, we assume in what follows that both $\widehat{c_\Gamma}$ and D_Γ are piecewise constant on the partition $\mathcal{P}_\Gamma$ of Γ (see (3.3)), and such that there exist two strictly positive real numbers $\underline{D}_\Gamma$ and $\overline{D}_\Gamma$ such that, for almost every $\boldsymbol{x} \in \Gamma$,

$$0 \le \widehat{c_\Gamma}(\boldsymbol{x}) \le 1, \qquad 0 < \underline{D}_\Gamma \le D_\Gamma(\boldsymbol{x}) \le \overline{D}_\Gamma.$$

3.2.3.3 Transmission conditions

When considering a transport problem, the advective term does not create or dissipate energy: the only related contribution possibly stems from the boundary, and is equal to zero in the case of no flow (homogeneous Neumann) boundary conditions. We aim at reproducing this property in our model. Specifically, we consider the following transmission conditions, which ensure that the advective terms do not contribute to the energy balance (see Theorem 3.2):

$$\begin{aligned} \{\{\boldsymbol{u} c - \boldsymbol{D}\nabla c\}\}_\Gamma \cdot \boldsymbol{n}_\Gamma &= \beta_\Gamma [\![c]\!]_\Gamma + (\{\{\boldsymbol{u}\}\}_\Gamma \cdot \boldsymbol{n}_\Gamma)\{\{c\}\}_\Gamma + \frac{1}{8}([\![\boldsymbol{u}]\!]_\Gamma \cdot \boldsymbol{n}_\Gamma)[\![c]\!]_\Gamma \text{ on } \Gamma, \\ [\![\boldsymbol{u} c - \boldsymbol{D}\nabla c]\!]_\Gamma \cdot \boldsymbol{n}_\Gamma &= \beta_\Gamma^\xi (\{\{c\}\}_\Gamma - c_\Gamma) + \frac{1}{2}[\![\boldsymbol{u}]\!]_\Gamma \cdot \boldsymbol{n}_\Gamma (\{\{c\}\}_\Gamma + c_\Gamma) \qquad \text{on } \Gamma, \end{aligned} \tag{3.9}$$

where ξ is the user-dependent model parameter introduced in Section 3.2.2.1, and we have set

$$\beta_\Gamma \coloneqq \frac{\mathcal{D}_\Gamma^n}{\ell_\Gamma}, \qquad \beta_\Gamma^\xi \coloneqq \beta_\Gamma \left(\frac{\xi}{2} - \frac{1}{4} \right)^{-1}.$$

The term $\mathcal{D}_\Gamma^n : \Gamma \to \mathbb{R}$ represents the normal diffusion-dispersion coefficient of the fracture, which is assumed piecewise constant on the partition $\mathcal{P}_\Gamma$ of Γ (see (3.3)), strictly positive almost everywhere on Γ, and such that, for almost every $\boldsymbol{x} \in \Gamma$,

$$0 < \underline{\beta}_\Gamma \le \beta_\Gamma(\boldsymbol{x}) \le \overline{\beta}_\Gamma,$$

for two given strictly positive real numbers $\underline{\beta}_\Gamma$ and $\overline{\beta}_\Gamma$.

3.2.3.4 Weak formulation

Let $H^1(\Omega_\mathrm{B})$ denote the broken Sobolev space spanned by scalar-valued functions on Ω_B whose restriction to every bulk subregion $\Omega_{\mathrm{B},i}$, $i \in \{1,2\}$, is in $H^1(\Omega_{\mathrm{B},i})$. We define the molecular diffusion bilinear form $a_D : H^1(\Omega_\mathrm{B}) \times H^1(\Omega_\mathrm{B}) \to \mathbb{R}$, the advection-reaction bilinear form $a_{\boldsymbol{u},f} : H^1(\Omega_\mathrm{B}) \times H^1(\Omega_\mathrm{B}) \to \mathbb{R}$, and the diffusion-advection-reaction bilinear form $a : H^1(\Omega_\mathrm{B}) \times H^1(\Omega_\mathrm{B})$ such that

$$\begin{aligned} a_D(c,z) &\coloneqq \int_{\Omega_\mathrm{B}} D\nabla c \cdot \nabla z, \\ a_{\boldsymbol{u},f}(c,z) &\coloneqq \int_{\Omega_\mathrm{B}} \Big(- c(\boldsymbol{u}\cdot\nabla z) + f^- cz \Big), \\ a(c,z) &\coloneqq a_D(c,z) + a_{\boldsymbol{u},f}(c,z). \end{aligned} \tag{3.10}$$

We also define their fracture-based counterparts $a_D^\Gamma : H^1(\Gamma) \times H^1(\Gamma) \to \mathbb{R}$, $a_{\boldsymbol{u},f}^\Gamma : H^1(\Gamma) \times H^1(\Gamma) \to \mathbb{R}$ and $a_\Gamma : H^1(\Gamma) \times H^1(\Gamma) \to \mathbb{R}$ such that

$$\begin{aligned} a_D^\Gamma(c_\Gamma, z_\Gamma) &\coloneqq \int_\Gamma D_\Gamma \nabla_\tau c_\Gamma \cdot \nabla_\tau z_\Gamma, \\ a_{\boldsymbol{u},f}^\Gamma(c_\Gamma, z_\Gamma) &\coloneqq \int_\Gamma \Big(- c_\Gamma(\boldsymbol{u}_\Gamma \cdot \nabla_\tau z_\Gamma) + \ell_\Gamma f_\Gamma^- c_\Gamma z_\Gamma \Big), \\ a_\Gamma(c_\Gamma, z_\Gamma) &\coloneqq a_D^\Gamma(c_\Gamma, z_\Gamma) + a_{\boldsymbol{u},f}^\Gamma(c_\Gamma, z_\Gamma). \end{aligned} \tag{3.11}$$

The global bilinear form $\mathcal{A}_\xi^\mathrm{transp} : \big(H^1(\Omega_\mathrm{B}) \times H^1(\Gamma)\big) \times \big(H^1(\Omega_\mathrm{B}) \times H^1(\Gamma)\big) \to \mathbb{R}$, that additionally takes into account terms that stem from the coupling equations, is defined as follows:

$$\begin{aligned} \mathcal{A}_\xi^\mathrm{transp}((c,c_\Gamma),(z,z_\Gamma)) \coloneqq a(c,z) + a_\Gamma(c_\Gamma,z_\Gamma) &+ \int_\Gamma (\{\{\boldsymbol{u}\}\}_\Gamma \cdot \boldsymbol{n}_\Gamma)\{\{c\}\}_\Gamma [\![z]\!]_\Gamma \\ &+ \int_\Gamma \Big(\beta_\Gamma [\![c]\!]_\Gamma [\![z]\!]_\Gamma + \frac{1}{8}([\![\boldsymbol{u}]\!]_\Gamma \cdot \boldsymbol{n}_\Gamma)[\![c]\!]_\Gamma [\![z]\!]_\Gamma \Big) \\ &+ \int_\Gamma \frac{1}{2}([\![\boldsymbol{u}]\!]_\Gamma \cdot \boldsymbol{n}_\Gamma)(\{\{c\}\}_\Gamma + c_\Gamma)(\{\{z\}\}_\Gamma - z_\Gamma) \\ &+ \int_\Gamma \beta_\Gamma^\xi (\{\{c\}\}_\Gamma - c_\Gamma)(\{\{z\}\}_\Gamma - z_\Gamma). \end{aligned} \tag{3.12}$$

With these spaces and bilinear forms, the weak formulation of problem (3.7)–(3.8)–(3.9) reads: Find $(c, c_\Gamma) \in H^1(\Omega_\mathrm{B}) \times H^1(\Gamma)$ such that, for all $(z, z_\Gamma) \in H^1(\Omega_\mathrm{B}) \times H^1(\Gamma)$

$$\mathcal{A}_\xi^\mathrm{transp}((c,c_\Gamma),(z,z_\Gamma)) = \int_{\Omega_\mathrm{B}} f^+ \widehat{c} z + \int_\Gamma \ell_\Gamma f_\Gamma^+ \widehat{c_\Gamma} z_\Gamma. \tag{3.13}$$

3.2.3.5 Coercivity

In the following theorem, we prove the coercivity of the global transport bilinear form defined by (3.12) and show that, thanks to the new transmission conditions (3.8), the advective terms do not dissipate energy. This result is the key ingredient to derive a stability result for problem (3.13).

Theorem 3.2 (Coercivity)**.** *Let $\xi > 1/2$. Then, for all $(z, z_\Gamma) \in H^1(\Omega_B) \times H^1(\Gamma)$, it holds*

$$\begin{aligned}\mathcal{A}_\xi^{\text{transp}}((z, z_\Gamma), (z, z_\Gamma)) = \|\boldsymbol{D}^{1/2}\nabla z\|_{\Omega_B}^2 + \|D_\Gamma^{1/2}\nabla_\tau z_\Gamma\|_\Gamma^2 + \|\chi_B^{1/2} z\|_{\Omega_B}^2 + \|\chi_\Gamma^{1/2} z_\Gamma\|_\Gamma^2 \\ + \|(\beta_\Gamma^\xi)^{1/2}(\{\{z\}\}_\Gamma - z_\Gamma)\|_\Gamma^2 + \|(\beta_\Gamma)^{1/2}[\![z]\!]_\Gamma\|_\Gamma^2,\end{aligned} \tag{3.14}$$

with $\chi_B := \dfrac{|f|}{2}$ *and* $\chi_\Gamma := \dfrac{\ell_\Gamma |f_\Gamma|}{2}$.

Remark 3.3 (Energy balance). Equation (3.14) can be interpreted as a global energy balance. The transmission conditions (3.9) are designed so that the advective terms do not contribute to this balance. Additionally, if z is continuous across Γ, also all terms related to the diffusion-dispersion across the fracture, collected in the second line of (3.14), disappear.

Proof. Let $(z, z_\Gamma) \in H^1(\Omega_B) \times H^1(\Gamma)$. By definition of the global bilinear form $\mathcal{A}_\xi^{\text{transp}}$ (3.12), it holds

$$\begin{aligned}\mathcal{A}_\xi^{\text{transp}}((z, z_\Gamma), (z, z_\Gamma)) &= a(z, z) + a_\Gamma(z_\Gamma, z_\Gamma) \\ &\quad + \|(\beta_\Gamma^\xi)^{1/2}(\{\{z\}\}_\Gamma - z_\Gamma)\|_\Gamma^2 + \|(\beta_\Gamma)^{1/2}[\![z]\!]_\Gamma\|_\Gamma^2 \\ &\quad + \int_\Gamma \frac{1}{2}([\![\boldsymbol{u}]\!]_\Gamma \cdot \boldsymbol{n}_\Gamma)(\{\{z\}\}_\Gamma + z_\Gamma)(\{\{z\}\}_\Gamma - z_\Gamma) \\ &\quad + \int_\Gamma \Big((\{\{\boldsymbol{u}\}\}_\Gamma \cdot \boldsymbol{n}_\Gamma)\{\{z\}\}_\Gamma [\![z]\!]_\Gamma + \frac{1}{8}([\![\boldsymbol{u}]\!]_\Gamma \cdot \boldsymbol{n}_\Gamma)[\![z]\!]_\Gamma^2\Big),\end{aligned} \tag{3.15}$$

Using the definitions (3.10) and (3.11) of the bilinear forms a and a_Γ, we obtain

$$a(z, z) = \|\boldsymbol{D}^{1/2}\nabla z\|_{\Omega_B}^2 + a_{\boldsymbol{u},f}(z, z), \qquad a_\Gamma(z_\Gamma, z_\Gamma) = \|D_\Gamma^{1/2}\nabla_\tau z_\Gamma\|_\Gamma^2 + a_{\boldsymbol{u},f}^\Gamma(z_\Gamma, z_\Gamma). \tag{3.16}$$

Expanding the bilinear form $a_{\boldsymbol{u},f}$ according to its definition (3.10), we get

$$\begin{aligned}a_{\boldsymbol{u},f}(z, z) &= \int_{\Omega_B} \Big(- z(\boldsymbol{u} \cdot \nabla z) + f^- z^2\Big) \\ &= \int_{\Omega_B} \Big(- \boldsymbol{u} \cdot \nabla(\frac{z^2}{2}) + f^- z^2\Big) \\ &= \int_{\Omega_B} \Big(\frac{1}{2}(\nabla \cdot \boldsymbol{u})z^2 + f^- z^2\Big) - \frac{1}{2}\int_\Gamma [\![\boldsymbol{u} z^2]\!]_\Gamma \cdot \boldsymbol{n}_\Gamma \\ &= \|\chi_B^{1/2} z\|_{\Omega_B}^2 - \frac{1}{2}\int_\Gamma \Big([\![\boldsymbol{u}]\!]_\Gamma \cdot \boldsymbol{n}_\Gamma \{\{z^2\}\}_\Gamma + \{\{\boldsymbol{u}\}\}_\Gamma \cdot \boldsymbol{n}_\Gamma [\![z^2]\!]_\Gamma\Big),\end{aligned} \tag{3.17}$$

where we have used an integration by parts together with the boundary condition (3.1d) to pass to the third line while, to pass to the fourth line, we have used (3.1b) to write $\frac{1}{2}(\nabla\cdot\boldsymbol{u})+f^-=\frac{f}{2}+f^-=\frac{|f|}{2}$ followed by the relation

$$[\![ab]\!]_\Gamma=[\![a]\!]_\Gamma\{\{b\}\}_\Gamma+\{\{a\}\}_\Gamma[\![b]\!]_\Gamma. \tag{3.18}$$

Similarly, expanding $a^\Gamma_{\boldsymbol{u},f}$ according to its definition (3.11), we find

$$\begin{aligned}
a^\Gamma_{\boldsymbol{u},f}(z_\Gamma,z_\Gamma)&=\int_\Gamma\Big(-z_\Gamma(\boldsymbol{u}_\Gamma\cdot\nabla_\tau z_\Gamma)+\ell_\Gamma f_\Gamma^- z_\Gamma^2\Big)\\
&=\int_\Gamma\Big(-\boldsymbol{u}_\Gamma\cdot\nabla(\frac{z_\Gamma^2}{2})+\ell_\Gamma f_\Gamma^- z_\Gamma^2\Big)\\
&=\int_\Gamma\Big(\frac{1}{2}(\nabla_\tau\cdot\boldsymbol{u}_\Gamma)z_\Gamma^2+\ell_\Gamma f_\Gamma^- z_\Gamma^2\Big)\\
&=\int_\Gamma\Big(\frac{1}{2}(\ell_\Gamma f_\Gamma+[\![\boldsymbol{u}]\!]_\Gamma\cdot\boldsymbol{n}_\Gamma)z_\Gamma^2+\ell_\Gamma f_\Gamma^- z_\Gamma^2\Big)\\
&=\|\chi_\Gamma^{1/2}z_\Gamma\|_\Gamma^2+\frac{1}{2}\int_\Gamma([\![\boldsymbol{u}]\!]_\Gamma\cdot\boldsymbol{n}_\Gamma)z_\Gamma^2,
\end{aligned} \tag{3.19}$$

where we have, at first, integrated by parts and used (3.1e) to pass to the third line, then we have used (3.1c) after recalling that $\boldsymbol{u}_\Gamma:=-K_\Gamma\nabla_\tau p_\Gamma$ to pass to the fourth line, and invoked the definition of χ_Γ to conclude. Plugging (3.16), (3.17) and (3.19) into (3.15), we obtain

$$\begin{aligned}
\mathcal{A}_\xi^{\mathrm{transp}}((z,z_\Gamma),(z,z_\Gamma))&=\|\boldsymbol{D}^{1/2}\nabla z\|_{\Omega_{\mathrm{B}}}^2+\|D_\Gamma^{1/2}\nabla_\tau z_\Gamma\|_\Gamma^2+\|\chi_{\mathrm{B}}^{1/2}z\|_{\Omega_{\mathrm{B}}}^2+\|\chi_\Gamma^{1/2}z_\Gamma\|_\Gamma^2\\
&\quad+\|(\beta_\Gamma^\xi)^{1/2}(\{\{z\}\}_\Gamma-z_\Gamma)\|_\Gamma^2+\|(\beta_\Gamma)^{1/2}[\![z]\!]_\Gamma\|_\Gamma^2\\
&\quad+\int_\Gamma\Big((\{\{\boldsymbol{u}\}\}_\Gamma\cdot\boldsymbol{n}_\Gamma)\Big(\cancel{\{\{z\}\}_\Gamma[\![z]\!]_\Gamma}-\frac{1}{2}[\![z^2]\!]_\Gamma\Big)-\frac{1}{2}([\![\boldsymbol{u}]\!]_\Gamma\cdot\boldsymbol{n}_\Gamma)\{\{z^2\}\}_\Gamma\Big)\\
&\quad+\int_\Gamma\frac{1}{2}\Big(([\![\boldsymbol{u}]\!]_\Gamma\cdot\boldsymbol{n}_\Gamma)z_\Gamma^2+([\![\boldsymbol{u}]\!]_\Gamma\cdot\boldsymbol{n}_\Gamma)(\{\{z\}\}_\Gamma+z_\Gamma)(\{\{z\}\}_\Gamma-z_\Gamma)\Big)\\
&\quad+\int_\Gamma\frac{1}{8}([\![\boldsymbol{u}]\!]_\Gamma\cdot\boldsymbol{n}_\Gamma)[\![z]\!]_\Gamma^2,
\end{aligned}$$

where, to cancel the last term in the third line, we have used formula (3.18) with $a=b=z$ to infer $\frac{1}{2}[\![z^2]\!]_\Gamma=\{\{z\}\}_\Gamma[\![z]\!]_\Gamma$. Rearranging the terms on Γ, we arrive at

$$\begin{aligned}
\mathcal{A}_\xi^{\mathrm{transp}}((z,z_\Gamma),(z,z_\Gamma))&=\|\boldsymbol{D}^{1/2}\nabla z\|_{\Omega_{\mathrm{B}}}^2+\|D_\Gamma^{1/2}\nabla_\tau z_\Gamma\|_\Gamma^2+\|\chi_{\mathrm{B}}^{1/2}z\|_{\Omega_{\mathrm{B}}}^2+\|\chi_\Gamma^{1/2}z_\Gamma\|_\Gamma^2\\
&\quad+\|(\beta_\Gamma^\xi)^{1/2}(\{\{z\}\}_\Gamma-z_\Gamma)\|_\Gamma^2+\|(\beta_\Gamma)^{1/2}[\![z]\!]_\Gamma\|_\Gamma^2\\
&\quad+\int_\Gamma\frac{1}{2}([\![\boldsymbol{u}]\!]_\Gamma\cdot\boldsymbol{n}_\Gamma)\Big(\cancel{z_\Gamma^2}-\{\{z^2\}\}_\Gamma+\{\{z\}\}_\Gamma^2-\cancel{z_\Gamma^2}+\frac{1}{4}[\![z]\!]_\Gamma^2\Big).
\end{aligned} \tag{3.20}$$

Using the formula

$$\{\{ab\}\}_\Gamma = \{\{a\}\}_\Gamma\{\{b\}\}_\Gamma + \frac{1}{4}[\![a]\!]_\Gamma[\![b]\!]_\Gamma$$

with $a = b = z$ to write $\{\{z^2\}\}_\Gamma = \{\{z\}\}_\Gamma^2 + \frac{1}{4}[\![z]\!]_\Gamma^2$ in the last line of (3.20), (3.14) follows. □

3.3 Discrete setting

The HHO method is built upon a polygonal mesh of the domain Ω defined prescribing a set of mesh elements $\mathcal{T}_h$ and a set of mesh faces $\mathcal{F}_h$.

The set of mesh elements $\mathcal{T}_h$ is a finite collection of open disjoint polygons with nonzero area such that $\overline{\Omega} = \bigcup_{T\in\mathcal{T}_h}\overline{T}$ and $h = \max_{T\in\mathcal{T}_h} h_T$, with h_T denoting the diameter of T. We also denote by ∂T the boundary of a mesh element $T \in \mathcal{T}_h$. The set of mesh faces $\mathcal{F}_h$ is a finite collection of open disjoint line segments in $\overline{\Omega}$ with nonzero length such that, for all $F \in \mathcal{F}_h$, (i) either there exist two distinct mesh elements $T_1, T_2 \in \mathcal{T}_h$ such that $F \subset \partial T_1 \cap \partial T_2$ (and F is called an interface) or (ii) there exist a (unique) mesh element $T \in \mathcal{T}_h$ such that $F \subset \partial T \cap \partial\Omega$ (and F is called a boundary face). We assume that $\mathcal{F}_h$ is a partition of the mesh skeleton in the sense that $\bigcup_{T\in\mathcal{T}_h}\partial T = \bigcup_{F\in\mathcal{F}_h}\overline{F}$.

Remark 3.4 (Mesh faces). Despite working in two space dimensions, we use the terminology "face" over "edge" in order to (i) be consistent with the standard HHO nomenclature and (ii) stress the fact that faces *need not* coincide with polygonal edges (but can be subsets thereof); see also Remark 3.6.

We denote by $\mathcal{F}_h^{\mathrm{i}}$ the set of all interfaces and by $\mathcal{F}_h^{\mathrm{b}}$ the set of all boundary faces, so that $\mathcal{F}_h = \mathcal{F}_h^{\mathrm{i}} \cup \mathcal{F}_h^{\mathrm{b}}$. The length of a face $F \in \mathcal{F}_h$ is denoted by h_F. For any mesh element $T \in \mathcal{T}_h$, $\mathcal{F}_T$ is the set of faces that lie on ∂T and, for any $F \in \mathcal{F}_T$, $\boldsymbol{n}_{TF}$ is the unit normal to F pointing out of T. Symmetrically, for any $F \in \mathcal{F}_h$, $\mathcal{T}_F$ is the set containing the mesh elements sharing the face F (two if F is an interface, one if F is a boundary face).

To account for the presence of the fracture, we make the following

Assumption 3.5 (Geometric compliance with the fracture)**.** The mesh is compliant with the fracture, i.e., there exists a subset $\mathcal{F}_h^\Gamma \subset \mathcal{F}_h^{\mathrm{i}}$ such that $\overline{\Gamma} = \bigcup_{F\in\mathcal{F}_h^\Gamma}\overline{F}$. As a result, $\mathcal{F}_h^\Gamma$ is a (1-dimensional) mesh of the fracture.

Remark 3.6 (Polygonal meshes and geometric compliance with the fracture). Fulfilling Assumption 3.5 does not pose particular problems in the context of polygonal methods, even when the fracture discretization is nonconforming in the classical sense. Consider, e.g., the situation illustrated in Figure 3.2, where the fracture lies at the intersection of two nonmatching Cartesian submeshes. In this

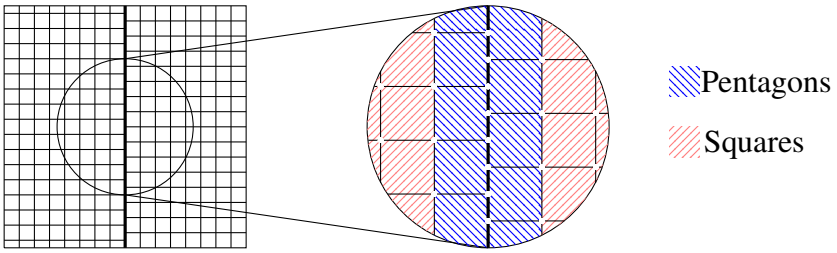

Figure 3.2: Treatment of nonconforming fracture discretizations.

case, no special treatment is required provided the mesh elements in contact with the fracture are treated as pentagons with two coplanar faces instead of rectangles. This is possible since, as already pointed out, the set of mesh faces $\mathcal{F}_h$ does not need to coincide with the set of polygonal edges of $\mathcal{T}_h$.

The set of vertices of the fracture is denoted by $\mathcal{V}_h$ and, for all $F \in \mathcal{F}_h^\Gamma$, we denote by $\mathcal{V}_F$ the vertices of F. Symmetrically, for any $V \in \mathcal{V}_h$, $\mathcal{F}_V$ is the set containing the fracture faces sharing the vertex V (two if V is an internal vertex, one if V is on the boundary on the fracture). For all $F \in \mathcal{F}_h^\Gamma$ and all $V \in \mathcal{V}_F$, $\boldsymbol{\tau}_{FV}$ denotes the unit vector tangent to the fracture and oriented so that it points out of F from V. Finally, $\mathcal{V}_h^{\mathrm{i}}$ is the set containing the internal vertices and $\mathcal{V}_h^{\mathrm{b}}$ is the set containing the points in $\partial\Gamma$, so that $\mathcal{V}_h = \mathcal{V}_h^{\mathrm{i}} \cup \mathcal{V}_h^{\mathrm{b}}$.

To avoid dealing with jumps of the problem data inside mesh elements, as well as on boundary and fracture faces, we additionally make the following

Assumption 3.7 (Compliance with the problem data)**.** The mesh is compliant with the data, i.e.: (i) for each mesh element $T \in \mathcal{T}_h$, there exists a unique sudomain $\omega_{\mathrm{B}} \in \mathcal{P}_{\mathrm{B}}$ (see (3.2)) such that $T \subset \omega_{\mathrm{B}}$; (ii) for each fracture face $F \in \mathcal{F}_h^\Gamma$, there is a unique subdomain $\omega_\Gamma \in \mathcal{P}_\Gamma$ (see (3.3)) such that $F \subset \omega_\Gamma$.

3.4 The Hybrid High-Order method

In this section, we formulate the HHO discretization of problems (3.6) (Darcy flow) and (3.13) (passive transport).

3.4.1 Darcy flow

We start with the discretization of problem (3.6), which is closely inspired by [56]. Through this section, we denote by $l \geq 0$ a fixed integer polynomial degree.

3.4.1.1 Discrete bulk Darcy velocity unkonwns, bulk Darcy velocity reconstruction, and permeability-weighted product of Darcy velocities

Let an element $T \in \mathcal{T}_h$ be fixed, and denote by $\boldsymbol{K}_T$ the (constant) restriction to T of the bulk permeability. For any integer $m \geq 0$, set

$$\boldsymbol{U}_T^m \coloneqq \boldsymbol{K}_T \nabla \mathbb{P}^m(T), \tag{3.21}$$

with $\mathbb{P}^m(T)$ denoting the space spanned by the restriction to T of two-valuate polynomials of total degree up to m. We define the following space of fully discontinuous bulk Darcy velocity unknowns:

$$\widehat{\underline{\boldsymbol{U}}}_h^l \coloneqq \left\{ \underline{\boldsymbol{q}}_h \coloneqq (\boldsymbol{q}_T, (q_{TF})_{F\in\mathcal{F}_T})_{T\in\mathcal{T}_h} \ : \ \begin{array}{l} \text{for all } T \in \mathcal{T}_h,\ \boldsymbol{q}_T \in \boldsymbol{U}_T^l \text{ and} \\ q_{TF} \in \mathbb{P}^l(F) \text{ for all } F \in \mathcal{F}_T \end{array} \right\}.$$

For any $T \in \mathcal{T}_h$, the element-based unknown $\boldsymbol{q}_T$ represents the Darcy velocity inside the element, while the face-based unknown q_{TF}, $F \in \mathcal{F}_T$, represents the normal Darcy velocity exiting T through F. Futhermore, we denote by $\underline{\boldsymbol{U}}_T^l$ the restriction of $\widehat{\underline{\boldsymbol{U}}}_h^l$ to T and, for any $\underline{\boldsymbol{q}}_h \in \widehat{\underline{\boldsymbol{U}}}_h^l$, we let $\underline{\boldsymbol{q}}_T \coloneqq (\boldsymbol{q}_T, (q_{TF})_{F\in\mathcal{F}_T}) \in \underline{\boldsymbol{U}}_T^l$. The following subspace of $\widehat{\underline{\boldsymbol{U}}}_h^l$ strongly incorporates the continuity of Darcy velocity unknowns at each interface $F \in \mathcal{F}_h^{\mathrm{i}} \setminus \mathcal{F}_h^{\Gamma}$ contained in the bulk region, as well as the homogeneous Neumann boundary condition on $\partial\Omega_{\mathrm{B}}$:

$$\underline{\boldsymbol{U}}_h^l \coloneqq \left\{ \underline{\boldsymbol{q}}_h \in \widehat{\underline{\boldsymbol{U}}}_h^l \ : \ \begin{array}{l} [\![\underline{\boldsymbol{q}}_h]\!]_F = 0 \text{ for all } F \in \mathcal{F}_h^{\mathrm{i}} \setminus \mathcal{F}_h^{\Gamma}, \\ q_F = 0 \text{ for all } F \in \mathcal{F}_h^{\mathrm{b}} \end{array} \right\}, \tag{3.22}$$

where, for all $F \in \mathcal{F}_h^{\mathrm{b}}$, we have set $q_F \coloneqq q_{TF}$ with T denoting the unique mesh element such that $F \in \mathcal{F}_T$ and, for all $F \in \mathcal{F}_h^{\mathrm{i}}$, we have defined the jump operator such that, for any $\underline{\boldsymbol{q}}_h \in \widehat{\underline{\boldsymbol{U}}}_h^l$,

$$[\![\underline{\boldsymbol{q}}_h]\!]_F \coloneqq \sum_{T\in\mathcal{T}_F} q_{TF}.$$

For all $T \in \mathcal{T}_h$, we define the local discrete Darcy velocity reconstruction operator $\boldsymbol{F}_T^{l+1} : \underline{\boldsymbol{U}}_T^l \to \boldsymbol{U}_T^{l+1}$ (see (3.21)) such that, for all $\underline{\boldsymbol{q}}_T = (\boldsymbol{q}_T, (q_{TF})_{F\in\mathcal{F}_T}) \in \underline{\boldsymbol{U}}_T^l$, $\boldsymbol{F}_T^{l+1}\underline{\boldsymbol{q}}_T$ solves

$$\int_T \boldsymbol{F}_T^{l+1}\underline{\boldsymbol{q}}_T \cdot \nabla w_T = \int_T \boldsymbol{q}_T \nabla \pi_T^l w_T + \sum_{F\in\mathcal{F}_T} \int_F q_{TF}(w_T - \pi_T^l w_T), \tag{3.23}$$

for all $w_T \in \mathbb{P}^{l+1}(T)$ with $\pi_T^l : L^1(T) \to \mathbb{P}^l(T)$ denoting the L^2-orthogonal projector on $\mathbb{P}^l(T)$. Notice that the $\boldsymbol{F}_T^{l+1}\underline{\boldsymbol{q}}_T$ provides a representation of the Darcy velocity

inside T one degree higher than the element-based unknown $\boldsymbol{q}_T$. It can be checked that condition (3.23) defines a unique element of $\boldsymbol{U}_T^{l+1}$, and that it is equivalent to [56, Eq. (19)] with discrete divergence operator expanded according to its definition.

Based on this Darcy velocity reconstruction operator, we define the global permeability-weighted product of Darcy velocities $a_{K,h}^l : \underline{\boldsymbol{U}}_h^l \times \underline{\boldsymbol{U}}_h^l \to \mathbb{R}$ such that, for all $(\underline{\boldsymbol{u}}_h, \underline{\boldsymbol{q}}_h) \in \underline{\boldsymbol{U}}_h^l \times \underline{\boldsymbol{U}}_h^l$,

$$a_{K,h}^l(\underline{\boldsymbol{u}}_h, \underline{\boldsymbol{q}}_h) \coloneqq \sum_{T\in\mathcal{T}_h} \left(\int_T \boldsymbol{K}_T^{-1} \boldsymbol{F}_T^{l+1} \underline{\boldsymbol{u}}_T \cdot \boldsymbol{F}_T^{l+1} \underline{\boldsymbol{q}}_T + s_{K,T}^l(\underline{\boldsymbol{u}}_T, \underline{\boldsymbol{q}}_T) \right). \tag{3.24}$$

Here, the first term is the Galerkin contribution responsible for consistency while, for all $T \in \mathcal{T}_h$, $s_{K,T}^l : \underline{\boldsymbol{U}}_T^l \times \underline{\boldsymbol{U}}_T^l \to \mathbb{R}$ is the stabilization bilinear form such that, for all $(\underline{\boldsymbol{u}}_T, \underline{\boldsymbol{q}}_T) \in \underline{\boldsymbol{U}}_T^l \times \underline{\boldsymbol{U}}_T^l$,

$$s_{K,T}^l(\underline{\boldsymbol{u}}_T, \underline{\boldsymbol{q}}_T) \coloneqq \sum_{F\in\mathcal{F}_T} \int_F \frac{h_F}{K_{TF}} (\boldsymbol{F}_T^{l+1} \underline{\boldsymbol{u}}_T \cdot \boldsymbol{n}_{TF} - u_{TF})(\boldsymbol{F}_T^{l+1} \underline{\boldsymbol{q}}_T \cdot \boldsymbol{n}_{TF} - q_{TF}),$$

where, for all $F \in \mathcal{F}_T$, we have set $K_{TF} \coloneqq \boldsymbol{K}_T \boldsymbol{n}_{TF} \cdot \boldsymbol{n}_{TF}$.

3.4.1.2 Discrete fracture pressure unknowns, fracture pressure reconstruction, and tangential diffusion bilinear form

The space of discrete fracture pressure unknowns is given by

$$\underline{P}_{\Gamma,h}^l \coloneqq \left\{ \underline{z}_h^\Gamma \coloneqq ((z_F^\Gamma)_{F\in\mathcal{F}_h^\Gamma}, (z_V^\Gamma)_{V\in\mathcal{V}_h}) \ : \ \begin{array}{l} z_F^\Gamma \in \mathbb{P}^l(F) \text{ for all } F \in \mathcal{F}_h^\Gamma, \\ z_V^\Gamma \in \mathbb{R} \text{ for all } V \in \mathcal{V}_h \end{array} \right\}. \tag{3.25}$$

For all $F \in \mathcal{F}_h^\Gamma$, we denote by $\underline{P}_{\Gamma,F}^l$ the restriction of $\underline{P}_{\Gamma,h}^l$ to F, and set $\underline{z}_F^\Gamma \coloneqq (z_F^\Gamma, (z_V^\Gamma)_{V\in\mathcal{V}_F}) \in \underline{P}_{\Gamma,F}^l$. We also introduce the following subspace which embeds the zero-mean value constraint:

$$\underline{P}_{\Gamma,h,0}^l \coloneqq \left\{ \underline{z}_h^\Gamma \in \underline{P}_{\Gamma,h}^l \ : \ \int_\Gamma z_h^\Gamma = 0 \right\}, \tag{3.26}$$

where $z_h^\Gamma \in \mathbb{P}^l(\mathcal{F}_h^\Gamma)$ is the broken polynomial function on $\mathcal{F}_h^\Gamma$ such that $(z_h^\Gamma)_{|F} \coloneqq z_F^\Gamma$ for all $F \in \mathcal{F}_h^\Gamma$.

Let $F \in \mathcal{F}_h^\Gamma$ and denote by K_F the (constant) restriction to F of the fracture permeability. We define the local fracture pressure reconstruction operator $r_{K,F}^{l+1} : \underline{P}_{\Gamma,F}^l \to \mathbb{P}^{l+1}(F)$ such that, for all $\underline{z}_F^\Gamma = (z_F^\Gamma, (z_V^\Gamma)_{\mathcal{V}_F}) \in \underline{P}_{\Gamma,F}^l$, $r_{K,F}^{l+1} \underline{z}_F^\Gamma$ is such that, for all $w_F^\Gamma \in \mathbb{P}^{l+1}(F)$,

$$\int_F K_F \nabla_\tau r_{K,F}^{l+1} \underline{z}_F^\Gamma \cdot \nabla_\tau w_F^\Gamma = -\int_F \left(z_F^\Gamma \nabla_\tau \cdot (K_F \nabla_\tau w_F^\Gamma) \right) + \sum_{V\in\mathcal{V}_F} z_V^\Gamma (K_F \nabla_\tau w_F^\Gamma)(V) \cdot \boldsymbol{\tau}_{FV}. \tag{3.27}$$

This relation defines a unique element $\nabla_\tau r_{K,F}^{l+1}\underline{z}_F^\Gamma$, hence a polynomial $r_{K,F}^{l+1}\underline{z}_F^\Gamma \in \mathbb{P}^{l+1}(F)$ up to an additive constant, which we fix by additionally imposing that

$$\int_F \left(r_{K,F}^{l+1}\underline{z}_F^\Gamma - z_F^\Gamma\right) = 0.$$

The reconstruction $r_{K,F}^{l+1}\underline{z}_F^\Gamma$ provides inside F a representation of the fracture pressure one degree higher than the element-based fracture unknown z_F^Γ.

We can now define the tangential diffusion bilinear form $a_{K,h}^{\Gamma,l} : \underline{P}_{\Gamma,h}^l \times \underline{P}_{\Gamma,h}^l \to \mathbb{R}$ such that

$$a_{K,h}^{\Gamma,l}(\underline{z}_h^\Gamma, \underline{q}_h^\Gamma) \coloneqq \sum_{F\in\mathcal{F}_h^\Gamma}\left(\int_F K_F \nabla_\tau r_{K,F}^{l+1}\underline{z}_F^\Gamma \cdot \nabla_\tau r_{K,F}^{l+1}\underline{q}_F^\Gamma + s_{K,F}^{\Gamma,l}(\underline{z}_F^\Gamma, \underline{q}_F^\Gamma)\right), \tag{3.28}$$

where the first term is the Galerkin contribution responsible for consistency, while $s_{K,F}^{\Gamma,l} : \underline{P}_{\Gamma,F}^l \times \underline{P}_{\Gamma,F}^l \to \mathbb{R}$ is the stabilization bilinear form such that, for all $(\underline{z}_F^\Gamma, \underline{q}_F^\Gamma) \in \underline{P}_{\Gamma,F}^l \times \underline{P}_{\Gamma,F}^k$,

$$s_{K,F}^{\Gamma,l}(\underline{z}_F^\Gamma, \underline{q}_F^\Gamma) \coloneqq \sum_{V\in\mathcal{V}_F}\frac{K_F}{h_F}(R_{K,F}^{l+1}\underline{z}_F^\Gamma(V) - z_V^\Gamma)(R_{K,F}^{l+1}\underline{q}_F^\Gamma(V) - q_V^\Gamma), \tag{3.29}$$

with $R_{K,F}^{l+1} : \underline{P}_{\Gamma,F}^l \to \mathbb{P}^{l+1}(F)$ such that, for all $\underline{z}_F^\Gamma \in \underline{P}_{\Gamma,F}^k$, $R_{K,F}^{l+1}\underline{z}_F^\Gamma \coloneqq z_F^\Gamma + (r_{K,F}^{l+1}\underline{z}_F^\Gamma - \pi_F^k r_{K,F}^{l+1}\underline{z}_F^\Gamma)$.

3.4.1.3 Discrete flow problem

Let an integer $k \geq 0$ be fixed. Following [11], in order to have a sufficiently accurate representation of the Darcy velocity when writing the HHO approximation of degree k of the transport problem (3.13), we solve the flow problem (3.6) with an HHO approximation of degree $2k$. Thus, the bulk velocity, bulk pressure, and fracture pressure will be sought, respectively, in $\underline{\boldsymbol{U}}_h^{2k}$ (see (3.22)), $P_{\mathrm{B},h}^{2k} \coloneqq \mathbb{P}^{2k}(\mathcal{T}_h)$ (the space of broken polynomials of total degree $\leq 2k$ over $\mathcal{T}_h$), and $\underline{P}_{\Gamma,h}^{2k}$ (see (3.26)). The discrete counterparts of the continuous bilinear forms defined in Section 3.2.2 are the bilinear forms $a_{K,h}^{\xi,2k} : \underline{\boldsymbol{U}}_h^{2k} \times \underline{\boldsymbol{U}}_h^{2k} \to \mathbb{R}$, $b_h^{2k} : \underline{\boldsymbol{U}}_h^{2k} \times P_{\mathrm{B},h}^{2k} \to \mathbb{R}$,

$d_h^{2k} : \underline{\boldsymbol{U}}_h^{2k} \times \underline{P}_{\Gamma,h}^{2k} \to \mathbb{R}$ such that

$$a_{K,h}^{\xi,2k}(\underline{\boldsymbol{u}}_h, \underline{\boldsymbol{q}}_h) \coloneqq a_{K,h}^{2k}(\underline{\boldsymbol{u}}_h, \underline{\boldsymbol{q}}_h) + \sum_{F\in\mathcal{F}_h^\Gamma} \int_F \left(\lambda_F^\xi [\![\underline{\boldsymbol{u}}_h]\!]_F [\![\underline{\boldsymbol{q}}_h]\!]_F + \lambda_F \{\{\underline{\boldsymbol{u}}_h\}\}_F \{\{\underline{\boldsymbol{q}}_h\}\}_F \right),$$

$$b_h^{2k}(\underline{\boldsymbol{u}}_h, p_h) \coloneqq \sum_{T\in\mathcal{T}_h} \left(-\int_T \boldsymbol{u}_T \cdot \nabla p_T + \sum_{F\in\mathcal{F}_T} \int_F u_{TF} p_T \right),$$

$$d_h^{2k}(\underline{\boldsymbol{u}}_h, \underline{p}_h^\Gamma) \coloneqq \sum_{F\in\mathcal{F}_h^\Gamma} \int_F [\![\underline{\boldsymbol{u}}_h]\!]_F p_F^\Gamma,$$

where the bilinear forms $a_{K,h}^{2k}$ and $a_{K,h}^{\Gamma,2k}$ are defined by (3.24) and (3.28), respectively, and, for all $p_h \in P_{\mathrm{B},h}^{2k}$ and all $T \in \mathcal{T}_h$, we have set $p_T \coloneqq p_{h|T}$.

Letting $\mathcal{A}_{\xi,h,2k}^{\mathrm{flow}} : \left(\underline{\boldsymbol{U}}_h^{2k} \times P_{\mathrm{B},h}^{2k} \times \underline{P}_{\Gamma,h}^{2k}\right) \times \left(\underline{\boldsymbol{U}}_h^{2k} \times P_{\mathrm{B},h}^{2k} \times \underline{P}_{\Gamma,h}^{2k}\right) \to \mathbb{R}$ be the global bilinear form such that

$$\begin{aligned}\mathcal{A}_{\xi,h,2k}^{\mathrm{flow}}((\underline{\boldsymbol{u}}_h, p_h, \underline{p}_h^\Gamma), (\underline{\boldsymbol{q}}_h, z_h, \underline{z}_h^\Gamma)) \coloneqq\ & a_{K,h}^{\xi,2k}(\underline{\boldsymbol{u}}_h, \underline{\boldsymbol{q}}_h) + b_h^{2k}(\underline{\boldsymbol{u}}_h, z_h) - b_h^{2k}(\underline{\boldsymbol{q}}_h, p_h) \\ & + d_h^{2k}(\underline{\boldsymbol{q}}_h, \underline{p}_h^\Gamma) - d_h^{2k}(\underline{\boldsymbol{u}}_h, \underline{z}_h^\Gamma) + a_{K,h}^{\Gamma,2k}(\underline{p}_h^\Gamma, \underline{z}_h^\Gamma),\end{aligned}$$

the HHO discretization of problem (3.6) reads: Find $(\underline{\boldsymbol{u}}_h, p_h, \underline{p}_h^\Gamma) \in \underline{\boldsymbol{U}}_h^{2k} \times P_{\mathrm{B},h}^{2k} \times \underline{P}_{\Gamma,h,0}^{2k}$ such that, for all $(\underline{\boldsymbol{q}}_h, z_h, \underline{z}_h^\Gamma) \in \underline{\boldsymbol{U}}_h^{2k} \times P_{\mathrm{B},h}^{2k} \times \underline{P}_{\Gamma,h}^{2k}$,

$$\mathcal{A}_{\xi,h,2k}^{\mathrm{flow}}((\underline{\boldsymbol{u}}_h, p_h, \underline{p}_h^\Gamma), (\underline{\boldsymbol{q}}_h, z_h, \underline{z}_h^\Gamma)) = \int_{\Omega_{\mathrm{B}}} f z_h + \int_\Gamma \ell_\Gamma f_\Gamma z_h^\Gamma. \tag{3.30}$$

3.4.2 Passive transport

We now formulate the HHO discretization of the passive transport problem (3.13). In what follows, the polynomial degree k is the same as in Section 3.4.1.3.

3.4.2.1 Discrete bulk concentration unknowns, bulk concentration reconstruction, and diffusion-dispersion diffusion bilinear form

We define the fully discontinuous space of bulk concentration unknowns as follows:

$$\widehat{\underline{P}}_{\mathrm{B},h}^k \coloneqq \left\{ \underline{z}_h = (z_T, (z_{TF})_{F\in\mathcal{F}_T})_{T\in\mathcal{T}_h} \ : \ \begin{array}{l} \text{for all } T \in \mathcal{T}_h,\ z_T \in \mathbb{P}^k(T) \text{ and} \\ z_{TF} \in \mathbb{P}^k(F) \text{ for all } F \in \mathcal{F}_T \end{array} \right\}.$$

For all $T \in \mathcal{T}_h$, we denote by $P_{\mathrm{B},T}^k$ the restriction of $\widehat{\underline{P}}_{\mathrm{B},h}^k$ to T, and we set $\underline{z}_T = (z_T, (z_{TF})_{F\in\mathcal{F}_T}) \in \underline{P}_{\mathrm{B},T}^k$. For any interface $F \in \mathcal{F}_h^{\mathrm{i}}$ shared by distinct elements

$T_1, T_2 \in \mathcal{T}_F$, we introduce the jump and average operators such that, for any $\underline{z}_h \in \widehat{\underline{P}}^k_{\mathrm{B},h}$,

$$[\![\underline{z}_h]\!]_F = z_{T_1F} - z_{T_2F}, \qquad \{\{\underline{z}_h\}\}_F = \frac{z_{T_1F} + z_{T_2F}}{2}.$$

The following subspace of $\widehat{\underline{P}}^k_{\mathrm{B},h}$ strongly incorporates the continuity of concentration unknowns across interfaces contained in the bulk region:

$$\underline{P}^k_{\mathrm{B},h} \coloneqq \left\{ \underline{z}_h \in \widehat{\underline{P}}^k_{\mathrm{B},h} \ : \ [\![\underline{z}_h]\!]_F = 0 \text{ for all } F \in \mathcal{F}_h^{\mathrm{i}} \setminus \mathcal{F}_h^{\Gamma} \right\}. \tag{3.31}$$

Let now an element $T \in \mathcal{T}_h$ be fixed, and denote by $\boldsymbol{D}_T$ the restriction to T of the bulk diffusion-dispersion tensor. We define the bulk concentration reconstruction operator $r^{k+1}_{D,T} : \underline{P}^k_{\mathrm{B},T} \to \mathbb{P}^{k+1}(T)$ such that, for all $\underline{z}_T = (z_T, (z_{TF})_{F\in\mathcal{F}_t}) \in \underline{P}^k_{\mathrm{B},T}$, $r^{k+1}_{D,T}\underline{z}_T$ solves

$$\int_T \boldsymbol{D}_T \nabla r^{k+1}_{D,T}\underline{z}_T \cdot \nabla w_T = -\int_T \Big(z_T \nabla\cdot(\boldsymbol{D}_T\nabla w_T)\Big) + \sum_{F\in\mathcal{F}_T}\int_F z_{TF}(\boldsymbol{D}_T\nabla w_T\cdot\boldsymbol{n}_{TF}),$$

for all $w_T \in \mathbb{P}^{k+1}(T)$. This condition defines $r^{k+1}_{D,T}\underline{z}_T$ up to a constant, which we fix by additionally imposing that

$$\int_T \Big(r^{k+1}_{D,T}\underline{z}_T - z_T \Big) = 0.$$

The polynomial $r^{k+1}_{D,T}\underline{z}_T$ provides a representation of the concentration inside T one degree higher than the element-based unknown z_T.

We are now ready to define a global molecular diffusion bilinear form closely inspired by [83]. More precisely, we let $a^k_{D,h} : \underline{P}^k_{\mathrm{B},h} \times \underline{P}^k_{\mathrm{B},h} \to \mathbb{R}$ be such that, for all $(\underline{c}_h, \underline{z}_h) \in \underline{P}^k_{\mathrm{B},h} \times \underline{P}^k_{\mathrm{B},h}$,

$$a^k_{D,h}(\underline{c}_h, \underline{z}_h) \coloneqq \sum_{T\in\mathcal{T}_h}\left(\int_T \boldsymbol{D}_T \nabla r^{k+1}_{D,T}\underline{c}_T \cdot \nabla r^{k+1}_{D,T}\underline{z}_T + s^k_{D,T}(\underline{c}_T, \underline{z}_T)\right),$$

where the first term is the Galerkin contribution responsible for consistency, while $s^k_{D,T} : \underline{P}^k_{\mathrm{B},T} \times \underline{P}^k_{\mathrm{B},T} \to \mathbb{R}$ is the stabilization bilinear form such that, for all $(\underline{c}_T, \underline{z}_T) \in \underline{P}^k_{\mathrm{B},T} \times \underline{P}^k_{\mathrm{B},T}$,

$$s^k_{D,T}(\underline{c}_T, \underline{z}_T) \coloneqq \sum_{F\in\mathcal{F}_T}\int_F \frac{D_{TF}}{h_F}(R^{k+1}_{D,T}\underline{c}_T - c_{TF})(R^{k+1}_{D,T}\underline{z}_T - z_{TF}),$$

with $D_{TF} \coloneqq \boldsymbol{D}_T\boldsymbol{n}_{TF}\cdot\boldsymbol{n}_{TF}$ for all $F \in \mathcal{F}_T$ and $R^{k+1}_{D,T} : \underline{P}^k_{\mathrm{B},T} \to \mathbb{P}^{k+1}(T)$ such that, for all $\underline{z}_T \in \underline{P}^k_{\mathrm{B},T}$, $R^{k+1}_{D,T}\underline{z}_T \coloneqq z_T + (r^{k+1}_{D,T}\underline{z}_T - \pi^k_T r^{k+1}_{D,T}\underline{z}_T)$.

3.4.2.2 Fracture concentration unknowns, fracture concentration reconstruction, and diffusion-dispersion bilinear form

The fracture concentration is sought in the space $\underline{P}^k_{\Gamma,h}$ defined by (3.25) with $l = k$. For all $F \in \mathcal{F}^\Gamma_h$, we define the fracture concentration reconstruction operator $r^{k+1}_{D,F} : \underline{P}^k_{\Gamma,F} \to \mathbb{P}^{k+1}(F)$ as in (3.27) setting $l = k$ and replacing K_F by $D_F := D_{\Gamma|F}$. Similary, we denote by $a^{\Gamma,k}_{D,h} : \underline{P}^k_{\Gamma,h} \times \underline{P}^k_{\Gamma,h} \to \mathbb{R}$ the tangential molecular diffusion bilinear form defined as (3.28)–(3.29) with $l = k$ and K_F replaced by D_F.

3.4.2.3 Darcy velocities and advection-reaction bilinear forms in the bulk region and in the fracture

In order to discretize the advection-reaction terms that appear in the passive transport problem, we need suitable representations of the Darcy velocity both in the bulk region and inside the fracture.

Denote by $(\underline{\boldsymbol{u}}_h, p_h, \underline{p}^\Gamma_h) \in \underline{\boldsymbol{U}}^{2k}_h \times P^{2k}_{\mathrm{B},h} \times \underline{P}^{2k}_{\Gamma,h,0}$ the solution of the discrete flow problem (3.30). For any $T \in \mathcal{T}_h$, taking in (3.30) $\underline{\boldsymbol{q}}_h = \underline{\boldsymbol{0}}$, z_h such that $z_{T'} = 0$ for all $T' \in \mathcal{T}_h \setminus \{T\}$ while z_T spans $\mathbb{P}^{2k}(T)$, and $\underline{z}^\Gamma_h = \underline{0}$, we infer the following local balance for the discrete bulk Darcy velocity:

$$\int_T -\boldsymbol{u}_T \nabla z_T + \sum_{F \in \mathcal{F}_T} \int_F u_{TF} z_T = \int_T f z_T \qquad \forall z_T \in \mathbb{P}^{2k}(T). \tag{3.32}$$

Additionally, by definition (3.22) of $\underline{\boldsymbol{U}}^{2k}_h$, the Darcy velocity thus defined has continuous normal components across interfaces contained in the bulk in the sense that $[\![\underline{\boldsymbol{u}}_h]\!]_F = 0$ for all $F \in \mathcal{F}^{\mathrm{i}}_h \setminus \mathcal{F}^\Gamma_h$. Thus, $\underline{\boldsymbol{u}}_h$ is the natural candidate to play the role of the Darcy velocity in the bulk region.

Let now a fracture face $F \in \mathcal{F}^\Gamma_h$ be fixed, and define the fracture Darcy velocity $\underline{\boldsymbol{u}}^\Gamma_F = (\boldsymbol{u}^\Gamma_F, (u^\Gamma_{FV})_{V \in \mathcal{V}_F})$ such that

$$\boldsymbol{u}^\Gamma_F := -K_F \nabla_\tau r^{2k+1}_{K,F} \underline{p}^\Gamma_F,$$

and, for all $V \in \mathcal{V}_F$,

$$u^\Gamma_{FV} := \begin{cases} \boldsymbol{u}^\Gamma_F(V) \cdot \boldsymbol{\tau}_{FV} + \gamma^{\mathrm{num}}_{FV}(\underline{p}^\Gamma_F) & \text{if } V \in \mathcal{V}^{\mathrm{i}}_h \\ 0 & \text{if } V \in \mathcal{V}^{\mathrm{b}}_h, \end{cases}$$

where, for all $V \in \mathcal{V}_F$, $\gamma^{\mathrm{num}}_{FV} : \underline{P}^{2k}_{\Gamma,F} \to \mathbb{R}$ is the boundary residual operator defined as in [89, Lemma 3]. With this choice for the fracture Darcy velocity, the following local balance holds for all $F \in \mathcal{F}^\Gamma_h$:

$$-\int_F \boldsymbol{u}^\Gamma_F \cdot \nabla_\tau z^\Gamma_F + \sum_{V \in \mathcal{V}_F} u^\Gamma_{FV}(z^\Gamma_F(V) - z^\Gamma_V) = \int_F \Big(\ell_\Gamma f_\Gamma + [\![\underline{\boldsymbol{u}}_h]\!]_F\Big) z^\Gamma_F, \tag{3.33}$$

for all $\underline{z}_F^\Gamma \in \underline{P}_{\Gamma,F}^{2k}$. Moreover, the discrete fracture Darcy velocity is continuous across internal vertices, that is to say,

$$\sum_{F\in\mathcal{F}_V} u_{FV}^\Gamma = 0 \text{ for all } V \in \mathcal{V}_h^{\mathrm{i}}. \tag{3.34}$$

$\underline{\boldsymbol{u}}_F^\Gamma$ is therefore the natural candidate to play the role of the Darcy velocity inside the fracture.

We now have all the ingredients to define discrete counterparts of the advective terms in the bulk region and inside the fracture. More precisely, closely following [75], we define the advection-reaction bilinear forms $a_{\boldsymbol{u},f,h}^k : \underline{P}_{\mathrm{B},h}^k \times \underline{P}_{\mathrm{B},h}^k \to \mathbb{R}$ and $a_{\boldsymbol{u},f,h}^{\Gamma,k} : \underline{P}_{\Gamma,h}^k \times \underline{P}_{\Gamma,h}^k$ such that

$$\begin{aligned}
a_{\boldsymbol{u},f,h}^k(\underline{c}_h,\underline{z}_h) &:= \sum_{T\in\mathcal{T}_h}\Bigg(\int_T c_T(-\boldsymbol{u}_T\cdot\nabla z_T + f^- z_T) \\
&\qquad + \sum_{F\in\mathcal{F}_T}\int_F u_{TF}c_T(z_T - z_{TF}) + s_{\boldsymbol{u},T}^k(\underline{c}_T,\underline{z}_T)\Bigg), \\
a_{\boldsymbol{u},f,h}^{\Gamma,k}(\underline{c}_h^\Gamma,\underline{z}_h^\Gamma) &:= \sum_{F\in\mathcal{F}_h^\Gamma}\Bigg(\int_F c_F^\Gamma(-\boldsymbol{u}_F^\Gamma\cdot\nabla_\tau z_F^\Gamma + \ell_\Gamma f_\Gamma^- z_F^\Gamma) \\
&\qquad + \sum_{V\in\mathcal{V}_F} u_{FV}^\Gamma c_F^\Gamma(V)(z_F^\Gamma(V) - z_V^\Gamma) + s_{\boldsymbol{u},F}^{\Gamma,k}(\underline{c}_F^\Gamma,\underline{z}_F^\Gamma)\Bigg),
\end{aligned} \tag{3.35}$$

where, for all $T \in \mathcal{T}_h$ and all $F \in \mathcal{F}_h^\Gamma$, $s_{\boldsymbol{u},T}^k : \underline{P}_{\mathrm{B},T}^k \times \underline{P}_{\mathrm{B},T}^k \to \mathbb{R}$ and $s_{\boldsymbol{u},F}^{\Gamma,k} : \underline{P}_{\Gamma,F}^k \times \underline{P}_{\Gamma,F}^k \to \mathbb{R}$ are the upwind stabilization bilinear forms respectively in the bulk and inside the fracture such that

$$\begin{aligned}
s_{\boldsymbol{u},T}^k(\underline{c}_T,\underline{z}_T) &:= \sum_{F\in\mathcal{F}_T}\int_F \frac{|u_{TF}| - u_{TF}}{2}(c_T - c_{TF})(z_T - z_{TF}), \\
s_{\boldsymbol{u},F}^{\Gamma,k}(\underline{c}_F^\Gamma,\underline{z}_F^\Gamma) &:= \sum_{V\in\mathcal{V}_F}\frac{|u_{FV}^\Gamma| - u_{FV}^\Gamma}{2}(c_F^\Gamma(V) - c_V^\Gamma)(z_F^\Gamma(V) - z_V^\Gamma).
\end{aligned} \tag{3.36}$$

3.4.2.4 Passive transport problem

We are now ready to state the HHO discretization of the transport problem (3.13). At the discrete level, the counterpart of the continuous bilinear form defined in (3.12) is the bilinear form $\mathcal{A}_{\xi,h,k}^{\mathrm{transp}} : \left(\underline{P}_{\mathrm{B},h}^k \times \underline{P}_{\Gamma,h}^k\right) \times \left(\underline{P}_{\mathrm{B},h}^k \times \underline{P}_{\Gamma,h}^k\right) \to \mathbb{R}$ such

that

$$\begin{aligned}\mathcal{A}^{\mathrm{transp}}_{\xi,h,k}((\underline{c}_h,\underline{c}_h^\Gamma),(\underline{z}_h,\underline{z}_F^\Gamma)) &:= a^k_{D,h}(\underline{c}_h,\underline{z}_h)+a^k_{\boldsymbol{u},f,h}(\underline{c}_h,\underline{z}_h)+a^{\Gamma,k}_{D,h}(\underline{c}_h^\Gamma,\underline{z}_h^\Gamma)+a^{\Gamma,k}_{\boldsymbol{u},f,h}(\underline{c}_h^\Gamma,\underline{z}_h^\Gamma)\\ &+\sum_{F\in\mathcal{F}_h^\Gamma}\int_F\left(\beta_F^\xi(\{\{\underline{c}_h\}\}_F-c_F^\Gamma)(\{\{\underline{z}_h\}\}_F-z_F^\Gamma)+\beta_F[\![\underline{c}_h]\!]_F[\![\underline{z}_h]\!]_F\right)\\ &+\sum_{F\in\mathcal{F}_h^\Gamma}\int_F\left(\{\{\underline{\boldsymbol{u}}_h\}\}_F\{\{\underline{c}_h\}\}_F[\![\underline{z}_h]\!]_F+\frac{1}{8}[\![\underline{\boldsymbol{u}}_h]\!]_F[\![\underline{c}_h]\!]_F[\![\underline{z}_h]\!]_F\right)\\ &+\sum_{F\in\mathcal{F}_h^\Gamma}\int_F\frac{1}{2}[\![\underline{\boldsymbol{u}}_h]\!]_F(\{\{\underline{c}_h\}\}_F+c_F^\Gamma)(\{\{\underline{z}_h\}\}_F-z_F^\Gamma),\end{aligned}\tag{3.37}$$

where the role of the terms in the last three lines is to enforce the transmission conditions (3.9) on Γ. The HHO discretization of problem (3.13) then reads: Find $(\underline{c}_h,\underline{c}_h^\Gamma)\in\underline{P}^k_{\mathrm{B},h}\times\underline{P}^k_{\Gamma,h}$ such that

$$\mathcal{A}^{\mathrm{transp}}_{\xi,h,k}((\underline{c}_h,\underline{c}_h^\Gamma),(\underline{z}_h,\underline{z}_F^\Gamma))=\int_{\Omega_{\mathrm{B}}}f^+\widehat{c}z_h+\int_\Gamma\ell_\Gamma f_\Gamma^+\widehat{c}_\Gamma z_h^\Gamma,\tag{3.38}$$

for all $(\underline{z}_h,\underline{z}_h^\Gamma)\in\underline{P}^k_{\mathrm{B},h}\times\underline{P}^k_{\Gamma,h}$. We now prove the discrete counterpart of the Theorem 3.2.

Theorem 3.8 (Discrete coercivity)**.** *Let $\xi>1/2$. Then, for all $(\underline{z}_h,\underline{z}_h^\Gamma)\in\underline{P}^k_{\mathrm{B},h}\times\underline{P}^k_{\Gamma,h}$, it holds*

$$\begin{aligned}\mathcal{A}^{\mathrm{transp}}_{\xi,h,k}((\underline{z}_h,\underline{z}_h^\Gamma),(\underline{z}_h,\underline{z}_F^\Gamma)) &= a^k_{D,h}(\underline{z}_h,\underline{z}_h)+a^{\Gamma,k}_{D,h}(\underline{z}_h^\Gamma,\underline{z}_h^\Gamma)\\ &+\sum_{T\in\mathcal{T}_h}\left(\|\chi_{\mathrm{B},T}^{1/2}z_T\|_T^2+\sum_{F\in\mathcal{F}_T}\frac{1}{2}\||u_{TF}|^{1/2}(z_T-z_{TF})\|_F^2\right)\\ &+\sum_{F\in\mathcal{F}_h^\Gamma}\left(\|\chi_{\Gamma,F}^{1/2}z_F^\Gamma\|_F^2+\sum_{V\in\mathcal{V}_F}\frac{1}{2}|u_{FV}^\Gamma|(z_F^\Gamma(V)-z_V^\Gamma)^2\right)\\ &+\sum_{F\in\mathcal{F}_h^\Gamma}\left(\beta_F^\xi\|\{\{\underline{z}_h\}\}_F-z_F^\Gamma\|_F^2+\beta_F\|[\![\underline{c}_h]\!]_F\|_F^2\right),\end{aligned}\tag{3.39}$$

where, for all $T\in\mathcal{T}_h$ and all $F\in\mathcal{F}_h^\Gamma$, $\chi_{\mathrm{B},T}:=(\chi_{\mathrm{B}})_{|T}$ and $\chi_{\Gamma,F}:=(\chi_\Gamma)_{|F}$, respectively.

Remark 3.9 (Upwind contributions). Unlike the continuous case (see Theorem 3.2), we have in the second and third lines of the energy balance (3.39) upwind-related contributions of bulk and fracture region, respectively. These could be removed at the price of having coercivity in a weaker norm.

Proof. The proof is similar to the one of the Theorem 3.2. Let $(\underline{z}_h,\underline{z}_h^\Gamma)\in\underline{P}^k_{\mathrm{B},h}\times\underline{P}^k_{\Gamma,h}$

be fixed and set $(\underline{\boldsymbol{z}}_h, \underline{\boldsymbol{z}}_h^\Gamma) \in \underline{P}_{\mathrm{B},h}^{2k} \times \underline{P}_{\Gamma,h}^{2k}$ such that,

$$\begin{aligned} \forall T \in \mathcal{T}_h, \qquad (\underline{\boldsymbol{z}}_h)_{|T} = \underline{\boldsymbol{z}}_T = (\boldsymbol{z}_T, (\boldsymbol{z}_{TF})_{F\in\mathcal{F}_T}) &:= (\frac{z_T^2}{2}, (\frac{z_{TF}^2}{2})_{F\in\mathcal{F}_T}), \\ \forall F \in \mathcal{F}_h^\Gamma, \qquad (\underline{\boldsymbol{z}}_h^\Gamma)_{|F} = \underline{\boldsymbol{z}}_F^\Gamma = (\boldsymbol{z}_F^\Gamma, (\boldsymbol{z}_V^\Gamma)_{V\in\mathcal{V}_F}) &:= (\frac{(z_F^\Gamma)^2}{2}, (\frac{(z_V^\Gamma)^2}{2})_{V\in\mathcal{V}_F}). \end{aligned} \tag{3.40}$$

Using the definition of the global bilinear form $\mathcal{A}_{\xi,h,k}^{\mathrm{transp}}$ (3.37) with $(\underline{c}_h, \underline{c}_h^\Gamma) = (\underline{z}_h, \underline{z}_h^\Gamma)$, we immediately obtain the terms in the first and last line of (3.39). Let now $\mathcal{I}_1 := a_{\boldsymbol{u},f,h}^k(\underline{z}_h, \underline{z}_h)$, $\mathcal{I}_2 := a_{\boldsymbol{u},f,h}^{\Gamma,k}(\underline{z}_h^\Gamma, \underline{z}_h^\Gamma)$, and let $\mathcal{I}_3$ gather the remaining coupling terms, that is to say, the two last lines on the right-hand side of (3.37) with $\underline{c}_h = \underline{z}_h$ and $c_F^\Gamma = z_F^\Gamma$ for all $F \in \mathcal{F}_h^\Gamma$. Expanding $\mathcal{I}_1$ and $\mathcal{I}_2$ according to their respective definitions (3.35), and recalling the definitions of the stabilization bilinear forms $s_{\boldsymbol{u},T}^k$ and $s_{\boldsymbol{u},F}^k$ (3.36), it is inferred that

$$\mathcal{I}_1 = \sum_{T\in\mathcal{T}_h}\left(\int_T\Big(-\boldsymbol{u}_T\cdot\nabla\boldsymbol{z}_T + f^-z_T^2\Big) + \sum_{F\in\mathcal{F}_T}\int_F\Big(u_{TF}(\boldsymbol{z}_T-\boldsymbol{z}_{TF}) + \frac{1}{2}|u_{TF}|(z_T-z_{TF})^2\Big)\right), \tag{3.41a}$$

$$\mathcal{I}_2 = \sum_{F\in\mathcal{F}_h^\Gamma}\left(\int_F\Big(-\boldsymbol{u}_F^\Gamma\cdot\nabla_\tau\boldsymbol{z}_F^\Gamma + \ell_\Gamma f_\Gamma^- {z_F^\Gamma}^2\Big) + \sum_{V\in\mathcal{V}_F}\Big(u_{FV}^\Gamma(\boldsymbol{z}_F^\Gamma(V)-\boldsymbol{z}_V^\Gamma) + \frac{1}{2}|u_{FV}^\Gamma|(z_F^\Gamma(V)-z_V^\Gamma)^2\Big)\right). \tag{3.41b}$$

Using the local balances (3.32) in the bulk and (3.33) inside the fracture (that hold since $\boldsymbol{z}_T \in \mathbb{P}^{2k}(T)$ for all $T \in \mathcal{T}_h$ and $\underline{\boldsymbol{z}}_F^\Gamma \in \underline{P}_{\Gamma,F}^{2k}$ for all $F \in \mathcal{F}_h^\Gamma$) together with the fact that

$$\sum_{T\in\mathcal{T}_h}\sum_{F\in\mathcal{F}_T} u_{TF}\boldsymbol{z}_{TF} = \sum_{F\in\mathcal{F}_h^\Gamma}[\![\underline{\boldsymbol{u}}_h\underline{\boldsymbol{z}}_h]\!]_F,$$

which follows from $(\underline{\boldsymbol{u}}_h, \underline{\boldsymbol{z}}_h) \in \underline{\boldsymbol{U}}_h^{2k} \times \underline{P}_{\mathrm{B},h}^{2k}$, we finally get from (3.41a) and (3.41b)

$$\mathcal{I}_1 = \sum_{T\in\mathcal{T}_h}\left(\|\chi_{\mathrm{B},T}^{1/2}z_T\|_T^2 + \sum_{F\in\mathcal{F}_T}\frac{1}{2}\||u_{TF}|^{1/2}(z_T-z_{TF})\|_F^2\right) - \sum_{F\in\mathcal{F}_h^\Gamma}\int_F[\![\underline{\boldsymbol{u}}_h\underline{\boldsymbol{z}}_h]\!]_F, \tag{3.42a}$$

$$\mathcal{I}_2 = \sum_{F\in\mathcal{F}_h^\Gamma}\left(\|\chi_{\Gamma,F}^{1/2}z_F^\Gamma\|_F^2 + \sum_{V\in\mathcal{V}_F}\frac{1}{2}|u_{FV}^\Gamma|(z_F^\Gamma(V)-z_V^\Gamma)^2\right) + \sum_{F\in\mathcal{F}_h^\Gamma}\int_F[\![\underline{\boldsymbol{u}}_h]\!]_F\boldsymbol{z}_F^\Gamma. \tag{3.42b}$$

To conclude, it suffices to prove that the sum of the last term in the right-hand side of (3.42a) and the last term in the right-hand side of (3.42b) and $\mathcal{I}_3$ is equal to

zero. Using (3.18) to infer first that $[\![\underline{\boldsymbol{u}}_h \underline{\boldsymbol{z}}_h]\!]_F = [\![\underline{\boldsymbol{u}}_h]\!]_F \{\{\underline{\boldsymbol{z}}_h\}\}_F + \{\{\underline{\boldsymbol{u}}_h\}\}_F [\![\underline{\boldsymbol{z}}_h]\!]_F$ and then that $[\![\underline{\boldsymbol{z}}_h]\!]_F = [\![\underline{z}_h]\!]_F \{\{\underline{z}_h\}\}_F$, we get

$$\sum_{F\in\mathcal{F}_h^\Gamma}\int_F\Big([\![\underline{\boldsymbol{u}}_h]\!]_F \boldsymbol{z}_F^\Gamma - [\![\underline{\boldsymbol{u}}_h\underline{\boldsymbol{z}}_h]\!]_F\Big)+\mathcal{I}_3 = \sum_{F\in\mathcal{F}_h^\Gamma}\int_F\Big([\![\underline{\boldsymbol{u}}_h]\!]_F(1/2\{\{\underline{z}_h\}\}_F^2+1/8[\![\underline{z}_h]\!]_F^2-\{\{\underline{\boldsymbol{z}}_h\}\}_F)\Big),$$

that concludes the proof since $\{\{\underline{\boldsymbol{z}}_h\}\}_F = \frac{1}{2}(\{\{\underline{z}_h\}\}_F^2 + \frac{1}{4}[\![\underline{z}_h]\!]_F^2)$. □

Remark 3.10 (Polynomial degree and local conservation). The use of polynomials of degree $2k$ to solve the discrete flow problem (3.38) is required in the proof of Theorem 3.8. Indeed, to pass from (3.41) to (3.42), the argument is that both the local balances (3.32) and (3.33) are valid when we use as test functions $\underline{\boldsymbol{z}}_h \in \underline{\boldsymbol{P}}_{\mathrm{B},h}^{2k}$ and $\underline{\boldsymbol{z}}_h^\Gamma \in \underline{\boldsymbol{P}}_{\Gamma,h}^{2k}$ defined by (3.40).

3.4.3 Extension to the unsteady case

In the numerical tests of Sections 3.5.2–3.5.3 below, we consider the physically relevant situation of unsteady passive transport with a steady Darcy velocity field. The extension of the HHO scheme (3.38) to this situation is briefly discussed in what follows.

The transport problem can be extended to the unsteady case by assuming that the unknowns depend on the time and adding the unsteady contributions $\phi \mathrm{d}_t c$ and $\ell_\Gamma \phi_\Gamma \mathrm{d}_t c_\Gamma$ in, respectively, (3.7a) and (3.8a), where $\phi : \Omega_\mathrm{B} \to \mathbb{R}$ and $\phi_\Gamma : \Gamma \to \mathbb{R}$ stand, respectively, for the porosity in the bulk region and in the fracture such that $0 < \phi < 1$ and $0 < \phi_\Gamma < 1$. In the numerical tests, we assume that these are piecewise constant on the partitions $\mathcal{P}_\mathrm{B}$ and $\mathcal{P}_\Gamma$ (see (3.2) and (3.3)), respectively. More generally, the porosities could also depend on time. Initial conditions for the bulk and the fracture concentration $c(t = 0, \cdot) = c^0(\cdot)$ and $c_\Gamma(t = 0, \cdot) = c_\Gamma^0(\cdot)$ close the problem. The functions $\widehat{c}$ and $\widehat{c_\Gamma}$ that represent the concentration of solute as it is injected in, respectively, the bulk and the fracture, will also be allowed to depend on time.

To discretize in time, we consider for sake of simplicity a uniform partition $(t^n)_{0\le n\le N}$ of the time interval $[0, t_F]$ with $t^0 = 0$, $t^N = t_F$ the final time of computation, and $t^n - t^{n-1} = \delta t$ the constant time step for all $1 \le n \le N$. For any sufficiently regular function of time φ taking values in a vector space V, we denote by $\varphi^n \in V$ its value at discrete time t^n and we introduce the backward differencing operator δ_t such that, for all $1 \le n \le N$,

$$\delta_\mathrm{t}\varphi^n := \frac{\varphi^n - \varphi^{n-1}}{\delta t} \in V.$$

With this notation, the discrete problem reads: For all $1 \le n \le N$, find $(\underline{c}_h^n, \underline{c}_h^{\Gamma,n}) \in \underline{P}_{\mathrm{B},h}^k \times \underline{P}_{\Gamma,h}^k$ such that, for all $(\underline{z}_h, \underline{z}_h^\Gamma) \in \underline{P}_{\mathrm{B},h}^k \times \underline{P}_{\Gamma,h}^k$,

$$\begin{aligned}\int_{\Omega_\mathrm{B}} \phi \delta_\mathrm{t} c_h^n z_h + \int_\Gamma \ell_\Gamma \phi_\Gamma \delta_\mathrm{t} c_h^{\Gamma,n} z_h^\Gamma + \mathcal{A}_{\xi,h,k}^{\mathrm{transp}}((\underline{c}_h^n, \underline{c}_h^{\Gamma,n}), (\underline{z}_h, \underline{z}_F^\Gamma)) \\ = \int_{\Omega_\mathrm{B}} f^+ \widehat{c}^n z_h + \int_\Gamma \ell_\Gamma f_\Gamma^+ \widehat{c}_\Gamma^n z_h^\Gamma.\end{aligned} \tag{3.43}$$

The initial condition is discretized taking c_h^0 and $c_h^{\Gamma,0}$ equal to the L^2-orthogonal projections on $\mathbb{P}^k(\mathcal{T}_h)$ and $\mathbb{P}^l(\mathcal{F}_h^\Gamma)$ of c^0 and c_Γ^0, respectively. Notice that it is not necessary to prescribe face values for the concentration in the bulk region, nor vertex values for the concentration in the fracture, as these discrete unknowns do not appear in the discretization of the time derivative.

3.5 Numerical results

This section contains an extensive numerical validation of the HHO method. We first study numerically the convergence rates achieved by the method, and then propose two more physical test cases in which fractures act as barriers or conduits, depending on the value of the permeability parameters.

3.5.1 Convergence for a steady problem

We start by a numerical study of the convergence rates obtained by the method for both the flow problem (3.30) and the steady passive transport problem (3.38).

3.5.1.1 Analytical solution

We approximate problems (3.30) and (3.38) on the square domain $\Omega = (0,1)^2$ crossed by the fracture $\Gamma = \{\boldsymbol{x} \in \Omega \ : \ x_1 = 0.5\}$, and set $\ell_\Gamma = 0.01$ and $\xi = 3/4$. For the flow problem, we consider the exact solutions corresponding to the bulk and fracture pressures

$$p(\boldsymbol{x}) \coloneqq \begin{cases} \cos(2x_1)\cos(\pi x_2) & \text{if } x_1 < 0.5 \\ \cos(\pi x_1)\cos(\pi x_2) & \text{if } x_1 > 0.5 \end{cases}, \qquad p_\Gamma(\boldsymbol{x}) \coloneqq \{\{c\}\}_\Gamma - \lambda_\Gamma [\![\boldsymbol{u}]\!]_\Gamma \cdot \boldsymbol{n}_\Gamma,$$

and let $\boldsymbol{u}_{|\Omega_{\mathrm{B},i}} = -\boldsymbol{K}\nabla p_{|\Omega_{\mathrm{B},i}}$ for $i \in \{1,2\}$ and $\boldsymbol{u}_\Gamma = -K_\Gamma \nabla_\tau p_\Gamma$, with $\kappa_\Gamma^\tau = 1$, $\kappa_\Gamma^n = 0.01$ and

$$\boldsymbol{K} \coloneqq \frac{\cos(1)}{\sin(1) + \pi/2} \begin{bmatrix} \kappa_\Gamma^n/(2\ell_\Gamma) & 0 \\ 0 & 1 \end{bmatrix}, \qquad K_\Gamma \coloneqq \kappa_\Gamma^\tau \ell_\Gamma.$$

For the passive transport problem, the exact solutions corresponding to the bulk and fracture concentrations are given by

$$c(\boldsymbol{x}) \coloneqq \begin{cases} \exp\left(2/\pi \cos(\pi x_1)\left(\beta_\Gamma - \frac{1}{8}\cos(\pi x_2)\frac{\kappa_\Gamma^n}{\ell_\Gamma}\frac{\cos(1)(\sin(1)-\pi/2)}{\sin(1)+\pi/2}\right)\right) & \text{if } x_1 < 1/2 \\ \exp\left(2/\pi(\cos(\pi x_1)-\pi)\left(\beta_\Gamma - \frac{1}{8}\cos(\pi x_2)\frac{\kappa_\Gamma^n}{\ell_\Gamma}\frac{\cos(1)(\sin(1)-\pi/2)}{\sin(1)+\pi/2}\right)\right) & \text{if } x_1 > 1/2 \end{cases}, \tag{3.44}$$
$$c_\Gamma(\boldsymbol{x}) \coloneqq \frac{[\![\boldsymbol{u}c - \boldsymbol{D}\nabla c]\!]_\Gamma \cdot \boldsymbol{n}_\Gamma - \{\{c\}\}_\Gamma\left(1/2[\![\boldsymbol{u}]\!]_\Gamma \cdot \boldsymbol{n}_\Gamma + \beta_\Gamma^\xi\right)}{1/2[\![\boldsymbol{u}]\!]_\Gamma \cdot \boldsymbol{n}_\Gamma - \beta_\Gamma^\xi},$$

with $\boldsymbol{D} = \boldsymbol{I}_2$, the identity matrix of $\mathbb{R}^{2\times 2}$, $\mathcal{D}_\Gamma^\tau = 1$ and $\mathcal{D}_\Gamma^n = 0.01$. The source terms f, f_Γ are inferred from (3.1b) and (3.1c), respectively. The right-hand sides of (3.7a) and (3.8a) are also modified by introducing nonzero terms in accordance with the expressions of c and c_Γ; see (3.44). It can be checked that, with this choice of analytical solutions, the jump and average of p, $\boldsymbol{u}$, c, $\boldsymbol{D}\nabla c$ are not identically zero on the fracture, which enables us to test the weak enforcement of the transmission conditions (3.4) for the flow problem and (3.9) for the passive transport problem.

3.5.1.2 Error measures

On the spaces of discrete bulk unknowns $\underline{\boldsymbol{U}}_h^{2k}$ and $\underline{P}_h^k$, we define the norms $\|\cdot\|_{\boldsymbol{U},h}$ and $\|\cdot\|_{D,h}$ such that, for all $\underline{\boldsymbol{q}}_h \in \underline{\boldsymbol{U}}_h^{2k}$ and all $\underline{z}_h \in \underline{P}_h^k$,

$$\|\underline{\boldsymbol{q}}_h\|_{\boldsymbol{U},h}^2 \coloneqq \sum_{T\in\mathcal{T}_h} (\overline{K}_{\mathrm{B},T})^{-1}\left(\|\boldsymbol{q}_T\|_T^2 + \sum_{F\in\mathcal{F}_T} h_F\|q_{TF}\|_F^2\right),$$
$$\|\underline{z}_h\|_{D,h}^2 \coloneqq \sum_{T\in\mathcal{T}_h} \varrho_{\boldsymbol{D},T}^{-1}\left(\|\boldsymbol{D}_T^{1/2}\nabla z_T\|_T^2 + \sum_{F\in\mathcal{F}_T}\frac{D_{TF}}{h_F}\|z_T - z_{TF}\|_F^2\right),$$

where, for any $T \in \mathcal{T}_h$, $\overline{K}_{\mathrm{B},T}$ is the largest eigenvalue of the (constant) permeability tensor $\boldsymbol{K}_T$, while $\varrho_{\boldsymbol{D},T} \coloneqq \overline{D}_{\mathrm{B},T}/\underline{D}_{\mathrm{B},T}$ is the bulk anisotropy ratio with $\overline{D}_{\mathrm{B},T}, \underline{D}_{\mathrm{B},T} > 0$ denoting, respectively, the largest and smallest eigenvalue of the (constant) local bulk diffusion-dispersion tensor $\boldsymbol{D}_T$.

On the spaces of discrete fracture unknowns $\underline{P}_{\Gamma,h}^{2k}$ and $\underline{P}_{\Gamma,h}^k$ we define the norms $\|\cdot\|_{\Gamma,K,h}$ and $\|\cdot\|_{\Gamma,D,h}$ such that, for all $\underline{v}_h^\Gamma \in \underline{P}_{\Gamma,h}^{2k}$ and all $\underline{z}_h^\Gamma \in \underline{P}_{\Gamma,h}^k$,

$$\|\underline{v}_h^\Gamma\|_{\Gamma,K,h}^2 \coloneqq \sum_{F\in\mathcal{F}_h^\Gamma}\left(\|K_F^{1/2}\nabla_\tau v_F^\Gamma\|_F^2 + \sum_{V\in\mathcal{V}_F}\frac{K_F}{h_F}(v_F^\Gamma(V) - v_V^\Gamma)^2\right),$$
$$\|\underline{z}_h^\Gamma\|_{\Gamma,D,h}^2 \coloneqq \sum_{F\in\mathcal{F}_h^\Gamma}\left(\|D_F^{1/2}\nabla_\tau z_F^\Gamma\|_F^2 + \sum_{V\in\mathcal{V}_F}\frac{D_F}{h_F}(z_F^\Gamma(V) - z_V^\Gamma)^2\right).$$

For the flow problem, we monitor the following errors defined as the difference between the numerical solution and suitable projections of the exact solution:

$$\|\underline{\boldsymbol{u}}_h - \underline{\boldsymbol{I}}_h^{2k}\boldsymbol{u}\|_{\boldsymbol{U},h},\ \|\underline{p}_h^\Gamma - \underline{I}_h^{2k}p_\Gamma\|_{\Gamma,K,h},\ \|p_h - \pi_h^{2k}p\|_{L^2(\Omega_\mathrm{B})},\ \|p_h^\Gamma - \pi_{\Gamma,h}^{2k}p_\Gamma\|_{L^2(\Gamma)},\quad (3.45)$$

where $\underline{\boldsymbol{I}}_h^l\boldsymbol{u} \coloneqq (\boldsymbol{K}_T\nabla y_T, (\pi_F^l(\boldsymbol{u}\cdot\boldsymbol{n}_{TF})_{F\in\mathcal{F}_T})_{T\in\mathcal{T}_h}$ with $y_T \in \mathbb{P}^l(T)$ is such that $\int_T(\boldsymbol{K}_T\nabla y_T - \boldsymbol{u})\cdot\nabla v_T = 0$ for all $v_T \in \mathbb{P}^l(T)$, $\underline{I}_{\Gamma,h}^{2k}p_\Gamma \coloneqq ((\pi_F^{2k}p_{\Gamma|F})_{F\in\mathcal{F}_h^\Gamma}, (p_\Gamma(V))_{V\in\mathcal{V}_h})$ with π_F^{2k} denoting the L^2-orthogonal projector on $\mathbb{P}^{2k}(F)$, and $\pi_h^{2k}p$ and $\pi_{\Gamma,h}^{2k}p_\Gamma$ denote, respectively, the L^2-orthogonal projections of p and p_Γ on $P_{\mathrm{B},h}^{2k}$ and $P_{\Gamma,h}^{2k}$,

Similarly, for the passive transport problem we consider the following error measures:

$$\|\underline{c}_h - \underline{I}_h^k c\|_{D,h},\quad \|\underline{c}_h^\Gamma - \underline{I}_{\Gamma,h}^k c_\Gamma\|_{\Gamma,D,h},\quad \|c_h - \pi_h^k c\|_{L^2(\Omega_\mathrm{B})},\quad \|c_h^\Gamma - \pi_{\Gamma,h}^k c_\Gamma\|_{L^2(\Gamma)},\quad (3.46)$$

where $\underline{I}_h^k c \coloneqq ((\pi_T^k c_{|T})_{T\in\mathcal{T}_h}, (\pi_F^k(c_{|F}))_{F\in\mathcal{F}_h})$ with π_T^k and π_F^k denoting, respectively, the L^2-orthogonal projectors on $\mathbb{P}^k(T)$ and $\mathbb{P}^k(F)$, $\underline{I}_{\Gamma,h}^k c_\Gamma \coloneqq ((\pi_F^k c_{\Gamma|F})_{F\in\mathcal{F}_h^\Gamma}, (c_\Gamma(V))_{V\in\mathcal{V}_h})$, and $\pi_h^k c$ and $\pi_{\Gamma,h}^k c_\Gamma$ denote, respectively, the L^2-orthogonal projections of c and c_Γ on $P_{\mathrm{B},h}^k$ and $P_{\Gamma,h}^k$.

3.5.1.3 Results

We consider the triangular, Cartesian and nonconforming mesh families of Figure 3.3.

In Figure 3.4, we display the errors (3.45) for the flow problem as functions of the meshsize. The flow problem (3.30) is solved using polynomials two times higher than for the passive transport problem, so higher convergence rates than for the passive transport problem are to be expected. More specifically, on the triangular mesh we observe convergence in h^{2k+1} of the discretization error measured in the energy-like norms $\|\underline{\boldsymbol{u}}_h - \underline{\boldsymbol{I}}_h^{2k}\boldsymbol{u}\|_{\boldsymbol{U},h}$ and $\|\underline{p}_h^\Gamma - \underline{I}_h^{2k}p_\Gamma\|_{\Gamma,K,h}$, and convergence in h^{2k+2} for the error measured in the L^2-norms $\|p_h - \pi_h^{2k}p\|_{L^2(\Omega_\mathrm{B})}$ and $\|p_h^\Gamma - \pi_{\Gamma,h}^{2k}p_\Gamma\|_{L^2(\Gamma)}$. Slightly better convergence rates are observed on Cartesian and nonconforming meshes, as already noticed in [56].

For the passive transport problem (3.38), we plot in Figure 3.5 the errors (3.46) as functions of the meshsize. For both the energy-like norms of the error $\|\underline{c}_h - \underline{I}_h^k c\|_{D,h}$ and $\|\underline{c}_h^\Gamma - \underline{I}_{\Gamma,h}^k c_\Gamma\|_{\Gamma,D,h}$, we obain convergence in h^{k+1}. For the L^2-norms of the error $\|c_h - \pi_h^k c\|_{L^2(\Omega_\mathrm{B})}$ and $\|c_h^\Gamma - \pi_{\Gamma,h}^k c\|_{L^2(\Gamma)}$, on the other hand, we obtain convergence in h^{k+2} using piecewise linear or quadratic polynomials, and between h and h^2 using piecewise constant polynomials.

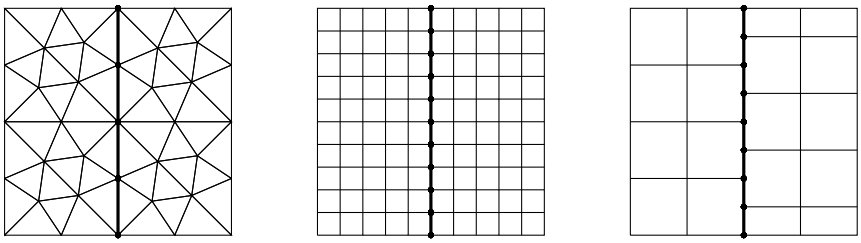

(a) Triangular (b) Cartesian (c) Nonconforming

Figure 3.3: Mesh families for the numerical tests

3.5.2 Unsteady transport with impermeable fractures

We next consider a physical test case modelling the unsteady passive displacement of a solute in a porous medium in which the fractures act as barriers.

The configuration is depicted in Figure 3.6a. More specifically, the computational domain is the unit square $\Omega = (0,1)^2$, with fractures of constant thickness $\ell_\Gamma = 10^{-2}$ corresponding to

$$\Gamma = \left\{ \boldsymbol{x} = (x_1, x_2) \in \Omega \ : \ \begin{array}{l} x_1 < 0.75 \text{ and } x_2 \in \{0.25, 0.75\}), \text{ or} \\ (x_1 > 0.25 \text{ and } x_2 = 0.5) \end{array} \right\}.$$

The injection well is located in $(0.5, 0)$, the production one in $(0.5, 1)$, and both are modeled by the source term f defined such that

$$f(\boldsymbol{x}) = \frac{1}{2}\Bigg(\tanh\left(200(0.025 - \sqrt{(x_1^2 - 0.5) + x_2^2})\right) - \tanh\left(200(0.025 - \sqrt{(x_1^2 - 0.5) + (x_2 - 1)^2})\right)\Bigg).$$

The fracture source term f_Γ is set to 0. It can be checked that the average of f in Ω_B is zero, so the compatibility condition (3.5) is verified. We set the user parameter $\xi = 0.75$.

Concerning the flow problem, we select the values of the permeability in the bulk and in the fracture so as to obtain impermeable fractures. More specifically, in the bulk we set $\boldsymbol{K} = 10^{-3}\boldsymbol{I}$, while in the fractures the tangential and normal permeability are, respectively, $\kappa_\Gamma^\tau = 10^{-3}$ and $\kappa_\Gamma^n = 10^{-6}$. In Figure 3.6a, we display the bulk pressure p obtained with such parameters and the plot over $x_1 = 0.5$. We can clearly see that the pressure jumps across the fractures and decreases from the injection to the production well.

We consider the unsteady passive transport problem (3.43), set the final time $t_F = 100$ and the time step $\delta t = 1$. At $t = 0$, there is not solute in the bulk nor

in the fractures. The concentration of injected solute in the bulk is given, for all $\boldsymbol{x} \in \Omega_{\mathrm{B}}$, by $\widehat{c}(t, \boldsymbol{x}) = 1$ if $t < 30$ and $\widehat{c}(t, \boldsymbol{x}) = 0$ otherwise. Since we do not have wells in the fracture, we set $\widehat{c}_\Gamma \equiv 0$. The porosity in the bulk and in the fracture is set to $\phi = \phi_\Gamma = 10^{-1}$. Following [11, 121], the diffusion-dispersion tensor in the bulk is defined locally for all $T \in \mathcal{T}_h$ such that

$$\boldsymbol{D}_T = \phi d_{\mathrm{m}} \boldsymbol{I}_2 + \phi |\boldsymbol{F}_T^{2k+1}] \underline{\boldsymbol{u}}_T | (d_{\mathrm{l}} \boldsymbol{E}_{\boldsymbol{u},T} + d_{\mathrm{t}} (\boldsymbol{I}_2 - \boldsymbol{E}_{\boldsymbol{u},T})),$$

where $\boldsymbol{E}_{\boldsymbol{u},T} \coloneqq |\boldsymbol{F}_T^{2k+1} \underline{\boldsymbol{u}}_T|^{-2} \left(\boldsymbol{F}_T^{2k+1} \underline{\boldsymbol{u}}_T \otimes \boldsymbol{F}_T^{2k+1} \underline{\boldsymbol{u}}_T \right)$ and $|\boldsymbol{F}_T^{2k+1} \underline{\boldsymbol{u}}_T|$ is the Euclidean norm of $\boldsymbol{F}_T^{2k+1} \underline{\boldsymbol{u}}_T$, while $d_{\mathrm{m}} = 10^{-5}$, $d_{\mathrm{l}} = 1$ and $d_{\mathrm{t}} = 10^{-2}$ denote, respectively, the molecular diffusion, longitudinal, and transverse dispersion coefficients. Notice that the high-order reconstruction of the Darcy velocity is needed to define $\boldsymbol{D}_T$ since, if using constant elements $k = 0$, we do not have cell-based DOFs for the flux. The fracture counterpart of the diffusion-dispersion coefficient is defined, for all $F \in \mathcal{F}_h^\Gamma$, as follows

$$D_F = \ell_\Gamma \phi_\Gamma d_{\mathrm{m}}^\Gamma \boldsymbol{I}_2 + \phi_\Gamma |\boldsymbol{u}_F^\Gamma| (d_{\mathrm{l}}^\Gamma \boldsymbol{E}_{\boldsymbol{u},F} + d_{\mathrm{t}}^\Gamma (\boldsymbol{I}_2 - \boldsymbol{E}_{\boldsymbol{u},F})),$$

with $\boldsymbol{E}_{\boldsymbol{u},F} \coloneqq |\boldsymbol{u}_F^\Gamma|^{-2} \left(\boldsymbol{u}_F^\Gamma \otimes \boldsymbol{u}_F^\Gamma \right)$ and where $d_{\mathrm{m}}^\Gamma = 10^{-5}$, $d_{\mathrm{l}}^\Gamma = 1$ and $d_{\mathrm{t}}^\Gamma = 10^{-2}$ denote, respectively, the fracture molecular diffusion, longitudinal, and transverse dispersion coefficients. We set the normal diffusion-dispersion coefficient of the fracture $\mathcal{D}_\Gamma^n$ equal to 1. A more in-depth investigation of the meaning of this term is postponed to a future work.

We run the test case on the Cartesian mesh depicted in Figure 3.3b of meshsize $h = 7.81 \cdot 10^{-3}$ with $k = 2$. In Figure 3.6b, we display the bulk concentration at different time t. As expected, the solute follows the corridors designed by the fractures that act as barriers and goes from the injection to the production well.

3.5.3 Unsteady transport with permeable fractures

We next focus on the case where the fractures act as conduits. The domain is still the square unit $\Omega = (0, 1)^2$, the fractures of constant thickness $\ell_\Gamma = 10^{-2}$ are located in

$$\Gamma = \{\boldsymbol{x} \in \Omega \ : \ x_1 \in \{2/32, 8/32, 13/32, 19/32, 24/32, 30/32\} \text{ and } 0.25 < x_2 < 0.75\}.$$

The configuration is depicted in Figure 3.7a. The only parameters that differ from the previous test case of Section 3.5.2 are the fracture permeabilities: to obtain permeable fractures, we set the normal permeability $\kappa_\Gamma^n = 10^{-3}$ and the tangential one $\kappa_\Gamma^\tau = 10^{-1}$. With this choice, it is expected that the flow is attracted by the fractures.

In Figure 3.7a, we display the bulk pressure p and Darcy velocity $\boldsymbol{u}$ where, for the latter, the color scale correspond to the value of the magnitude. As expected, the flow is from the injection well towards the fractures near the bottom of the domain, and from the fractures to the production well near the top of the domain.

In Figure 3.7b, we display the bulk concentration c at different times. We can distincly see that the solute channeled by the fractures flows towards the production well faster than the solute in the surrounding bulk medium.

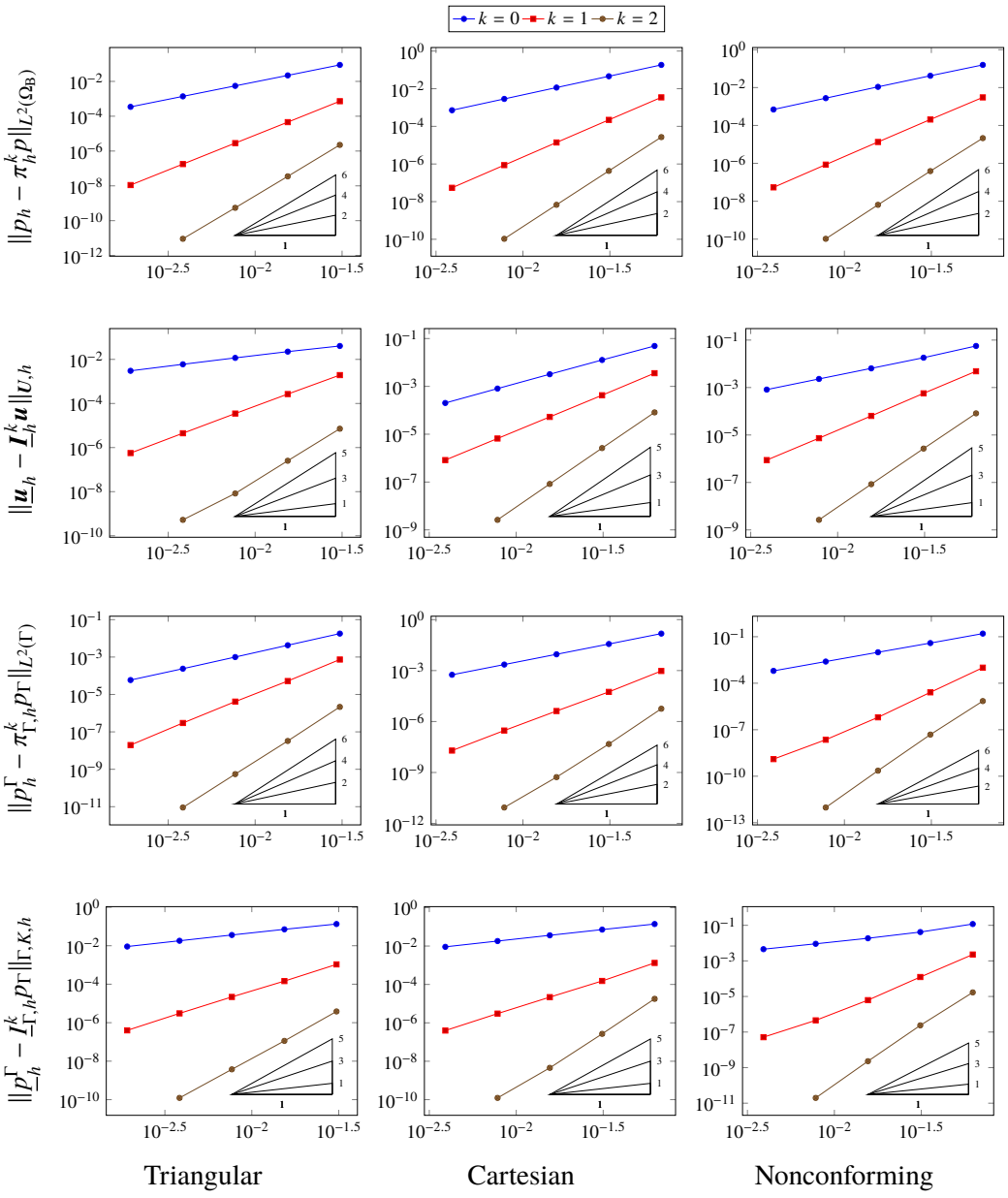

Figure 3.4: Convergence results for the test case of Section 3.5.1. Errors (3.45) for the flow problem v. h on the triangular, Cartesian and nonconforming mesh families of Figure 3.3.

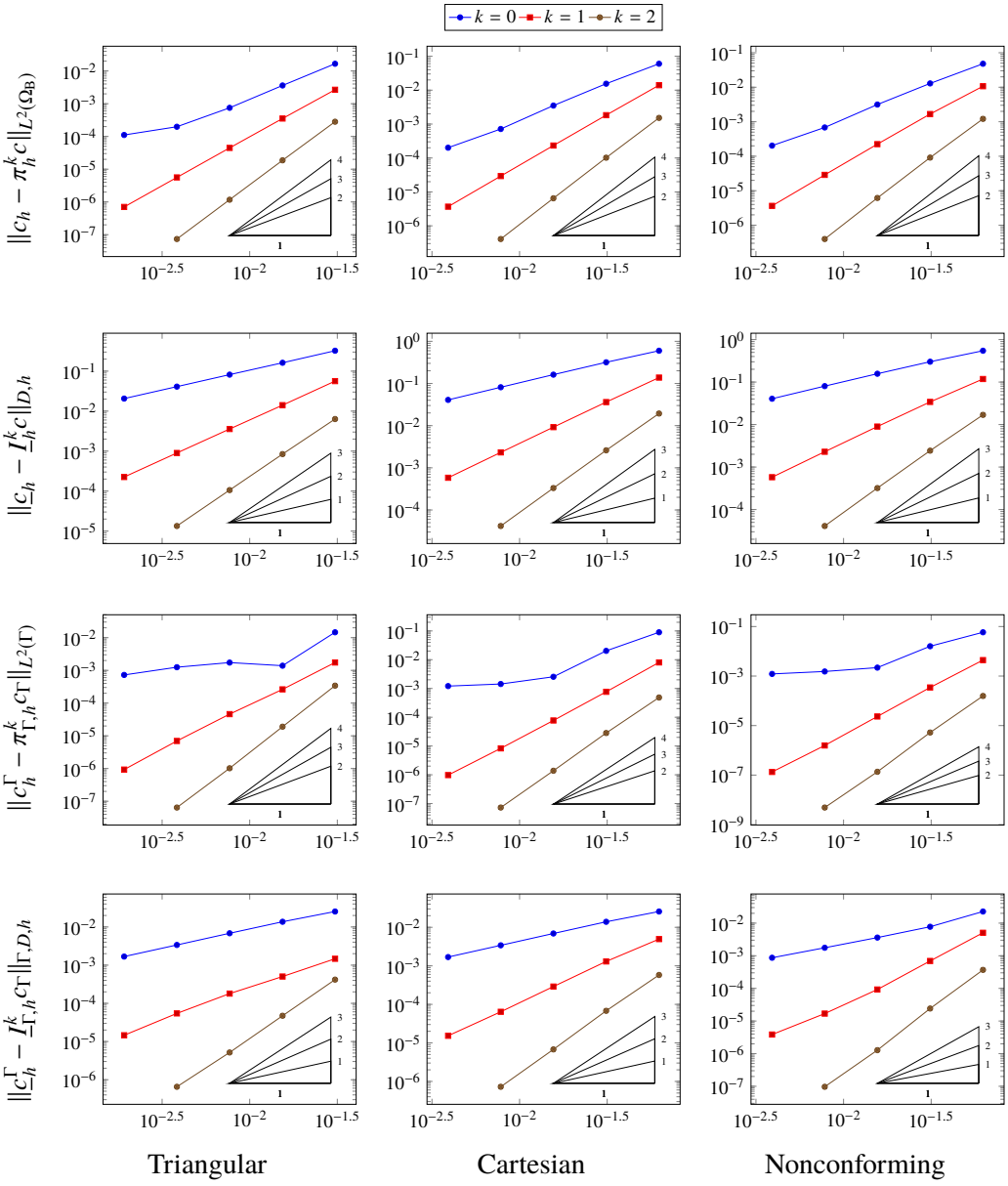

Figure 3.5: Convergence results for the test case of Section 3.5.1. Errors (3.46) for the passive transport problem v. h on the triangular, Cartesian and nonconforming mesh families of Figure 3.3.

(a) Domain configuration (left), bulk pressure p (middle) and bulk pressure profile over $x_1 = 0.5$ (right).

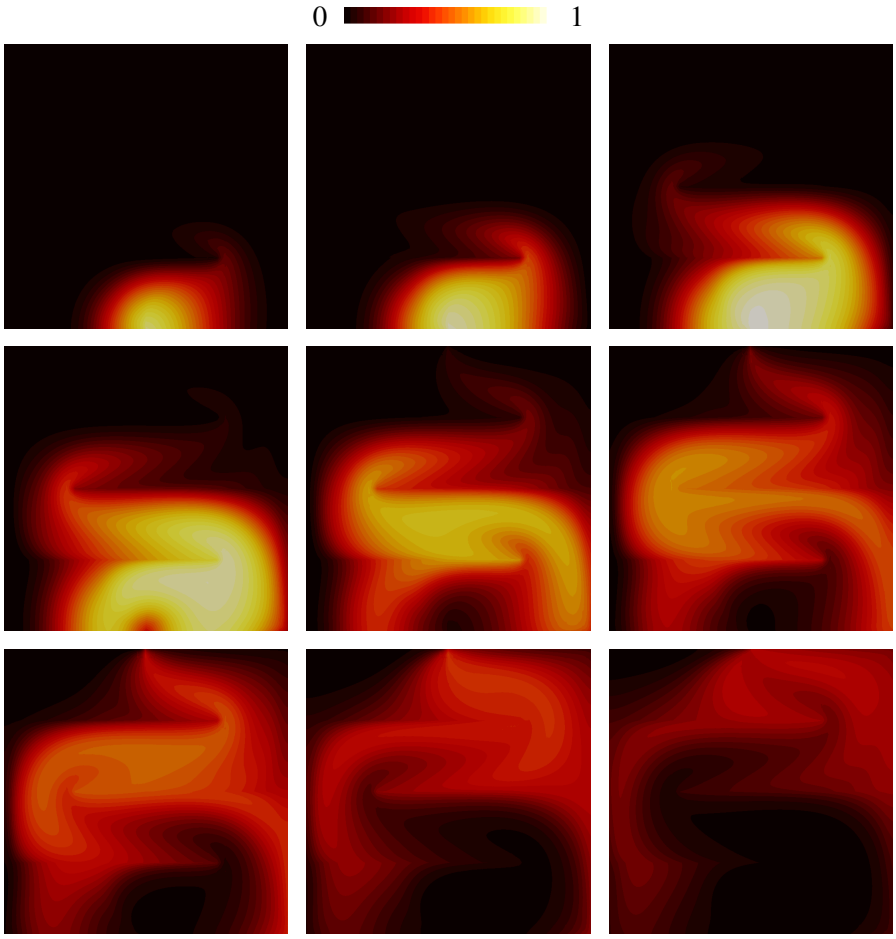

(b) Snapshots of the bulk concentration c at times (from left to right, top to bottom): $t = 5,\ 10,\ 20,\ 30,\ 40,\ 50,\ 60,\ 80,\ 100$.

Figure 3.6: Configuration and numerical results for the test of Section 3.5.2 (unsteady transport with impermeable fractures).

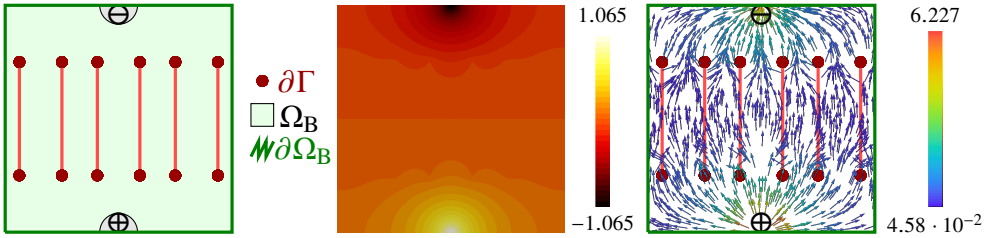

(a) Domain configuration (left), bulk pressure p (middle), and Darcy velocity $\boldsymbol{u}$ (right).

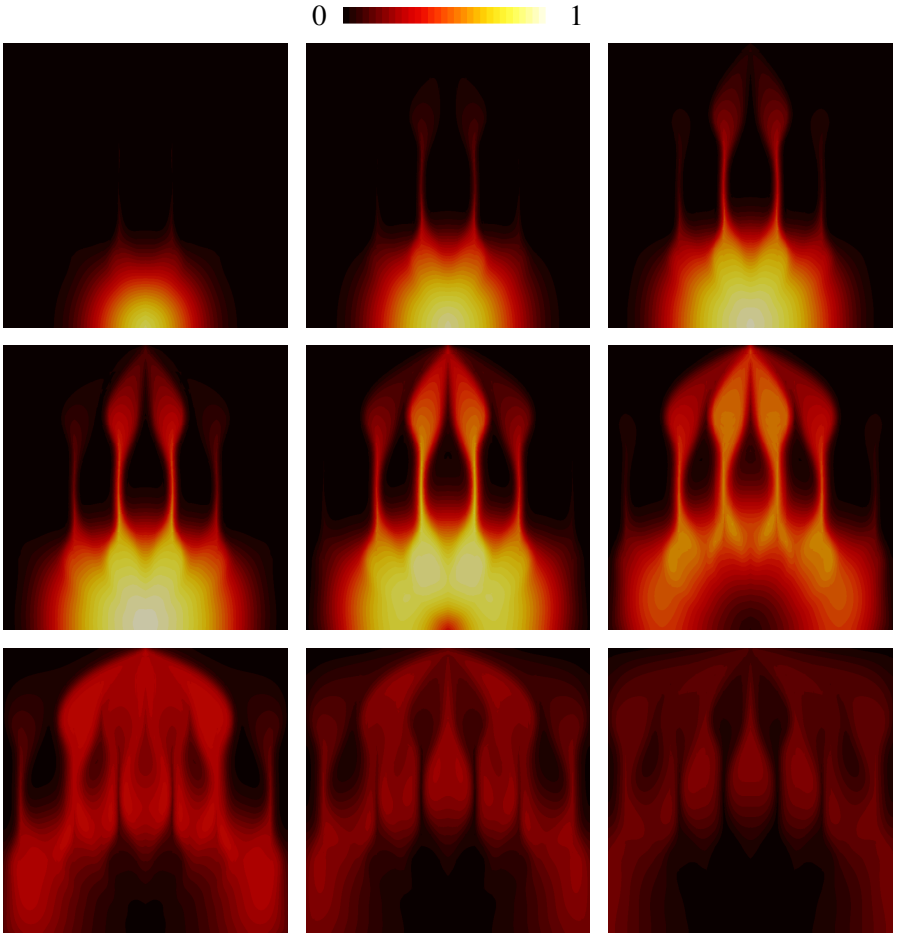

(b) Snapshots of the bulk concentration c at times (from left to right, top to bottom): $t = 5,\ 10,\ 15,\ 20,\ 30,\ 40,\ 60,\ 80,\ 100$.

Figure 3.7: Configuration and numerical results for the test of Section 3.5.3 (unsteady transport with permeable fractures).

Appendix A

The convective Cahn–Hilliard problem

This appendix has been published in the following conference proceedings (see [58]):

Finite Volumes for Complex Applications VIII,
Hyperbolic, Elliptic and Parabolic Problems, 2017, Pages 517–526.

Contents

A.1 The convective Cahn–Hilliard equation

Let $\Omega \subset \mathbb{R}^d$, $d \in \{2, 3\}$, denote a bounded connected convex polyhedral domain with Lipschitz boundary $\partial\Omega$ and outward normal $\boldsymbol{n}$, and let $t_F > 0$. The convective Cahn–Hilliard problem consists in finding the order-parameter $c : \Omega \times (0, t_F) \to \mathbb{R}$

and the chemical potential $w : \Omega \times (0, t_F) \to \mathbb{R}$ such that

$$\mathrm{d}_t c - \frac{1}{\mathrm{Pe}}\Delta w + \nabla \cdot (\boldsymbol{u} c) = 0 \qquad \text{in } \Omega \times (0, t_F) \tag{A.1a}$$

$$w = \Phi'(c) - \gamma^2 \Delta c \qquad \text{in } \Omega \times (0, t_F) \tag{A.1b}$$

$$c(\cdot, 0) = c_0(\cdot) \qquad \text{in } \Omega \tag{A.1c}$$

$$-\nabla c \cdot \boldsymbol{n} = -\nabla w \cdot \boldsymbol{n} = 0 \qquad \text{on } \partial\Omega \times (0, t_F) \tag{A.1d}$$

where $\gamma > 0$ is the interface parameter (usually taking small values), $\mathrm{Pe} > 0$ is the Péclet number, $\boldsymbol{u}$ the velocity field such that $\nabla \cdot \boldsymbol{u} = 0$ in Ω and Φ the free-energy such that $\Phi(c) := \frac{1}{4}(1-c^2)^2$. This formulation is an extension of the Cahn–Hilliard model originally introduced in [51, 52] and a first step towards coupling with the Navier–Stokes equations.

In this work we extend the HHO method of [59] to incorporate the convective term in (A.1a). Therein, a full stability and convergence analysis was carried out for the non-convective case, leading to optimal estimates in $(h^{k+1} + \delta t)$ (with h denoting the meshsize and δt the time step) for the the $C^0(H^1)$-error on the order-parameter and $L^2(H^1)$-error on the chemical potential. The convective term is treated in the spirit of [75], where a HHO method fully robust with respect to the Péclet number was presented for a locally degenerate diffusion-advection-reaction problem.

The proposed method offers various assets: (i) fairly general meshes are supported including polyhedral elements and nonmatching interfaces; (ii) arbitrary polynomial orders, including the case $k = 0$, can be considered; (iii) when using a first-order (Newton-like) algorithm to solve the resulting system of nonlinear algebraic equations, element-based unknowns can be statically condensed at each iteration.

The rest of this Chapter is organized as follows: in Section A.2, we recall discrete setting including notations and assumptions on meshes, define localy discrete operators and state the discrete formulation of (A.1). In Section A.3, we provide an extensive numerical validation.

A.2 The Hybrid High-Order method

In this section we recall some assumptions on the mesh, introduce the notation, and state the HHO discretization.

A.2.1 Discrete setting

We consider sequences of refined meshes that are regular in the sense of [81, Chapter 1]. Each mesh $\mathcal{T}_h$ in the sequence is a finite collection $\{T\}$ of nonempty,

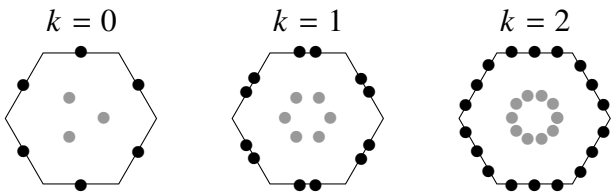

Figure A.1: Local DOF space $P_T^{k+1,k}$ for $k = 0, 1, 2$. Internal DOFs (in gray) can be statically condensed at each Newton iteration.

disjoint, polyhedral elements such that $\overline{\Omega} = \bigcup_{T\in\mathcal{T}_h} \overline{T}$ and $h = \max_{T\in\mathcal{T}_h} h_T$ (with h_T the diameter of T). For all $T \in \mathcal{T}_h$, the boundary of T is decomposed into planar faces collected in the set $\mathcal{F}_T$. For admissible mesh sequences, $\mathrm{card}(\mathcal{F}_T)$ is bounded uniformly in h. Interfaces are collected in the set $\mathcal{F}_h^{\mathrm{i}}$, boundary faces in $\mathcal{F}_h^{\mathrm{b}}$ and we define $\mathcal{F}_h := \mathcal{F}_h^{\mathrm{i}} \cup \mathcal{F}_h^{\mathrm{b}}$. For all $T \in \mathcal{T}_h$ and all $F \in \mathcal{F}_T$, the diameter of F is denoted by h_F and the unit normal to F pointing out of T is denoted by $\vec{n}_{TF}$.

To discretize in time, we consider for sake of simplicity a uniform partition $(t^n)_{0\le n\le N}$ of the time interval $[0, t_F]$ with $t^0 = 0$, $t^N = t_F$ and $t^n - t^{n-1} = \delta t$ for all $1 \le n \le N$. For any sufficiently regular function of time φ taking values in a vector space V, we denote by $\varphi^n \in V$ its value at discrete time t^n, and we introduce the backward differencing operator δ_{t} such that, for all $1 \le n \le N$,

$$\delta_{\mathrm{t}}\varphi^n := \frac{\varphi^n - \varphi^{n-1}}{\delta t} \in V.$$

A.2.2 Local space of degrees of freedom

For any integer $l \ge 0$ and X a mesh element or face, we denote by $\mathbb{P}^l(X)$ the space spanned by the restrictions to X of d-variate polynomials of order l. Let

$$\underline{P}_h^{k+1,k} := \left(\bigtimes_{T\in\mathcal{T}_h} \mathbb{P}^{k+1}(T)\right) \times \left(\bigtimes_{F\in\mathcal{F}_h} \mathbb{P}^{k}(F)\right)$$

be the global degrees of freedoms (DOFs) space with single-valued interface unknowns. We denote by $\underline{v}_h = ((v_T)_{T\in\mathcal{T}_h}, (v_F)_{F\in\mathcal{F}_h})$ a generic element of $\underline{P}_h^{k+1,k}$ and by v_h the piecewise polynomial function such that $v_h|_T = v_T$ for all $T \in \mathcal{T}_h$. For any $T \in \mathcal{T}_h$, we denote by $\underline{P}_T^{k+1,k}$ and $\underline{v}_T = (v_T, (v_F)_{F\in\mathcal{F}_T})$ the restrictions to T of $\underline{P}_h^{k+1,k}$ and $\underline{v}_h$, respectively.

A.2.3 Local diffusive contribution

Consider a mesh element $T \in \mathcal{T}_h$. We define the local potential reconstruction $r_T^{k+1} : \underline{P}_T^{k+1,k} \to \mathbb{P}^{k+1}(T)$ such that, for all $\underline{v}_T := (v_T, (v_F)_{F\in\mathcal{F}_T}) \in \underline{P}_T^k$ and all

$z \in \mathbb{P}_T^{k+1}$,

$$\int_T \nabla r_T^{k+1} \underline{v}_T \cdot \nabla z \;=\; -\int_T v_T \Delta z + \sum_{F\in\mathcal{F}_T} \int_F v_F \nabla z \cdot \boldsymbol{n}_{TF},$$

with closure condition $\int_T (r_T^{k+1}\underline{v}_T - v_T) = 0$. We introduce the local diffusive bilinear form a_T on $\underline{P}_T^{k+1,k} \times \underline{P}_T^{k+1,k}$ such that, for all $(\underline{u}_T, \underline{v}_T) \in \underline{P}_T^{k+1,k} \times \underline{P}_T^{k+1,k}$

$$a_T(\underline{u}_T, \underline{v}_T) := \int_T \nabla r_T^{k+1} \underline{u}_T \cdot \nabla r_T^{k+1} \underline{v}_T + s_T(\underline{u}_T, \underline{v}_T),$$

with stabilization bilinear form $s_T : \underline{P}_T^{k+1,k} \times \underline{P}_T^{k+1,k} \to \mathbb{R}$ such that

$$s_T(\underline{u}_T, \underline{v}_T) := \sum_{F\in\mathcal{F}_T} h_F^{-1} \int_F \pi_F^k(u_F - u_T)\pi_F^k(v_F - v_T),$$

where, for all $F \in \mathcal{F}_h$, $\pi_F^k : L^1(F) \to \mathbb{P}^k(F)$ denotes the L^2-orthogonal projector onto $\mathbb{P}^k(F)$.

A.2.4 Local convective contribution

For any mesh element $T \in \mathcal{T}_h$, we define the local convective derivative reconstruction $\mathrm{G}_{\boldsymbol{u},T}^{k+1} : \underline{P}_T^k \to \mathbb{P}^{k+1}(T)$ such that, for all $\underline{v}_T := (v_T, (v_F)_{F\in\mathcal{F}_T}) \in \underline{P}_T^k$ and all $w \in \mathbb{P}^{k+1}(T)$,

$$\int_T \mathrm{G}_{\boldsymbol{u},T}^{k+1} \underline{v}_T w \;=\; -\int_T v_T \boldsymbol{u} \cdot \nabla w + \sum_{F\in\mathcal{F}_T} \int_F v_F (\boldsymbol{u} \cdot \boldsymbol{n}_{TF}) w.$$

The local convective contribution $b_{\boldsymbol{u},T}$ on $\underline{P}_T^k \times \underline{P}_T^k$ is such that, for all $(\underline{u}_T, \underline{v}_T) \in \underline{P}_T^k \times \underline{P}_T^k$

$$b_{\boldsymbol{u},T}(\underline{u}_T, \underline{v}_T) := -\int_T u_T \mathrm{G}_{\boldsymbol{u},T}^{k+1} \underline{v}_T + s_{\boldsymbol{u},T}(\underline{u}_T, \underline{v}_T).$$

with local upwind stabilization bilinear form $s_{\boldsymbol{u},T} : \underline{P}_T^k \times \underline{P}_T^k \to \mathbb{R}$ such that

$$s_{\boldsymbol{u},T}(\underline{u}_T, \underline{v}_T) := \sum_{F\in\mathcal{F}_T} \int_F \frac{|\boldsymbol{u} \cdot \boldsymbol{n}_{TF}| - \boldsymbol{u} \cdot \boldsymbol{n}_{TF}}{2} (u_F - u_T)(v_F - v_T).$$

Notice that the actual computation of $\mathrm{G}_{\boldsymbol{u},T}^{k+1}$ is not required, as one can simply use its definition to expand the cell-based term in the bilinear form $b_{\boldsymbol{u},T}$.

A.2.5 Discrete problem

Denote by $\underline{P}_{h,0}^k := \{\underline{v}_h = ((v_T)_{T\in\mathcal{T}_h}, (v_F)_{F\in\mathcal{F}_h}) \in \underline{P}_h^k | \int_\Omega v_h = 0\}$ the zero-average DOFs subspace of $\underline{P}_h^k$. We define the global bilinear forms a_h and $b_{\boldsymbol{u},h}$ on $\underline{P}_h^k \times \underline{P}_h^k$ such that, for all $(\underline{u}_h, \underline{v}_h) \in \underline{P}_h^k \times \underline{P}_h^k$

$$a_h(\underline{u}_h, \underline{v}_h) := \sum_{T\in\mathcal{T}_h} a_T(\underline{u}_T, \underline{v}_T), \qquad b_{\boldsymbol{u},h}(\underline{u}_h, \underline{v}_h) := \sum_{T\in\mathcal{T}_h} b_{\boldsymbol{u},T}(\underline{u}_T, \underline{v}_T).$$

The discrete problem reads: For all $1 \le n \le N$, find $(\underline{c}_h^n, \underline{w}_h^n) \in \underline{P}_{h,0}^k \times \underline{P}_h^k$ such that

$$\begin{aligned}
&\int_\Omega \delta_t c_h^n \varphi_h + \frac{1}{\mathrm{Pe}} a_h(\underline{w}_h^n, \underline{\varphi}_h) + b_{\boldsymbol{u},h}(\underline{c}_h^n, \underline{\varphi}_h) = 0 && \forall \underline{\varphi}_h \in \underline{U}_h^k \\
&\int_\Omega w_h^n \psi_h = \int_\Omega \Phi'(c_h^n)\psi_h + \gamma^2 a_h(\underline{c}_h^n, \underline{\psi}_h) && \forall \underline{\psi}_h \in \underline{U}_h^k
\end{aligned}$$

where $\underline{c}_h^0 \in \underline{P}_{h,0}^k$ solves $a_h(\underline{c}_h^0, \underline{\varphi}_h) = -\int_\Omega \Delta c_0 \varphi_h$ for all $\underline{\varphi}_h \in \underline{P}_h^k$.

A.3 Numerical test cases

In this section, we numerically validate the HHO method.

A.3.1 Disturbance of the steady solution

For the first test case, we use a piecewise constant approximation ($k = 0$), discretize the domain $\Omega = (0,1)^2$ by a triangular mesh ($h = 1.92 \cdot 10^{-3}$) with $\gamma = 5 \cdot 10^{-2}$, $\delta t = \gamma^2$ and $\mathrm{Pe} = 1$. The initial condition for the order-parameter and the velocity field are given by

$$c_0(\boldsymbol{x}) := \tanh\left(\frac{2x_1 - 1}{2\sqrt{2}\gamma^2}\right), \quad \boldsymbol{u}(\boldsymbol{x}) := 20 \cdot \begin{pmatrix} x_1(x_1-1)(2x_2-1) \\ -x_2(x_2-1)(2x_1-1) \end{pmatrix}, \quad \forall \vec{x} \in \Omega.$$

The result is depicted in Figure A.2 and shows that the method is well-suited to capture the interface dynamics subject to a strong velocity fields.

A.3.2 Thin interface between phases

For the second example, we also use a piecewise constant approximation ($k = 0$) with a Cartesian discretization of the domain $\Omega = (0,1)^2$, where $h = 1.95 \cdot 10^{-3}$. The interface parameter is taken to be very small $\gamma = 5 \cdot 10^{-3}$, the time step is

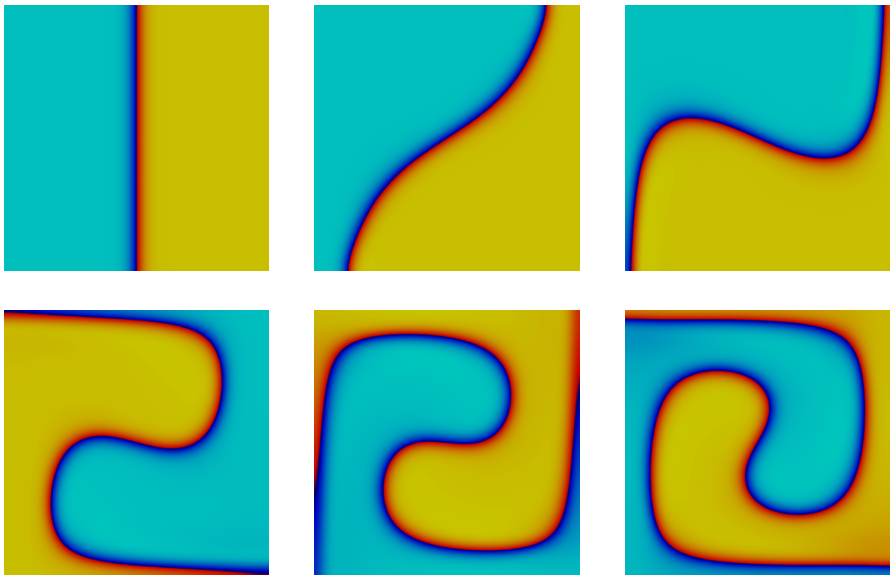

Figure A.2: Steady solution perturbed by a circular velocity field (left to right, top to bottom).

$\delta t = 1 \cdot 10^{-5}$ and $\mathrm{Pe} = 50$. The initial condition for the order-parameter is taken to be a random value between -1 and 1 inside a circular partition of the Cartesian mesh and -1 outside. The velocity field is given by

$$\boldsymbol{u}(\boldsymbol{x}) := \frac{1}{2}\left(1 + \tanh(80 - 200\|\boldsymbol{x} - (0.5, 0.5)\|_2)\right) \cdot \begin{pmatrix} 2x_2 - 1 \\ 1 - 2x_1 \end{pmatrix}, \quad \forall \boldsymbol{x} \in \Omega.$$

See Figure A.3 for the numerical result. The method is robust with respect to γ and is also well-suited to approach the thin high-gradient area of the order-parameter.

A.3.3 Effect of the Péclet number

The Péclet number is the ratio of the contributions to mass transport by convection to those by diffusion: when Pe is greater than one, the effects of convection exceed those of diffusion in determining the overall mass flux. In the last test case, we compare several time evolutions obtained with different values of the Péclet number ($\mathrm{Pe} \in \{1, 50, 200\}$), starting from the same initial condition. We use a Voronoi discretization of the domain $\Omega = (0, 1)^2$, where $h = 9.09 \cdot 10^{-3}$, and use piecewise linear approximation ($k = 1$). We choose $\gamma = 1 \cdot 10^{-2}$, $\delta t = 1 \cdot 10^{-4}$ and $t_F = 1$. The initial condition is given by a random value between -1 and 1 inside a circular domain of the Voronoi mesh and -1 outside. The convective term is

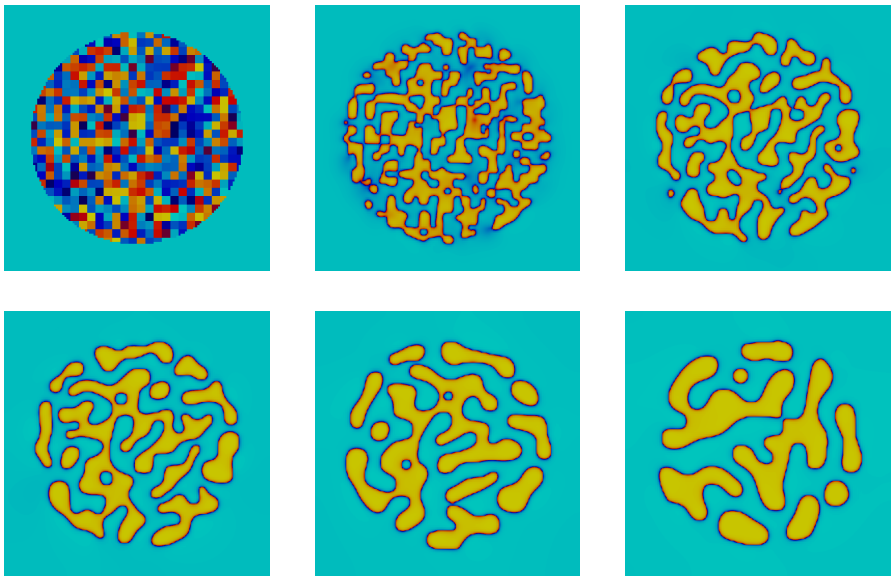

Figure A.3: Evolution of spinodal decomposition with thin interface (left to right, top to bottom).

given by

$$\boldsymbol{u}(\boldsymbol{x}) := \begin{pmatrix} \sin(\pi x_1)\cos(\pi x_2) \\ -\cos(\pi x_1)\sin(\pi x_2) \end{pmatrix}, \quad \forall \boldsymbol{x} \in \Omega.$$

Snapshots of the order parameter at several times are shown on Figure A.4 for each value of the Péclet number. For each case, the method takes into account the value of Pe and appropriately models the evolution of the order parameter by prevailing advection to diffusion when $\mathrm{Pe} \gg 1$.

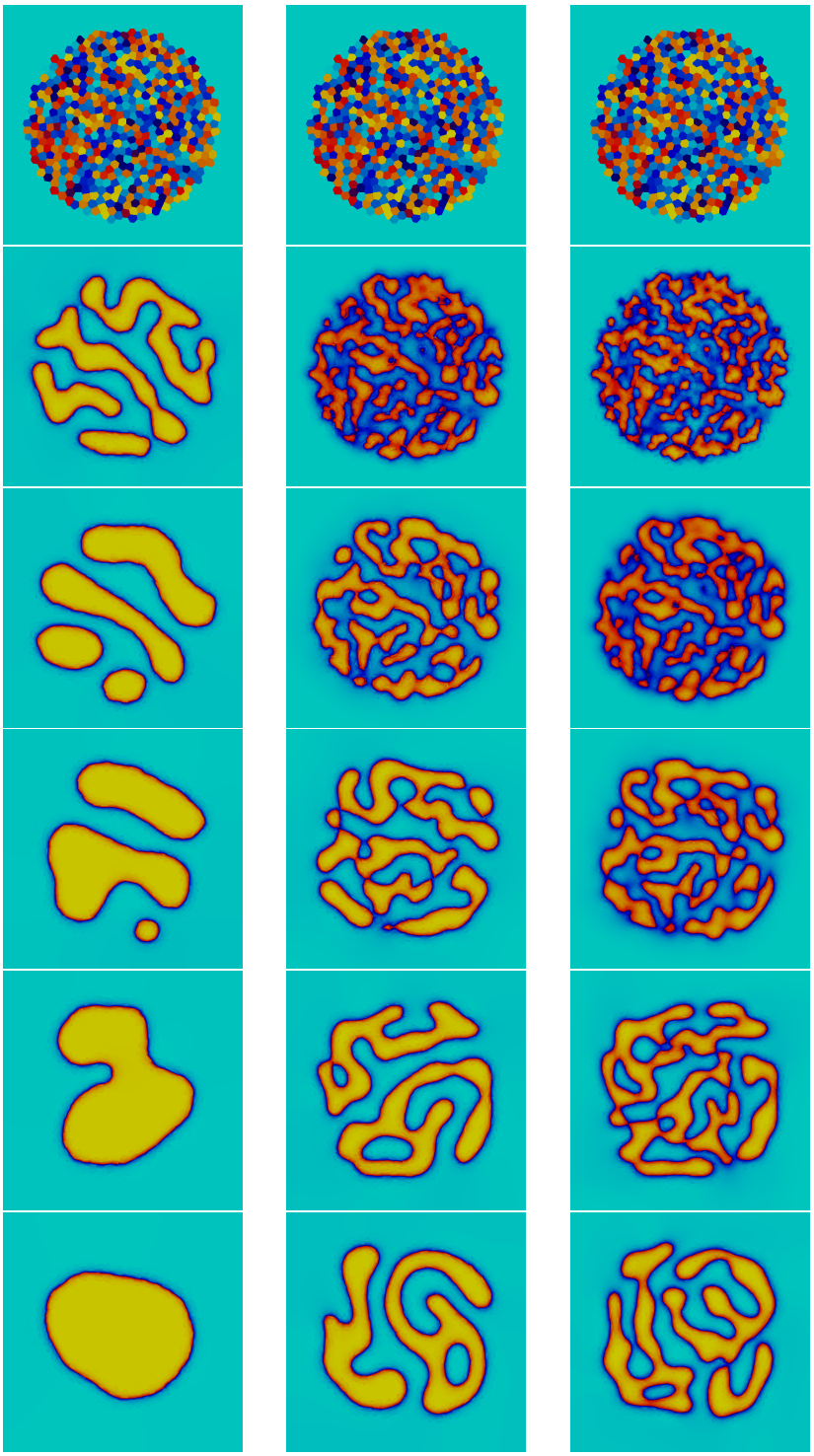

Figure A.4: Comparison at the same time between evolution of solutions with different Péclet number (top to bottom). Left: Pe = 1, middle: Pe = 50, right: Pe = 200. Displayed times are $t = 0, 1 \cdot 10^{-2}, 6 \cdot 10^{-2}, 2 \cdot 10^{-1}, 5 \cdot 10^{-1}, 1$.

Appendix B

Résumé de la thèse en Français

Contents

Dans ce manuscrit de thèse, nous développons des méthodes de nouvelle génération, appelées Hybrides d'Ordre Élevé (HHO: Hybrid High–Order, en anglais), pour la résolution numérique de problèmes d'interfaces. Plus précisément, deux sortes d'interfaces sont considérées ici : les interfaces diffuses, et celles agissant comme frontières internes au domaine computationnel. Dans ce chapitre d'introduction, nous commençons par faire un bref état de l'art des méthodes HHO et présentons ses avantages dans le contexte des problèmes d'interfaces. Ensuite, nous discutons des problèmes aux interfaces sur lesquels nous nous focalisons, et décrivons le contenu et les contributions principales de chacun des chapitres de ce manuscrit.

B.1 Méthodes Hybrides d'Ordre Élevé : état de l'art

Les méthodes HHO sont une famille de méthodes numériques de nouvelle génération pour la discrétisation d'Équations aux Dérivées Partielles (EDPs), introduite en premier lieu dans [77, 83]. Le terme *Hybride* fait référence au fait que deux sortes d'inconnus discrets soient utilisés, qui sont des polynômes brisés basés respectivement sur le maillage et son squelette. Le terme *Ordre Élevé* souligne la possibilité d'augmenter l'ordre d'approximation dans l'optique d'accélérer la convergence en présence de solution (localement) régulière, ou lorsque l'on fait appel à des techniques d'adaptation.

Les ingrédients des méthodes HHO sont : (i) des *reconstructions locales* d'opérateurs différentiels obtenues en reproduisant une intégration par parties où les inconnus discrets hybrides jouent le rôle de fonction à l'intérieur de chaque élément et sur ses faces ; (ii) des *termes de stabilisation* obtenus par pénalisation des résidus d'ordre élevé, qui disparaissent lorsqu'ils sont appliqués à l'interpolation de fonctions polynômiales jusqu'à un certain ordre. Cette construction subtile confère un certain nombre de caractéristiques intéressantes propres à la méthode : (i) elle supporte des maillages polytopiques généraux, pouvant contenir des éléments polygonaux ou dont les faces ne concordent pas d'un élément à l'autre ; (ii) elle autorise l'utilisation d'ordre d'approximation arbitraire; (iii) elle délivre des résultats de stabilité de la forme *inf–sup* pour les problèmes mixtes ; (iv) elle est localement conservative ; (v) la possibilité d'éliminer les inconnus présents à l'intérieur de chaque élément rend l'implémentation efficace ; (vi) la construction de la méthode est indépendante du choix de la dimension. Depuis leur introduction, les méthodes HHO ont connu un développement vigoureux et ont été utilisées dans la discrétisation de nombreuses EDPs, linéaires ou non, provenant de divers domaines de la physique numérique. Outre les travaux pionniers portant sur les problèmes de diffusion variable [78, 82, 83] et d'élasticité linéaire quasi incompressible [77, 80], nous pouvons citer ici les applications portant sur les équations de diffusion-convection-réaction où la diffusion est localement dégénérée [75], les problèmes de poroélasticité linéaire [29] ou non-linéaire [39], d'écoulements de Stokes [5] pouvant être entraînés par des forces massiques dont la partie irrotationelle est grande [84], d'électrostatique [85, 88], d'écoulements incompressibles gouvernés par les équations d'Oseen [6] ou de Navier–Stokes [37, 86], d'élasticité non-linéaire [38], de déformations finies de matériaux hyperélastiques [2], de plasticité associative incrémentale avec petites déformations [1], de détection adaptative des surfaces de débit pour les écoulements de Bingham [54] d'approximation spectrale d'opérateurs elliptiques [53], des problèmes elliptiques aux interfaces [50] ou d'obstacle [64], le modèle de plaque de type Kirchhoff–Love [32], la discrétisation des opérateurs elliptiques non-liéaires Leray–Lions [73, 74], ou encore du problème de Brinkman [36] et des problèmes elliptiques hautement oscillant [65]. Dans [63], les auteurs présentent une implémentation générique de la méthode HHO sur des maillages polytopiques de dimension arbitraire. Des extensions plus récentes de la méthode comprennent la version adaptative [88] et *hp* [7], ainsi que le support de mailles courbées [35].

Il est bon de conclure cet état de l'art en soulignant le fait que des liens entre les méthodes HHO et d'autres technologies récentes existent, notamment avec les méthodes de Galerkin Discontinues Hybrides [55, 69], les méthodes Éléments Virtuels mixtes [21] ou non-conformes [18] et les méthodes de Discrétisation du Gradient [91]. La version HHO de plus bas ordre peut être comparée aux Volumes Finies mixtes [90] ou hybrides [96] et également aux méthodes de Différences

Finies Mimétiques [47, 48, 117].

B.2 Application aux problèmes d'interfaces

Hormis les avantages généraux qui ont été discutés à la section précédente, les méthodes HHO possèdent des avantages spécifiques aux problèmes d'interfaces que l'on considère dans ce manuscrit, dont on présente les grandes lignes dans cette section.

Les modèles à interface diffuse

Les modèles à interface diffuse décrivent l'évolution d'un système dans lequel deux (ou possiblement plus) phases non-miscibles sont présentes. Ces modèles sont basés sur une description thermodynamique telle que l'énergie du fluide dépend non seulement de ses variables locales mais également de leur gradient local : un tel fluide est dit doué de *capillarité interne* ; cf. [114]. Beaucoup de procédés industriels impliquent des écoulements de fluides multiphasiques pilotés par les effets capillaires. Les travaux du **Chapitre** 1 ont été effectués dans le cadre d'une collaboration avec Saint–Gobain Recherche, où les modèles à interface diffuse sont utilisés lors de la simulation de phénomènes physiques comme (i) l'encrassement des tubes d'élastomères thermoplastiques utilisés dans la distribution des boissons, ou (ii) au cours de l'élaboration des verres qui, lors des premières étapes de fusion, met en jeu des liquides mouillants sur des grains plus réfractaires à la fusion. L'optimisation de ces procédés passe par une meilleure compréhension des phénomènes locaux qui, compte-tenu des échelles, sont fortement influencés par des forces capillaires.

L'un des avantages des modèles à interface diffuse réside dans le fait que l'interface n'est pas explicitement suivie, mais plutôt décrite au travers d'une fonction de phase régularisée, appelée *paramètre d'ordre*, prenant des valeurs constantes dans chacune des phases (typiquement ± 1) mais qui varie continûment au travers de l'interface sur une longueur caractéristique γ ; cf. Figure B.1a. Comme expliqué dans [42, 113], les modèles à interface diffuse peuvent être vus comme une régularisation des modèles dits *sharp*, où chaque phase est décrite par un système d'EDPs et où les phases communiquent entre elles à l'aide de conditions de transmissions, basées au niveau de l'interface. Dans les modèles *sharp*, l'interface entre les phases est souvent décrite numériquement comme l'ensemble de niveau zéro d'une fonction lisse et le calcul numérique des équations de l'interface nécessite des mailles adaptatives qui s'ajustent à l'interface. En pratique, ces contraintes posent de sérieux défis lors de la simulation d'écoulements qui, comme ceux considérés ici, impliquent un très grand nombre d'interfaces, ainsi

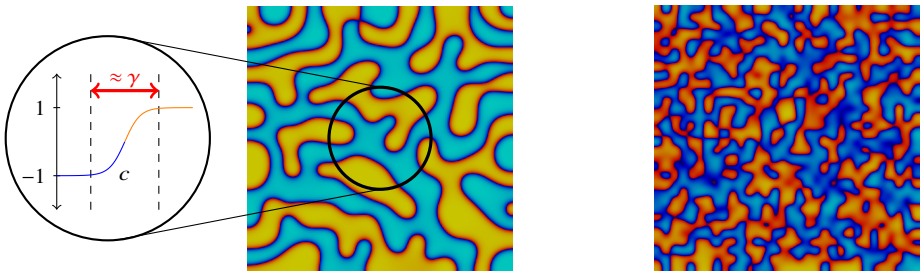

(a) Variation du paramètre d'ordre entre les phases

(b) Premiers instants de simulation d'une décomposition spinodale

Figure B.1: Variation du paramètre d'ordre entre deux phases (gauche) et simulation d'une décomposition spinodale impliquant un grand nombre d'interfaces (droite).

que des phénomènes de séparation et de coalescence ; cf. Figure B.1b, où est affiché une capture des premiers instants de simulation d'une décomposition spinodale. Ces difficultés sont encore plus prononcées lors de simulation en dimension trois. Dans les modèles à interface diffuse en revanche, les discontinuités au niveau de l'interface sont lissées le long de couches d'épaisseur fine et la résolution numérique peut être faite sur des maillages fixes, ce qui, d'un point de vue pratique, implique d'importantes simplifications.

Concernant l'aspect modélisation des interfaces diffuses, la méthode de discrétisation choisie devra remplir certains critères pour pouvoir capturer avec suffisement de précision la séparation de phase. En effet, des zones à fort gradient sont présentes près de l'interface, et si l'on considère le phénomène de décomposition spinodale, ces zones se propagent sur l'ensemble du domaine computationnel, rendant l'adaptation locale inefficace ; cf. Figure B.1b. Comme les méthodes HHO sont fondées sur des espaces polynômiaux discontinus, elles peuvent s'adapter par construction à ces brusques variations entre les phases. De plus, la possibilité d'augmenter l'ordre d'approximation permet de capturer de petits détails également sur des maillages relativement grossiers. Enfin, si l'on considère des problèmes où l'interface est localisée, dans lesquels l'adaptation de maillage est une stratégie efficace, les méthodes HHO restent très flexibles grâce au support de potentiels raffinements non-conformes ou même de déraffinements par aglomération des mailles ; cf. [35, 88].

La contribution principale de cette thèse dans l'approximation numérique des modèles à interface diffuse est le développement et l'analyse d'une nouvelle méthode HHO pour les équations de Cahn–Hilliard, un modèle à interface diffuse décrivant le processus de séparation de phase. En enrichissant les espaces d'inconnus discrets de la méthode HHO originelle de [83], il vient une variante

des méthodes HHO avec laquelle nous pouvons prouver la bonne position de la formulation discrète et des taux de convergences optimaux pour la norme d'énergie de l'erreur de discrétisation. L'analyse s'articule autour de nouveaux résultats d'analyse fonctionnelle discrète adaptés aux espaces hybrides des méthodes HHO, valides en dimension deux et trois, qui sont les inégalités discrètes d'Agmon et Gagliardo–Nirenberg–Poincaré. Un panel complet de cas tests numériques est proposé pour confirmer les résultats théoriques et pour mettre en valeur la capacité de la méthode dans le suivi des interfaces, même en présence de forts champs de convection. Ces travaux ont donné lieu à un article complet paru dans le Journal d'Analyse Numérique SIAM [59], ainsi qu'à un article de conférence [58].

Frontières internes

Le deuxième type d'interfaces que l'on considère dans ce manuscrit sont les interfaces agissant comme frontières internes au domaine. Plus spécifiquement, nous nous focalisons sur l'approximation numérique de l'écoulement et du transport passif en milieu poreux fracturé. Ce thème de recherche est une branche très active des géosciences computationnelles. L'une des raisons principales de cette activité est sans aucun doute le large spectre d'applications qui en découle, comme l'extraction du pétrole, la fracturation hydrolique, le stockage géologique de CO_2 ou encore l'enfouissement souterrain de déchets toxiques/radioactifs.

Les fractures sont omniprésentes en sous-sol et peuvent être causées par des forces tectoniques, changements de température ou par schistosité ; cf. [123]. On retrouve généralement regroupés dans la catégorie des fractures les *craquements*, qui sont des fractures partielles ou incomplètes ; les *fissures*, séparant distinctement différentes surfaces ; les *diaclases*, qui sont des surfaces de fracture sans déplacement ; les *entailles*, qui sont des fissures liées à des tensions de petites échelles, allant de plusieurs centimètres à quelques décimètres de longueur et de quelques millimètres à quelques centimètres de largeur.

Un trait spécifique des fractures est qu'une dimension caractéristique est bien plus petite que les deux autres. Malgré cette différence d'échelle, la présence de fractures dans un milieu poreux peut avoir un impact significatif sur les écoulements. En réalité, les fractures peuvent avoir une perméabilité considérablement différente de celle du milieu poreux dans lequel elles se trouvent, et peuvent de ce fait agir comme des barrières naturelles à l'écoulement, ou au contraire, agir comme des conduits naturels et accélérer le processus de migration des contaminants dangereux. Dans le contexte d'extraction du pétrole par exemple, il a été observé que les fractures près des forages ont pour effet d'augmenter la productivité des puits ; cf. [127] et les références qui en découlent. Un autre exemple, plus d'actualité, est celui de l'isolement géologique des déchets radioactifs. La présence de fractures dans les zones de dépôt, due notamment au

creusement des galeries, peut accéléler considérablement le processus de migration des radionucléides.

Le développement de schémas numériques robustes et fiables pour modéliser de tels phénomènes est d'une importance cruciale afin obtenir des simulations numériques fiables, qui sont un outil primordial pour assurer la protection de l'environnement et celui de l'homme. C'est dans ce contexte délicat que la robustesse des méthodes HHO par rapport à l'anisotropie et l'hétérogénéité des coefficients physiques est un véritable atout. De plus, comme déjà indiqué dans la section précédente, les espaces polynômiaux discontinus sous-jacents aux méthodes HHO peuvent s'adapter aux brusques variations éventuelles des inconnus à travers la fracture. Le support de maillages polytopiques des méthodes HHO est également un atout, puisqu'il permet un traitement limpide des géométries complexes telles que la présence de nœuds pendants ou bien la non-conformité des éléments décrivant la fracture. Enfin, les propriétés de conservation locale des méthodes HHO jouent également un rôle majeur, non seulement dans la reproduction au niveau discret de principes physiques clés, mais aussi lors du couplage de l'écoulement avec le transport.

Les contributions principales de cette thèse sont : (i) le développement et l'analyse d'une méthode HHO pour les modèles réduits d'écoulements de Darcy en milieu poreux fracturé, c'est-à-dire où les fractures sont traitées comme des interfaces ; (ii) l'introduction, l'analyse de stabilité et la validation numérique d'un nouveau modèle réduit basé sur un argument d'énergie, décrivant le transport passif en milieu poreux fracturé. Pour obtenir l'écoulement, nous utilisons une combinaison des formulations mixtes [78] et primales [82] des méthodes HHO pour les problèmes de diffusion variable et prouvons la bonne position de la formulation du problème discret avec des taux de convergences optimaux pour la norme d'énergie de l'erreur de discrétisation. L'analyse repose sur le lien étroit entre l'estimation d'erreur des formulations mixtes et primales. D'autre part, en utilisant la méthode HHO de [75], nous résolvons le nouveau modèle réduit pour le transport passif piloté par un champ de vitesse, solution du problème d'écoulement découplé. Pour appuyer ces travaux, un ensemble de cas tests numériques est proposé, mettant en avant la capacité de la méthode à capturer le comportement de l'écoulement et du phénomène de transport passif qui en découle, en prenant en compte la présence et la perméabilité des fractures. Ces travaux ont donné lieu à un article complet paru dans le Journal sur le Calcul Scientifique SIAM [56] et à un article complet soumis au Journal International de Géomathématiques [57].

List of Figures

Bibliography

[1] M. Abbas, A. Ern, and N. Pignet. *A Hybrid High-Order method for incremental associative plasticity with small deformations*. Submitted. Preprint hal-01768411. 2018 (cited on pages 2, 140).

[2] M. Abbas, A. Ern, and N. Pignet. *Hybrid High-Order methods for finite deformations of hyperelastic materials*. To appear in Comput. Mech. 2018. DOI: 10.1007/s00466-018-1538-0 (cited on pages 2, 140).

[3] R. A. Adams and J. Fournier. "Cone conditions and properties of Sobolev spaces". In: *J. Math. Anal. Appl.* 61.3 (1977), pp. 713–734. ISSN: 0022-247x. DOI: 10.1016/0022-247X(77)90173-1 (cited on pages 32, 41).

[4] R. A. Adams and J. J. F. Fournier. *Sobolev spaces*. Second. Vol. 140. Pure and Applied Mathematics (Amsterdam). Elsevier/Academic Press, Amsterdam, 2003, pp. xiv+305 (cited on page 43).

[5] J. Aghili, S. Boyaval, and D. A. Di Pietro. "Hybridization of mixed high-order methods on general meshes and application to the Stokes equations". In: *Comput. Meth. Appl. Math.* 15.2 (2015), pp. 111–134. DOI: 10.1515/cmam-2015-0004 (cited on pages 2, 57, 140).

[6] J. Aghili and D. A. Di Pietro. "An advection-robust Hybrid High-Order method for the Oseen problem". In: *J. Sci. Comput.* (2018). Published online. DOI: 10.1007/s10915-018-0681-2 (cited on pages 2, 140).

[7] J. Aghili, D. A. Di Pietro, and B. Ruffini. "An *hp*-Hybrid High-Order method for variable diffusion on general meshes". In: *Comput. Meth. Appl. Math.* 17.3 (2017), pp. 359–376. DOI: 10.1515/cmam-2017-0009 (cited on pages 2, 140).

[8] S. Agmon. *Lectures on Elliptic Boundary Value Problems*. Vol. 369. First edition 1965. AMS Chelsea Publications, 2010 (cited on page 32).

[9] A. Agosti, P. Antonietti, P. Ciarletta, M. Grasselli, and M. Verani. "A Cahn–Hilliard–type equation with application to tumor growth dynamics". In: *M2AS Math. Methods Appl. Sci.* 40.18 (2017), pp. 7598–7626. DOI: 10.1002/mma.4548 (cited on page 8).

[10] C. Alboin, J. Jaffré, J. E. Roberts, and C. Serres. "Modeling fractures as interfaces for flow and transport in porous media". In: *Fluid Flow and Transport in Porous Media: Mathematical and Numerical Treatment*. Ed. by Amer. Math. Soc. Contemp. Math. Vol. 295. 2002, pp. 13–24. Rapport IRSN-DES/497 (cited on page 99).

[11] D. Anderson and J. Droniou. "An arbitrary order scheme on generic meshes for miscible displacements in porous media". In: *SIAM J. Sci. Comput.* (2018). Accepted for publication. URL: https://arxiv.org/abs/1707.04038 (cited on pages 21, 100, 113, 125).

[12] P. Angot, F. Boyer, and F. Hubert. "Asymptotic and Numerical Modelling of Flows in Fractured Porous Media". In: *ESAIM: Math. Model Numer. Anal.* 43.2 (2009), pp. 239–275. DOI: 10.1051/m2an/2008052 (cited on pages 61, 99).

[13] P. Angot, T. Gallouët, and R. Herbin. "Convergence of finite volume methods on general meshes for non smooth solution of elliptic problems with cracks". In: *Finite Volumes for Complex Applications II* (1999), pp. 215–222 (cited on pages 56, 99).

[14] P. F. Antonietti, L. Beirão da Veiga, S. Scacchi, and M. Verani. "A C^1 virtual element method for the Cahn–Hilliard equation with polygonal meshes". In: *SIAM J. Numer. Anal.* 54.1 (2016), pp. 34–56. DOI: 10.1137/15M1008117 (cited on pages 10, 24).

[15] P. F. Antonietti, C. Facciola, A. Russo, and M. Verani. *Discontinuous Galerkin approximation of flows in fractured porous media*. MOX report No. 22/2016. Preprint MOX:22-2016. 2016 (cited on pages 18, 57).

[16] P. F. Antonietti, C. Facciola, A. Russo, and M. Verani. *Discontinuous Galerkin approximation of flows in fractured porous media on polytopic grids*. MOX report No. 55/2016. Preprint MOX:55-2016. 2016 (cited on pages 18, 57, 99).

[17] P. F. Antonietti, L. Formaggia, A. Scotti, M. Verani, and N. Verzotti. "Mimetic finite difference approximation of flows in fractured porous media". In: *ESAIM: Math. Model Numer. Anal.* 50.3 (2016), pp. 809–832. DOI: 10.1051/m2an/2015087 (cited on pages 17, 56, 63, 101, 104).

[18] B. Ayuso de Dios, K. Lipnikov, and G. Manzini. "The nonconforming virtual element method". In: *ESAIM: Math. Model Numer. Anal. (M2AN)* 50.3 (2016), pp. 879–904. DOI: 10.1051/m2an/2015090 (cited on pages 3, 140).

[19] V. E. Badalassi, H. D. Ceniceros, and S. Banerjee. "Computation of multiphase systems with phase field models". In: *J. Comput. Phys.* 190 (2003), pp. 371–397. DOI: 10.1016/S0021-9991(03)00280-8 (cited on page 24).

[20] P. Bastian, Z. Chen, R. E. Ewing, R. Helmig, H Jakobs, and V. Reichenberger. "Numerical Simulation of Multiphase Flow in Fractured Porous Media". In: *Numerical Treatment of Multiphase Flows in Porous Media* 52 (1999), pp. 50–68. DOI: 10.1007/3-540-45467-5_4 (cited on pages 56, 99).

[21] L. Beirão da Veiga, F. Brezzi, L. D. Marini, and A. Russo. "Mixed virtual element methods for general second order elliptic problems on polygonal meshes". In: *ESAIM: Math. Model. Numer. Anal.* 50.3 (2016), pp. 727–747. DOI: 10.1051/m2an/2015067 (cited on pages 3, 140).

[22] L. Beirão da Veiga and G. Manzini. "A virtual element method with arbitrary regularity". In: *IMA J. Numer. Anal.* 34.2 (2014), pp. 759–781. DOI: 10.1093/imanum/drt018 (cited on page 24).

[23] M. F. Benedetto, S. Berrone, A. Borio, S. Pieraccini, and S. Scialò. "A Hybrid Mortar Virtual Element Method for Discrete Fracture Network Simulations". In: *J. Comput. Phys.* 306.C (2016), pp. 148–166. DOI: 10.1016/j.jcp.2015.11.034 (cited on pages 18, 57).

[24] M. F. Benedetto, S. Berrone, S. Pieraccini, and S. Scialò. "The Virtual Element Method for discrete fracture network simulations". In: *Comput. Meth. Appl. Mech. Engrg.* 280 (2014), pp. 135–156. DOI: 10.1016/j.cma.2014.07.016 (cited on pages 17, 57, 99).

[25] M. F. Benedetto, S. Berrone, and S. Scialò. "A globally conforming method for solving flow in discrete fracture networks using the Virtual Element Method". In: *Finite Elements in Analysis and Design* 109 (2016), pp. 23–36. DOI: 10.1016/j.finel.2015.10.003 (cited on pages 18, 57).

[26] S. Berrone, S. Pieraccini, and S. Scialò. "Flow simulations in porous media with immersed intersecting fractures". In: *J. Comput. Phys.* 345 (2017), pp. 768–791. DOI: 10.1016/j.jcp.2017.05.049 (cited on page 99).

[27] S. Berrone, S. Pieraccini, and S. Scialò. "Non-stationary transport phenomena in networks of fractures: Effective simulations and stochastic analysis". In: *Comput. Meth. Appl. Mech. Engrg.* 315 (2016), pp. 1098–1112. DOI: 10.1016/j.cma.2016.12.006 (cited on page 99).

[28] S. Berrone, S. Pieraccini, and S. Scialò. "On simulations of discrete fracture network flows with an optimization-based extended finite element method". In: *SIAM J. Sci. Comput.* 35 (2013), pp. 908–935. DOI: 10.1137/120882883 (cited on pages 17, 56).

[29] D. Boffi, M. Botti, and D. A. Di Pietro. "A nonconforming high-order method for the Biot problem on general meshes". In: *SIAM J. Sci. Comput.* 38.3 (2016), A1508–A1537. DOI: 10.1137/15M1025505 (cited on pages 2, 140).

[30] D. Boffi, F. Brezzi, and M. Fortin. *Mixed finite element methods and applications*. Vol. 44. Springer Series in Computational Mathematics. Berlin Heidelberg: Springer, 2013 (cited on page 67).

[31] D. Boffi and D. A. Di Pietro. "Unified formulation and analysis of mixed and primal discontinuous skeletal methods on polytopal meshes". In: *ESAIM: Math. Model Numer. Anal.* 52.1 (2018), pp. 1–28. DOI: 10.1051/m2an/2017036 (cited on pages 3, 57).

[32] F. Bonaldi, D. A. Di Pietro, G. Geymonat, and F. Krasucki. "A Hybrid High-Order method for Kirchhoff–Love plate bending problems". In: *ESAIM: Math. Model Numer. Anal.* 52.2 (2018), pp. 393–421. DOI: 10.1051/m2an/2017065 (cited on pages 2, 140).

[33] W. M. Boon and J. M. Nordbotten. "Robust discretization of flow in fractured porous media". In: *SIAM J. Numer. Anal.* 56.4 (2016), pp. 2203–2233. DOI: 10.1137/17M1139102 (cited on pages 18, 57, 99).

[34] J. Bosch, D. Kay, M. Stoll, and A. J. Wathen. "Fast solvers for Cahn–Hilliard inpainting". In: *SIAM J. Imaging Sci.* 7.1 (2014), pp. 67–97. DOI: 10.1137/130921842 (cited on page 8).

[35] L. Botti and D. A. Di Pietro. "Numerical assessment of Hybrid High-Order methods on curved meshes and comparison with discontinuous Galerkin methods". In: *J. Comput. Phys.* 370 (2018), pp. 58–84. DOI: 10.1016/j.jcp.2018.05.017 (cited on pages 2, 4, 140, 142).

[36] L. Botti, D. A. Di Pietro, and J. Droniou. "A Hybrid High-Order discretisation of the Brinkman problem robust in the Darcy and Stokes limits". In: *Comput. Meth. Appl. Mech. Engrg.* 341 (2018), pp. 278–310. DOI: 10.1016/j.cma.2018.07.004 (cited on pages 2, 140).

[37] L. Botti, D. A. Di Pietro, and J. Droniou. *A Hybrid High-Order method for the incompressible Navier–Stokes equations based on Temam's device*. Submitted. Preprint 1807.07345. July 2018 (cited on pages 2, 140).

[38] M. Botti, D. A. Di Pietro, and P. Sochala. "A Hybrid High-Order method for nonlinear elasticity". In: *SIAM J. Numer. Anal.* 55.6 (2017), pp. 2687–2717. DOI: 10.1137/16M1105943 (cited on pages 2, 140).

[39] M. Botti, D. A. Di Pietro, and P. Sochala. *Analysis of a Hybrid High-Order–discontinuous Galerkin discretization method for nonlinear poroelasticity*. Submitted. Preprint hal-01785810. May 2018 (cited on pages 2, 140).

[40] F. Boyer. "A theoretical and numerical model for the study of incompressible mixture flows". In: *Comput. & Fluids* 31 (2002), pp. 41–68. DOI: 10.1016/S0045-7930(00)00031-1 (cited on page 24).

[41] F. Boyer, L. Chupin, and B. A. Franck. "Numerical study of viscoelastic mixtures through a Cahn–Hilliard fluid". In: *Eur J. Mech. B Fluids* 23 (2004), pp. 759–780. DOI: 10.1016/j.euromechflu.2004.03.001 (cited on page 24).

[42] F. Boyer, C. Lapuerta, S. Minjeaud, B. Piar, and M. Quintard. "Cahn–Hilliard/Navier–Stokes Model for the Simulation of Three-Phase Flows". In: *Transp. Porous. Med.* 82.3 (2010), pp. 463–483. DOI: 10.1007/s11242-009-9408-z (cited on pages 3, 141).

[43] K. Brenner, M. Groza, C. Guichard, G. Lebeau, and R. Masson. "Gradient discretization of hybrid dimensional Darcy flows in fractured porous media". In: *Numer. Math.* 134.3 (2016), pp. 569–609. DOI: 10.1007/s00211-015-0782-x (cited on pages 17, 56).

[44] K. Brenner, M. Groza, L. Jeannin, R. Masson, and J. Pellerin. "Immiscible two-phase Darcy flow model accounting for vanishing and discontinuous capillary pressures: application to the flow in fractured porous media". In: *Comput. Geosci.* 21 (2017). DOI: 10.1007/s10596-017-9675-7 (cited on page 62).

[45] K. Brenner, J. Hennicker, R. Masson, and P Samier. "Hybrid-dimensional modelling of two-phase flow through fractured porous media with enhanced matrix fracture transmission conditions". In: *J. Comput. Phys.* 357 (2018), pp. 100–124. DOI: 10.1016/j.jcp.2017.12.003 (cited on page 99).

[46] K. Brenner, J. Hennicker, R. Masson, and P. Samier. "Gradient discretization of hybrid dimensional Darcy flows in fractured porous media with discontinuous pressure at matrix fracture interfaces". In: *IMA J. Numer. Anal.* 37.3 (2017), pp. 1551–1585. DOI: 10.1093/imanum/drw044 (cited on pages 17, 56, 61, 62).

[47] F. Brezzi, K. Lipnikov, and M. Shashkov. "Convergence of the Mimetic Finite Difference method for diffusion problems on polyhedral meshes". In: *SIAM J. Numer. Anal.* 43.5 (2005), pp. 1872–1896. DOI: 10.1137/040613950 (cited on pages 3, 141).

[48] F. Brezzi, K. Lipnikov, M. Shashkov, and V. Simoncini. "A new discretization methodology for diffusion problems on generalized polyhedral meshes". In: *Comput. Methods Appli. Mech. Engrg.* 196.37–40 (2007), pp. 3682–3692. DOI: 10.1016/j.cma.2006.10.028 (cited on pages 3, 141).

[49] A. Buffa and C. Ortner. "Compact embeddings of broken Sobolev spaces and applications". In: *IMA J. Numer. Anal.* 4.29 (2009), pp. 827–855. DOI: 10.1093/imanum/drn038 (cited on page 30).

[50] E. Burman and A. Ern. "An unfitted Hybrid High-Order method for elliptic interface problems". In: *SIAM J. Numer. Anal.* 56.3 (2018), pp. 1525–1546. DOI: 10.1137/17M1154266 (cited on pages 2, 140).

[51] J. W. Cahn. "On spinoidal decomposition". In: *Acta Metall. Mater.* 9 (1961), pp. 795–801. DOI: 10.1016/0001-6160(61)90182-1 (cited on pages 24, 132).

[52] J. W. Cahn and J. E. Hilliard. "Free energy of a nonuniform system, I, interfacial free energy". In: *J. Chem. Phys.* 28 (1958), pp. 258–267. DOI: 10.1063/1.1744102 (cited on pages 24, 132).

[53] V. Calo, M. Cicuttin, Q. Deng, and Ern. *Spectral approximation of elliptic operators by the Hybrid High-Order method*. Submitted. Preprint hal-01628698. 2018 (cited on pages 2, 140).

[54] K. Cascavita, J. Bleyer, X. Chateau, and A. Ern. *Hybrid discretization methods with adaptive yield surface detection for Bingham pipe flows,* To appear in J. Sci. Comput. 2018. DOI: 10.1007/s10915-018-0745-3 (cited on pages 2, 140).

[55] P. Castillo, B. Cockburn, I. Perugia, and D. Schötzau. "An a priori error analysis of the local discontinuous Galerkin method for elliptic problems". In: *SIAM J. Numer. Anal.* 38 (2000), pp. 1676–1706. DOI: 10.1137/S0036142900371003 (cited on pages 3, 140).

[56] F. Chave, D. A. Di Pietro, and L. Formaggia. "A Hybrid High-Order method for Darcy flows in fractured porous media". In: *SIAM J. Sci. Comput.* 40.2 (2018), A1063–A1094. DOI: 10.1137/17M1119500 (cited on pages 6, 55, 99, 100, 110, 112, 123, 144).

[57] F. Chave, D. A. Di Pietro, and L. Formaggia. *A Hybrid High-Order method for passive transport in fractured porous media*. Submitted. Preprint hal-01784181. 2018 (cited on pages 6, 97, 144).

[58] F. Chave, D. A. Di Pietro, and F. Marche. "A Hybrid High-Order method for the convective Cahn–Hilliard problem in mixed form". In: *Finite Volumes for Complex Applications VIII – Hyperbolic, Elliptic and Parabolic Problems*. Ed. by C. Cancès and P. Omnes. 2017, pp. 517–526. DOI: 10.1007/978-3-319-57394-6_58 (cited on pages 5, 7, 131, 143).

[59] F. Chave, D. A. Di Pietro, F. Marche, and F. Pigeonneau. "A Hybrid High-Order method for the Cahn–Hilliard problem in mixed form". In: *SIAM J. Numer. Anal.* 54.3 (2016), pp. 1873–1898. DOI: 10.1137/15M1041055 (cited on pages 5, 6, 23, 132, 143).

[60] L. Cherfils, H. Fakih, and A. Miranville. "A Cahn—Hilliard system with a fidelity term for color image inpainting". In: *J. Math. Imaging Vis.* 54.1 (2016), pp. 171–131. DOI: 10.1007/s10851-015-0593-9 (cited on page 8).

[61] L. Cherfils, H. Fakih, and A. Miranville. "A complex version of the Cahn–Hilliard equation for grayscale image inpainting". In: *Multiscale Model. Simul.* 15.1 (2017), pp. 575–605. DOI: 10.1137/15M1040177 (cited on page 8).

[62] A. Chernyshenko, M. Olshanskii, and Y. Vassilevski. "A Hybrid Finite Volume-Finite Element Method for bulk-surface coupled problems". In: *J. Comput. Phys.* 352 (2016), pp. 516–533. DOI: 10.1016/j.jcp.2017.09.064 (cited on page 99).

[63] M. Cicuttin, D. A. Di Pietro, and A. Ern. "Implementation of Discontinuous Skeletal methods on arbitrary-dimensional, polytopal meshes using generic programming". In: *J. Comput. Appl. Math.* (2017). Published online. DOI: 10.1016/j.cam.2017.09.017 (cited on pages 2, 140).

[64] M. Cicuttin, A. Ern, and T. Gudi. *Discontinuous-Skeletal methods with linear and quadratic reconstructions for the elliptic obstacle problem*. Submitted. Preprint hal-01718883. 2018 (cited on pages 2, 140).

[65] M. Cicuttin, A. Ern, and S. Lemaire. *A Hybrid High-Order Method for Highly Oscillatory Elliptic Problems*. To appear in Comput. Methods Appl. Math. 2018. DOI: 10.1515/cmam-2018-0013 (cited on pages 2, 140).

[66] K. H. Coats, W. D. George, C. Chu, and B. E. Marcum. "Three-Dimensional Simulation of Steamflooding". In: *Society of Petroleum Engineers* 14.6 (1974), pp. 573–592. DOI: 10.2118/4500-PA (cited on page 77).

[67] B. Cockburn, D. A. Di Pietro, and A. Ern. "Bridging the Hybrid High-Order and Hybridizable Discontinuous Galerkin methods". In: *ESAIM: Math. Model Numer. Anal. (M2AN)* (2015). Published online. DOI: 10.1051/m2an/2015051 (cited on pages 25, 29).

[68] B. Cockburn, D. A. Di Pietro, and A. Ern. "Bridging the Hybrid High-Order and Hybridizable Discontinuous Galerkin methods". In: *ESAIM: Math. Model Numer. Anal.* 50.3 (2016), pp. 635–650. DOI: 10.1051/m2an/2015051 (cited on page 3).

[69] B. Cockburn, J. Gopalakrishnan, and R. Lazarov. "Unified hybridization of discontinuous Galerkin, mixed, and continuous Galerkin methods for second order elliptic problems". In: *SIAM J. Numer. Anal.* 47.2 (2009), pp. 1319–1365. DOI: 10.1137/070706616 (cited on pages 3, 25, 140).

[70] M. I. M. Copetti and C. M. Elliott. "Numerical analysis of the Cahn–Hilliard equation with a logarithmic free energy". In: *Numer. Math.* 63 (1992), pp. 39–65. DOI: 10.1007/BF01385847 (cited on pages 10, 24).

[71] C. D'Angelo and A. Scotti. "A Mixed Finite Element Method for Darcy Flow in Fractured Porous Media with non-matching Grids". In: *ESAIM: Math. Model Numer. Anal.* 46.2 (2012), pp. 465–489. DOI: 10.1051/m2an/2011148 (cited on page 99).

[72] M. Del Pra, A. Fumagalli, and A. Scotti. "Well-posedness of fully coupled fracture/bulk Darcy flow with XFEM". In: *SIAM J. Numer. Anal.* 55.2 (2017), pp. 785–811. DOI: 10.1137/15M1022574 (cited on pages 101, 104).

[73] D. A. Di Pietro and J. Droniou. "$W^{s,p}$-approximation properties of elliptic projectors on polynomial spaces, with application to the error analysis of a Hybrid High-Order discretisation of Leray–Lions problems". In: *Math. Models Methods Appl. Sci.* 27.5 (2017), pp. 879–908. DOI: 10.1142/S0218202517500191 (cited on pages 2, 11, 65, 75, 140).

[74] D. A. Di Pietro and J. Droniou. "A Hybrid High-Order method for Leray–Lions elliptic equations on general meshes". In: *Math. Comp.* 86.307 (2017), pp. 2159–2191. DOI: 10.1090/mcom/3180 (cited on pages 2, 11, 26, 28, 30, 65, 75, 86, 140).

[75] D. A. Di Pietro, J. Droniou, and A. Ern. "A discontinuous-skeletal method for advection-diffusion-reaction on general meshes". In: *SIAM J. Numer. Anal.* 53.5 (2015), pp. 2135–2157. DOI: 10.1137/140993971 (cited on pages 2, 6, 11, 100, 117, 132, 140, 144).

[76] D. A. Di Pietro, J. Droniou, and G. Manzini. "Discontinuous Skeletal Gradient Discretisation methods on polytopal meshes". In: *J. Comput. Phys.* 355 (2018), pp. 397–425. DOI: 10.1016/j.jcp.2017.11.018 (cited on page 3).

[77] D. A. Di Pietro and A. Ern. "A hybrid high-order locking-free method for linear elasticity on general meshes". In: *Comput. Meth. Appl. Mech. Engrg.* 283 (2015), pp. 1–21. DOI: 10.1016/j.cma.2014.09.009 (cited on pages 2, 51, 57, 71, 139, 140).

[78] D. A. Di Pietro and A. Ern. "Arbitrary-order mixed methods for heterogeneous anisotropic diffusion on general meshes". In: *IMA J. Numer. Anal.* 37.1 (2016), pp. 40–63. DOI: 10.1093/imanum/drw003 (cited on pages 2, 6, 57, 67, 68, 73, 76, 140, 144).

[79] D. A. Di Pietro and A. Ern. "Discrete functional analysis tools for discontinuous Galerkin methods with application to the incompressible Navier–Stokes equations". In: *Math. Comp.* 79 (2010), pp. 1303–1330. DOI: 10.1090/S0025-5718-10-02333-1 (cited on page 30).

[80] D. A. Di Pietro and A. Ern. "Equilibrated tractions for the Hybrid High-Order method". In: *C. R. Acad. Sci. Paris, Ser. I* 353 (2015), pp. 279–282. DOI: 10.1016/j.crma.2014.12.009 (cited on pages 2, 140).

[81] D. A. Di Pietro and A. Ern. *Mathematical aspects of discontinuous Galerkin methods*. Vol. 69. Mathématiques & Applications (Berlin) [Mathematics & Applications]. Springer, Heidelberg, 2012, pp. xviii+384. ISBN: 978-3-642-22979-4. DOI: 10.1007/978-3-642-22980-0 (cited on pages 26, 27, 65, 85, 132).

[82] D. A. Di Pietro, A. Ern, and S. Lemaire. "A review of Hybrid High-Order methods: formulations, computational aspects, comparison with other methods". In: *Building bridges: Connections and challenges in modern approaches to numerical partial differential equations*. Ed. by G. Barrenechea, F. Brezzi, A. Cangiani, and M. Georgoulis. Lecture Notes in Computational Science and Engineering 114. Springer, 2016. Chap. 7. DOI: 10.1007/978-3-319-41640-3_7 (cited on pages 2, 6, 57, 140, 144).

[83] D. A. Di Pietro, A. Ern, and S. Lemaire. "An arbitrary-order and compact-stencil discretization of diffusion on general meshes based on local reconstruction operators". In: *Comput. Meth. Appl. Math.* 14.4 (2014). Open access (editor's choice), pp. 461–472. DOI: 10.1515/cmam-2014-0018 (cited on pages 2, 4, 25, 31, 51, 57, 58, 70, 76, 88, 89, 115, 139, 140, 142).

[84] D. A. Di Pietro, A. Ern, A. Linke, and F. Schieweck. "A discontinuous skeletal method for the viscosity-dependent Stokes problem". In: *Comput. Meth. Appl. Mech. Engrg.* 306 (2016), pp. 175–195. DOI: 10.1016/j.cma.2016.03.033 (cited on pages 2, 140).

[85] D. A. Di Pietro, B. Kapidani, R. Specogna, and F. Trevisan. "An arbitrary-order discontinuous skeletal method for solving electrostatics on general polyhedral meshes". In: *IEEE Transactions on Magnetics* 53.6 (2017), pp. 1–4. DOI: 10.1109/TMAG.2017.2666546 (cited on pages 2, 140).

[86] D. A. Di Pietro and S. Krell. "A Hybrid High-Order method for the steady incompressible Navier–Stokes problem". In: *J. Sci. Comput.* 74.3 (2018), pp. 1677–1705. DOI: 10.1007/s10915-017-0512-x (cited on pages 2, 140).

[87] D. A. Di Pietro and S. Lemaire. "An extension of the Crouzeix–Raviart space to general meshes with application to quasi-incompressible linear elasticity and Stokes flow". In: *Math. Comp.* 84.291 (2015), pp. 1–31. DOI: 10.1090/S0025-5718-2014-02861-5 (cited on page 45).

[88] D. A. Di Pietro and R. Specogna. "An a posteriori-driven adaptive Mixed High-Order method with application to electrostatics". In: *J. Comput. Phys.* 326.1 (2016), pp. 35–55. DOI: 10.1016/j.jcp.2016.08.041 (cited on pages 2, 4, 140, 142).

[89] D. A. Di Pietro and R. Tittarelli. "Numerical Methods for PDEs. State of the Art Techniques". In: ed. by L. Formaggia D. A. Di Pietro A. Ern. SEMA-SIMAI 15. Springer, 2018. Chap. An introduction to Hybrid High-Order methods. ISBN: 978-3-319-94675-7 (Print) 978-3-319-94676-4 (eBook). URL: http://arxiv.org/abs/1703.05136 (cited on page 116).

[90] J. Droniou and R. Eymard. "A Mixed Finite Volume scheme for anisotropic diffusion problems on any grid". In: *Numer. Math.* 105.1 (2006), pp. 35–71. DOI: 10.1007/s00211-006-0034-1 (cited on pages 3, 140).

[91] J. Droniou, R. Eymard, T. Gallouët, C. Guichard, and R. Herbin. *The gradient discretisation method*. Vol. 82. Mathématiques et Applications. Springer, 2018. ISBN: 978-3-319-79041-1 (Softcover) 978-3-319-79042-8 (eBook). DOI: 10.1007/978-3-319-79042-8 (cited on pages 3, 140).

[92] J. Droniou, J. Hennicker, and R. Masson. *Numerical analysis of a two-phase flow discrete fracture model*. Submitted. Preprint arXiv:1612.07373. 2016 (cited on pages 17, 56).

[93] Q. Du and R. A. Nicolaides. "Numerical analysis of a continuum model of phase transition". In: *SIAM J. Numer. Anal.* 28 (1991), pp. 1310–1322. DOI: 10.1137/0728069 (cited on pages 10, 24).

[94] C. M. Elliott, D. A. French, and F. A. Milner. "A second order splitting method for the Cahn–Hilliard equation". In: *Numer. Math.* 54 (1989), pp. 575–590. DOI: 10.1007/BF01396363 (cited on pages 10, 24).

[95] A. Ern and J.-L. Guermond. *Theory and practice of finite elements*. Vol. 159. Applied Mathematical Sciences. New York: Springer-Verlag, 2004, pp. xiv+524. ISBN: 0-387-20574-8 (cited on page 86).

[96] R. Eymard, T. Gallouët, and R. Herbin. "Discretization of heterogeneous and anisotropic diffusion problems on general nonconforming meshes. SUSHI: a scheme using stabilization and hybrid interfaces". In: *IMA J. Numer. Anal.* 30 (2010), pp. 1009–1043. DOI: 10.1093/imanum/drn084 (cited on pages 3, 140).

[97] I. Faille, E. Flauraud, F. Nataf, S. Pégaz-Fiornet, F. Schneider, and F. Willien. "A new fault model in geological basin modelling. Application of finite volume scheme and domain decomposition methods". In: *Finite Volumes for Complex Applications III* (2002), pp. 543–550 (cited on pages 56, 99).

[98] X. Feng and O. A. Karakashian. "Fully discrete dynamic mesh discontinuous Galerkin methods for the Cahn–Hilliard equation of phase transition". In: *Math. Comp.* 76 (2007), pp. 1093–1117. DOI: 10.1090/S0025-5718-07-01985-0 (cited on pages 10, 24).

[99] X. Feng and A. Prohl. "Numerical analysis of the Cahn–Hilliard equation and approximation for the Hele–Shaw problem". In: *Interfaces Free Bound.* 7 (2005), pp. 1–28. DOI: 10.4171/IFB/111 (cited on pages 10, 24).

[100] L. Formaggia, A. Quarteroni, and C. Vergara. "On the physical consistency between three-dimensional and one-dimensional models in haemodynamics". In: *J. Comput. Phys.* 244 (2013), pp. 97–112. DOI: 10.1016/j.jcp.2012.08.001 (cited on page 99).

[101] A. Fumagalli. "Numerical modelling of flows in fractured porous media by the XFEM method". PhD thesis. Polytechnic University of Milan, Italy, 2012 (cited on pages 13, 14).

[102] A. Fumagalli and E. Keilegavlen. "Dual Virtual Element Method for Discrete Fractures Networks". In: *SIAM J. Sci. Comput.* 40.1 (2018), B228–B258. DOI: 10.1137/16M1098231 (cited on page 99).

[103] A. Fumagalli and A. Scotti. "A reduced model for flow and transport in fractured porous media with non-matching grids". In: *Numerical Mathematics and Advanced Applications 2011*. 2013, pp. 499–507. DOI: 10.1007/978-3-642-33134-3_53 (cited on page 99).

[104] H. Garcke, K. F. Lam, R. Nürnberg, and S. Emanuel. "A multiphase Cahn–Hilliard–Darcy model for tumour growth with necrosis". In: *Math. Models Methods Appl. Sci.* 28.3 (2018), pp. 525–577. DOI: 10.1142/S0218202518500148 (cited on page 8).

[105] H. Garcke, K. F. Lam, E. Sitka, and V. Styles. "A Cahn–Hilliard–Darcy model for tumour growth with chemotaxis and active transport". In: *Math. Models Methods Appl. Sci.* 26.6 (2016), pp. 1095–1148. DOI: 10.1142/S0218202516500263 (cited on page 8).

[106] G. N. Gatica. *A simple introduction to the mixed finite element method*. SpringerBriefs in Mathematics. Theory and applications. Springer, Cham, 2014, pp. xii+132. ISBN: 978-3-319-03694-6; 978-3-319-03695-3. DOI: 10.1007/978-3-319-03695-3 (cited on page 85).

[107] A. A. Golovin, A. A. Nepomnyashchy, S. H. Davis, and M. A. Zaks. "Convective Cahn–Hilliard models: from coarsening to roughening". In: *Phys. Rev. Lett.* 86.8 (2001), pp. 1550–1553. DOI: 10.1103/PhysRevLett.86.1550 (cited on page 10).

[108] P. Grisvard. *Singularities in Boundary Value Problems*. Paris: Masson, 1992. DOI: 10.1007/978-3-0348-8625-3_8 (cited on pages 38, 53).

[109] S. Gross, M. A. Olshanskii, and A. Reusken. "A trace finite element method for a class of coupled bulk-interface transport problems". In: *ESAIM: Math. Model Numer. Anal.* 49.5 (2015), pp. 1303–1330. DOI: 10.1051/m2an/2015013 (cited on page 99).

[110] R. Guo and Y. Xu. "Efficient solvers of discontinuous Galerkin discretization for the Cahn–Hilliard equations". In: *J. Sci. Comput.* 58 (2014), pp. 380–408. DOI: 10.1007/s10915-013-9738-4 (cited on pages 10, 24).

[111] R. Herbin and F. Hubert. "Benchmark on discretization schemes for anisotropic diffusion problems on general grids". In: *Finite Volumes for Complex Applications V*. Ed. by R. Eymard and J.-M. Hérard. John Wiley & Sons, 2008, pp. 659–692 (cited on page 45).

[112] J. G. Heywood and R. Rannacher. "Finite-element approximation of the nonstationary Navier–Stokes problem. Part IV: error analysis for second-order time discretization". In: *SIAM J. Numer. Anal.* 27.2 (1990), pp. 353–384. DOI: 10.1137/0727022 (cited on page 33).

[113] D. Jacqmin. "Calculations of two phase Navier–Stokes flows using phase-field modelling". In: *J. Comput. Phys.* 155 (1999), pp. 96–127. DOI: 10.1006/jcph.1999.6332 (cited on pages 3, 24, 141).

[114] D. Jamet, D. Torres, and J. U. Brackbill. "On the theory and computation of surface tension: the elimination of parasitic currents through energy conservation in the Second-Gradient Method". In: *J. Comput. Phys.* 182 (2002), pp. 262–276. DOI: 10.1006/jcph.2002.7165 (cited on pages 3, 141).

[115] D. Kay, V. Styles, and E. Süli. "Discontinuous Galerkin finite element approximation of the Cahn–Hilliard equation with convection". In: *SIAM J. Numer. Anal.* 47.4 (2009), pp. 2660–2685. DOI: 10.1137/080726768 (cited on pages 10, 11, 24–26).

[116] J. Kim, K. Kang, and J. Lowengrub. "Conservative multigrid methods for Cahn–Hilliard fluids". In: *J. Comput. Phys.* 193 (2004), pp. 357–379. DOI: 10.1016/j.jcp.2003.07.035 (cited on page 24).

[117] Y. Kuznetsov, K. Lipnikov, and M. Shashkov. "The Mimetic Finite Difference method on polygonal meshes for diffusion-type problems". In: *Comput. Geosci.* 8.4 (2004), pp. 301–324. DOI: 10.1007/s10596-004-3771-1 (cited on pages 3, 141).

[118] C. Lehrenfeld. "Hybrid Discontinuous Galerkin methods for solving incompressible flow problems". PhD thesis. Rheinisch-Westfälischen Technischen Hochschule Aachen, 2010 (cited on page 31).

[119] K. Lipnikov and G. Manzini. "A high-order mimetic method on unstructured polyhedral meshes for the diffusion equation". In: *J. Comput. Phys.* 272 (2014), pp. 360–385. DOI: 10.1016/j.jcp.2014.04.021 (cited on page 25).

[120] V. Martin, J. Jaffré, and J. E. Roberts. "Modeling fractures and barriers as interfaces for flow in porous media". In: *SIAM J. Matrix Analysis and Applications* 26.5 (2005), pp. 1667–1691. DOI: 10.1137/S1064827503429363 (cited on pages 14, 56, 99).

[121] D. W. Peaceman. "Improved treatment of dispersion in numerical calculation of multidimensional miscible displacement". In: *Soc. Petrol. Eng. J.* 6 (1966), pp. 213–216. DOI: 10.2118/1362-PA (cited on page 125).

[122] A. Scotti, L. Formaggia, and F. Sottocasa. "Analysis of a mimetic finite difference approximation of flows in fractured porous media". In: *ESAIM: Math. Model Numer. Anal.* (2017). Accepted for publication. DOI: 10.1051/m2an/2017028 (cited on pages 61, 99, 104).

[123] "Fractured Formation Evaluation". In: *Fundamentals of Well-Log Interpretation*. Ed. by O. Serra. Vol. 15. Developments in Petroleum Science. Elsevier, 1986. Chap. 11, pp. 499–543. DOI: 10.1016/S0376-7361(08)70588-0 (cited on pages 5, 143).

[124] C. Templier. "Etude expérimentale de la précipitation dans les alliages à base d'aluminium obtenus par implantation ionique de Cu, Ag et Xe." PhD thesis. Université de Poitiers, 1987 (cited on page 7).

[125] M. R. Todd, P. M. O'Dell, and G. J. Hirasaki. "Methods for Increased Accuracy in Numerical Reservoir Simulators". In: *Society of Petroleum Engineers* 12.6 (1972), pp. 515–530. DOI: 10.2118/3516-PA (cited on page 77).

[126] S. Tremaine. "On the Origin of Irregular Structure in Saturn's Rings". In: *The Astron. J.* 125.2 (2003), pp. 894–901. DOI: 10.1086/345963 (cited on page 8).

[127] J. Wang, X. Wang, W. Xu, C. Lu, W. Dong, and C. Zhang. *Productivity Analysis of Volume Fractured Vertical Well Model in Tight Oil Reservoirs*. Mathematical Problems in Engineering, Volume 2017, Article ID 9589321, 14 pages. DOI: 10.1155/2017/9589321 (cited on pages 5, 143).

[128] J. Wang and X. Ye. "A weak Galerkin element method for second-order elliptic problems". In: *J. Comput. Appl. Math.* 241 (2013), pp. 103–115. DOI: 10.1016/j.cam.2012.10.003 (cited on page 25).

[129] G. N. Wells, E. Kuhl, and K. Garikipati. "A discontinuous Galerkin method for the Cahn–Hilliard equation". In: *Journal of Computational Physics* 218.2 (2006), pp. 860–877. DOI: 10.1016/j.jcp.2006.03.010 (cited on pages 10, 24).

[130] X. Wu, G. J. Zwieten, and K. G. Zee. "Stabilized second-order convex splitting schemes for Cahn–Hilliard models with application to diffuse-interface tumor-growth models". In: *J. Numer. Methods Bio. Engrg.* 30.2 (2014), pp. 180–203. DOI: 10.1002/cnm.2597 (cited on page 8).

[131] Y. Xia, Y. Xu, and C.-W. Chu. "Local discontinuous Galerkin methods for the Cahn–Hilliard type equations". In: *Journal of Computational Physics* 227.1 (2007), pp. 472–491. DOI: 10.1016/j.jcp.2007.08.001 (cited on pages 10, 24).

Résumé

Le but de cette thèse est de développer et d'analyser les méthodes Hybrides d'Ordre Élevé (HHO: Hybrid High-Order, en anglais) pour des problèmes d'interfaces. Nous nous intéressons à deux types d'interfaces (*i*) les interfaces diffuses, et (*ii*) les interfaces traitées comme frontières internes du domaine computationnel. La première moitié de ce manuscrit est consacrée aux interfaces diffuses et plus précisément aux célèbres équations de Cahn–Hilliard qui modélisent le processus de séparation de phase par lequel les deux composants d'un fluide binaire se séparent pour former des domaines purs en chaque composant. Dans la deuxième moitié, nous considérons des modèles à dimension hybride pour la simulation d'écoulements de Darcy et de transports passifs en milieu poreux fracturé, dans lequel la fracture est considérée comme un hyperplan (d'où le terme hybride) qui traverse le domaine computationnel.

Mots clés: méthodes Hybrides d'Ordre Élevé, maillages polytopiques, ordre d'approximation arbitraire, équations de Cahn–Hilliard, séparation de phase, écoulement en milieu poreux fracturé, écoulement de Darcy, déplacement miscible, transport passif, formulation mixte, formulation primale, analyse fonctionnelle discrète.

Abstract

The purpose of this Ph.D. thesis is to design and analyse Hybrid High-Order (HHO) methods on some interface problems. By interface, we mean (*i*) diffuse interface, and (*ii*) interface as an immersed boundary. The first half of this manuscrit is dedicated to diffuse interfaces, more precisely we consider the so called Cahn–Hilliard problem that models the process of phase separation, by which the two components of a binary fluid spontaneously separate and form domains pure in each component. In the second half, we deal with the interface as an immersed boundary and consider a hybrid dimensional model for the simulation of Darcy flows and passive transport in fractured porous media, in which the fracture is considered as an hyperplane that crosses our domain of interest.

Keywords: Hybrid High–Order methods, polyhedral meshes, arbitrary order, Cahn–Hilliard equation, phase separation, fractured porous media flow, Darcy flow, miscible displacement, passive transport, mixed formulation, primal formulation, discrete functional analysis.